

# Coherent Control of Molecular Dynamics with Shaped Femtosecond Pulses

Dissertation  
an der Fakultät für Physik  
der Ludwig-Maximilians-Universität München

Dirk Zeidler

München, 19.10.2001

Dissertation eingereicht am 19.10.2001

1. Gutachter: Prof. Dr. Dr. h.c. K.-L. Kompa
2. Gutachter: Prof. Dr. E. Riedle

Tag der mündlichen Prüfung: 24.5.2002

*A few weeks of development and testing  
can save a whole afternoon in the library.*



Publications in context with this work:

1. "Adaptive compression of tunable pulses from a non-collinear type OPA to below 20fs by feedback-controlled pulse shaping",  
D. Zeidler, T. Hornung, D. Proch, and M. Motzkus,  
*Appl. Phys. B* **70**, S125-S131 (2000)
2. "Optimal control of one-and two-photon transitions with shaped femtosecond pulses and feedback",  
T. Hornung, R. Meier, D. Zeidler, K.-L. Kompa, D. Proch, and M. Motzkus,  
*Appl. Phys. B* **70**, 277-284 (2000)
3. "Evolutionary algorithms and their application to optimal control studies",  
D. Zeidler, S. Frey, K.-L. Kompa, and M. Motzkus,  
*Phys. Rev. A* **64**, 023420 (2001)
4. "A new high resolution femtosecond pulse shaper",  
G. Stobrawa, M. Hacker, T. Feurer, D. Zeidler, M. Motzkus, and F. Reichel,  
*Appl. Phys. B* **72**, 627 (2001)
5. "Optical Parametric Amplification of Shaped White Light Continuum",  
D. Zeidler, T. Witte, D. Proch, and M. Motzkus,  
*Opt. Lett.*, **26**, 1921 (2001)
6. "Programmable amplitude and phase modulated fs laser pulses in the mid-infrared",  
T. Witte, D. Zeidler, D. Proch, and M. Motzkus,  
*Opt. Lett.* **27**, 131 (2002)
7. "Amplification of Tailored White Light Continuum"  
D. Zeidler, T. Witte, D. Proch, and M. Motzkus,  
*Appl. Phys. B*, in print
8. "Optimal Control of Ground-State Dynamics in Polymers",  
D. Zeidler, S. Frey, W. Wohlleben, M. Motzkus, F. Busch, T. Chen, W. Kiefer, A. Materny,  
*J. Chem. Phys.* **116**, 5231 (2002)



# Zusammenfassung

Kohärente Kontrolle von Moleküldynamik befaßt sich mit der Steuerung quantenmechanischer Systeme mittels ultrakurzer, zeitlich geeignet geformter Laserfelder. Dabei wird die Kohärenz des Laserfeldes ausgenutzt, um durch phasenrichtige Überlagerung von Wellenfunktionen konstruktive Interferenz für eine definierte Ziel-Wellenfunktion zu erreichen. Das Ziel kohärenter Kontrolle, die selektive Präparation eines Zielzustandes, ist eine der Hauptvoraussetzungen für modenselektive Chemie.

Der auf eine spezifische Anregung hin maßgeschneiderte Laserpuls, welcher als Störung das System vom Anfangs- in den Zielzustand treibt, kann bei komplexen Systemen in der Regel nicht mehr vorab durch quantenmechanische Rechnungen bestimmt werden, da oftmals nicht einmal mehr der Hamilton-Operator des Systems bekannt ist. Ein Ansatz ist, das erforderliche Laserfeld in einer Regelschleife zu bestimmen, welche ein aus dem Experiment gewonnenes Signal als Rückkopplung benutzt. Diese Optimierungsschleife wird solange durchlaufen, bis ein den Anforderungen genügender Puls gefunden wurde. Bisherige Experimente auf diesem Gebiet beschränkten sich zu Beginn dieser Arbeit größtenteils auf den Wellenlängenbereich von Ti:Sa Lasern und deren Harmonischen.

Diese Arbeit befaßt sich mit Grundlagen der rückgekoppelten Formung ultrakurzer Laserpulse im Hinblick sowohl auf die Etablierung ihrer technischen Voraussetzungen in geeigneten Wellenlängenbereichen als auch der Anwendung auf geeignete Modellsysteme. Die Rückkopplungsschleife wurde zunächst eingehend an einem einfachen Optimierungsexperiment mit bekanntem Ergebnis getestet, und erst dann wurden Kontrollexperimente mit steigender Komplexität durchgeführt. Aus den optimierten Pulsen wurde ein physikalisches Verständnis des Optimierungsvorganges abgeleitet.

Im ersten Teil dieser Arbeit wurde die erforderliche Technik so weit implementiert und standardisiert, daß weiterführende Kontrollexperimente auf die Module der Regelschleife ohne weiteres zurückgreifen können. Zu den technischen Voraussetzungen gehörte unter anderem die Frequenzkonvertierung der Ti:Sa Laserpulse bei 800 nm in einen für die zu untersuchenden Systeme geeigneten Wellenlängenbereich. Dazu wurden nichtkollineare optisch-parametrische Verstärkerstufen im Rahmen dieser Arbeit in verschiedenen Ausführungen gebaut. Sie erzeugen routinemäßig im sichtbaren Wellenlängenbereich durchstimmbare Pulse mit sub-20 fs Zeitdauer. Die erforderlichen Nachweismethoden zur Analyse ultrakurzer Pulse wurden ebenfalls implementiert.

Pulsformer mit zylindrischen statt sphärischen Spiegeln wurden im Rahmen dieser Arbeit zur Modulation ultrakurzer Pulse aufgebaut und in ihrer Funktionsweise in Theorie und Experiment erklärt. Die in Zusammenarbeit mit der Arbeitsgruppe von Thomas Feurer an der Universität Jena und der Jenoptik GmbH entstandene Flüssigkristallmaske, das zentrale Element unserer Pulsformer, welche die Erzeugung komplexerer Pulsformen als mit bisher erhältlichen Masken erlaubt, wurde vorgestellt.

Durch Implementierung eines Pulsformers in eine nichtkollineare optisch-parametrische Verstärkerstufe zur Formung des Weißlichts, welches als Seed für den Verstärkungsprozeß dient, konnten u. a. phasenkohärente Zweifarbdoppelpulse mit einstellbaren Wellenlängen, Zeitabständen und relativen Phasen zwischen den beiden Pulsen demonstriert werden. Es wurde nachgewiesen, daß eine Phase, welche dem Seed aufgeprägt wird, während des Verstärkungsprozesses erhalten bleibt. Kontrollexperimente, welche Pulse mit den obigen Eigenschaften in elektronisch ansteuerbarer Form benötigen, werden mit diesem Aufbau erstmals möglich.

Eine evolutionäre Strategie, welche als Optimierungsalgorithmus in der Rückkopplungsschleife diente, wurde entwickelt und anhand eines einfachen Optimierungsexperimentes, der Pulscompression durch Phasenkompensation, sowohl im Experiment als auch in der Simulation getestet.

Im zweiten Teil der Arbeit wurde als Anwendungsbeispiel für rückgekoppelte Optimierungen die Pulskompression von breitbandigen Spektren im sub-20fs-Bereich gewählt. Dieses Experiment diente gleichzeitig als ein weiterer Test für das Verhalten der Regelschleife im Grenzfall eines physikalisch unerreichbaren Optimierungszieles.

Es wurde gezeigt, daß eine geeignete Abbildung zwischen den dem Algorithmus zugänglichen Optimierungsparametern und den Steuerparametern des Pulsformers ein Instrument darstellt, um aus den optimalen elektrischen Feldern Rückschlüsse auf die physikalischen Eigenschaften des Systems ziehen zu können. Eine solche Parametrisierung unterstützt eine Herauspräparation des gesuchten Effektes, der die Optimierung letztendlich bewerkstelligt, und beeinflusst Konvergenzgeschwindigkeit und Rauschunempfindlichkeit der Optimierung.

Sogenannte „bright“ und „dark pulses“, d. h. Pulse, die in einem Medium absorbiert bzw. ungehindert transmittiert werden, wurden am Zweiphotonen-Übergang  $3s \rightarrow 5s$  in Natrium demonstriert. Mit einer Parametrisierung der Phasenfunktion der Pulse wurden die für die Eigenschaften „bright“ und „dark“ verantwortlichen, bereits bekannten physikalischen Prozesse, nämlich symmetrische bzw. antisymmetrische spektrale Phase, im Optimierungsprozeß implementiert, und das Konzept der Parametrisierung daran getestet.

Ein Beispiel für die modenselektive Präparation von Vibrationszuständen in einem vielatomigen Molekül ist die Kontrolle der Grundzustandsdynamik in Polydiazetylen. In einem Raman-Schritt, bei welchem der Stokes-Puls geformt wird, konnte die Besetzung der Gerüstschwingungen von Polydiazetylen im Grundzustand kontrolliert werden. Dabei wurde neben dem Anregungs- und Stokes-Puls ein Abtast-Puls eingestrahlt, der in dieser CARS-Anordnung (coherent anti-Stokes Raman scattering) ein Anti-Stokes-Signal erzeugte, welches frequenz aufgelöst als Rückkopplung diente. Von drei bzw. vier innerhalb der Laserbandbreite anregbaren Moden konnten einzelne Moden sowie Kombinationsmoden mit hoher Selektivität angeregt werden. Auch hier halfen spezielle Parametrisierungen, einen der für die Kontrolle zuständigen Prozesse, ein Tannor-Rice-Schema, zu identifizieren. Da sowohl die Amplituden als auch die Phasen der einzelnen Moden beeinflusst werden konnten, ist eine Wellenpaketfokussierung zu einer vorgegebenen Zeit möglich, was gleichbedeutend mit der Erzeugung von Lokalmode und somit der Kontrolle einer unimolekularen Reaktion ist.

Ausgehend von der Kontrolle einer unimolekularen Reaktion wurden die Möglichkeiten der Kontrolle einer bimolekularen Reaktion diskutiert. Der als Beispiel gewählte  $\text{NaH}_2$  - Stoßkomplex stellt ein geeignetes Objekt für zukünftige Kontrollexperimente an bimolekularen Reaktionen und speziell konischen Durchschneidungen dar. Erste zeitaufgelöste Experimente wurden vorgestellt.



# Summary

Coherent control of molecular dynamics deals with the steering of quantum mechanical systems with suitably shaped ultrashort laser fields. The coherence properties of the laser field are exploited to achieve constructive interference for a predefined target wave function via a phase-correct superposition of wave functions. The goal of coherent control, the selective preparation of a target state, is an important prerequisite for mode-selective chemistry.

The laser pulse tailored to drive the system from the initial to the target state as a perturbation can in general not be determined by a quantum-mechanical calculation, since usually even the Hamiltonian of the system is unknown. A practical alternative is to determine the required shape of the laser field in a feedback-controlled regulation loop which uses a signal derived from the experiment as feedback. The loop is repeated until a pulse that suits the requirements is obtained. Experiments in this area have until recently mostly been limited to the wavelength regime of Ti:Sa lasers and their fundamentals.

This work deals with the fundamentals of feedback-controlled shaping of ultrashort laser pulses with respect to both establishment of its technical prerequisites and its application to suitable model systems. The feedback loop has been tested using a simple optimization experiment with known outcome; then it was applied to experiments of progressively increasing complexity. From the optimized pulses, physical insight into the optimization process has been gained.

In the first part of this work, the required technology has been implemented and standardized such that control experiments might employ it as a standard tool. One of the technical prerequisites was the frequency conversion of the 800 nm Ti:Sa laser pulses to a wavelength range suited to the particular systems. To this end, non-collinear optical parametric amplifiers have been built in different designs that routinely produce tunable sub-20 fs pulses in the visible. The characterization techniques for ultrashort pulses have been implemented as well.

Pulse shapers with cylindrical instead of spherical mirrors have been implemented for the modulation of broadband pulses, and their functionality has been explained both theoretically and experimentally. A new liquid crystal device, the core of our pulse shapers, has been developed in cooperation with the group of Thomas Feurer at the Universität Jena and the Jenoptik GmbH which allows for the generation of more complex pulse shapes than with other commercially available devices to date.

Using a pulse shaper to modulate the white light continuum that serves as the seed for the non-collinear optical parametric amplifier, generation of phase-locked two-color double pulses has been achieved, with tunable wavelengths, delays, and relative carrier phases between the single pulses. The basic principle, phase conservation during optical parametric amplification, has been demonstrated. With this setup, control experiments which require pulses with the above described attributes in electronically controllable form are possible for the first time.

An evolutionary strategy used as the optimization algorithm in the feedback loop has been programmed and characterized both in simulation and experiment using a simple optimization experiment, namely pulse recompression by phase compensation.

In the second part of this work, pulse recompression of ultra-broadband spectra in the sub-20fs regime serves as an example of utility of feedback-controlled optimization. This experiment simultaneously served as a further test of the feedback loop in the limit of a physically unreachable optimization goal.

It has been demonstrated that a suitable parameterization of the electric field, implemented by a mapping of the optimization parameters adjusted by the algorithm to the physical parameters

controlling the liquid crystal mask affords a means of acquiring physical knowledge from the retrieved optimal electric fields. A parameterization helps to dissect the physical processes mediating the control process, thereby assuring fast, secure convergence and robustness against signal noise.

So-called "bright" and "dark" pulses, i.e. pulses that are absorbed by a medium or transmitted, respectively, have been demonstrated for the case of the two-photon transition  $\text{Na}(3s \rightarrow 5s)$ . The physical constraints responsible for pulses being either "bright" or "dark", namely a symmetric or anti-symmetric spectral phase, have been incorporated in the parameterization with the purpose of testing the concept of parameterization for such studies.

An example of mode-selective preparation of vibrational states in a polyatomic molecule is the control of the ground state dynamics in polydiacetylene. In a Raman step with a shaped Stokes pulse, the population of the backbone vibrations of polydiacetylene in its ground state could be controlled. A consecutive probe pulse in a CARS (coherent anti-Stokes Raman scattering) arrangement generates an anti-Stokes signal which, once frequency-resolved, served as feedback. Of the three or four modes, respectively, accessible within the pulse bandwidth, single modes as well as combinations of modes could be excited with high selectivity. Again, suitable parameterizations helped to identify one of the processes responsible for the control as a Tannor-Rice scheme. Since both the amplitude and the phase of each mode could be influenced, the focusing of a wave packet at a predefined time, or, equivalently, the generation of local modes represents the control of a unimolecular reaction.

Starting from the control of a unimolecular reaction, the possibilities of controlling a bimolecular reaction were addressed. The  $\text{NaH}_2$  collision complex was chosen as a suitable system for the control of bimolecular reactions generally and a conical intersection in particular. First time-resolved experiments have been presented.

# Contents

<b>Introduction</b>	<b>1</b>
<b>I Coherent Control Technology</b>	<b>5</b>
<b>1 Non-collinear optical parametric amplification</b>	<b>6</b>
1.1 Frequency-Mixing . . . . .	6
1.2 Non-collinear frequency mixing . . . . .	10
1.3 Generation of ultrashort pulses . . . . .	11
1.4 Experimental realization . . . . .	13
<b>2 Femtosecond pulse shaping</b>	<b>16</b>
2.1 Filtering in the time and frequency domain . . . . .	16
2.2 4f-configuration . . . . .	17
2.3 Theoretical model of a pulse shaper . . . . .	18
2.4 Pulse shaping with LC-SLMs . . . . .	23
2.5 The high resolution femtosecond pulse shaping device . . . . .	28
2.6 Alternative pulse shaping methods . . . . .	31
<b>3 Amplification of tailored white light continuum</b>	<b>35</b>
3.1 Experiment . . . . .	36
3.2 Phase and amplitude transfer . . . . .	38
3.3 Summary . . . . .	42
<b>4 Evolutionary algorithms for coherent control</b>	<b>43</b>
4.1 Evolutionary algorithms . . . . .	43
4.2 The role of steering parameters . . . . .	48
4.3 The role of parameterization . . . . .	57
4.4 Summary . . . . .	59
<b>II Coherent Control Experiments</b>	<b>60</b>
<b>5 Adaptive broadband pulse compression</b>	<b>61</b>
5.1 Compression of pulses from a non-collinear OPA . . . . .	61
5.2 Hollow fiber compression . . . . .	68
5.3 Summary . . . . .	68
<b>6 Control of two-photon transitions: Dark and bright pulses</b>	<b>70</b>
6.1 Experiment . . . . .	70
6.2 Results . . . . .	70
6.3 Summary . . . . .	77

---

<b>7</b>	<b>Control of Ground State Dynamics in Polydiacetylene</b>	<b>78</b>
7.1	Introduction . . . . .	78
7.2	Experiment . . . . .	79
7.3	Results . . . . .	82
7.4	Summary . . . . .	95
<b>8</b>	<b>Towards control of bimolecular reactions: Dynamics of the NaH<sub>2</sub> exciplex</b>	<b>96</b>
8.1	High pressure Alkali vapor cell . . . . .	99
8.2	Experiment . . . . .	100
8.3	Discussion . . . . .	105
	<b>Summary and outlook</b>	<b>106</b>
<b>A</b>	<b>The Titanium:Sapphire laser system</b>	<b>109</b>
<b>B</b>	<b>Characterization of ultrashort pulses</b>	<b>110</b>
B.1	Autocorrelation . . . . .	111
B.2	Cross-correlation . . . . .	112
B.3	Frequency-resolved optical gating . . . . .	112
	<b>Abbreviations</b>	<b>117</b>
	<b>Bibliography</b>	<b>118</b>

# Introduction

Mode-selective control of chemical reactions has been the ambitious goal of many years of investigation. Chemistry, which can be viewed as the breaking and making of bonds, classically attempts to influence the equilibrium in the formation of products from educts by macroscopic parameters such as temperature, pressure, concentration, etc. Nevertheless, this macroscopic provision of activation energy for a chemical reaction invokes the problem of selectivity since the activation energy is equipartitioned over all bonds and not only those that must be activated. Consequently, a chemical reaction often yields a broad variety of by-products.

With the invention of lasers, mode-selective chemistry aimed to minimize the amount of by-products by activating only those bonds which are essential for the reaction. This goal has been achieved only in a few small systems for two reasons: First, it is usually necessary to excite the system to a higher vibrational state in order to overcome the activation energy. The anharmonicity of the potential, however, impedes the excitation of more than one vibrational transition with a narrow-band laser. Second, intramolecular vibrational energy redistribution [1] in highly excited molecules dissipates the energy into other vibrational modes on an ultrashort time scale.

Therefore, the ability to selectively deposit energy with lasers is not sufficient for control. Nevertheless, another property of the laser field, its coherence, enables control of quantum mechanical interferences. An initial wave function is transferred to a target wave function by phase-coherently manipulating the quantum system such that constructive interference is achieved for the target state. Thus, the dynamics of a chemical or physical process is steered towards this predefined quantum state. Three schemes have been demonstrated to achieve quantum control in small systems:

(1) *Phase control* as suggested by Brumer and Shapiro [2] uses two phase-locked cw lasers resonant to a single transition between the states  $|a\rangle$  and  $|b\rangle$  by a one- and a multi-photon excitation, respectively (Fig. 1a). These two excitation paths add coherently, and in direct analogy with the double slit experiment, the resulting transition probability depends on the relative phase between the two lasers. Experimentally, this has been demonstrated in atoms and molecules [3, 4].

(2) With *STIRAP* (stimulated Raman scattering involving adiabatic passage), 100% population transfer between two levels  $|a\rangle$  and  $|b\rangle$  can be achieved [5]. STIRAP uses an intermediate level  $|c\rangle$  and two laser fields to couple the initial and final state (Fig. 1b). The intermediate level is coupled to the final level by a laser (Stokes) field before the intermediate level is coupled to the initial level with the pump field, with a small temporal overlap between the pulses. With the Stokes laser preceding the pump pulse, the system is prepared at the beginning of the interaction in a trapped state and remains there such that the population is directly transferred from the initial to the final state while the population of the intermediate level is negligible throughout.

(3) *Time domain control* has been proposed by Tannor, Kosloff, and Rice [6] and exploits the dynamics of the system in the excited state for control (Fig. 1c). This so-called Tannor-Rice pump-dump scheme usually incorporates two pulses with different frequencies: the first pulse (pump) excites the system to the excited potential energy surface; the second pulse (dump) is suitably delayed and transfers population to a target state  $|b\rangle$ . The one-dimensional control parameter is the delay between pump and dump pulse. This scheme has been successfully incorporated in controlling the fragmentation of molecules [7–9].

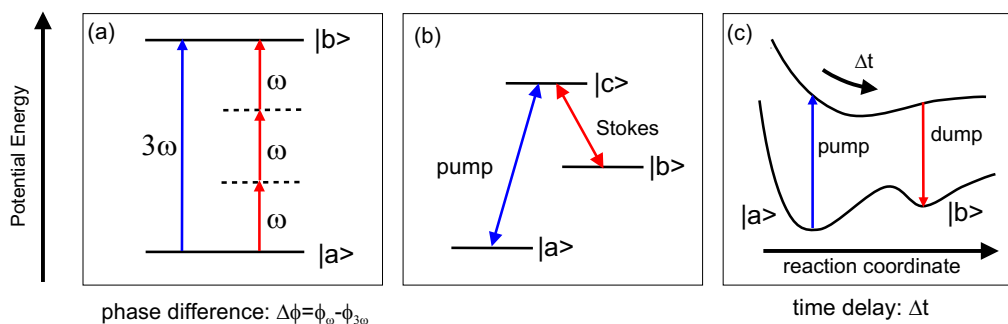


**Figure 1:** Schemes for coherent control using one control parameter: (a) Brumer-Shapiro phase control, (b) STIRAP as proposed by Bergmann *et al.*, (c) Tannor-Kosloff-Rice time-domain control.

The approaches (1)-(3) have been used successfully only in small systems because they feature relatively simple control fields with only one control parameter (time or phase) each. For larger molecules with complex potential energy surfaces it is conceivable that more control parameters, i.e. more complex control fields, are necessary.

From a theoretical point of view, finding the electric field which produces the desired target wave function is feasible if the Hamiltonian of the quantum mechanical system is known. In principle then, it remains to synthesize this particular electric field in the laboratory and to verify the calculation. However, if the required electric fields cannot be produced with sufficient fidelity, a comparison between experiment and theory is not really meaningful. For complex molecules, moreover, the Hamiltonian may not be known or cannot be approximated at all. Even if the Hamiltonian is known, the calculation of the optimal electric field may be intractable on a quantum mechanical level.

To overcome these difficulties, Judson and Rabitz proposed that the optimal electric field be determined recursively within a feedback-controlled experiment [10]. In their approach, an ultrashort laser pulse excites a sample, and a signal which is characteristic of the system (e.g. a target state) is monitored, as depicted in Fig. 2 [11, 12]. The amplitude of this probe signal serves as feedback for the optimization algorithm, which controls a pulse shaper and proposes a new pulse. The feedback signal of this modified pulse serves again as input for the algorithm, which proposes yet another pulse, and so forth until some convergence criterion is met. Since no a-priori knowledge of the physical system is necessary, this feedback scheme is applicable even if a theoretical investigation of the system is intractable on a quantum mechanical level. From the optimized laser field, insight into the physics of the system under investigation can be gained. The hardware for the implementation of such a feedback loop experiment comprises a source for ultrashort laser pulses, a computer-controlled pulse shaper and an optimization algorithm. The temporal shaping of ultrashort pulses is realized by complex filtering of their spectrum in the Fourier domain. Of critical importance in this concept is a reliable optimization algorithm which efficiently spots the global optimum in a multidimensional parameter space under the influence of experimental noise. Evolutionary algorithms have proven robust under such conditions.

Pioneering examples of such optimizations were reported by the groups of Gerber [13] and Wilson [14], who reported control of the dissociation of a complex organometallic compound and of the fluorescence excitation of a dye molecule, respectively. Subsequent experiments on different types of systems followed:

(1) Applications to atoms were the excitation of Rydberg wave packets [15], two-photon transitions [16] and the control of high harmonics generation [17, 18].

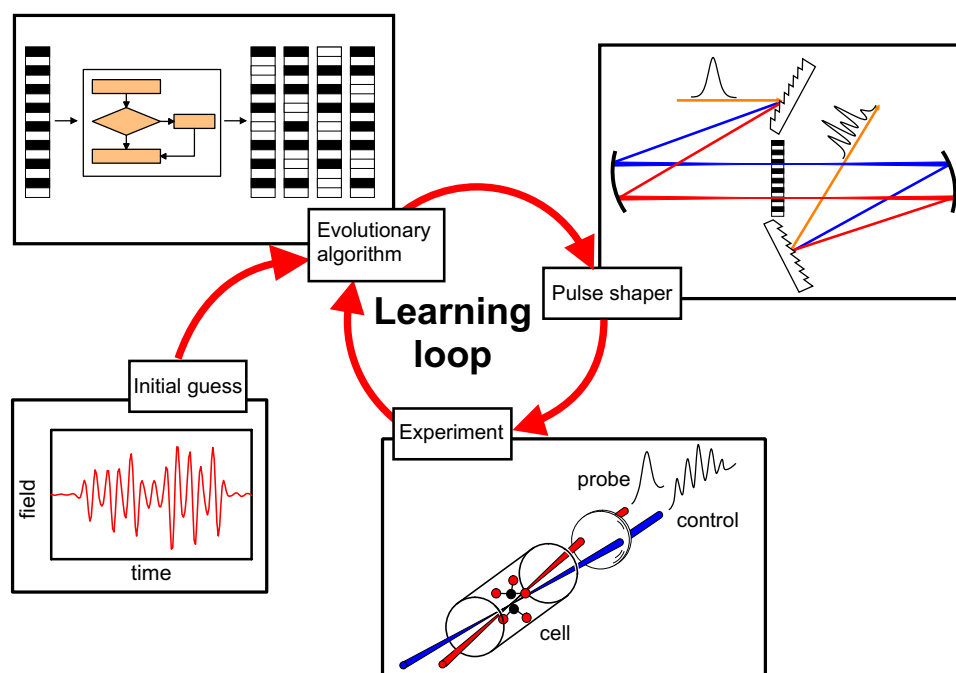


**Figure 2:** A closed-loop process for teaching a laser to control quantum systems. The loop is initiated with either an educated initial guess or even a random field. A laser control field design is created with a pulse shaper and then applied to the sample. The response of the system is measured and fed back to an optimization algorithm which suggests an improved field design and so forth until the objective is satisfactorily achieved.

(2) For molecular systems, control efforts can be divided into two main families: (a) Control of dissociation yields, as for dissociation of CsCl [19, 20], Fe(CO)<sub>5</sub> [21], CpFe(CO)<sub>2</sub>Cl [13, 22], CpMn(CO)<sub>3</sub> [23], and several small carbohydrate derivatives [24]. (b) Control of molecular dynamics, such as in K<sub>2</sub> [25, 26], CO<sub>2</sub> and SF<sub>6</sub> [27], Li<sub>2</sub> [28], Na<sub>2</sub>K [29], and CCl<sub>4</sub> and methanol [30].

This work investigates and establishes the fundamentals of feedback-controlled experiments with respect to both technological aspects and applications to the control of complex molecules.

The task of controlling molecular dynamics in a complex system has to be broken up into several steps. Pulse generation and pulse shaping must be provided in an appropriate wavelength range. For the implementation of the feedback loop, an optimization algorithm must be realized, and the reliability of the feedback loop must be tested with a simple control system. With this tested loop in hand, a series of control experiments on model systems of increasing complexity, from pulse compression over atomic systems to complex molecular systems, can be performed stepwise using the acquired knowledge. The process responsible for the optimization is identified in each experiment via the use of a parameterization in order to gain physical insight into the control process which is, after all, the purpose of control experiments.

The thesis is divided into a more technically oriented part and an experimental part of four chapters each. The first, technical, part covers the description of the fundamental prerequisites for coherent control experiments such as ultrashort pulse sources, pulse shaping, and optimization algorithms.

Chapter one explains the generation of ultrashort pulses in the visible via non-collinear optical parametric amplification.

Chapter two gives an introduction to the possibilities and limitations of pulse shaping with pixelized modulators.

A broadband source and a pulse shaper can be combined to form a novel device capable of producing high-energy pulses such as two-color phase-locked double pulses with adjustable colors, delay, and phase. White-light shaping and its underlying principle, phase conservation during parametric amplification, is demonstrated in chapter three.

In chapter four, the optimization algorithm steering the pulse shaper is presented. Pulse recompression serves as the testing environment for the algorithm, ensuring secure convergence of the subsequent feedback-controlled experiments. The principles and advantages of a parameterization, which is a mapping between the optimization parameters accessible to the algorithm and the physical steering parameters of the pulse shaper, are demonstrated.

The experimental part opens in chapter five with a description of the adaptive compression of ultrashort pulses from a non-collinear OPA to below 20fs.

Chapter six moves from the pure control of electric fields to the control of an atomic system, specifically the  $\text{Na}(3s \rightarrow 5s)$  two-photon transition, for which "bright" and "dark" pulses, i.e. pulses that do or do not effect a two-photon transition, are produced with the feedback approach.

Control of a unimolecular reaction in a complex molecular system is demonstrated in chapter seven, wherein the control of vibrational ground state dynamics in a polymer is presented. The excitation of normal modes can be steered with high precision, which allows for wave packet focusing into a local mode.

Chapter eight reports on a promising candidate for the control of bimolecular reactions at the example of the  $\text{NaH}_2$  collision complex which represents the one of simplest conceivable bimolecular reactions. Preliminary results of time-resolved experiments on the collision complex are presented.



**Part I**

**Coherent Control Technology**

## 1

# Non-collinear optical parametric amplification

The technique of producing fs pulses with mode-locked fs Ti:Sa lasers has become sophisticated over the last decade. High power output pulses are easily produced via chirped pulse amplification in regenerative amplifiers, turn-key devices that are commercially available and contain almost no user-serviceable parts.

Nevertheless, these devices are only capable of producing pulses at Ti:Sa wavelengths in the NIR around 800 nm and their harmonics. This is sufficient for non-resonant experiments where only the enormous temporary energy density (on the order of  $10^{21}$  W/cm<sup>2</sup> nowadays for high-end laser facilities) of a femtosecond laser pulse is of interest. In most experiments, though, it is obligatory to adapt the wavelengths to the molecule under study. Hence, the frequency of the ultrashort pulses must usually be converted.

## 1.1 Frequency-Mixing

Frequency mixing occurs in nonlinear media where the principle of linear superposition of electromagnetic waves breaks down at sufficiently high electric fields. The reason for this is the nonlinearity of the electron binding forces within the atoms at high field strengths, and therefore the nonlinear dependence of the polarization of matter on the electric field. As a result, the presence of a strong field changes the properties of matter (such as the refractive index  $n$ ) of the material through which it travels and thereby influences the propagation of other waves coincident with the primary field.

Frequency mixing can be viewed in two different schemes: sum frequency mixing / generation (SFM, SFG) and difference frequency mixing / generation (DFM, DFG). In the photon picture, SFM is equivalent to the fusion of two low-energy photons to one high-energy photon, whereas DFG is described by the fission of a high-energy photon into two low energy photons. From this point of view, it is immediately clear that conservation of energy

$$\omega_3 = \omega_1 + \omega_2 \tag{1.1}$$

has to be met as well as the conservation of momentum, which is commonly written as  $\Delta k = 0$ , where  $\Delta k$  is the so-called *phase mismatch* (written in its scalar form here for simplicity)

$$\Delta k = k_1 + k_2 - k_3. \tag{1.2}$$

In the case of DFG, the photon with the highest energy is the pump photon, denoted here and further on with the index three. Photon one and two are called signal and idler photon. This will be explained later.

In the wave picture, the interaction of these three photons is modeled by a system of partial differential equations derived from the nonlinear wave equation (see, e.g. [31–33])

$$\frac{dA_1}{dz} = +i\kappa A_2^* A_3 \exp(-i\Delta kz) \quad (1.3)$$

$$\frac{dA_2^*}{dz} = -i\kappa A_1 A_3^* \exp(+i\Delta kz) \quad (1.4)$$

$$\frac{dA_3}{dz} = +i\kappa A_2 A_1 \exp(+i\Delta kz). \quad (1.5)$$

Here,  $\kappa$  is a constant which is proportional to the corresponding element  $d$  of the susceptibility tensor, and  $A = \sqrt{n/\omega}E$ , with  $E$  being the amplitude of the field.

Several assumptions have been used in order to derive these equations, such as Kleinman's symmetry rule (all coefficients of the susceptibility tensor with permuted indices are equal [34]), monochromatic, scalar waves  $E \sim \exp(i(kz - \omega t))$  propagating in  $z$ -direction, no absorption, and no changes of polarization of each individual wave during the interaction. For ultrashort pulses, the right sides of Eqs. 1.3-1.5 are replaced by integrals [35].

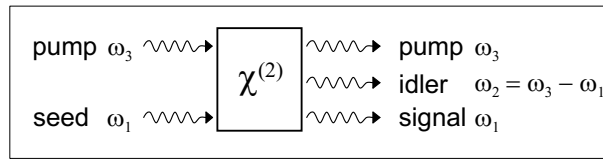


**Figure 1.1:** Frequency mixing scheme of the optical parametric amplification process. From here on, the indices (1), (2), and (3) always correspond to signal, idler, and pump pulse, respectively

For the special case of optical parametric amplification, see Fig. 1.1, it can be assumed that no depletion of the pump wave at  $\omega_3$  occurs. Then 1.3-1.4 simplifies to

$$\frac{dA_1}{dz} = +i\kappa A_3(0)A_2^* \exp(-i\Delta kz) \quad (1.6)$$

$$\frac{dA_2^*}{dz} = -i\kappa A_3(0)A_1 \exp(+i\Delta kz) \quad (1.7)$$

For  $\Delta k = 0$ , the solution of these equations is

$$A_1(z) = A_1(0)\cosh(\kappa A_3(0)z) \quad (1.8)$$

$$A_2^*(z) = -iA_1(0)\sinh(\kappa A_3(0)z). \quad (1.9)$$

The evolution of the intensities  $I_{1,2}(z) \propto |A_{1,2}(z)|^2$  is illustrated in Fig. 1.2:

It is observed that with increasing intensity of the signal wave at  $\omega_1$ , the intensity of a second wave at  $\omega_2$  also increases. The second wave is essential to carry away the surplus energy and momentum in the conversion of a pump photon into a signal photon. Because this wave is usually only an experimentally undesired, "idle" by-product, it is called idler. The accumulation of the idler is easily understood since signal and idler can exchange their roles via the inverse process wherein a pump photon and an idler photon create a signal photon. Therefore, an increasing signal creates an increasing idler, and vice versa. For this process, it is essential that signal and idler waves interfere constructively, which requires  $\Delta k = 0$ .

For  $\Delta k \neq 0$ , an expression for the conversion efficiency  $\eta$  between pump and signal wave is found by approximating  $A_2(z)$  and  $A_3(z) = \text{const}$  in Eqs. 1.3 and integrating Eq. 1.3 from  $z = 0$  to  $z = L$ ,

$$\eta \propto d_{eff}^2 L^2 \text{sinc}^2\left(\frac{\Delta k L}{2}\right) \quad (1.10)$$

where  $L$  is the interaction length which is usually given by the crystal length and  $d_{eff}$  the effective nonlinearity. Eq. 1.10 reveals two important facts:

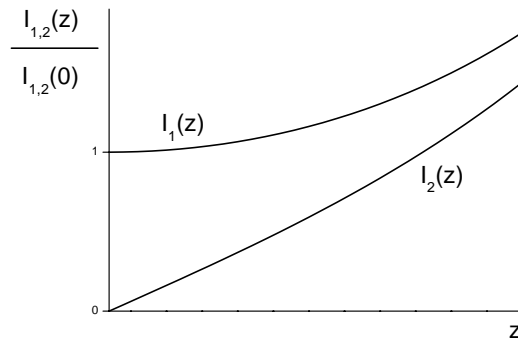


**Figure 1.2:** Evolution of signal (1) and idler (2) wave intensity vs propagation length in a collinear optical parametric amplifier

(1) The conversion efficiency is maximized for  $\Delta k = 0$ . Therefore, phase-matching is essential, which means that after the "splitting" of a pump photon into a signal and idler photon no net photon momentum remains.

(2) The conversion efficiency scales with the square of the interaction length  $L$ . This means that for high amplification gain, thick crystals should be used. However, two complications result: For ultrashort pulses, the acceptance bandwidth described by the "sinc" term in Eq. 1.10 may become too small when the crystal length exceeds the spatial dimensions of the pulse in direction of propagation. Also long crystals cause additional pulse broadening by idler walk-off, since the idler's group velocity is higher than that of the signal as depicted in Fig. 1.3. Since these are undesired effects, thin crystals are commonly used in collinear OPAs. The resulting conversion efficiency is relatively low, so typical setups comprise a multi-stage amplification wherein the idler is split off before each amplification stage.

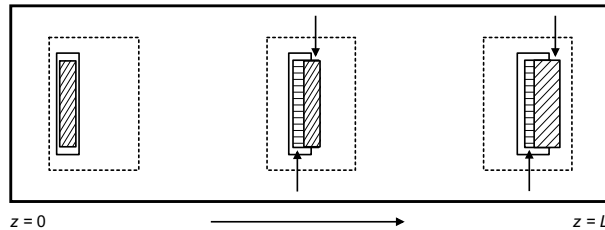


**Figure 1.3:** Pulse broadening due to idler walk-off in a collinear beam geometry: the idler (diagonally hatched box) pulse travels from left to right at a higher group velocity than signal (empty box) and pump (dashed box) pulse. Snapshots are taken at three different times. The spatially advanced idler generates signal by frequency mixing via the inverse mixing process  $\omega_2 = \omega_3 - \omega_1$  (upper arrows), which in turn again generates idler and so on. On the trailing edge of signal, idler is generated via the normal process  $\omega_1 = \omega_3 - \omega_2$  (lower arrows, horizontally hatched box). Since these waves cannot interfere constructively, collinear DFM cannot produce significantly higher bandwidths (or shorter pulses) than the input pulses.

Phase-matching is achieved via the dependence of the refractive index  $n$  on the orientation of polarization of the incoming wave to the crystal axis  $c$ . Beams that are polarized in the plane of the  $c$ -axis and the beam itself are called ordinary and are subject to the ordinary refractive index  $n_o$ , whereas beams polarized perpendicular to that plane experience the extraordinary refractive index  $n_e$ . A beam that is polarized at an angle  $\theta$  to the  $c$ -axis experiences the refractive index

$$n(\theta) = \left( \frac{\cos^2(\theta)}{n_o^2} + \frac{\sin^2(\theta)}{n_e^2} \right)^{-\frac{1}{2}} \quad (1.11)$$

The wavelength dependence of  $n_e$  and  $n_o$  can be approximated by Sellmeier's equation (e.g. for

BBO [36, 37]):

$$n_o^2 = 2.7405 + \frac{0.0184}{\lambda^2 - 0.0179} - 0.0155\lambda^2 \quad (1.12)$$

$$n_e^2 = 2.3730 + \frac{0.0128}{\lambda^2 - 0.0156} - 0.0044\lambda^2 \quad (1.13)$$

where  $\lambda$  must be inserted in units of  $\mu\text{m}$ . With the crystal angle  $\theta$ , it is possible to match the indices of refraction of signal and pump or to match the phases.

For the operation of this scheme, different polarizations of the pump, seed and idler have to be used. These classify the different types of phase-matching, as shown in Tab. 1.1.

Type	Signal	Idler	Pump
I	o	o	e
IIa	o	e	e
IIb	e	o	e

Table 1.1: Different types of phase-matching, "o" and "e" refer to ordinary and extraordinary polarization, respectively.

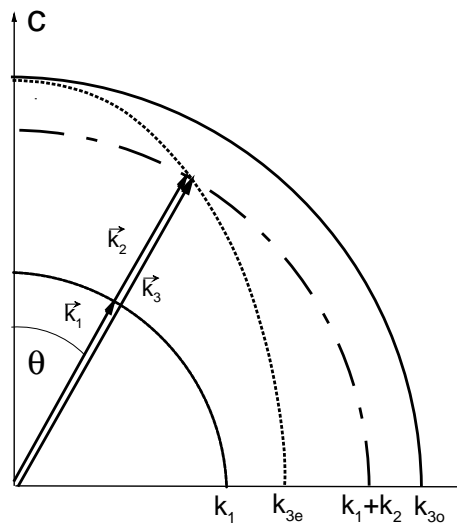


**Figure 1.4:** Phase matching (type I, ooe) in a negative uniaxial crystal, i.e.  $n_o > n_e$ , via the polarization dependent refractive index.  $\theta$  denotes the angle between pump polarization (extraordinary) and crystal axis  $c$ .

For a plane light wave propagating in a uniaxial crystal, the wave vector  $\vec{k}$  only matches the Poynting vector in the special cases  $\theta = 0$  and  $\theta = \pi/2$ . The direction of the Poynting vector, which is the direction of energy flux, is given by the normal to the tangent that touches the  $n(\theta)$ -curve at its intersection with the  $\vec{k}$ -vector. The angular difference between these two directions is denoted as the *walk-off angle* and is given for a negative uniaxial crystal [35]

$$\tan \rho = \left( \frac{n_o}{n_e} \right)^2 \tan \theta - \theta \quad (1.14)$$

Technically, optical parametric amplification [38–44] is performed by producing a broad seed continuum, i.e. by white light continuum (WLC) generation via focusing of ultrashort pulses in a medium, and subsequent amplification in a frequency mixing process. Phase-matching is achieved for the desired output wavelength by the choice of the angle  $\theta$  between the pump polarization and the crystal axis  $c$ , see Fig.1.4. The angle  $\theta$  is thus the means of wavelength

selection used in common collinear OPA design. Because of the effects arising from the different group velocities of signal and idler as described in Fig. 1.3, the necessarily thin crystals require a complicated multi-pass amplification setup.

## 1.2 Non-collinear frequency mixing

To generate pulses significantly shorter than the input pulses, it is necessary to increase their spectral width. Therefore, the amplification process via frequency mixing has to be chosen such that the amplification bandwidth encompasses a wide spectrum. As discussed, the limitation of collinear setups is the group velocity mismatch between signal and idler. Since in a collinear beam geometry the number of free parameters (crystal orientation) is not sufficient to ensure both phase-matching and group velocity matching, a second parameter has to be introduced. This second parameter may be the angle between pump and seed beam. This non-collinear beam geometry approach for ultrabroadband-phasematching is sketched in Fig. 1.5 and has been proposed first by Hache and coworkers [45].

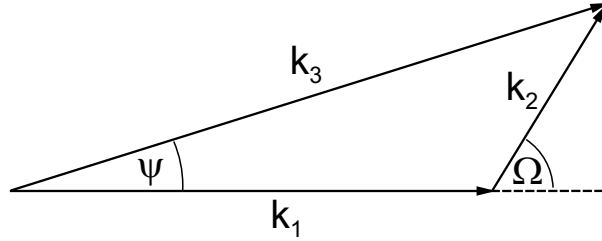


**Figure 1.5:** Arrangement of seed, pump, and idler wave vector in the non-collinear setup.

In order to account for the non-collinear beam geometry, the phase-matching condition has to be rewritten in vectorial notation,

$$\Delta\vec{k} = \vec{k}_1 + \vec{k}_2 - \vec{k}_3 \quad (1.15)$$

Mathematically speaking, broadband operation means that the phase-matching condition  $\Delta\vec{k} = 0$  is not only satisfied for one seed wavelength  $\lambda = \lambda_1^0$ , but for a wavelength range around  $\lambda_1^0$  [38, 42]. Writing  $\Delta\vec{k} = \Delta\vec{k}(\lambda_1)$  as a Taylor series around  $\lambda_1^0$ ,

$$\Delta\vec{k}(\lambda_1) = \Delta\vec{k}_0 + \frac{\partial\Delta\vec{k}}{\partial\lambda_1}\Delta\lambda_1 + \frac{1}{2}\frac{\partial^2\Delta\vec{k}}{\partial\lambda_1^2}(\Delta\lambda_1)^2 + \dots \quad (1.16)$$

with  $\Delta\vec{k}_0 = \Delta\vec{k}(\lambda_1^0)$  and  $\Delta\lambda_1 = \lambda_1 - \lambda_1^0$ , a first approximation for broadband amplification leads not only to  $\Delta\vec{k}_0$  vanishing, but also its first derivative with respect to the seed wavelength at the center wavelength of the seed:

$$\left.\frac{\partial\Delta\vec{k}}{\partial\lambda_1}\right|_{\lambda_1=\lambda_1^0} = 0 \quad (1.17)$$

Decomposed into the components parallel and perpendicular to the wave vector of the seed, compare Fig. 1.5 and [42],

$$\Delta k_{\perp} = k_2 \sin \Omega - k_3 \sin \Psi \quad (1.18)$$

$$\Delta k_{\parallel} = k_1 + k_2 \cos \Omega - k_3 \cos \Psi, \quad (1.19)$$

Eq. 1.17 reads

$$\frac{\partial \Delta k_{\perp}}{\partial \lambda_1} = \frac{\partial k_2}{\partial \lambda_1} \sin \Omega + k_2 \frac{\partial \Omega}{\partial \lambda_1} \cos \Omega = 0 \quad (1.20)$$

$$\frac{\partial \Delta k_{\parallel}}{\partial \lambda_1} = \frac{\partial k_1}{\partial \lambda_1} + \frac{\partial k_2}{\partial \lambda_1} \cos \Omega - k_2 \frac{\partial \Omega}{\partial \lambda_1} \sin \Omega = 0, \quad (1.21)$$

since  $k_3 \neq k_3(\lambda_1)$ . Adding Eqs. 1.20 and 1.21 after multiplication by  $\sin \Omega$  and  $\cos \Omega$ , respectively, yields an expression that is Eq. 1.17

$$\frac{\partial k_2}{\partial \lambda_1} + \frac{\partial k_1}{\partial \lambda_1} \cos \Omega = 0. \quad (1.22)$$

The partial derivatives can be transformed to

$$\frac{\partial k_1}{\partial \lambda_1} = \frac{\partial k_1}{\partial \omega_1} \frac{\partial \omega_1}{\partial \lambda_1} = \frac{1}{v_{g1}} \left( -\frac{2\pi c}{\lambda_1^2} \right) \quad (1.23)$$

$$\frac{\partial k_2}{\partial \lambda_1} = \frac{\partial k_2}{\partial \lambda_2} \frac{\partial \lambda_2}{\partial \lambda_1} = \frac{\partial k_2}{\partial \omega_2} \frac{\partial \omega_2}{\partial \lambda_2} \frac{\partial \lambda_2}{\partial \lambda_1} = \frac{1}{v_{g2}} \left( -\frac{2\pi c}{\lambda_1^2} \right) \left( -\frac{\lambda_2^2}{\lambda_1^2} \right). \quad (1.24)$$

Finally, these expressions are inserted into Eq. 1.22 to yield the so-called *projection condition* [38, 42]

$$v_{g1} = v_{g2} \cos \Omega. \quad (1.25)$$

The projection of the group velocity of the idler in the direction of the seed pulse equals the group velocity of the seed. The physical consequence of this is illustrated in Fig. 1.6. The idler does not overtake the signal pulse, and, hence, no pulse broadening occurs. The important benefit from this is that long crystals can be used which ensure high conversion efficiency.

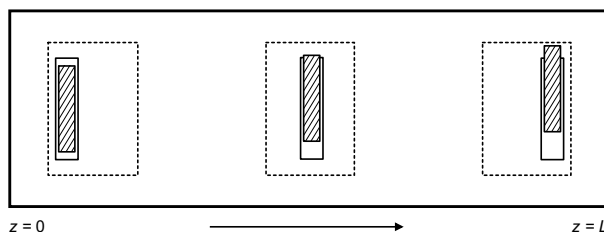


**Figure 1.6:** With a non-collinear beam geometry, the idler vertically travels away from the signal, assuring group velocity matching in the crystal. Since the non-collinear angle  $\Omega$  is much smaller than shown here ( $\Omega \approx 4^\circ$ ), only a slight elongation of the beam profile in this direction is observed.

A further issue must be addressed regarding non-collinear phase-matching in the crystal. Except in collinear phase-matching, two solutions exist for the direction of  $\vec{k}_1$  [46], namely  $(\theta - \psi)$  and  $(\theta + \psi)$ , as shown in Fig. 1.7. Here,  $\theta$  is defined as the angle between the  $c$ -axis and the pump wave vector  $\vec{k}_3$ . The advantage of the  $(\theta - \psi)$ -solution is that phase-matching is achieved for a larger variety of angles since a circle drawn around the end point of  $\vec{k}_1$  follows the  $\vec{k}_3(\theta)$  curve. Nevertheless, the non-tangential phase-matching solution  $(\theta + \psi)$  has the advantage that in a negative uniaxial crystal the Poynting vector propagates in a direction  $\rho > \theta$ , as can be easily verified from Fig. 1.7. If BBO is chosen as the noncollinear crystal, the walkoff-angle is very close to the noncollinear angle, which ensures highly efficient conversion.

In the experiments, no significant difference has been found between these two setups.

### 1.3 Generation of ultrashort pulses

Experimentally, fulfilling the non-collinear phase-matching geometry requires the computation of the non-collinear angles in order to obtain an educated guess for the initial alignment. This is performed in several steps as indicated here.

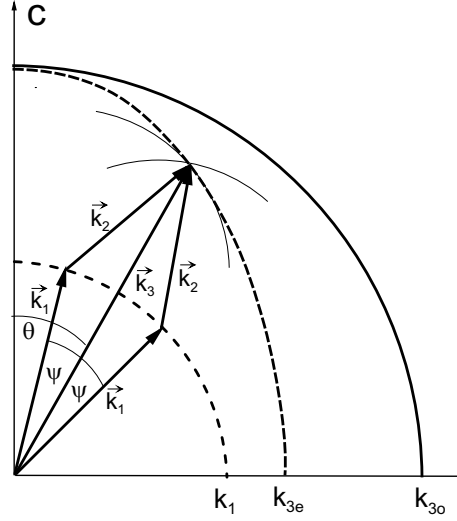


**Figure 1.7:** Type I phase-matching with and without fulfilling the tangential condition.

1. Choose  $\lambda_3$  (pump) and  $\lambda_1$  (center wavelength to be amplified)
2. Compute  $\lambda_2$  (idler) via Eq. 1.1
3. Compute  $k_1 = k_o(\lambda_1)$  and  $k_2 = k_o(\lambda_2)$  via Sellmeier Eqs. 1.12, 1.13
4. Compute  $v_{g1}(\lambda_1)$  and  $v_{g2}(\lambda_2)$
5. Compute  $\Omega$  by the projection condition 1.25
6. Compute  $|\vec{k}_3|$  and  $\psi$  from  $k_1$ ,  $k_2$ , and  $\Omega$
7. Compute the phase-matching angle  $\theta_3$  between  $\vec{k}_3$  and the crystal axis  $\vec{c}$  via  $n_3 = (\lambda_3/2\pi)k_3$  and Eq. 1.11
8. Compute external angles by Snell's law

These angles are conveniently measured by the position of the spots of seed and pump reflected by the crystal onto the base plate.



## 1.4 Experimental realization

The experimental setup is depicted in Fig. 1.8 for a one-stage, single-color non-collinear optical parametric amplifier (OPA) and in Fig. 1.9 for a two-color version which fits onto the same footprint as the single color setup. A small, sub-20fs pump-probe spectrometer can therefore be placed in a box of about  $80\text{cm} \times 40\text{cm} \times 15\text{cm}$  in size.

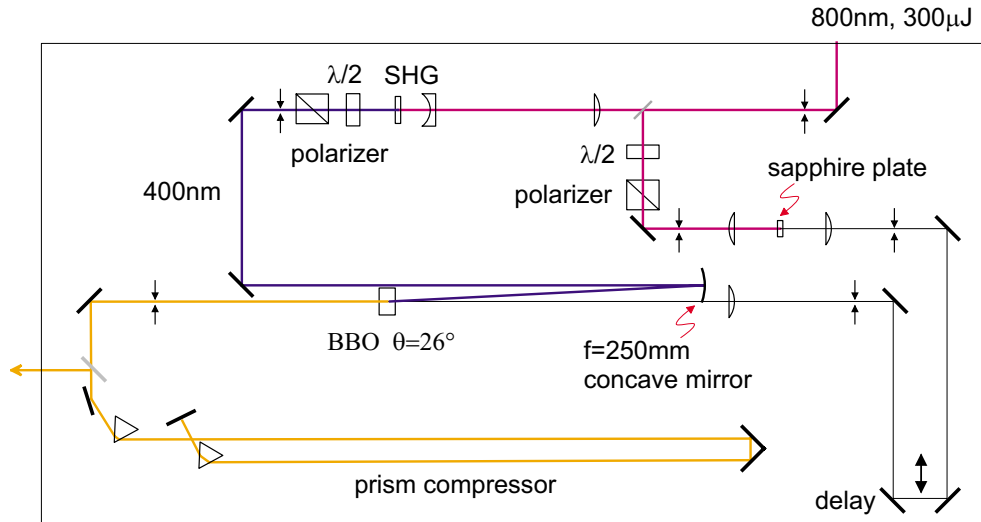


**Figure 1.8:** Setup of a non-collinear single OPA. The continuum (seed) is produced in a 1mm thick sapphire plate from a small fraction of the fundamental pulses (800nm, 100fs, 1kHz) supplied by the Ti:Sa regenerative amplifier system. A pinhole and the waveplate / polarizer combination serve to attenuate the pulse energy to a suitable level for the build-up of a single filament of WLC. The main part of the fundamental pulse is frequency-doubled (BBO, 2mm) and focused with a  $f=250\text{mm}$  spherical mirror (HR 400/0° coated). The focus is placed 30-40 mm in front of the parametric crystal which is cut at  $\theta=26^\circ$ . The output pulses are compressed with a fused silica (FS) prism compressor setup.

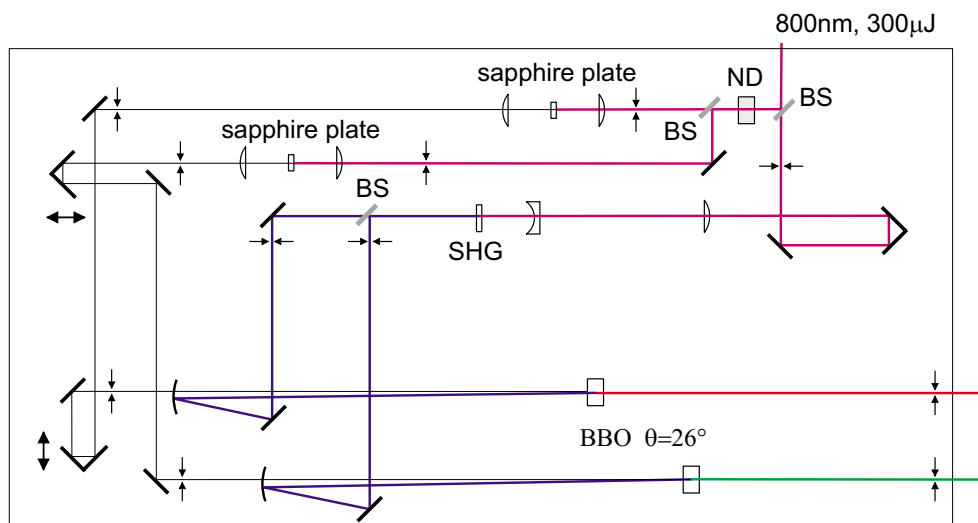


**Figure 1.9:** Setup of a non-collinear dual OPA. The two different pulses leave the setup almost concurrently, obviating long compensation lines. The setup of each stage is basically comparable to that of Fig. 1.8. The attenuation of the WLC generation pulses is performed with a ND1.0 filter.

When the amplification stage is run without a seed, a rainbow of colors is emitted in a cone around the pump beam. This so-called *parametric super-fluorescence* [47–49] originates from the

spontaneous fission of a pump photon into a seed and an idler photon via the amplification from photon noise. It has been demonstrated [47] that this so-called *self phase-matching* occurs in the direction of minimal group velocity mismatch (GVM) between signal and idler, which is equivalent to Eq. 1.25. Hence the direction of the cone indicates the noncollinear angle for the seed beam. Turning on the seed light again, with good adjustment of the noncollinear beam setup, leads to a decrease in brightness of the superfluorescence cone, indicating an effective conversion from seed to signal energy which consumes the energy otherwise available for superfluorescence. The output spectrum of the OPA can be tuned by adjusting the delay between pump and seed, as shown in Fig. 1.10. This is due to the fact that the WLC is strongly chirped, i.e. different colors occur at different temporal positions within the pulse envelope. By changing the delay between pump and seed, only the spectral portion of seed which temporally overlaps with the pump is amplified. In order to obtain output spectra with a spectral width comparable to that of the WLC, two schemes are conceivable:

- (1) Precompression of the WLC as developed by the groups of De Silvestri [50] and Kobayashi [51]
- (2) Lengthening of the pump pulse by means of a glass rod as proposed by the group of Riedle [52]. A thick SHG crystal for the generation of the pump pulses [38] may equally well be used.

With a further slight adjustment of the crystal angle, it is possible to extend the wavelength range down to 500nm. It is also possible to amplify the NIR wavelengths of the WLC, as demonstrated in [42].

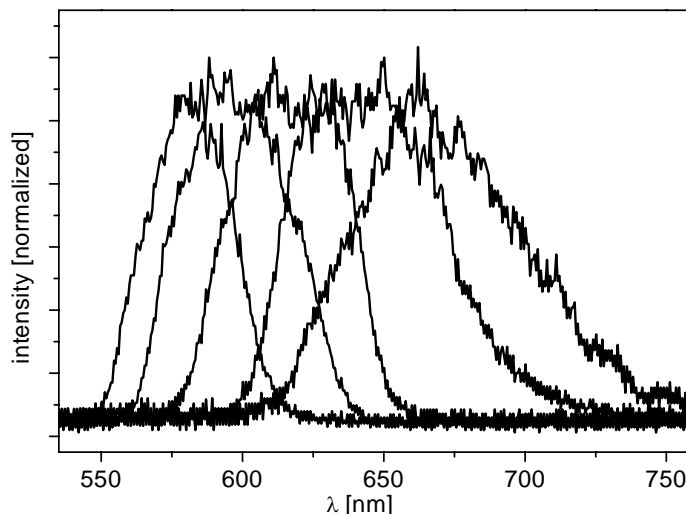


**Figure 1.10:** The spectrum of a non-collinear OPA can easily be tuned by changing the delay between pump and seed.

The spectra shown in Fig. 1.10 are routinely compressed to below 20 fs with a pair of FS prisms, as shown in Fig. 1.11. Here, the autocorrelation measurement was performed using a  $10\mu\text{m}$  BBO crystal as nonlinear element.

For comparison, an autocorrelation trace using a silicon carbide (SiC) diode [53] is shown in Fig. 1.12. This method has the advantage that effects arising from the limited conversion bandwidth of SHG crystals do not occur. Again, a sub-20fs pulse is obtained at a central wavelength of 620nm.

The measurements above suffer from the fact that the autocorrelator used only one beam splitter and so technically measured not an autocorrelation, but rather a crosscorrelation between the reflected pulse and the transmitted pulse which experienced additional GVD from the 1mm FS beam splitter substrate.

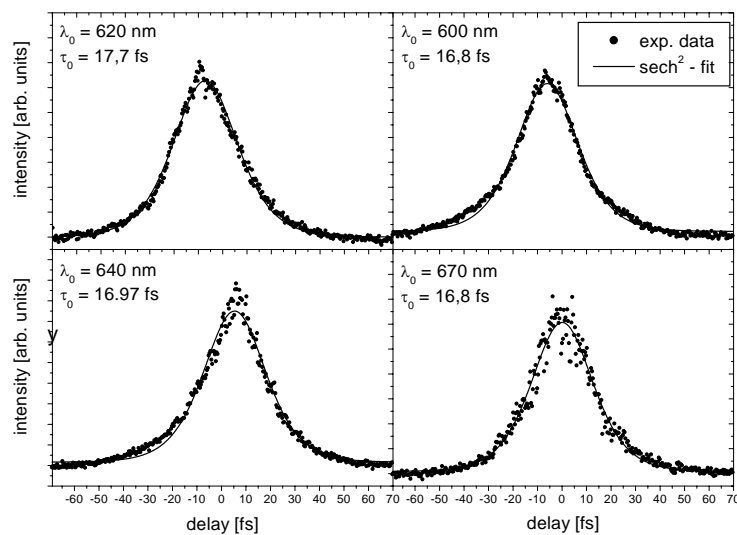


**Figure 1.11:** With a FS prism compressor, pulse durations below 20fs are routinely achieved using autocorrelation measurements with a  $10\mu\text{m}$  BBO.

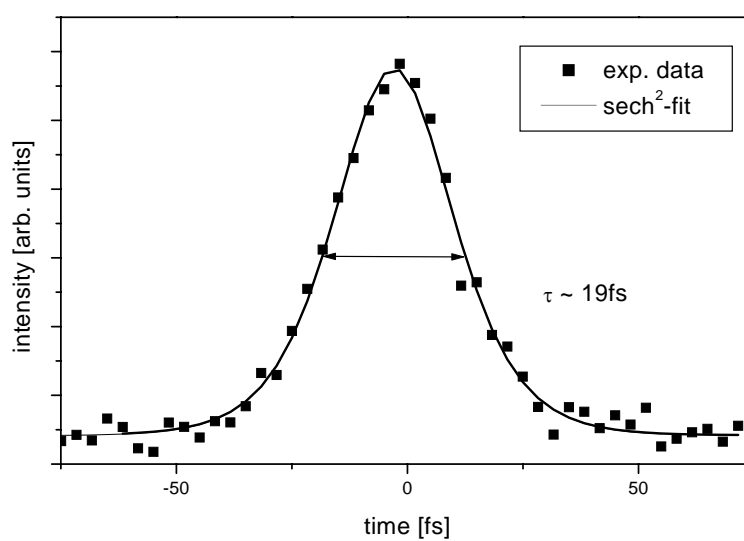


**Figure 1.12:** Autocorrelation trace measured with a SiC two-photon diode.

## 2

# Femtosecond pulse shaping

Tailoring of ultrashort pulses, originally introduced by Heritage and coworkers [54] is the crucial prerequisite for all experiments presented in this thesis. Therefore, its basic principles and techniques are described in detail below.

A broad variety of approaches for pulse shaping has been proposed and realized so far. Most of them rely on spatial filtering of the dispersed spectrum. By working in the frequency domain, waveform generation – which is sequential in time – is transferred to a modulation parallel in space.

Chapter 2 focuses on the theory of pulse shaping using spatial light modulators (SLM), which affords computer-controlled waveform synthesis. Theoretical predictions are compared to experimental data. An overview of the different approaches for fs pulse shaping is given. Some parts of this section closely follow references [55] and [56]. For more details, the reader is referred to these articles and [57].

## 2.1 Filtering in the time and frequency domain

The most intuitive approach for generating shaped laser pulses is to operate directly in the time domain by using an ultrafast optical "shutter" to slice out the desired shape of the laser pulse. The limitation of this approach is that the shortest temporal features that can be controlled are on the order of 1ns (electro-optical shutters). This is four to five orders of magnitude too long for the goal of tailoring pulses with structures as fine as several tens of femtoseconds.

The solution is to modulate the electric field in the frequency domain rather than in the time domain. The femtosecond pulse shaping approach described here is based on the linear, time-invariant filter. Linear filtering is commonly used to process signals in a broad frequency range and is applied here to generate specially shaped optical waveforms on the femtosecond time scale. A description of linear filtering can be formulated either in the time domain, as mentioned above, or in the frequency domain.

In the frequency domain, a filter is characterized by its frequency response function  $\tilde{H}(\omega)$ . The output of the linear filter,  $E_{out}(\omega)$ , is the product of the input signal,  $E_{in}(\omega)$ , and the frequency response,  $\tilde{H}(\omega)$ ,

$$\tilde{E}_{out}(\omega) = \tilde{E}_{in}(\omega)\tilde{H}(\omega). \quad (2.1)$$

In the time domain, the filter is characterized by an impulse response function  $H(t)$ . As a trivial consequence of Fourier transform relations, the output of the filter,  $E_{out}(t)$ , in response to an input pulse,  $E_{in}(t)$ , is given by the convolution of  $E_{in}(t)$  and  $H(t)$

$$E_{out}(t) = E_{in}(t) \star H(t) = \int E_{in}(t')H(t-t')dt', \quad (2.2)$$

where  $\star$  denotes convolution.  $E_{in}(t)$ ,  $E_{out}(t)$ , and  $H(t)$  are related to  $\tilde{E}_{in}(\omega)$ ,  $\tilde{E}_{out}(\omega)$ , and  $\tilde{H}(\omega)$ , respectively, by Fourier transformation, as for example

$$\tilde{H}(\omega) = \mathbb{F}[H(t)] \equiv \int_{-\infty}^{\infty} H(t) \exp(-i\omega t) dt \quad (2.3)$$

and

$$H(t) = \mathbb{F}^{-1}[\tilde{H}(\omega)] \equiv \frac{1}{2\pi} \int_{-\infty}^{\infty} \tilde{H}(\omega) \exp(i\omega t) d\omega. \quad (2.4)$$

If the input,  $E_{in}(t)$ , is a delta function, the output is simply  $H(t)$ . Therefore, for a sufficiently short input pulse, the problem of generating a specific output pulse shape is equivalent to the task of determining a linear filter with the desired impulse response. For a delta function input pulse, the input spectrum  $\tilde{E}_{in}(\omega)$  is equal to unity, and the output spectrum is equal to the frequency response of the filter. Therefore, generation of a desired output waveform can be accomplished by implementing a filter with the required frequency response.

With frequency domain filtering, no ultrafast modulators are necessary because the filter function is static. The smallest temporal features of the tailored waveforms are within the regime of the FWHM of the input pulse.

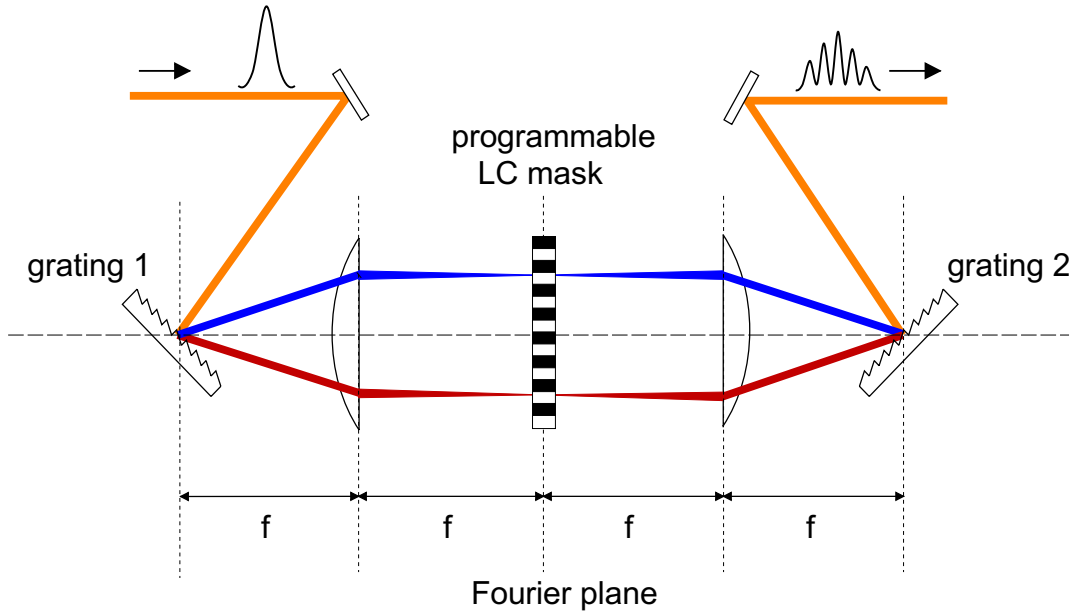
## 2.2 4f-configuration

Figure 2.1 shows the basic pulse shaping apparatus, which consists of a pair of diffraction gratings and lenses, arranged in a configuration known as a "zero dispersion pulse compressor", and a pulse shaping mask [58]. The individual frequency components of the incident ultrashort pulse are angularly dispersed by the first diffraction grating, and then imaged by the first lens, spatially separating the frequency components along one dimension. Essentially, the first lens performs a Fourier transform. Spatially patterned amplitude and phase masks or a SLM are placed in this plane in order to manipulate the amplitude and phase of the frequency components. All the frequencies are then recombined into a single collimated beam by means of a second lens and grating. The shape of the output pulse is determined by the Fourier transform of the pattern transferred by the masks onto the spectrum.

The shaper is properly aligned if the output pulses are identical to the input pulses as long as no shaping pattern is applied. This is the case if and only if the lenses are arranged at  $2f$  distance, with the gratings located at the outside focal planes of the telescope. Then the first lens performs a spatial Fourier transform from the plane of the first grating onto the Fourier plane, while the second lens performs an inverse Fourier transform from the masking plane onto the plane of the second grating. Note that the term "inverse" refers to the type of mathematical operation and not to the question whether the second Fourier transform compensates the first. If and only if the lenses and gratings of the 4f-configuration are set exactly at the focal distances, maintaining the direction of the optical axis which is influenced by the angular orientation of lenses and gratings, the first Fourier transform will be exactly inverse to the second Fourier transform. The total effect of these two consecutive transforms is then that the input pulse is unchanged if no pulse shaping mask is present.

The absence of dispersion can be achieved only if several approximations are valid, as for instance that the lenses are thin and aberration-free, that chromatic dispersion caused by the lenses or other elements in the pulse shaper is small, and that the gratings have a flat spectral response. Distortion-free propagation through the "zero dispersion compressor" in the configuration of Fig. 2.1 has been observed with pulses down to roughly 70 fs [58–60]. For substantially shorter pulses, especially in the sub-20 fs range, more care must be taken to satisfy these approximations. Replacing the lenses by spherical or cylindrical mirrors, as demonstrated in section 2.5 as well as in chapter 5, avoids these problems and ensures dispersion-free operation [61–65].

Phase-only filters which have the advantage of being inherently loss-free are used in many pulse shaping experiments. However, phase-only filtering restricts the degrees of freedom. This can



**Figure 2.1:** Basic 4f-configuration of a frequency domain pulse shaper. A SLM is positioned at the Fourier plane.

be seen from Eqs. 2.3 and 2.4 where the filter function is in general complex, which means that for each frequency component, two degrees of freedom, amplitude and phase, must be given. In general, phase-only shaping is sufficient only when the target time-domain waveform is not fully specified. Furthermore, no analytical method exists to compute the impulse response function for a desired output waveform. As a consequence, several authors have employed simulated annealing algorithms to design either binary [66] or gray-level [67–69] phase-only filters, which were tested in pulse shaping experiments using either binary phase masks or liquid crystal modulators, respectively. A more promising approach than generating the phase mask patterns by simulated annealing seems to be a method by Hacker *et al.* [70] which uses an iterative projection scheme to generate the phase mask corresponding to a given response function.

## 2.3 Theoretical model of a pulse shaper

A quantitative description of the shaped output waveform  $E_{out}(t)$  is essential for a deeper understanding of the shaping process. The general statement of the previous section which connects the output waveform and the mask pattern via a Fourier transform is valid only in a first-order approximation since it neglects effects arising from diffraction at the mask pattern and spatio-temporal shaping effects, as will be explained in the forthcoming paragraphs. This section also addresses the effects due to pixelation of the mask.

### 2.3.1 Dependence of focal spot size on filter function

First, it is necessary to obtain a relation between the linear filtering function  $\tilde{H}(\omega)$  and the actual physical masking function with complex transmittance  $M(x)$  in terms of the linear filter formalism, Eqs. 2.1 and 2.2.

This relation is independent of the filtering process itself and can be calculated from the optical properties of the grating and the lenses alone.

To this end, the mapping between frequency and position in the Fourier plane is calculated from the diffraction equation of a grating as

$$x(\omega) \approx f \left. \frac{\partial \theta_d}{\partial \omega} \right|_{\omega=\omega_0} (\omega - \omega_0) = -\frac{2\pi cf}{\omega^2 d \cos(\theta_d)} (\omega - \omega_0) \equiv \alpha(\omega - \omega_0), \quad (2.5)$$

where diffraction into first order has been assumed:  $d$  is the grating period,  $f$  is the lens focal length, and  $\theta_d$  is the diffracted angle from the first grating. This linearization may break down for ultrashort pulses below 20fs or high grating dispersions such that the assumption that each pixel covers the same frequency range is no longer justified. For simplicity, it is assumed that the mapping between pixel and frequency is linear.

The field immediately behind the mask as a function of the frequency  $\omega$  and spatial coordinate  $x$  can be written as the product of the input electric field  $\tilde{E}_{in}(\omega)$ , the mask filter function  $M(x)$ , and a factor which accounts for a smearing out of the mask function due to the finite focal spot size at the mask (see [55, 56, 71] for details)

$$\tilde{E}_m(x, \omega) = TM(x)\tilde{E}_{in}(\omega) \exp \left[ -\frac{[x + \alpha(\omega - \omega_0)]^2}{w_0^2} \right] \quad (2.6)$$

with the spatial dispersion in units of cm (rad/s)<sup>-1</sup> as defined by Eq. 2.5 and the radius of the focused beam at the masking plane for any single frequency component,

$$w_0 = \frac{\cos(\theta_{in})}{\cos(\theta_d)} \frac{2cf}{\omega w_{in}}. \quad (2.7)$$

Here  $w_{in}$  is the input beam radius before the first grating,  $c$  is the speed of light,  $\theta_{in}$  is the input angle from the first grating and  $T$  describes the losses in the shaper. For  $\theta_d$ , the value of the center frequency  $\omega_0$  is used.

At first glance, the simultaneous appearance of  $x$  and  $\omega$  in Eq. 2.6 is somewhat confusing since  $x(\omega)$  has been just calculated. This formulation of Eq. 2.6 is imperative because, in the exp argument,  $x$  and  $\omega$  are mutually independent. This can be seen as follows: For an individual frequency  $\omega$ , the finite size of the focus causes this particular frequency to appear not only at  $x = \alpha(\omega - \omega_0)$ , but also in a Gaussian distribution around this location. Conversely, a Gaussian distribution of frequencies is present at each location  $x$ . One extreme case is  $\alpha \rightarrow -\infty$ , which is equivalent to infinitely high dispersion, for which  $\tilde{E}_m \equiv \tilde{E}_m(\omega)$  and the blurring may be ignored. The opposite extreme is  $\alpha = 0$ , i.e. infinitely low dispersion (mirror instead of grating), which means that only blurring occurs and all frequencies overlap at a Gaussian spot at  $x = 0$ . Here,  $\tilde{E}_m \equiv \tilde{E}_m(x)$ .

For realistic dispersions, Eq. 2.6 is a non-separable function of space  $x$  and frequency  $\omega$ . This implies that the spatial profiles of the focused spectral components can be altered by the mask – e.g., some spectral components may impinge on abrupt amplitude or phase steps on the mask, while others may not. This leads to different amounts of diffraction for different spectral components and results in an output field which may be a coupled function of space and time and thus may exhibit a complex mode structure. This space-time coupling has been analyzed by several authors [72–74] and will be presented in section 2.3.3.

Of course, one is usually interested in generating a spatially uniform output beam with a single desired temporal profile. In order to obtain an output field which is a function of frequency (and therefore time) only, one must perform an appropriate spatial filtering operation. This can be done coarsely by placing an iris after the pulse shaping setup. Including these spatial effects in the calculations, the filter function  $\tilde{H}(\omega)$  can then be approximated by [57, 75]

$$\tilde{H}(\omega) = \left( \frac{2}{\pi w_0^2} \right)^{\frac{1}{2}} \int M(x) \exp \left[ -\frac{(x - \alpha\omega)^2}{w_0^2} \right] dx \quad (2.8)$$

Equation 2.8 shows that the effective filter in the frequency domain is the mask function  $M(x)$  convoluted with the intensity profile of the beam. The main effect of this convolution is to limit

the FWHM spectral resolution  $\delta\omega$  of the pulse shaper to  $\delta\omega \approx \sqrt{\ln 2}w_0/\alpha$ . Physical features on the mask smaller than  $\sim w_0$  are smeared out by the convolution, and this determines the finest features which can be transferred onto the filtered spectrum. One consequence of this picture is that wavelength components impinging onto mask features which vary too fast for the available spectral resolution are in part diffracted out of the main beam and eliminated by the spatial filter. This can result in phase-to-amplitude conversion in the pulse shaping process [75, 76].

Conversely, in the limit  $w_0 \approx 0$ , the apparatus provides perfect spectral resolution, and the effective filter is just a scaled version of the mask. Eq. 2.8 provides an appropriate theoretical description, including the effect of diffraction losses due to mask features, provided that a suitable spatial filter is employed following the pulse shaping apparatus.

The effect of finite spectral resolution can be exemplified in the time domain by noting that the output pulse  $E_{out}(t)$  will be the convolution of the input pulse  $E_{in}(t)$  with the impulse response  $H(t)$  of the shaper. The impulse response in turn is obtained from the Fourier transform of Eq. 2.8 and can be written as the product

$$H(t) = m(t)g(t) \quad (2.9)$$

where

$$m(t) = \mathbb{F}^{-1}[M(\alpha\omega)] = \frac{1}{2\pi} \int M(\alpha\omega) \exp(i\omega t) d\omega \quad (2.10)$$

and

$$g(t) = \exp\left[-\frac{w_0^2 t^2}{8\alpha^2}\right]. \quad (2.11)$$

Thus, the impulse response is the product of two factors.  $m(t)$  is the Fourier transform of the mask (appropriately scaled) and corresponds to the infinite-resolution impulse response. The second factor,  $g(t)$ , is an envelope function which restricts the time window in which the tailored output pulse can accurately reflect the response of the infinite-resolution mask. The FWHM of this time window (in terms of intensity) is given by

$$T = \frac{4\alpha\sqrt{\ln 2}}{w_0} = \frac{2\sqrt{\ln 2}w_{in} \lambda}{c d \cos(\theta_{in})}. \quad (2.12)$$

The time window is proportional to the number of grating lines illuminated by the input beam, multiplied by the period of an optical cycle. A larger time window can only be obtained by expanding the input beam diameter. The shortest feature in the output shaped pulse is, of course, governed by the available optical bandwidth.

These results impose limits on the complexity of shaped pulses. The shortest temporal feature which can be realized,  $\delta t$ , is inversely related to the total bandwidth  $B$ : ( $B\delta t > 0.44$ ), and the maximum temporal window  $T$  is inversely related to the finest achievable spectral feature  $\delta f$ : ( $\delta f T > 0.44$ ). Assuming Gaussian-shaped spectra and pulses,  $T$ ,  $\delta t$ ,  $B$ , and  $\delta f$  all represent their respective FWHM.

### 2.3.2 Effects due to pixelation of the SLM

The pixelation of phase or phase-and-amplitude liquid crystal (LC) SLMs entails one significant limitation: the LC SLM can only produce a staircase approximation even when a smooth spectral profile is desired. The requirement that the actual spectral modulation should approximate a smooth function despite the fixed, finite size of the individual modulator elements, limits the temporal range over which pulse shaping can be successfully achieved. Essentially, this is a sampling limitation: the spectrum must vary sufficiently slowly that it is adequately sampled by the discrete modulator elements. For the case of pulse position modulation, for example, we require  $|\delta\Phi| < \pi$ , where  $\delta\Phi$  the phase change per pixel. The effect of pixelation for pulse shaping in general has been analyzed in [55]. Since the physical consequences of the discretized



mask pixels are essential for the understanding of everyday work with SLMs, the corresponding mathematics as described in [55] is outlined here.

Mathematically, the mask can be described as the convolution of a comb structure (the array of pixels) with a set of rectangular structures (pixels and gaps) multiplied by the (complex) filter coefficient  $B_n$  or  $B_g$  of the pixel or the pixel gap, respectively. These filter coefficients will be explained in detail in section 2.4; here, it is only important that the phase and amplitude of the frequency components at each pixel can be influenced by  $B_n$ . The mask function  $M(x)$  is thus

$$M(x) = \delta(x - x_0) \star \sum_{n=-N/2}^{N/2-1} B_n \delta(x - nw) \star \text{rect}(x/rw) + B_g \delta(x - (n + 1/2)w) \star \text{rect}(x/(1-r)w) \quad (2.13)$$

Here,  $w$  is the distance between two pixels,  $x_0$  is the displacement of the center pixel (corresponding to  $n = 0$ ) from the central frequency  $\omega_0$ ,  $r = w_p/(w_p + w_g)$  with  $w_p$  and  $w_g$  being the pixel width and the gap width, respectively, and  $N$  is the total number of pixels. The rect function is here defined symmetrically as

$$\text{rect}(x) = \begin{cases} 1 & : |x| \leq 1/2 \\ 0 & : |x| > 1/2 \end{cases} \quad (2.14)$$

To obtain the shaped field with a mask function given by  $B_n$ , the corresponding response function in time (Eq. 2.9) must be computed. This entails discrete Fourier transformation of Eq. 2.13 to obtain  $M(k)$ :

$$M(k) = \exp(ikx_0) \times \left[ \frac{\sin rkw}{\pi k} \left\{ \sum_{n=-\infty}^{\infty} A_{n/[N]} \delta\left(k - \frac{2\pi n}{Nw}\right) + B_g \frac{\sin(1-r)kw}{\pi k} \right\} \times \sum_{n=-\infty}^{\infty} (-1)^n \delta\left(k - \frac{2\pi n}{Nw}\right) \right] \quad (2.15)$$

Here,  $n/[N]$  refers to the remainder of  $n/N$ , and  $A_n$  is the discrete Fourier transform of  $B_n$ . Combining this expression with the response function 2.10, affords a superposition of equally spaced input pulses which are weighted by coefficients  $C_n$ ,

$$E_{out}(t) = \sum_n C_n E_{in}(t - n\tau) \quad (2.16)$$

with

$$C_n = \exp\left(\frac{2\pi i x_0 n}{Nw}\right) \exp\left(-\frac{1}{2} \left[\frac{\pi w_0 n}{Nw}\right]^2\right) \times \left\{ r A_{n/[N]} \text{sinc}\left(\frac{r\pi n}{N}\right) + (1-r) B_g (-1)^{n/N} \delta_{0,n/[N]} \text{sinc}\left(\frac{(1-r)\pi n}{N}\right) \right\} \quad (2.17)$$

and

$$\tau = 2\pi\alpha/Nw. \quad (2.18)$$

Since it is assumed that the full spectrum is passed through the mask,  $\tau$ , which may be regarded as a temporal "unit" and which reflects the physical properties of the shaper itself, must be smaller than the FWHM of the incident pulse. The two sinc terms of Eq. 2.17 describe diffraction

at the discrete pixels and gaps. The leakage through the transmitting gaps, as described by the second sinc term, always produces a small pulse appearing at time zero. This "time zero feature" has indeed been observed experimentally [60]. The first exp factor in Eq. 2.17 describes the phase shift due to a possible offset between the center pixel of the mask and the central frequency. The second exp factor expresses a smearing out of the mask pattern by the finite size of the focal spot and is equivalent to Eq.2.11, as can be easily seen by inserting Eq. 2.18 into Eq. 2.11. For negligible gaps ( $r = 1$ ) and centered mask ( $x_0 = 0$ ), eq. 2.17 simplifies to

$$C_n = A_{n/[N]} \text{sinc} \left( \frac{\pi n}{N} \right) \exp \left( -\frac{1}{2} \left[ \frac{\pi w_0 n}{N w} \right]^2 \right). \quad (2.19)$$

Eq. 2.16 is sufficient to describe any waveform as long as its smallest features are not shorter than the input pulse width. It should be noted, though, that only  $N$  of the  $C_n$  are independent so that the pulse shape can be uniquely determined only for a time interval

$$-N\tau/2 \leq t < N\tau/2 \quad (2.20)$$

Outside this temporal window, copies (so-called replica) of the waveform generated within the time window are produced. These appear with a temporal spacing of  $N\tau$  and are weighted by the sinc functions (second term in Eq. 2.19). The full result is weighted by a temporal window function (third term in Eq. 2.19) which fortunately removes most of the replica provided that the focal spot size is suitably chosen. For an infinitely small focus, the exponential drop of the Gaussian window would be non-existent and all the replica would remain intact. In experiments, the focused spot size at the masking plane can be approximately adapted to the pixel size. In this case the spectral filter function from Eq. 2.8 is a smoothed version of the spatial profile corresponding to the pixelated SLM. The corresponding Gaussian time window function significantly reduces the replica pulses predicted by Eq. 2.16. Thus, by increasing the focused spot size, the experimentalist can sacrifice some spectral resolution for the purpose of smoothing and eliminating replica pulses.

To produce a particular output shape, the output has to be written in terms of Eq. 2.19. Solving Eq. 2.19 with respect to the coefficients  $A_n$  yields the mask coefficients  $B_n$  by inverse Fourier transformation. Nevertheless, as a first-order approximation,  $C_n \equiv A_{n/[N]}$  can be assumed. If, for instance, we wish to create a double pulse at delays  $4\tau$  and  $-6\tau$  with amplitudes 1 and phases 0 and  $\pi/2$ , respectively, the coefficients  $C_4$  and  $C_{-6}$  in cartesian coordinates are set to  $1 + 0i$  and  $1/\sqrt{2} + 1/\sqrt{2}i$ , respectively. The coefficients  $B_n$  (see Eq. 2.31-2.33) are then calculated by inverse Fourier transformation of  $C_n = A_n$ . The experiments show good agreement between measured and calculated output pulses [60].

Due to the effects just discussed, LC SLMs with more than the 128 pixels used in current pulse shaping experiments would be desirable. A new LC device has been developed in cooperation with Jenoptik GmbH and will be presented in section 2.5.

### 2.3.3 Spatiotemporal shaping effects

In the derivation above, higher orders of diffraction of the focused frequency components at the mask were neglected. If they are carried along, it turns out that these higher orders cannot be simply removed by a spatial filter since the output pulses show a spatial shift along the  $x$  axis which linearly depends on the temporal shift [73].

Eq. 2.17 then changes to

$$E_{out}(x, t) = \sum_n C_n E_{in}(t - n\tau) \exp \left[ -\left( \frac{x - n\chi}{w_0} \right)^2 \right] \quad (2.21)$$

with

$$\chi = \delta\lambda f / Nw. \quad (2.22)$$

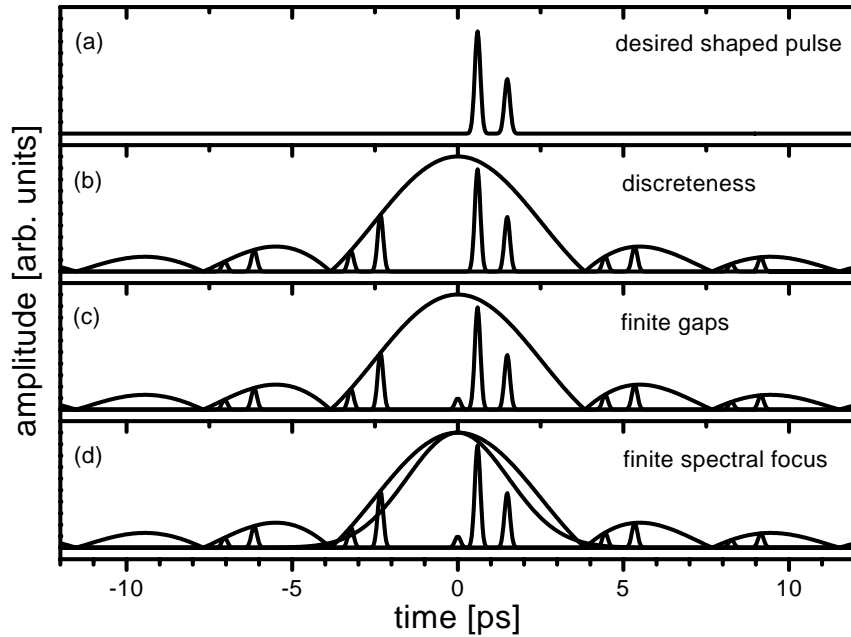


**Figure 2.2:** Visualization of Eq. 2.17. (a) Desired pulse shape. (b) The first sinc term produces copies outside the temporal window as given by Eq. 2.20. (c) The second sinc term (transmitting gaps) produces a time-zero feature. (d) The Gaussian blurring (second exp factor) mostly eliminates the replica.

As before, Eq. 2.21 shows the output pulse as a sequence of equally spaced input pulses, but now each individual pulse is additionally transversely displaced. The dependence between temporal and spatial shift is linear with the slope

$$\frac{\partial x}{\partial t} = -\frac{\chi}{\tau} = -\frac{cd \cos(\theta_i)}{\lambda} \quad (2.23)$$

Typical values for  $\partial x/\partial t$  are 0.15mm/ps. The maximum shift that can be produced is about 1.6mm for 128 pixels, so that this effect is in general not altogether negligible. The spatially shifted pulses are again weighted by a Gaussian envelope function so that substantially shifted structures are comparatively weak.

## 2.4 Pulse shaping with LC-SLMs

Liquid crystal modulator arrays have primarily been configured for either phase-only or phase-and-amplitude operation in pulse shaping applications. The LC array allows continuously variable phase control of each separate pixel and programmable control of the pulse shape on a millisecond time scale.

Figure 2.3 shows a schematic of a lateral cut through one pixel of an electronically addressed LC SLM. A thin layer of a nematic liquid crystal is sandwiched between two glass plates which are etched horizontally, i.e. along the  $x$ -direction. In order to apply the required electric field, the inside surface of each piece of glass is coated with a thin, transparent, electrically conducting film of indium tin oxide. One piece is patterned into a number of separate electrodes (or pixels) with the corresponding electrical connections. In the absence of an electric field, the thin, rod-like molecules of the nematic liquid crystal are aligned with their long axes along the furrows of the glass plates, i.e. the  $x$  direction. If an electric field  $E_{stat} = U/d$  is applied (in the  $z$  direction, which is the direction of propagation of the light,  $U$  being the voltage applied to the electrodes,  $d$  their separation), the liquid crystal molecules tilt along  $z$ , which causes a change

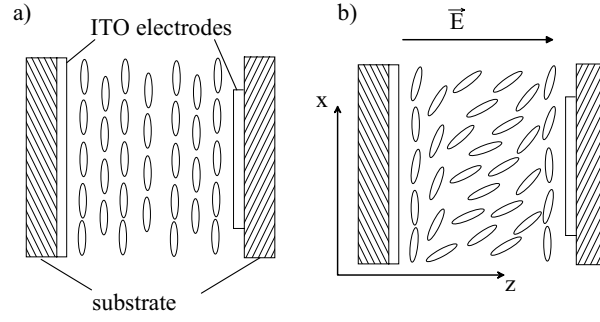


**Figure 2.3:** Side view of a single nematic crystal pixel. a) Without electric field, the rod-like crystals align themselves along the furrows etched into the substrate. b) An external field, applied by the transparent ITO electrodes, aligns the molecules along the direction of the field.

in the refractive index  $\Delta n(U) = n_e - n_o$  for  $x$ -polarized light, but not for light polarized in  $y$  direction (orthogonal to the LC axis). The difference in phase retardance  $\Delta\Phi$  for light polarized in the  $x$ - and  $y$ -direction is

$$\Delta\Phi = \frac{2\pi\Delta n(U)}{\lambda} \quad (2.24)$$

A maximum phase change of at least  $2\pi$  is required for complete phase control since larger phase shifts can be wrapped into the interval  $[0, 2\pi]$  due to the Fourier shifting theorem.

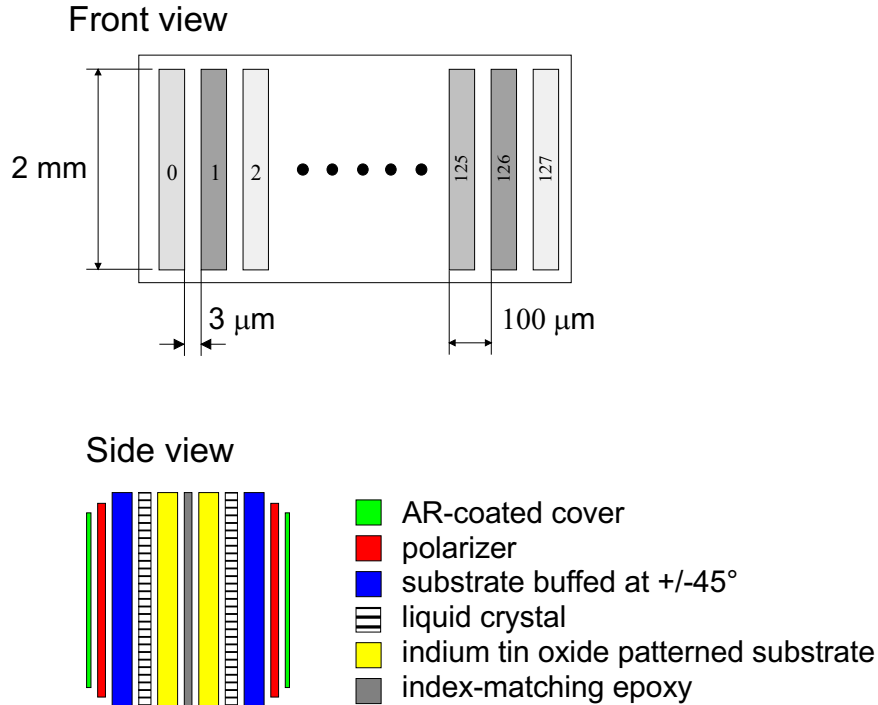


**Figure 2.4:** Schematic of the LC SLM, model SLM-256 by CRI Inc. The upper graph shows the front view. The direction of propagation is perpendicular to the plane of the sketch. 128 pixels of  $97\mu\text{m}$  width and  $2\text{mm}$  height form a total aperture of  $12.8 \times 2\text{mm}$ . The lower graph shows a lateral cut through one pixel.

Current commercially available LC SLMS have 128 pixels with  $100\mu\text{m}$  center-to-center pixel spacing and a  $12.8\text{mm}$  aperture. Figure 2.4 shows a schematic of a phase-and amplitude LC

SLM [71] that has been used in most experiments of this work. The two arrays are attached permanently with their pixels aligned and angular orientations fixed. The dual LC-SLM unit is often mounted between a pair of sheet polarizers which pass light polarized along the spectral dispersion direction (horizontal) in Fig. 2.5, denoted  $x$ . The modulator array is controlled by a special drive circuit which generates 256 separate, variable amplitude signals with 12 bit resolution to achieve independent phase and amplitude control of all 128 modulator elements. Each drive signal is supplied as a bipolar square wave of variable amplitude, typically at 2-10kHz or above, rather than as a variable amplitude dc level. The use of an ac drive signal is mandatory to prevent electromigration effects in the liquid crystal. The use of a square wave as opposed to a dc level does not change the operation of the modulator, since the rotation of the liquid crystal molecules cannot follow the modulation and thus depend only on the amplitude (not the sign) of the applied voltage.

**Phase shaping.** In the simplest configuration of a SLM, the LC molecules are prealigned in the  $x$ -direction, which is identical to the polarization direction of the incoming light. Then the filter function  $B_n$  for each pixel  $n$  is

$$B_n = \exp [i\Delta\Phi(U_n)], \quad (2.25)$$

$U_n$  being the voltage applied to pixel  $n$ . The mask acts as a phase retarder (i.e. a pure phase mask) where the relative phase between the frequencies on the pixels can be adjusted.

Exclusive phase control as achieved with the simple, single-layer LC setup can still be used to accomplish a number of pulse shaping tasks. For example, using the modulator array to impart a linear phase sweep onto the spectrum effects a temporal shift in the time domain. This relies on the fact that if  $F(t)$  and  $\tilde{F}(\omega)$  are a Fourier transform pair, then the delayed signal  $f(t - \tau)$  is the Fourier transform of  $\tilde{F}(\omega) \exp(2i\omega\tau)$ . The delay  $\tau$  is given by the relation

$$\tau = -\frac{\delta\Phi}{2\pi\delta f} \quad (2.26)$$

where  $\delta\Phi$  and  $\delta f$  are, respectively, the imposed phase change per pixel and the change in optical frequency from one pixel to the next. As pixelated LC arrays can be programmed to provide the desired phase function modulo  $2\pi$ , large phase sweeps can be achieved even though the maximum phase change can be as small as  $2\pi$ . However, in the case of any smoothly varying target phase function, as here, the phase change from one pixel to the next should remain small, such that the staircase phase pattern, generated by the discretely structured LC, represents a reasonably good approximation of the desired phase function.

Phase-only control can also be used to achieve programmable compression of chirped optical pulses [63, 65, 71, 77–79]. The shaper can be used to apply a spectral phase function which is equal and opposite to the residual phase variation of the pulse to be compressed (see chapter 5 Pulse compression). Pulse shapers with LC arrays have e.g. been used for compensation of residual dispersion in chirped pulse amplifier systems [62, 80] and for adaptive compression of chirped pulses.

**Amplitude shaping** In another possible setup the LC axis is prealigned at  $45^\circ$  with respect to the polarization. For  $x$ -polarized incoming light, the filter function for pixel  $n$  then becomes

$$B_n = \exp \left[ i\frac{\Delta\Phi(U_n)}{2} \right] \left\{ \hat{e}_x \cos \left[ \frac{\Delta\Phi(U_n)}{2} \right] + i\hat{e}_y \sin \left[ \frac{\Delta\Phi(U_n)}{2} \right] \right\}. \quad (2.27)$$

The LC filter now creates elliptically polarized light. With an additional polarizer behind the pixels which is crossed to the polarization of the incident light, an amplitude modulation results:

$$T(U_n) = |B_n|^2 \quad (2.28)$$

with

$$B_n = \exp \left[ i \frac{\Delta\Phi(U_n)}{2} \right] \left\{ \sin \left[ \frac{\Delta\Phi(U_n)}{2} \right] \right\}. \quad (2.29)$$

With this setup, an accurate phase versus voltage calibration can be obtained which is mandatory if an LC SLM is used for phase control. The array is used as an amplitude modulator for a continuous-wave (cw) laser. The laser is focused onto a single pixel of the multi-element modulator. Phase calibration is then obtained by measuring the voltage dependence of the transmission through the second crossed polarizer. Equation 2.29 shows that amplitude operation of a single SLM always involves an attenuation-dependent phase variation. Amplitude and phase modulation are not mutually independent which is obvious since of the two parameters to adjust for each pixel (phase and attenuation), only one (voltage  $U_n$ ) is accessible. Independent phase and amplitude modulation thus presupposes two LC SLMs.

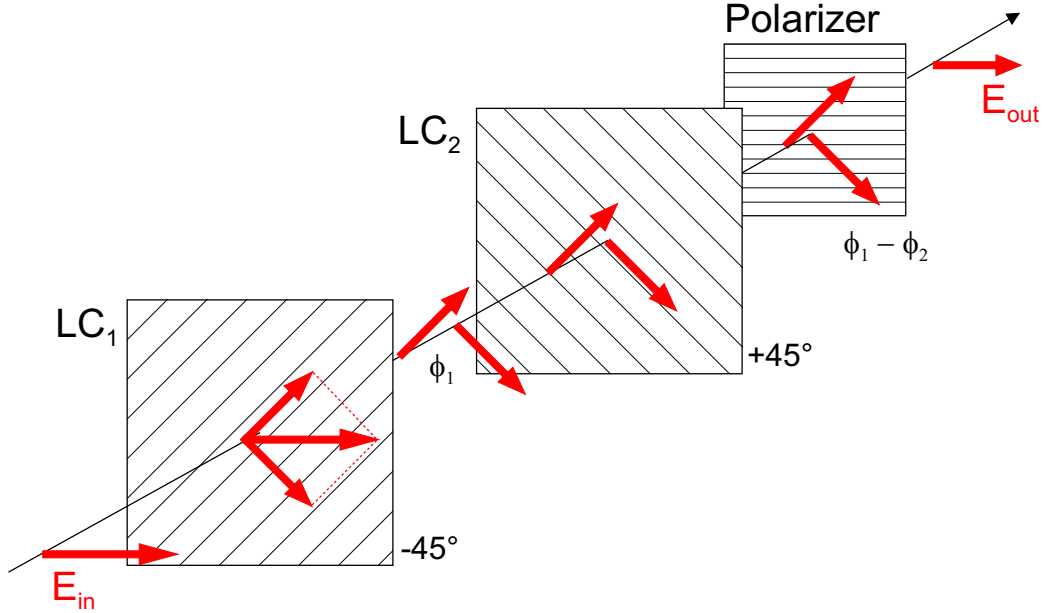
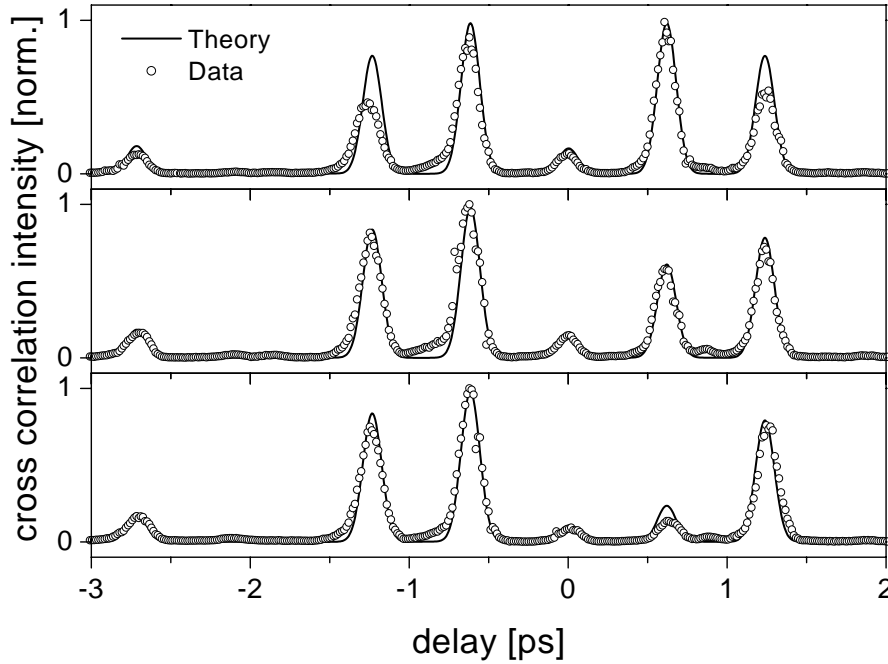


Figure 2.5: Setup for a dual LC-SLM

**Phase and amplitude shaping** Independent phase and amplitude modulation is achieved by combining two LC arrays into a single device, as shown in Figs. 2.4 and 2.5 [55]. With the propagation direction denoted  $z$  and the second transverse direction denoted  $y$ , the long axes of the liquid crystal molecules in the two SLMs are aligned at  $\pm 45^\circ$  with respect to the  $x$  axis. When a voltage is applied to one pixel in one of the two SLM layers, the liquid crystal molecules are rotated toward  $z$ , which results in a phase modulation for the component of light parallel to the liquid crystal axis in that SLM layer. For  $x$ -polarized light incident on a particular pixel  $n$ , the filter function is given by

$$\begin{aligned} B_n &= \left[ \exp(i\Delta\Phi_n^1(U_n^1))(\hat{e}_x + \hat{e}_y) + \exp(i\Delta\Phi_n^2(U_n^2))(\hat{e}_x - \hat{e}_y) \right] \\ &= \frac{1}{2} \exp \left[ \frac{i}{2} (\Delta\Phi_n^1(U_n^1) + \Delta\Phi_n^2(U_n^2)) \right] \times \\ &\quad \left\{ \cos \left( \frac{1}{2} (\Delta\Phi_n^1(U_n^1) - \Delta\Phi_n^2(U_n^2)) \right) \hat{e}_x + i \sin \left( \frac{1}{2} (\Delta\Phi_n^1(U_n^1) - \Delta\Phi_n^2(U_n^2)) \right) \hat{e}_y \right\} \end{aligned} \quad (2.30)$$



**Figure 2.6:** Cross-correlation measurements of a four-pulse sequence as generated by amplitude- and phase shaping. The amplitude of the third pulse at delay  $\approx 600$ fs is scanned while the other pulses are kept unaltered. A good agreement between experiment (open circles) and theory (solid line) is observed. The time-zero feature as well as one replica is clearly visible. From [60].

where  $\Delta\Phi_n^1(U_n^1)$  and  $\Delta\Phi_n^2(U_n^2)$  are the voltage dependent birefringences of respective LC array layers, respectively. If the output polarizer is oriented along  $x$ , the output phase and attenuation can be set independently by controlling  $\Delta\Phi_n^1 + \Delta\Phi_n^2$  and  $\Delta\Phi_n^1 - \Delta\Phi_n^2$ , respectively:

$$B_n = \frac{1}{2} \exp \left[ \frac{i}{2} (\Delta\Phi_n^1(U_n^1) + \Delta\Phi_n^2(U_n^2)) \right] \cos \left[ \frac{1}{2} (\Delta\Phi_n^1(U_n^1) - \Delta\Phi_n^2(U_n^2)) \right] \quad (2.31)$$

In this case neither mask acts as a phase or amplitude mask alone, but rather the two combined masks act together. Two parameters ( $T, \phi$ ) can be controlled for each pixel, since two parameters,  $U^1$  and  $U^2$  are accessible. The relation between these quantities is given by

$$T_n(U_n^1, U_n^2) = |B_n|^2 = \cos^2 \left[ \frac{1}{2} (\Delta\Phi_n^1(U_n^1) - \Delta\Phi_n^2(U_n^2)) \right] \quad (2.32)$$

$$\phi(U_n^1, U_n^2) = \arg B_n = \frac{1}{2} (\Delta\Phi_n^1(U_n^1) + \Delta\Phi_n^2(U_n^2)) \quad (2.33)$$

Pure phase shaping can now be obtained by setting  $(U_n^1, U_n^2)$  such that  $\Delta\Phi_n^1(U_n^1) - \Delta\Phi_n^2(U_n^2) = 1$ . Pure amplitude shaping is effected by setting  $(U_n^1, U_n^2)$  such that  $\Delta\Phi_n^1(U_n^1) + \Delta\Phi_n^2(U_n^2) = 0$ . Note that each LC array in the dual SLM must be calibrated by measuring its amplitude modulation response as a function of voltage, with the other LC array held at constant voltage. Fig. 2.6 shows the generation of a four-pulse sequence as obtained by amplitude and phase shaping with a  $2 \times 128$  SLM. The transmission and phase coefficients for each pixel were chosen as described at the end of section 2.3.2 with a simplified version of Eq. 2.19.

Pulse shaping using an optically addressed LC SLM has recently been reported [81]. This approach avoids pixelation of the SLM, and thus circumvents the side-effects described in section 2.3.2. Another promising extension of pulse shaping is femtosecond polarization pulse shaping [82].

## 2.5 The high resolution femtosecond pulse shaping device

As shown in section 2, the complexity of the shaped pulses depends on the number of pixels of the LC mask. In order to increase the shaping complexity, a novel liquid crystal display with 640 stripes has been successfully implemented. In contrast to previously used devices, the large active area allows for operation in high power laser systems. In this section, the new shaping apparatus is presented and its implementation for femtosecond pulse shaping is described [83]. With the increased number of pixels the manifold of accessible pulse modulations exceeds that of previous devices, which is especially important for sub-20 fs pulses [65].

### 2.5.1 Advantages of a SLM with 640 pixels

Section 2.3.2 reveals the fact that possible modulations are limited by LC-SLMs consisting of discrete stripes parallel to each other. A number of recent applications have shown that the 128 pixels used by most standard devices are not sufficient. In this section, a novel LC-SLM that has 640 stripes and a 12 bit resolution is reported. Combined with an all-reflective zero dispersion compressor it overcomes two major problems of standard devices. First, due to the large active area it is suitable for shaping high power laser pulses. Second, it allows for the first time the generation of waveforms that were not accessible before using LCDs, but are required by optimal control theory in order to control quantum systems. The experimental setup of this device is discussed, the capabilities are demonstrated, and the limits of the device are explored.

### 2.5.2 Experimental setup

The main components of the experimental apparatus are shown in Fig. 2.7. A Ti:Sa laser system (Coherent Vitesse / Quantronix / Positive Light ODIN) operated at a repetition rate of 1 kHz and a center wavelength of 804 nm serves as source for the ultrashort pulses. The pulse energy is 1 mJ, the spectral FWHM 24 nm, and the temporal FWHM 50 fs (assuming a Gaussian intensity profile). The pulses traverse a zero dispersion compressor and are subsequently characterized by a multi-shot FROG [84], see also appendix B, based on second harmonic generation. The SHG spectra are recorded by a CCD array having a 16 bit resolution. The design of the reflective zero dispersion compressor has been optimized (using ZEMAX 9.0) for minimum phase-front distortion of the output pulses.

The novel LCD (SLM-S 640/12) has 640 individual stripes (pixels), the area of each single stripe is  $97 \mu\text{m} \times 10 \text{ mm}$  and the gap between two stripes is  $3 \mu\text{m}$ . At a wavelength of 800 nm the thickness of the liquid crystal cell allows a maximum phase shift of  $6\pi$  (zero voltage). The average aligning time of the liquid crystals in the operating range between  $0.25\pi$  and  $2.25\pi$  is about 25 ms. The liquid crystals are aligned such that spectral components polarized perpendicular to the stripes may be retarded. Therefore, the LCD is perfectly matched to the high reflection efficiency for p-polarized light of the gratings in the visible and NIR spectral region. The two outer surfaces of the LCD have an antireflection coating and the LCD has a transmission of 95% in the wavelength range from 450 to 1500 nm. The damage threshold was measured to be  $300 \text{ GW/cm}^2$  (800 nm, 45 fs). At higher energies the structured polyimide layer of the LCD is damaged. The phase retardance at three different wavelengths of the LCD has been carefully measured and is shown in figure 2.8.

The two cylindrical mirrors have a focal length of 300 mm. Two 1800 lines/mm silver coated gratings offer the possibility to shape a spectral range of 96 nm at 810 nm with an average spectral resolution of 0.15 nm/pixel. Even for a pulse energy of 1 mJ the intensity impinging on the LCD mask in this pulse shaping setup is only about  $5 \text{ MW/cm}^2$  and, therefore, well below the damage threshold. The pulse width impinging on one pixel was approximated by a Gaussian pulse having a spectral FWHM of 0.15 nm. The relatively low intensity per pixel is a direct consequence of the large area which is covered by the dispersed spectrum. The overall transmission through the pulse shaper was measured to be 60% and is mainly determined by



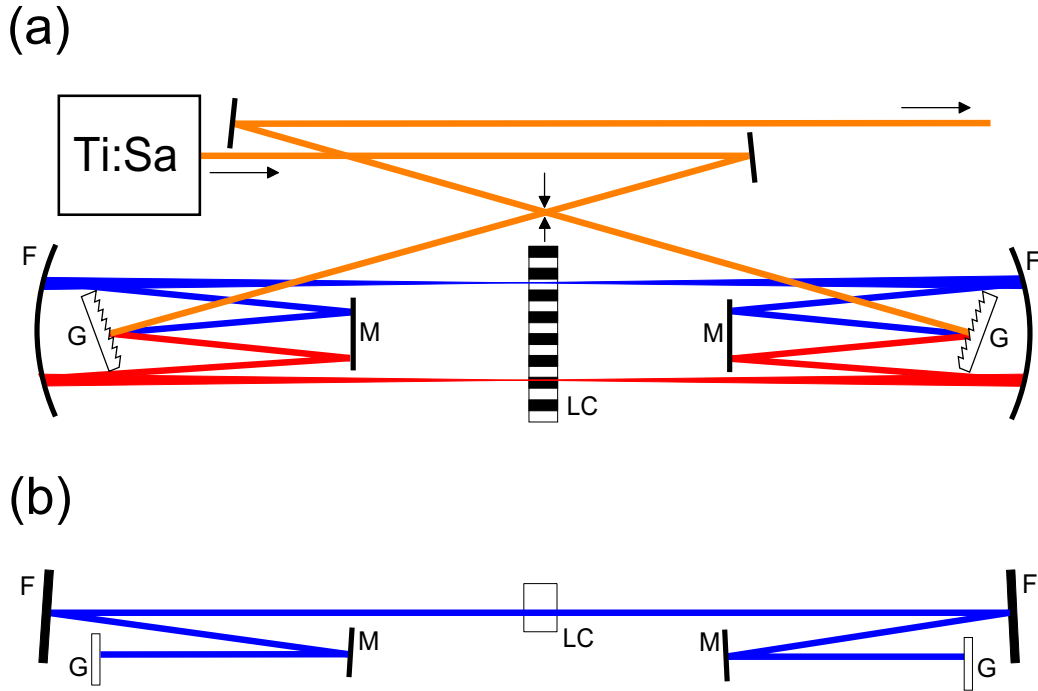


**Figure 2.7:** Sketch of the fs pulse shaping apparatus: (a) top view, (b) side view. The spectral phase of a laser pulse is manipulated in a 4-f arrangement with the novel LC-SLM in the Fourier plane. The 4f-arrangement presented here is a further development from that of section 5 which features the advantages of the dispersion-free all-reflective setup and concurrently avoids its disadvantage of imaging aberrations caused by the off-axis operation of the focusing mirrors, as depicted in Fig. 5.1. G: silver coated gratings (1800 lines/mm); F: cylindrical mirror  $f = 300$  mm; LC: SLM-S 640/12), M: folding mirrors.

the reflectivity of the gratings. Since no polarization filters are used the device is operated as a phase-only shaper.

### 2.5.3 Results and discussion

Since phase-only linear spectral filtering is used, the electric field of the emerging pulse is

$$E_{\text{out}}(\omega) = E_{\text{in}}(\omega) \exp[-i\Phi(\omega)] \quad (2.34)$$

where the phase  $\Phi(\omega)$  has a constant value between 0 and  $2\pi$  in the range  $[\omega_j, \omega_j + \Delta\omega]$  and  $j \in [1 \dots 640]$ . The frequency range  $\Delta\omega$  that is covered by one pixel is related to the spectral resolution of the gratings, the focal length of the focusing optics, and the beam diameter. The discrete nature of the phase modulation is inherent to the LCD mask and limits the accessible phase modulations where the limit is set by Nyquist's theorem [85]. In other words, the steepest slope of any applied phase function must not exceed  $\pi$  across one pixel ( $\Delta\omega$ ). For exactly this reason it is desirable to have as many pixels on the LCD as possible. On the other hand, the possibility of wrapping the phase increases the dynamical range [81], since it allows application of phase patterns modulo  $2\pi$ . Technical restrictions have until now limited the number of pixels to 128. With the new LCD described here it is possible to access phase modulations with a widely increased variability. In order to test the novel mask and to demonstrate the enhanced performance we have performed a number of pulse shaping experiments. In each experiment a specific type of modulation up to the corresponding Nyquist limit was applied to the mask in order to define the maximum working range of the device.

First, a FROG trace of the unshaped laser pulse was recorded. A reconstruction of the electric field shows that the pulse has no second but some residual third order phase. Applying a linearly

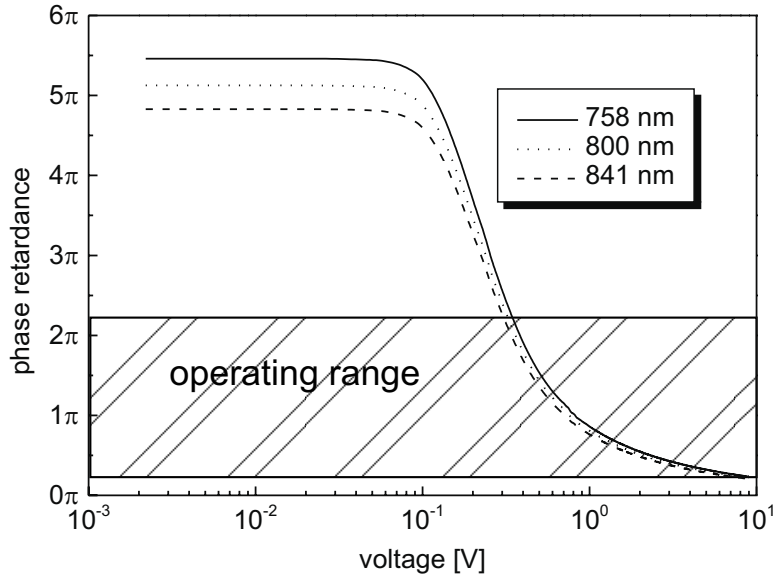


**Figure 2.8:** Phase retardance of the LCD as a function of the applied voltage for three different wavelengths.

increasing or decreasing phase allows one to shift the original pulse in time. For a spectral resolution of  $\Delta\lambda = 0.15$  nm/pixel the Nyquist limit for a purely linear phase is  $\Phi_1 = \pm 7187$  fs:

$$\Phi_1 = \frac{\lambda_0^2}{2c\Delta\lambda} \quad (2.35)$$

where  $c$  is the speed of light and  $\lambda_0$  the center wavelength of the laser pulse. As expected, for even larger linear phase modulations the original pulse structure is heavily distorted indicating that the Nyquist theorem is violated. Nevertheless, the accessible delay range is about 14 ps with a resolution of 7 fs. This makes the pulse shaper a valuable delay generator for pump-probe experiments with all the additional features of simultaneous pulse shaping.

Next, a purely quadratic phase modulation was applied to the LCD. The theoretical Nyquist limit amounts to  $\Phi_2 = \pm 102766$  fs<sup>2</sup>:

$$\Phi_2 = \frac{\lambda_0^4}{N\pi c^2 \Delta\lambda^2} \quad (2.36)$$

where  $N$  is the number of pixels. For this value the phase jump at the outer two pixels exceeds  $\pi$ . In order to produce a measurable effect, however, the Nyquist limit becomes important only at much higher quadratic phase modulations since it must be violated in a region of the LCD where the spectral intensity is non-zero. If the Nyquist limit is violated the temporal width of the pulses remains almost constant although the second order phase modulation is further increased. The experimental findings were in excellent agreement with the theoretical predictions [86]. Assuming a bandwidth limited input pulse with a spectral width of 24 nm, the present pulse shaping device allows one to stretch the original pulse from 51 fs to about 7 ps without any measurable distortions.

The last series of experiments deals with the generation of pulse trains by applying a sinusoidal phase pattern to the LCD. The periodicity of the pattern has been varied and the emerging pulses were again analyzed by the FROG setup. Figs. 2.9 show a series of FROG traces for different sinusoidal phase patterns. Note that in all cases the true replica of the original pulse (Fig. 2.9a) remain bandwidth limited. In the case of a low frequency (Fig. 2.9b) it is clearly evident that

the phase-only shaper shifts different portions of the spectrum in time corresponding to the applied spectral phase. If the frequency approaches the Nyquist limit, ghost replica appear in the FROG trace. As the frequency is further increased (Fig. 2.9d and e) the ghosts become more and more pronounced and move in the opposite direction as compared to the true pulse replica.

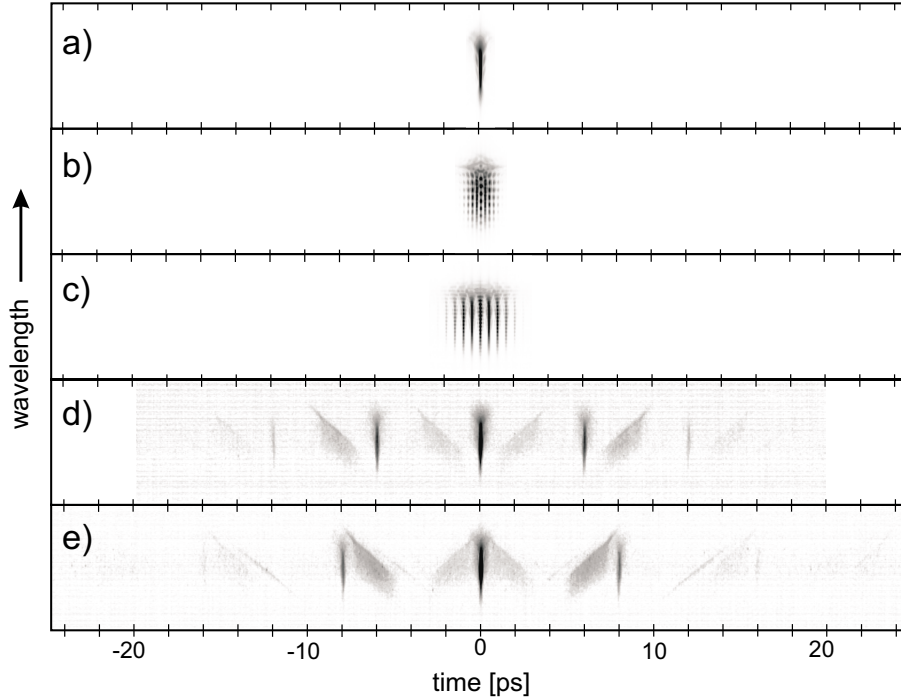


**Figure 2.9:** Sinusoidal phase modulations with variable spectral periodicity demonstrating the large dynamical range of the LCD: a) bandwidth limited input pulse, b)  $250 \text{ PHz}^{-1}$ , c)  $500 \text{ PHz}^{-1}$ , d)  $6000 \text{ PHz}^{-1}$ , e)  $8000 \text{ PHz}^{-1}$ .

Due to the nonlinear dispersion of the grating the spectral resolution is a function of the pixel position on the LCD and must not be assumed to be constant [87]. This effect becomes even more pronounced as the active area and the number of pixels of the LCD increases. Fig. 2.10 shows two FROG traces where a sinusoidal phase modulation with a period of  $1000 \text{ PHz}^{-1}$  was applied to the LCD. Calculating the proper position of each wavelength on the LCD leads to pre- and post-pulses which are true replica of the original pulse (Fig. 2.10a). However, the replica become artificially phase-modulated (Fig. 2.10) if the spectral resolution is fixed to the average value of  $0.15 \text{ nm/pixel}$ . A fixed spectral resolution results in a sinusoidal phase modulation with the periodicity being a function of the wavelength (pixel position). Therefore, the periodicity in time is no longer constant for all wavelengths, a fact that is readily observed in Fig. 2.10b). As a consequence, the pulse replica broaden in time with increasing delay time.

## 2.6 Alternative pulse shaping methods

### 2.6.1 Pulse shaping with AOMs

Programmable pulse shaping based on the use of an acousto-optic modulator has been developed by Warren and co-workers [88–91]. The apparatus is depicted in Fig. 2.11. The AOM crystal, typically  $\text{TeO}_2$ , is driven by a rf voltage signal, which induces a traveling acoustic wave in a piezoelectric transducer. The density wave travels across the modulator with velocity  $v_{ac}$ , giving rise to a refractive index grating via the photoelastic effect. The grating period  $\Lambda$  is given by  $v_{ac}/\nu$ , where  $\nu$  is the rf drive frequency. The grating may induce phase, amplitude, or frequency modulation through the use of a correspondingly modulated rf drive waveform.

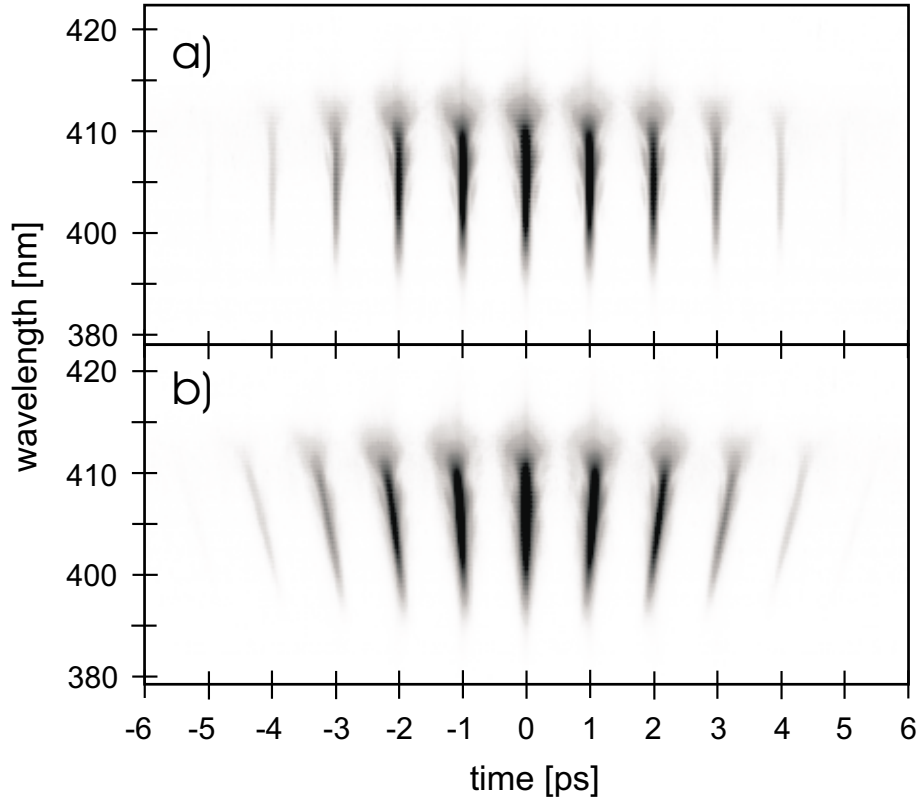


**Figure 2.10:** Influence of the nonlinear grating dispersion on the modulated output pulse: a) Sinusoidal phase modulation with spectral periodicity of  $1000 \text{ PHz}^{-1}$  taking into account the nonlinear grating dispersion and b) assuming an equally spaced wavelength pattern of  $0.15 \text{ nm/pixel}$ .

When the spatially dispersed frequency components diffract off the grating, the spectrum is modified according to the grating spatial modulation function. This results in the desired Fourier transform pulse shaping operation. Ideally the spatial grating  $s(x)$  is related to the input voltage  $v(t)$  through  $s(x) \sim v(x/v_{ac})$ . In practice there are a number of mechanisms which impair this ideal relationship.

In the following some of the typical operating characteristics of AOMs used for pulse shaping are briefly described. Further details are given in Refs. [88] and [90].

- The time for the acoustic wave to move across the modulator aperture  $l_a$  is  $t_o = l_a/v_{ac}$ . This aperture time determines how fast a specific spatial pattern can be loaded into the device. For  $\text{TeO}_2$  the aperture time is between  $1.2$  and  $10 \mu\text{s}$  [88, 89].
- The acoustic grating pattern propagates across the modulator. Although the grating appears frozen during readout by a single femtosecond or picosecond pulse, the pattern can shift significantly during the time elapsed between consecutive pulses. Therefore, the AOM technique cannot in general be used in conjunction with high repetition rate laser sources, since the pulse shape would change from pulse to pulse. This limitation is irrelevant for amplified ultrafast laser systems, which usually have a pulse repetition rate slower than the acoustic aperture time: This allows the acoustic pattern to be refreshed before, and synchronized to, each amplifier pulse. Hence, AOM pulse shaping is usually restricted to applications involving femtosecond amplifier systems.
- The number of independent acoustic features which can be stored within the full aperture of the AOM provides an upper limit to the pulse shaping complexity. The number of independent "pixels" of resolution available is proportional to  $N_{eff} \Delta\nu t_o = \Delta\nu l_a/v_{ac}$ , where  $\Delta\nu$  is the modulation bandwidth of the AOM, and  $\Delta\nu t_o$  the AOM time-bandwidth

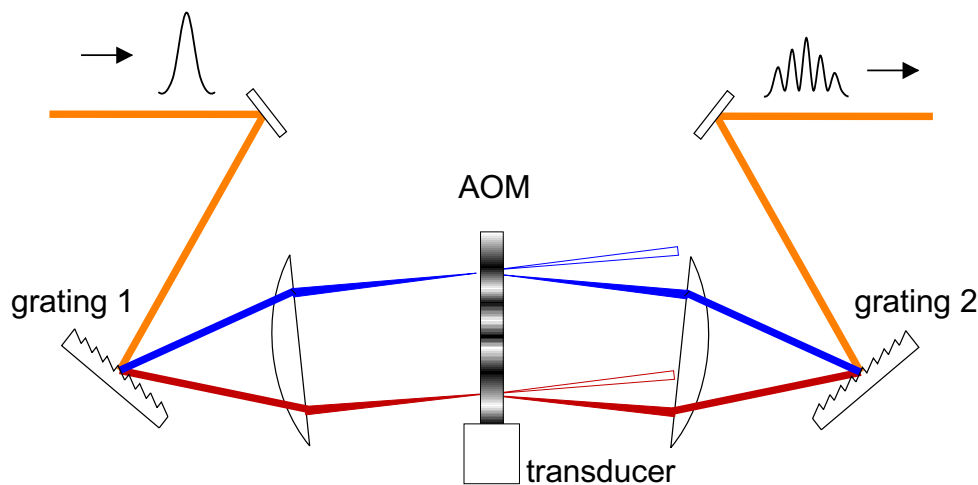


Figure 2.11: AOM pulse shaper.

product. An appropriate AOM is able to imprint up to nearly a thousand independent features onto the spectrum, provided that the 4f-configuration has sufficient resolution.

### 2.6.2 Pulse shaping with deformable mirrors

An intuitive technique to produce shaped pulses makes use of micro-machined membrane deformable mirrors (MMDMs) in a grating compressor. Basically, the design is comparable to that of Fig. 2.1, the only difference being that only one grating and one lens (or focusing mirror) is used. A highly reflective coated membrane which is supported by an ensemble of 10 to 20 piezo-electric actuators is placed in the Fourier plane. This mirror reflects all frequency components back onto the grating, and the output pulse is identical to the input pulse as long as the membrane is planar. When the actuators enforce a slight curvature of the membrane, the relative phase of each frequency component is changed proportionally to the path length difference induced by the deformation of the membrane. MMDMs can also be used in a prism compressor. The phase induced by the MMDM then adds to the chirp induced by the compressor.

Obviously, these devices can only be used for phase modulation. The operating wavelength range is limited only by the availability of gratings and reflective coatings for the particular region. The modulation depth is given by the maximal translation of the actuators which is on the order of several  $\mu\text{m}$ , or, equivalently, several  $\pi$  phase modulations. Since the phase modulation is inherently smooth – the membrane itself acts as a smoothing element due to its stiffness – pixelation effects are absent. Nevertheless, this also means the phase function cannot be wrapped into the interval  $[0, 2\pi]$  so that, in contrast to SLMs, the total modulation depth over the complete aperture amounts to only several  $\pi$ . Thus, merely a residual phase can be removed with MMDMs, which is the main application of these devices [64, 92–94].

### 2.6.3 Comparison of LC, AOM, and MMDM

Table 2.1 compiles the crucial characteristics of LC, AOM, and MMDM pulse shaping technology (for LC technology, the specifications of the CRI mask are used here). Each of the pulse shaping

approaches has its own specific merits, and an intelligent choice for a specific experiment must balance a number of trade-offs depending on its most important requirements.

	<b>LCM</b>	<b>AOM</b>	<b>MMDM</b>
<b>Pulse width</b>	Tested down to 13 fs. No obvious factors limiting the extension to shorter pulses.	Studied most extensively on the 100 fs time scale. Several factors are expected to make the AOM approach more difficult for much shorter pulses.	Tested down to 7fs. No obvious factors limiting the extension to shorter pulses.
<b>Programming time</b>	Determined by the liquid crystal medium response, typically on the order of several 10 ms.	Determined by the acoustic aperture time, which is on the order of $\mu$ s.	Determined by the mechanical response of the membrane. On the order of several ms.
<b>Pulse repetition rate</b>	Any repetition rate.	Pulse repetition rates must be slower than the acoustic aperture time. Not applicable to mode-locked systems.	Any repetition rate.
<b>Modulation format</b>	Independent, gray-level spectral amplitude and phase control.	Independent, gray-level spectral amplitude and phase control.	Continuous spectral phase control.
<b>Pulse shaping complexity</b>	Limited by the number of pixels. Current LC arrays: 128 and 640 pixels.	Of order 1000 with commercially available devices	Limited by the low number of actuators (10-20).
<b>Efficiency</b>	Transmissions approaching 100%.	10-15%, limited to low diffraction efficiency by acoustic nonlinearities.	Reflections approaching 100%.
<b>Fidelity</b>	Pixelated nature of the modulator can lead to temporal sidelobes for spectral patterns which vary too rapidly from one pixel to the next.	Under appropriate conditions very high quality waveforms have been demonstrated.	High quality waveforms because of inherently smooth phase functions.
<b>Damage threshold</b>	Low when built-in sheet polarizers are used. Medium without sheet polarizers.	High	High

Table 2.1: Comparison of LCMs, AOMs, and MMDMs. Pulse shaping complexity is usually defined as the number of independent features which may be placed onto the spectrum.

## 3

# Amplification of tailored white light continuum

For the achievement of further progress in controlling quantum phenomena, the development of techniques to produce high intensity shaped pulses in wavelength regimes other than those of Ti:Sa lasers will be crucial. Control of vibrationally mediated chemical reactions, for example, which proceed on the ground state potential energy surface (PES), may be achieved with shaped infrared (2-10 $\mu\text{m}$ ) wavelength pulses. Control of photochemical reactions, which in contrast occur on the excited PES, typically requires shaped UV pulses. Shaped pulses in these wavelength regimes have been produced recently [95–98]. Many biomolecules, which are prime candidates for coherent control studies [99] possess a broad absorption spectrum in the visible (VIS). In this wavelength regime, shaped pulses have been obtained mainly via the conventional approach of frequency conversion followed by pulse shaping [65]. Nevertheless, the power losses induced by frequency conversion combined with the limited efficiency of pulse shapers often precludes experiments which require high power ultrashort pulses. One obvious solution to this restriction is to carry out amplification after the shaping process [100, 101]. The crucial point is whether the characteristics of the shaped pulses survive the amplification process. We show that this is indeed the case and that, with our apparatus, pulse features which have been previously challenging can be generated easily [100, 102].

These results directly impact the realization of experiments which have been suggested by results of optimal control theory (OCT) [103]. For the control of various molecular systems, OCT predicts ultrashort broadband electrical fields following the Tannor-Rice pump-dump scheme [6] which typically incorporates two pulses with different frequencies: the first pulse (pump) excites the system to an excited state, the second pulse (dump) is suitably delayed to exploit the temporal evolution in the excited state and transfers population to a target state. Numerical simulations reveal that for selected systems not only the delay, but also the relative carrier phase difference influences the degree of control [104].

Electric fields with these attributes cannot be produced easily with the conventional approach of two independent laser sources, since path length fluctuations make it difficult to maintain a fixed phase between the pulses. Phase-locked double pulses of identical wavelength have been obtained with a pulse shaper [16, 55, 105] or a stabilized Michelson interferometer [106]. It should be noted that with the Michelson setup, the phase is controlled via the delay; therefore, delay and relative carrier phase cannot be set independently. Phase synchronization of two Ti:Sa oscillators of several nJ pulse energy has been reported recently [107]. Nevertheless, the most feasible approach to date for obtaining two-color pulses in the VIS with  $\mu\text{J}$  energies is amplitude and phase shaping of frequency-converted amplified Ti:Sa pulses. Since amplitude modulation involves significant losses, a second amplification stage must follow the shaping.

As an extension of the results presented in Ref. [100], wherein we reported amplitude and phase transfer during an optical parametric amplification process in a mixing crystal and demonstrated inherently phase-locked two-colour double pulses, we here show that chirp can be imposed on the

sub-pulses and that even more complex pulse structures can be generated. The scheme based on the broadband amplification of a shaped white light continuum (WLC) in a non-collinear beam geometry [38] is presented in detail.

### 3.1 Experiment

Fig. 3.1 shows the experimental setup. The WLC is produced in a 2mm sapphire plate from a small fraction of the fundamental pulse of a commercial Ti:Sa laser system (812nm, 100fs, 300  $\mu$ J, 1kHz). The pulse shaper to modify the WLC is based on a standard 4f-setup [56,65] with  $f=150$ mm cylindrical mirrors [62] and  $1/d=600/\text{mm}$  gratings. The liquid crystal (LC) mask (CRI SLM 256) consists of a stack of two arrays of  $N = 128$  pixels mounted between two sheet polarizers which can independently influence attenuation and phase of the incident spectrum. The accepted bandwidth of this shaper is  $\approx 110$ nm which is below the bandwidth of the WLC and the amplification bandwidth of the noncollinear mixing process. The grating dispersion has been chosen to achieve a good compromise between spectral resolution and bandwidth. Raising the bandwidth with a smaller dispersion would reduce the spectral resolution and thus sacrifice modulation fidelity. An LC mask with more stripes can avoid this bottleneck [83]. The pulses are characterized with a multishot SHG FROG (BBO,  $10\mu\text{m}$ ). The beam splitters used in the FROG setup are Cr coated 1mm fused silica (FS) wedges which assure a constant (30/30) splitting ratio over the entire wavelength range between 300nm and 1100nm. The voltages applied to each pixel are corrected for the wavelength dependence of the phase shift. This correction is crucial for minimizing the leakage of the WLC through the LCM pixels which would give rise to the amplification of undesired spectral components.

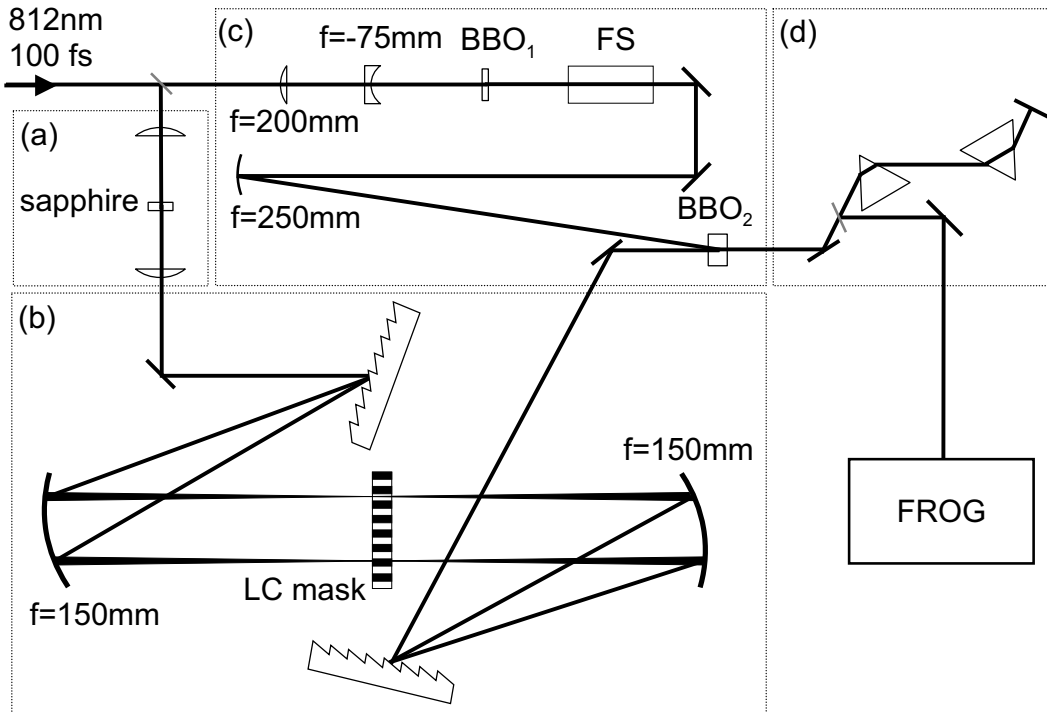


**Figure 3.1:** (a) WLC generation, (b) pulse shaper,  $1/d=600/\text{mm}$  gratings,  $f=150$ mm cylindrical mirrors, CRI phase and amplitude mask with  $2 \times 128$  pixels (c) amplification unit, BBO<sub>1</sub>: SHG 800nm  $\rightarrow$  400nm, BBO<sub>2</sub>: frequency mixing, FS: 15mm fused silica rod, (d) prism compressor. FROG: frequency-resolved optical gating.

To achieve the large amplification bandwidth vital for the effective transfer of all components of the tailored WLC, a non-collinear mixing process is used [108]. The shaped WLC is amplified in a 2mm BBO crystal pumped by the frequency-doubled Ti:Sa pulses. The angle between pump and



shaped seed is set to satisfy the condition for ultrabroad amplification bandwidth [38, 108–110]. The pump pulses are temporally stretched with a 15mm fused silica rod to ensure temporal overlap with the shaped, elongated seed pulses. This method obviates mechanical readjustments of the delay during operation. A fused silica prism compressor behind the amplification stage cancels the linear chirp of the WLC produced in the sapphire plate. It is adjusted for minimum output pulse length at a wavelength corresponding to the central mask wavelength. Tuning the transmitted center frequency either to the red or the blue results in a pulse lengthening in either direction owing to the imperfect phase elimination by the prism compressor over the entire tuning range. In principle, the shaper could be adjusted to produce a negatively pre-chirped WLC, which would make the prism compressor unnecessary.

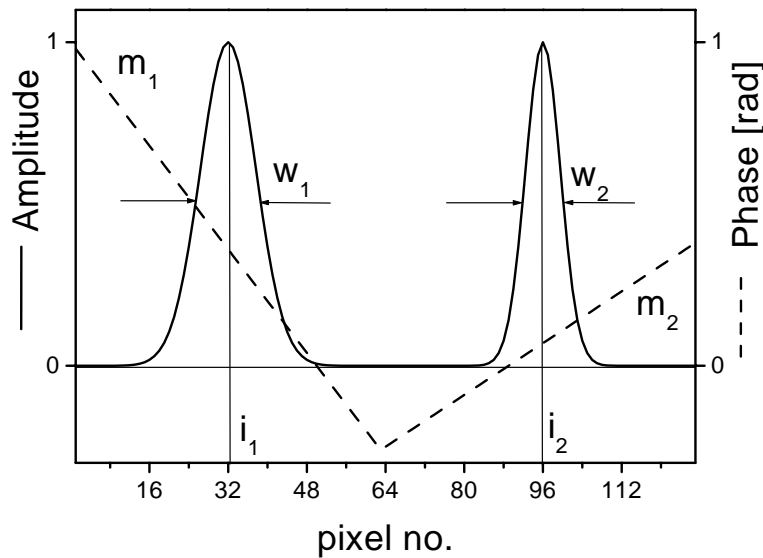


**Figure 3.2:** Amplitude (solid curve) and phase (dashed line) functions for the special case  $K = 2$  in eq. 3.2 imposed onto the WLC. The phase functions are defined within each transmission window.

Spectral and temporal properties of the output pulses are controlled by applying suitable amplitude and phase functions to the LC mask. Our approach to control the spectrum of the output pulses rests upon use of the mask transmission function  $T(i)$  ( $i$  being the pixel number), which consists of  $K$  Gaussian windows with a FWHM of  $w_k$  centered at pixels  $i_k$ . The center of the window  $i_k$  and its width  $w_k$  determine the frequency components that are subsequently amplified. The mask phase function  $\Phi_k(i)$  for each amplitude window is represented by a second order polynomial. Its linear term, for example, corresponds to a time shift and controls the delay between the individual output pulses:

$$T(i) = \sum_{k=1}^K \exp \left[ - \left( \frac{i - i_k}{w_k} \right)^2 \right] \quad (3.1)$$

$$\Phi_k(i) = c_k (i - i_k)^2 + m_k (i - i_k) + \phi_k \quad (3.2)$$

The polynomials  $\Phi_k(i)$  are defined within intervals between the arithmetic mean values  $(i_{k-1} + i_k)/2$  and  $(i_k + i_{k+1})/2$  of two adjacent centers of amplitude windows  $k$  and  $k + 1$  with  $i_0 = 0$  and  $i_{K+1} = N = 128$ . A graphical illustration of Eq. 3.2 is given in Fig. 3.2.

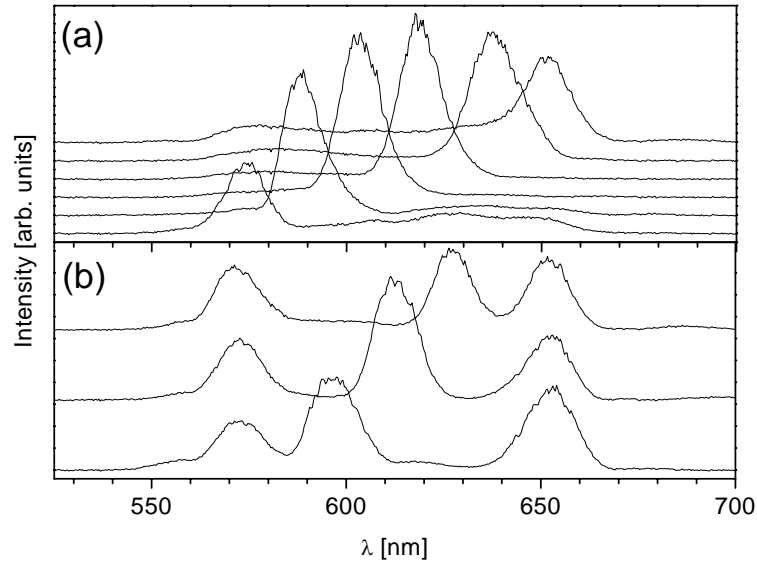


**Figure 3.3:** (a) Single spectra produced by scanning the center  $i_k$  of a single transmission window ( $i_1 = 10, 30, \dots, 110$ , from bottom to top). (b) Triple spectra generated by three windows, scanning the middle window ( $i_2 = 40, 60, 80$ , from bottom to top, corresponding to peak wavelengths of 595nm, 612nm, and 627nm).

## 3.2 Phase and amplitude transfer

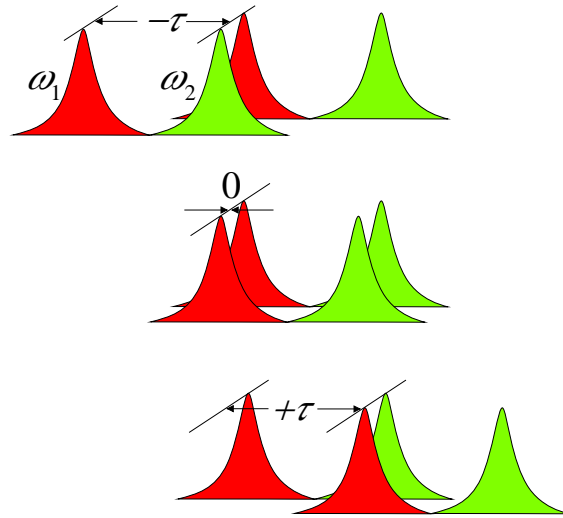
### Spectra

Fig. 3.3a shows the output spectra after amplification for different centers  $i_1$  ( $K = 1$  in Eq. 3.2) of a single transmission window. The expected direct dependence of the observed central wavelength on the center pixel of the transmission window is obvious. For amplified wavelengths corresponding to values of  $i_1$  near 0 or 128, residual signal is observed which is due to leakage through the transmitting gaps of the mask and the limited contrast of the sheet polarizers. In Fig. 3.3b triple peak spectra using three amplitude windows ( $K = 3$ ) have been generated where the middle window has been scanned, showing that the spectral shape of the white light is transferred. The adjustment of the output central wavelength via amplitude filtering has the advantage that undesired frequency components are mostly suppressed already in the WLC, i.e. before amplification, resulting in output pulses which are smooth by construction. The spectral width of the output can be easily tuned via the parameter  $w_k$ , which is useful for experiments that require simultaneous temporal and spectral resolution. Amplitude shaping of the WLC is also possible with a slit in the Fourier plane instead of the liquid crystal mask; this technique is already useful for the wavelength tuning of non-collinear optical parametric amplifiers.

### Two-color double pulses

The temporal properties of the output pulses are influenced via the phase. A dual pulse spectrum which peaks at 588nm and 647nm is generated with two amplitude windows ( $K = 2$  in Eq. 3.2). A temporal delay between these two frequency components is introduced by applying linear phase functions with differing slopes  $m_i$ . Fig. 3.4 explains the formation of the particular form of these FROG traces. Fig. 3.5 shows the corresponding FROG traces and the retrieved temporal intensities (below 40fs FWHM for each sub-pulse in all cases) for slope differences (Eq. 3.2)  $|m_1 - m_2| = 0$  (a), 0.3 (b), and 0.75 (c) rad/pixel. A beating period of 20fs (Fig. 3.5a) is in good agreement with the theoretically expected value for a spectral interference at the above mentioned wavelengths. The observed temporal separation is 82fs (Fig. 3.5b) and 145fs

(Fig. 3.5c), respectively.



**Figure 3.4:** Formation of the FROG traces as observed in Fig. 3.5. A two-colour double pulse with, for instance, a red ( $\omega_1$ ) and a green ( $\omega_2$ ) sub-pulse and a mutual delay  $\tau$  is assumed. In the FROG setup, two replica of the double pulse are produced and correlated with a delay  $t$  in the crystal. For a delay of  $t = -\tau$  of these replica, only the red part of the first pulse and the green part of the second pulse overlap and thus are correlated, leading to a signal at frequency  $\omega_1 + \omega_2$  as can be observed in the FROG traces for negative delays. For a delay  $t = 0$ , each color of the double pulse is mixed with its corresponding counterpart, leading to a double peak signal at  $2\omega_1$  and  $2\omega_2$ . For  $t = +\tau$ , the green part of the first pulse and the red part of the second pulse again produce a signal at  $\omega_1 + \omega_2$ .

The maximum delay achievable with this setup amounts to about 160fs and is limited by the temporal overlap between seed and pump. This delay time may be extended by further stretching the pump pulse. The ultimate limit is given by the maximal linear phase function which can be produced by the mask without violating the Nyquist theorem [55, 65, 83] ( $\approx 1$ ps). The generalization to pulse sequences with three or more pulses is straightforward.

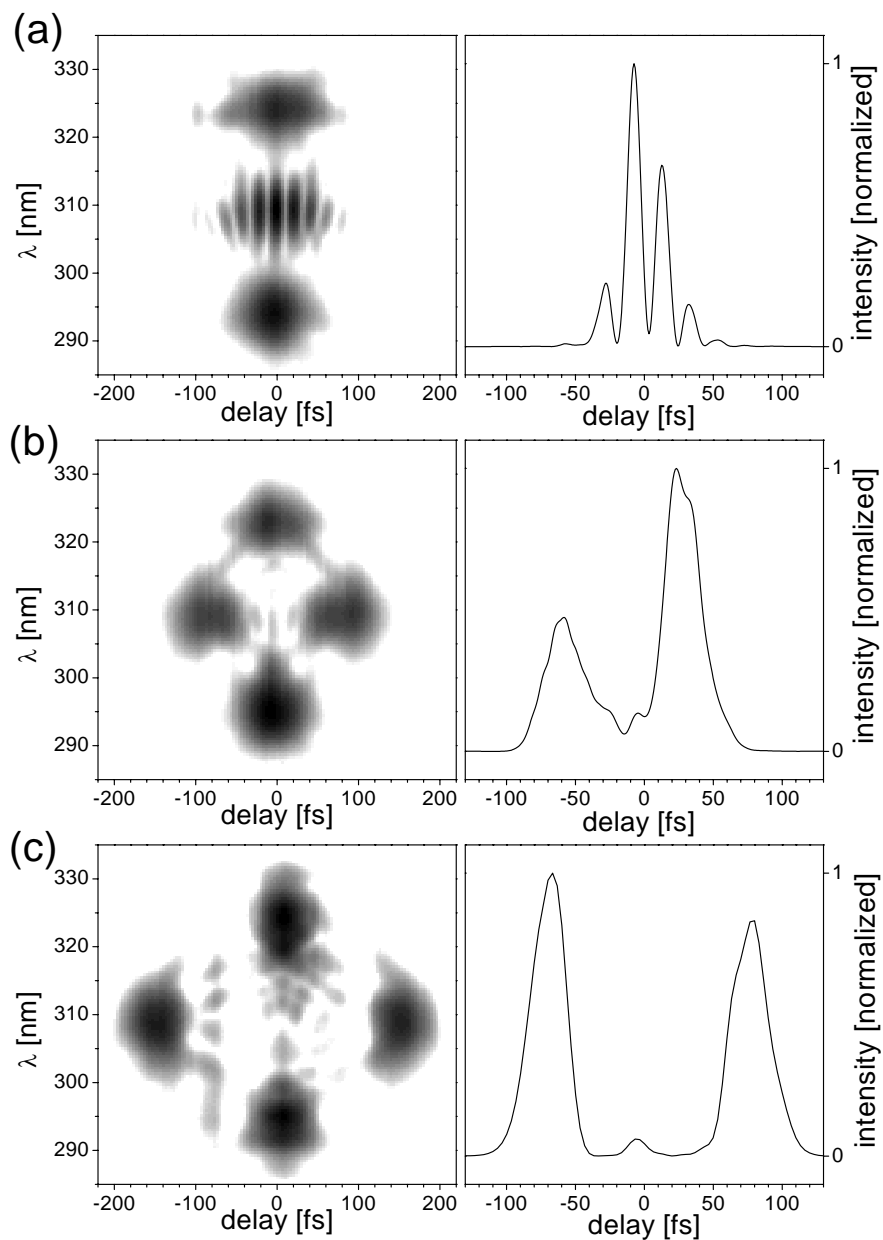
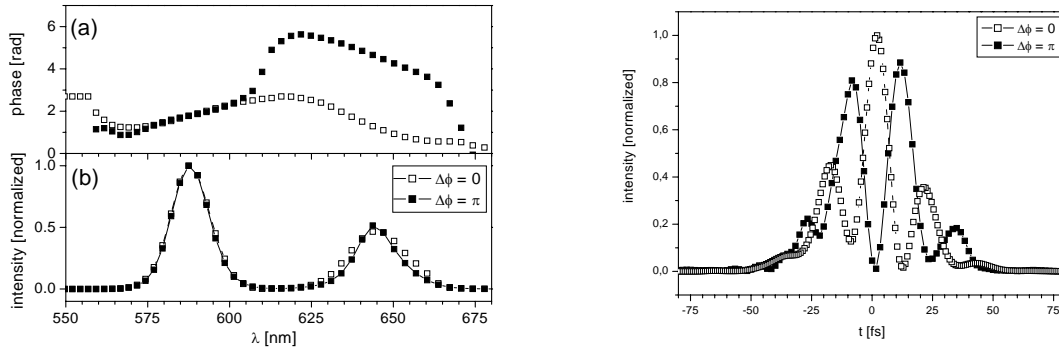


**Figure 3.5:** Experimental FROG traces (upper) and retrieved temporal intensities (lower) for two-color pulses (588nm, 647nm) and  $|m_1 - m_2| = 0$  (a,d), 0.3 (b,e), and 0.75 (c,f) rad/pixel in eq. 3.2.

## Control of phase transfer



(a) (■) Reconstructed spectral phase (a) and intensity (b) for a  $\pi$  phase step ( $\phi_1 = 0, \phi_2 = \pi$  in eq.2) introduced onto one part of the spectrum. (□) reference pulse with  $\phi_1 = \phi_2 = 0$ .

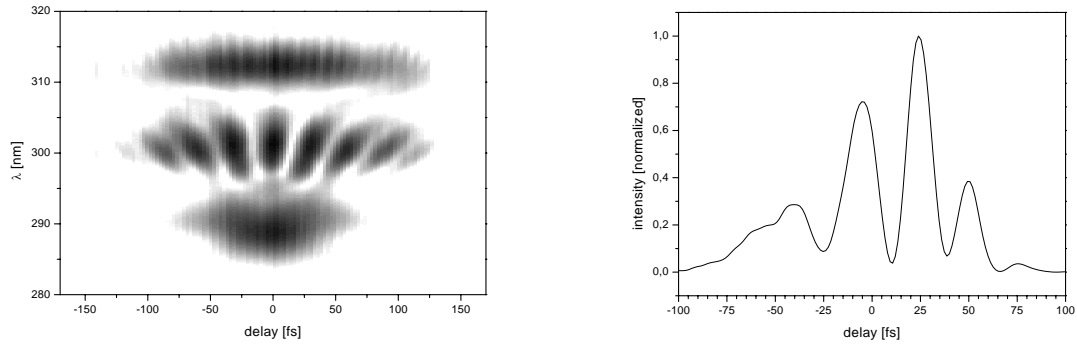
(b) Reconstructed temporal field. The beating structure shifts by  $\pi$  as a  $\pi$  phase jump is imposed onto one part of the spectrum.

**Figure 3.6:** Transfer of phase functions during the amplification process:  $\pi$  phase jump

The phase intentionally imposed onto the WLC in the shaper adds to the linear chirp carried over from the WLC generation process. Since the prism compressor mainly cancels the linear chirp produced by the optical components in the beam path, the phase function introduced by the shaper remains. The conservation of the phase function of the WLC during the amplification process is thus crucial for the generation of modulated pulses and provides control of the relative phase between the single pulses. This has been verified by generating a two-color double pulse (588nm, 647nm) with a temporal overlap between both sub-pulses. Fig. 3.6(a) shows the spectral amplitude and phase retrieved from FROG traces taken with and without a  $\pi$  phase shift between the two spectral components. This phase shift has no effect on the spectrum. A phase step of  $\Delta\phi \approx 3.34$  was retrieved, in good agreement with the expected value, showing that the phase between the two pulses is locked and can indeed be controlled. This result is further evidenced in Fig. 3.6(b), which shows a shift of  $\pi$  in the beating structure when the  $\pi$  phase step is imposed onto one part of the spectrum.

An important application of amplified chirped pulses involves experiments following the Tannor-Rice scheme, wherein specific excitation of the system or the focusing of a wave packet within the molecular system is achieved via the chirp. To investigate the chirp transfer during amplification, a double peak spectrum with temporal overlap of the sub-pulses was again generated. A slight chirp ( $c_1 = +0.01$  in Eq. 3.2) was imposed onto the red part of the spectrum. Phase conservation as demonstrated above should then permit chirped output pulses. This should cause a temporal elongation of the red sub-pulse as observed in Fig. 3.7(a) (without the chirp, both subpulses have approximately equal duration). Furthermore, the frequency of the SFM signal (red sub-spectrum plus blue sub-spectrum) should vary in time. Indeed, this is observed in Fig. 3.7(a) in the frequency curvature of the interference structure. The interference period of the reconstructed temporal intensity steadily decreases from  $\approx 35$ fs to  $\approx 20$ fs as seen in Fig. 3.7(b), which is again the expected behavior. If the sign of the chirp is opposite to that chosen in Fig. 3.7(a), the direction of the curvature of the SFM interference structure changes as expected, i.e. instead of pointing downwards, the curvature is directed upwards in the FROG trace. This demonstration of phase and, more significantly, chirp transfer during a parametric amplification process offers a means of cancelling high order chirps while avoiding shaping losses.

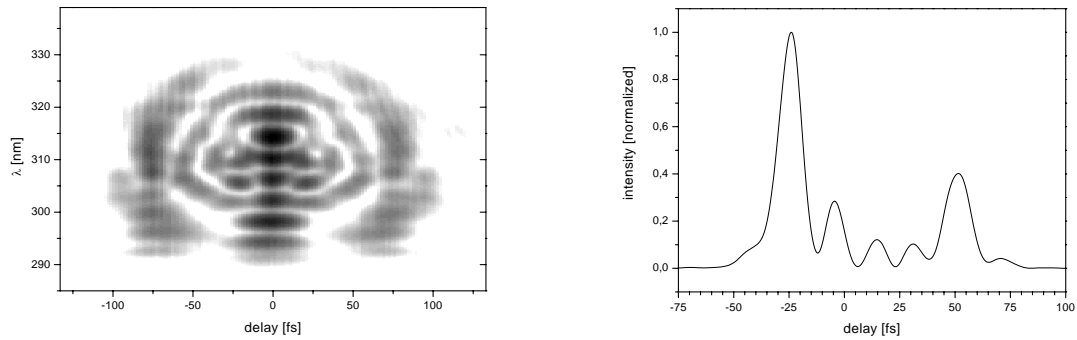
As a last example, Fig. 3.8(a) illustrates the generation of complex pulse structures. Here, a sinusoidal phase pattern  $\Phi(i) = \sin(ci)$ ,  $i$  being the pixel number, was imposed onto the WLC,



(a) FROG trace of a double pulse with one chirped sub-pulse. A quadratic phase function ( $c_1 = +0.01$  in Eq. 3.2) was imposed onto the red part of the spectrum.

(b) Reconstructed temporal field. The beating period steadily decreases from  $\approx 35$ fs to  $\approx 20$ fs.

**Figure 3.7:** Transfer of phase functions during the amplification process: Linear chirp



(a) FROG trace of a complex multiple pulse structure

(b) Reconstructed temporal field

**Figure 3.8:** Generation of complex modulated pulses with sinusoidal phase functions.

giving rise to a spectrally modulated multiple pulse structure as shown in Fig. 3.8(b).

### 3.3 Summary

Amplification of a shaped white light continuum permits the generation of complex spectra over a broad tuning range of 75nm owing to the wide amplification bandwidth of the non-collinear mixing process. Two-color phase-locked fs double pulses with adjustable delay, central frequency and carrier phase have been demonstrated. The transfer of chirp, as well as the controlled generation of highly complex multiple pulse structures, was demonstrated.

The suppression of undesired frequencies in the WLC facilitates the generation of smooth and stable spectra and prevents energy flow into unwanted spectral components, in particular the residual fundamental of the WLC. Since shaping takes place prior to amplification, phase and amplitude shaped pulses of several  $\mu$ J are obtained. The scheme is especially suitable for feedback-controlled coherent control studies [10, 111] because the pulse characteristics are tuned purely electronically within a few milliseconds.

---

## 4

# Evolutionary algorithms for coherent control

Of critical importance in the concept of feedback controlled experiments is a reliable optimization algorithm which searches for the global optimum in a multidimensional parameter space. The algorithms typically used for these experiments are termed evolutionary as they mimic the process of biological evolution [112, 113]. Minimizing the data acquisition time in complicated control experiments, which may be running stably for only a short time, is essential. Therefore, an efficient algorithm is highly desirable.

This last section of the technical part closes the feedback loop. It explains the implementation of evolutionary strategies for femtosecond pulse shaping and studies their performance (i.e. finding the global optimum, fast convergence) under different optimization conditions. The convergence behavior of an evolutionary strategy with respect to the number of free variables, steering parameters of the algorithm, and noise is exemplified in the subsequent section. The maximization of the second harmonic (SH) signal of ultrashort pulses [63, 65, 79] serves as a test environment. A numerical simulation of this experiment is feasible and allows for comparison of the simulations with experimental data. In the concluding section of this chapter the influence of different parameterizations of the shaped pulses on the optimization result is discussed. Several experiments serve to show that a restriction of the parameter space, i.e. the reduction of the number of independent variables, facilitates a grasp of the underlying principles of the physical process which has been optimized, without deteriorating the optimization result [111].

## 4.1 Evolutionary algorithms

### Optimization

Many problems encountered today in science or technology require an optimization of some merit or objective function, which depends on many variables. It is the purpose of this chapter to clarify the terminology of this field which will be introduced in an abstract form.

Imagine a situation wherein one must decide between two possibilities (a) and (b), each with different outcomes. Naturally, one chooses the option which better serves one's needs, which means that one *optimizes* between the two choices. This, obviously, requires a classification of the solutions, i.e. a scale to judge whether the first or the second solution, (a) or (b), is best. This scale clearly depends on the choice (a) or (b). In other words, one requires an *objective function* or *merit function* which depends on a set of *parameters*, in this case only one parameter  $x$  with either  $x = a$  or  $x = b$ . Because the number of possible outcomes in this example is finite, a finite number of evaluations of the merit function is sufficient for finding the global optimal solution.

*Optimization* entails picking the most expedient of many alternatives. The required scale which ranks these alternatives is called the *objective function* or *merit function* and must depend on a set of *parameters* or *variables* which label the alternatives.

In particular, optimization of a function  $f = f(x_1, \dots, x_N)$  involves determination of those values of the variables  $x_1, \dots, x_N$  for which  $f$  assumes its extremum. As long as the number of permitted values for the variables is finite and still small, it is conceivable to evaluate the objective function  $f$  for every set of the variables and thereby find its global optimum. Usually, however, this number is large or even infinite which makes the use of this "brute force attack" impossible. If  $f$  can be expressed analytically, differential calculus can be used to identify the optimum, provided that the equations to be solved are tractable and have an analytical solution. If neither of these schemes is applicable, optimization algorithms are generally used. Basically, all such procedures build on the same ground: Given an arbitrary point  $(x_1, \dots, x_N)$  in parameter space, the task is to propose a new point  $(x'_1, \dots, x'_N)$  which produces a result closer to the optimum. For the special case of  $N = 2$ , the merit function may be plotted as a surface versus the *parameter space* spanned by the two variables  $x_1, x_2$ . Two generic types of merit functions are depicted in Fig. 4.1.

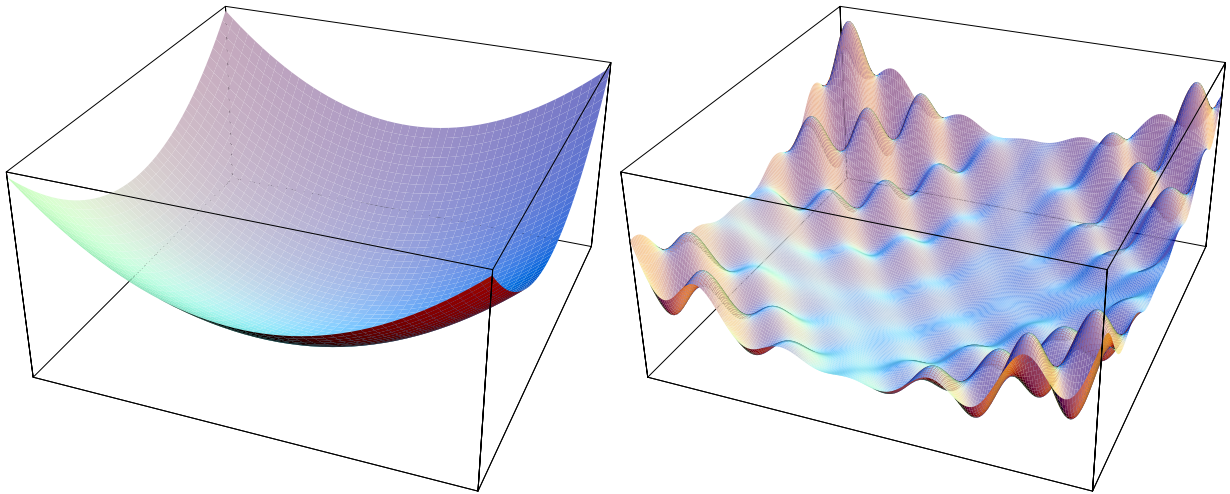


**Figure 4.1:** Simple (left) and complex (right) prototypes of a merit function for the case of minimization.

A distinction is made between one- and multidimensional optimization inasmuch as for a one-dimensional optimization a recursive bracketing of the optimum is possible. For more than one parameter, this approach is only feasible in the special case when all variables are decoupled. As a further complication in the optimization process, the simultaneous optimization of several objective functions can occur. Beyond that, optimization processes may have to meet constraints as well.

For all optimization algorithms, the procedure in finding, e.g., the minimum of an objective function  $f$ , starting from a randomly chosen initial point in parameter space, is to try to reach the bottom of the valley along a path of suitably chosen parameters. Given an arbitrary point in parameter space, the task of any optimization algorithm is thus to propose a new point which produces a result closer the optimum, which means to generate and propose a *search direction* in parameter space. A diagram which classifies several optimization algorithms according to their search strategy is shown in Fig. 4.2.

Based on the means of generating the new points in parameter space, all optimization algorithms developed so far can be classified as either deterministic or indeterministic. Deterministic schemes operate on the basis of a set of static rules. Starting from some fixed point in parameter space, they will always follow the same path and eventually arrive at the same result. Out of the vast number of deterministic methods we will mention only two, the simplex method [114] and gradient methods [85]. The simplex method calculates a new search point in an  $N$ -dimensional parameter space from a set of  $(N + 1)$  previously given points (the "simplex") by linear combination of these search points. This method is easy to implement, but rather slow in terms of number of function calls. Gradient methods ("steepest descent"), as the most intuitive approach, offer the advantage of enhanced optimization speed under proper conditions,



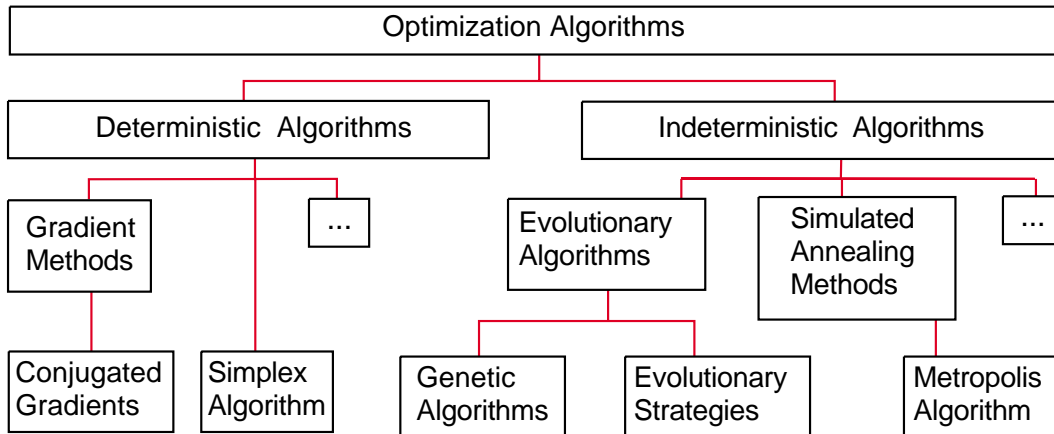


**Figure 4.2:** Different types of optimization strategies, classified by their search direction generators.

but entail two complications: a) they require the computation of directional differentials which is reasonable only for objective functions which can be expressed analytically. If the objective function is only known pointwise the calculation of those derivatives becomes time-consuming and unstable. b) The objective function may have a complex structure with many locally (but not globally) optimal solutions (see right side of Fig. 4.1), and a steepest-descent method is very likely to terminate in a sub-optimal solution. To decide whether a global optimum has been retrieved usually requires starting from various, randomly chosen initial points and observing whether the algorithm always returns the same final point in parameter space. This situation is aggravated once noise is added to the merit function [115]. A further problem is that computation time usually scales nonlinearly with an increasing number of variables to be optimized.

In the late 1960's, indeterministic algorithms were proposed which invoked chance in their search generators. Typical representatives are evolutionary strategies [112] and genetic algorithms [113] as well as simulated annealing methods like the metropolis algorithm [85, 116, 117] or the threshold accepting method [118]. These algorithms are robust against noise [119, 120], local sub-optimal solutions, and inaccuracy of input and output parameters [121]. Many more techniques relying on stochastic schemes have also been proposed [122, 123]. In the following, we will focus on evolutionary strategies.

## Concept and implementation

A prototype for an optimization strategy can be found in the evolution of species, through which organisms have adapted to their environment over the course of millions of years. The picture of evolution and genetics presented here is grossly simplified and seen rather as a practical working hypothesis than as *the* prototype of optimization which is to be duplicated most faithfully.

It is observed that individuals in nature generate more offspring than necessary to ensure the survival of the species. Descendants and parents differ in certain aspects. Only those descendants that have adapted to their environment by developing suitable attributes will survive and reproduce. This process is called selection. A fundamental question now is why descendants differ from their parents. A major advancement towards an understanding came from the pioneering work of Watson and Crick who, in 1953, proposed the double helix structure of DNA [124]. The information on the attributes of live beings is represented by the DNA molecule. DNA is composed of four basic molecules (nucleotides) which are identical except for the nitrogen base (adenosine and guanine, cytosine and thymine). A triplet of three successive nucleic acids codes an amino acid, and several amino acids form a protein which is the basic building module of all live beings. A gene is defined as a section of the DNA which is in charge of coding a protein. The genetic composition of an individual is called a genotype, whereas the physical appearance

is called a phenotype.

With this rather coarse toolkit of molecular genetics, the mechanisms which are responsible for the differences between descendants and their ancestors are identified as changes of the genotype on a molecular basis, specifically mutation and recombination. Mutation means random changes in the sequence of nucleic acids, whereas recombination refers to exchange of sections between two different parent DNA molecules.

```

0   Initialization;
1   Generate initial population;
2   Repeat
3     Determine fitness of each individual;
4     Select parents;
5     Generate offspring by
6       mutation;
7       recombination;
8       cloning;
9     Construct new population;
10  Until truncation criterion met;
11  Dump results;
12  End.
```

Table 4.1: Pseudocode for an evolutionary algorithm.

The basic idea of evolutionary algorithms is the attempt to imitate the classical picture of evolution in a computer code which simulates selection, mutation and recombination within a feedback-controlled regulation loop. The parameters are stored in a way comparable to the DNA since, up to a certain degree, the nucleic acids can be regarded as the biological analog of computer bits. A pseudo-code for a numerical implementation of such a loop which still uses biological notation is presented in table 4.1. The correspondence between biological and numerical terms is compiled in table 4.2.

Biology	Numeric
Gene	Number (float, binary)
DNA, genotype	Vector of numbers (Search point in parameter space)
Individual, phenotype	Physical consequence of a vector, here: electric field
Population	Set of vectors
Fitness	Objective function
Selection	Choice of vectors for creating new vectors
Generation	One loop pass
Mutation	Random changes of vector elements
Recombination	Exchange of elements between two vectors
Cloning	Duplication of a complete vector

Table 4.2: Analogies between biology and evolutionary algorithms

An initial set of vectors is generated either by an educated guess or at random. Each vector represents one search point in parameter space where the objective function is to be sampled. In analogy to evolution in nature, each search point is called an individual; the whole set of candidates is one population. The number of individuals in one population is kept constant. Algorithms which simulate a varying population size have been proposed [113] but have not been implemented in our procedures.

At the onset of each iteration loop, the objective function for each search point in parameter

space is determined, either by numerical calculation or experimentally. In biological terms, each individual is rated according to its fitness. A merit function which is derived from some experimental signal need not necessarily depend linearly on this particular signal. An intelligent (nonlinear) mapping may serve to alter the structure of the merit function such that the search proceeds in a desired predefined direction.

*Selection* determines those vectors which will serve as a basis for the next loop iteration. This process can either be stochastic or deterministic. We apply a deterministic selection rule where the  $m$  vectors which showed best merit values are chosen from the total number  $P$  of vectors while all others are discarded. According to [112], the ratio of  $m$  over  $P$  should be  $m/P \approx 1/7$ . The essential step within each iteration is replication, i.e., to generate new search points in parameter space by means of operators which mirror biological *recombination* and *mutation* processes. Numerical representations of recombination operators combine two parent vectors to create a new child vector. This pair is picked randomly from those selected in the preceding step. The vector elements of these parents are mixed following one of the schemes depicted in Fig. 4.3 and described below. For the sake of clarity, we introduce mathematical notation. A search point in parameter space is described by an  $N$ -dimensional vector  $\mathbf{x}$  of numbers

$$x_i \in \mathbf{R}, \quad i = 1, \dots, N. \quad (4.1)$$

Then one population is a set of  $P$  vectors

$$\mathbf{x}_j \in \mathbf{R}^N, \quad j = 1, \dots, P. \quad (4.2)$$

Let  $\mathcal{M} = \{\mathbf{x}_1, \dots, \mathbf{x}_m\}$  be the set of vectors with the  $m$  best values of the objective function, the so-called mating pool.

*Recombination*: Two parent vectors  $\mathbf{x}_{j'}, \mathbf{x}_{j''} \in \mathcal{M}$  are chosen with  $j' \neq j''$ . The recombination schemes are then classified as follows:

- a) Single point cross over: Randomly choose an index  $i'$  with  $1 \leq i' \leq N$ . The child vector  $\mathbf{y}$  is then

$$y_i = \begin{cases} (\mathbf{x}_{j'})_i, & i \leq i' \\ (\mathbf{x}_{j''})_i, & i > i' \end{cases} . \quad (4.3)$$

- b) Two point cross over: Randomly choose indices  $i', i''$  with  $1 \leq i' < i'' \leq N$ . The child vector  $\mathbf{y}$  is then

$$y_i = \begin{cases} (\mathbf{x}_{j'})_i, & 1 \leq i \leq i' \\ (\mathbf{x}_{j''})_i, & i' < i < i'' \\ (\mathbf{x}_{j'})_i, & i'' \leq i \leq N \end{cases} . \quad (4.4)$$

- c) Multiple cross over: Define a random sequence  $\mathbf{r}, r_i \in \{0, 1\}$ ,  $i = 1, \dots, N$  of length  $N$  with equal probability for 0 and 1:  $P(0) = P(1) = 0.5$ . The child vector  $\mathbf{y}$  is then constructed by

$$y_i = \begin{cases} (\mathbf{x}_{j'})_i, & r_i = 0 \\ (\mathbf{x}_{j''})_i, & r_i = 1 \end{cases} . \quad (4.5)$$

- d) Intermediate recombination creates a child vector by averaging of two parent vectors:

$$\mathbf{y} = \frac{\mathbf{x}_{j'} + \mathbf{x}_{j''}}{2}. \quad (4.6)$$

*Cloning*: It is also possible to carry the best vectors of the old generation over to the new one, which is termed cloning.

*Mutation:* The mutation operator stands for a random change of the value of a vector element, the probability of this change being  $P_{mut}$ . Construct a random sequence  $\mathbf{r}$  of length  $N$ ,  $r_i \in \{0, 1\}$ ,  $i = 1, \dots, N$  with the probabilities  $P(1) = P_{mut}$  and  $P(0) = 1 - P_{mut}$ . The new vector  $\mathbf{y}$  is created from its precursor by

$$y_i = \begin{cases} x_i + \sigma \cdot m_i, & r_i = 1 \\ x_i, & r_i = 0 \end{cases} \quad (4.7)$$

which means that the vector element is changed by a random amount if and only if a "1" appears in the random sequence  $\mathbf{r}$ . This assures that on average the fraction of changed vector elements is  $P_{mut}$ . Two factors,  $\sigma$  and  $m_i$ , control the extent of change. Each  $m_i$  is a random number with a Gaussian probability distribution centered around zero and of width 1,

$$P(m_i) = \frac{1}{\sqrt{2\pi}} e^{-\frac{m_i^2}{2}} \quad (4.8)$$

while  $\sigma$  is the so-called step length which determines the amount of change due to a mutation. A large  $\sigma$  will lead to new search points which are widely scattered in parameter space. The proper choice of  $\sigma$  is crucial for convergence speed and final convergence value. One suggestion is to tie  $\sigma$  to the number of successful applications of the mutation operator in some previous generation [112]. If, at a given step length  $\sigma_t$  in generation  $t$ , many mutations produce better fitness values than the vectors from which they have been generated, the algorithm is searching in a region of parameter space where changes very likely produce better fitness values. If, on the other hand, many mutated genes fail to produce improvement of the fitness value, the algorithm is searching in a region of parameter space where changes (at this given step length) are ineffective. This could indicate that an optimum of the objective has been approached. To achieve convergence in the former case, the step length may be increased, while in the latter it must be decreased. Mathematically, this may be expressed as follows: Let

$$\eta = \frac{n_{suc}}{n_{tot}} \leq 1 \quad (4.9)$$

be the ratio of successful individuals created by mutation in generation  $t - 1$ ,  $n_{suc}$ , to their overall number,  $n_{tot}$ . The step length  $\sigma_t$  of generation  $t$  is then set to be

$$\sigma_t = \begin{cases} \sigma_{t-1} \cdot q & \eta \leq \eta_c \\ \sigma_{t-1}/q, & \eta > \eta_c, \end{cases} \quad (4.10)$$

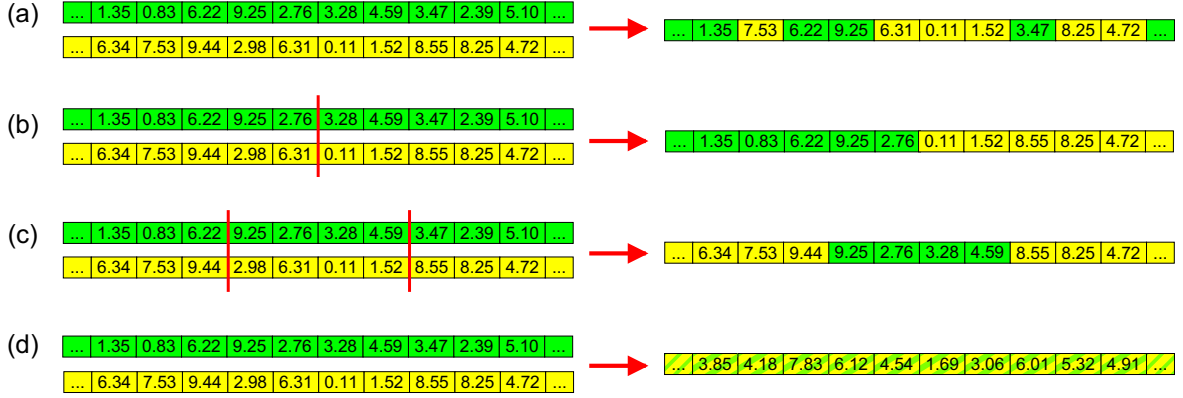
where  $0 \leq \eta_c \leq 1$  is a threshold value which determines whether the step length must be increased or decreased and  $0 < q < 1$  is a constant, which we call the contraction factor. With a value for  $\eta_c$  near 1, the algorithm will very likely get trapped in a possible sub-optimal (local) extremum as the step length tends to steadily decrease. If  $\eta_c$  is small, the step length will stay wide or even steadily increase. The algorithm may then fail to converge towards good solutions. Hence, there exists an "ideal" value for  $\eta_c$  which induces good convergence behavior. Monitoring the evolution of the step length versus generation seems a convenient criterion to indicate a contraction of the search in parameter space. The new vectors are assembled to form a new population which is tested in the next iteration of the loop.

The two classes of evolutionary algorithms, genetic algorithms [113, 125] and evolutionary strategies [112], basically differ in their search operators. While the former mainly use recombination operators, the latter primarily rely on mutation, although algorithms which employ both operators have been commonly used lately.

## 4.2 The role of steering parameters

The maximization of the time-integrated SH generation of the output pulses delivered by a Ti:Sa pumped optical parametric amplifier (OPA) serves to demonstrate the performance of

## Recombination



## Mutation



**Figure 4.3:** Different types of operators for generating new vectors. Recombination: (a) multiple cross over, (b) single-point cross-over, (c) two-point cross over, (d) intermediary recombination. Mutation: (e)

the algorithm under different conditions. SH optimization has been extensively studied [63, 65, 78, 79, 126, 127] and is attractive for several reasons: (a) the experimental realization is straightforward, (b) it is stable since there are no major noise sources other than the laser, (c) the physical process is well-understood and can be simulated fairly easily, which facilitates a comparison between experiment and theory, (d) since only the residual phase function of the pulses has to be compensated, it is sufficient to apply pure phase shaping.

### 4.2.1 Experiment

The experiment is sketched in Fig. 4.4. The Ti:Sa fs laser system pumps a collinear-type OPA which generates pulses at 600nm,  $\approx 100$ fs and  $\approx 5\mu$ J. This output is intentionally chirped in a prism compressor, resulting in a roughly 2-fold pulse length broadening. The pulse shaper features two  $1/d=1800/\text{mm}$  gratings blazed in the VIS and two  $f=150\text{mm}$  cylindrical lenses. The overall accepted bandwidth is  $(d/f)\cdot 128\cdot 100\mu\text{m}=47\text{nm}$  and thus exceeds the spectral bandwidth of the OPA. The CRI phase and amplitude mask is used as liquid crystal device. As the voltages applied to each pixel to control the phase and transmission can be digitally adjusted between 0 and 4095, the parameter space contains  $4096^2\cdot 128 \approx 10^{925}$  points. The 4096 voltages cover a phase shift range of  $\approx 10\pi$ . Because a range of only  $2\pi$  is needed, only about 1000 different voltages are ultimately required which reduces the parameter space to about  $10^{768}$  points. Though our mask may influence both phase and attenuation of the pulses, we used phase-only filtering in this particular experiment, thereby reducing the number of independent variables by a factor of 2. Phase filtering does not affect the energy of the pulses passing the shaper. A high SH intensity corresponds to a high average power density which indicates short pulses. For linear chirps it can be easily shown analytically that maximum SH intensity unambiguously corresponds to a Fourier limited pulse.

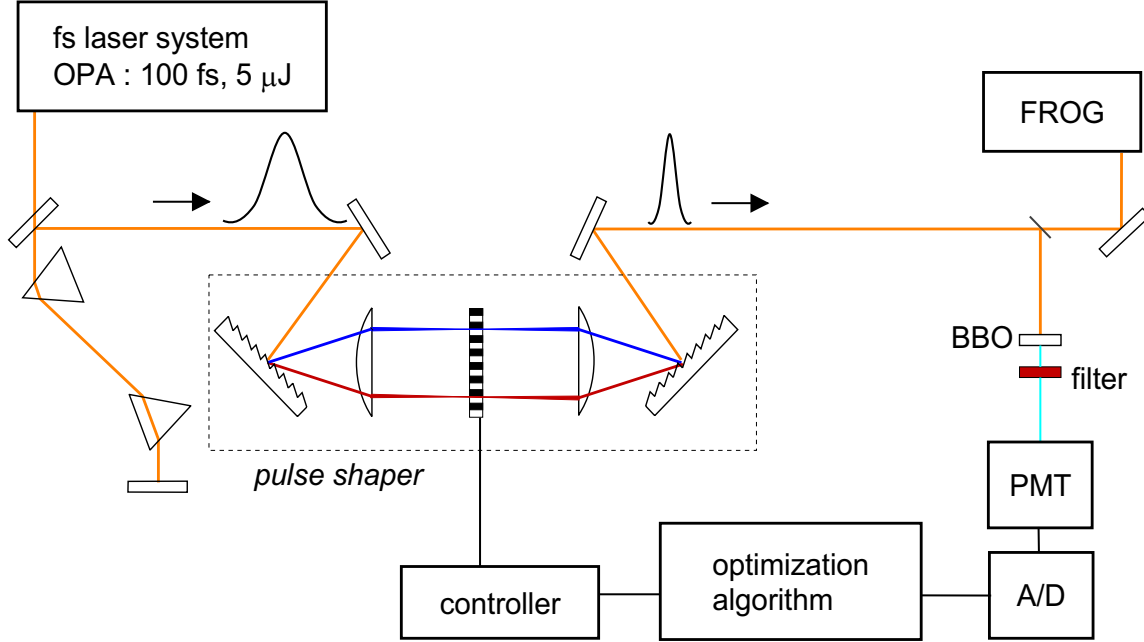


**Figure 4.4:** Setup for the computer-controlled pulse compression.

The frequency-doubled (BBO,  $100\mu\text{m}$ ) output pulses are recorded by a photomultiplier tube (Hamamatsu 1P28) which is protected by a filter (UG-11, 1mm) to block the fundamental. The PMT signal is integrated by a boxcar system and digitized to serve as feedback for the algorithm which controls the pixel voltages. The number of generations served as the truncation criterion. The experiments involved may run stably for only a limited duration of time, on the order of a few hours. To verify the optimization result, several runs have to be performed and the algorithm must reach the optimum each time within this period. Therefore, every run was terminated after 50 generations which took about seven minutes. Each data point represents one optimization run. After a successful optimization run, the SH intensity typically increased by a factor of 2.5. The pulse duration (FWHM) decreased by a factor of 2 with respect to the values observed when all pixels were switched off, as determined with frequency resolved optical gating (FROG).

#### 4.2.2 Simulation

To simulate the above-described experiment, the SH signal had to be computed. To this end, a discrete spectrum with a Gaussian amplitude

$$\tilde{E}(\omega_j) = \tilde{A}(\omega_j) \exp[i\tilde{\phi}^{ini}(\omega_j)], \quad j = 0, \dots, 127 \quad (4.11)$$

and a quadratic phase function

$$\tilde{\phi}^{ini}(\omega_j) = c \cdot \omega_j^2 \quad (4.12)$$

was used to model the input pulse for the shaper. The width of the spectrum was chosen to be similar to that impinging on the mask pixels in the experiment. Great care was taken that the chirp parameter  $c$  corresponded to experimental observation. The phase function  $\tilde{\phi}^{prop}$  proposed by the algorithm was applied to yield the output spectrum

$$\tilde{E}'(\omega_j) = \tilde{A}(\omega_j) \exp[i(\tilde{\phi}^{ini}(\omega_j) + \tilde{\phi}^{prop}(\omega_j))]. \quad (4.13)$$

The temporal profile was reconstructed by discrete inverse Fourier transformation,

$$E'(t_j) = \mathbb{F}^{-1}[\tilde{E}'(\omega_j)] = A'(t_j) \exp[i\phi'(t_j)]. \quad (4.14)$$

The SH value was calculated assuming the absence of saturation effects and an instantaneous SH intensity,  $I_{SH}(t_j)$ , proportional to the square of the fundamental intensity. Therefore,

$$I_{SH}(t_j) \propto I^2(t_j) \propto (|E'(t_j)|^2)^2 = (A'(t_j))^4. \quad (4.15)$$

Since the photomultiplier measures the time integrated SH intensity, the merit function  $f = f(\phi^{prop})$  is

$$f = \sum_{j=0}^{127} (A'(t_j))^4. \quad (4.16)$$

In the simulations, the increase in SH signal and corresponding decrease of the pulse duration with respect to the Fourier limited pulse ( $c = 0$  in equation 4.12) were comparable to those observed in the experiments.

### 4.2.3 Performance of evolutionary strategies

An evolutionary strategy with an adaptive step length control has been implemented in a LabView™ (National Instruments) programming environment. The particular algorithm uses 48 individuals per generation which is enforced by the technical setup of the mask controller cache memory. The eight individuals corresponding to the best fitness values serve as the starting point for the next generation. Cloning has not been incorporated. We observed that it strongly privileges locally optimal solutions in early generations and tends to contract the search volume before the global optimum can be attained. With unimodal objective functions, though, cloning can effect faster convergence. Experiment and simulations made use of the identical algorithm. In many publications dealing with feedback-controlled pulse shaping, the LCD voltages are the optimization variables. This means that the number of independent variables is fixed to the number of pixels of the mask. We used a mapping between voltages and phases. In order to be able to change the number of independent variables, the phase function to be imposed onto the spectrum was parameterized by defining a number  $J$  of interpolation points  $x_j$ ,  $j = 1, \dots, J$  which were connected by linear interpolation. Additionally, the phase values at these interpolation points were discretized, i.e. only values of the form  $i \cdot 2\pi/K$ ,  $i = 0, \dots, K - 1$  with  $K \in \mathbf{N}$  were allowed. Other interpolation schemes for the phases and/or amplitudes are conceivable as well, e.g. a cubic spline interpolation or an interpolation with a polynomial of order  $J$ .

The optimization was run repeatedly for different sets of steering parameters. Out of the ensemble of these parameters (such as mutation rate, the number of descendants by mutation, recombination, and cloning, the number of phases, the number of independent variables, and the parameters which steer the step length control,  $q$  and  $\eta_c$ ) only two were tuned while all others were kept fixed.

In each scan, a standard parameter set was used for those parameters which were kept fixed. Each parent vector created four descendants by mutation and two by recombination. The mutation probability  $P_{mut}$  was set to 0.1, and 64 independent variables with 64 possible phase values were optimized. The step length adjustment parameters (see eq. 4.10) were set to  $q = 0.9$  and  $\eta_c = 0.6$ . Additionally, a 1% noise was assumed in the simulations to account for the inevitable noise in the experiments (see end of section 4.2.3 for the implementation of noise in the simulations).

In each optimization run, the best, the worst, and the average SH values were stored for each pass of the loop, i.e. for one set of 48 parameters to monitor the evolution of the SH signal

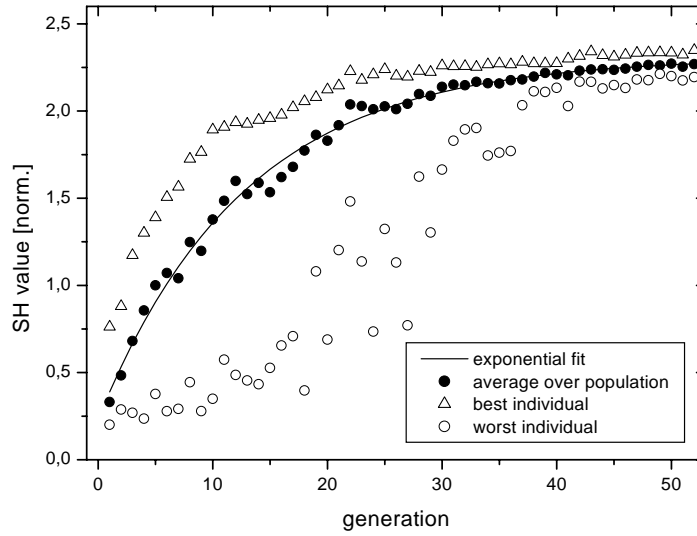


**Figure 4.5:** Evaluation of the optimization data. The average ( $\bullet$ ), the best ( $\triangle$ ) and the worst ( $\circ$ ) fitness values are recorded for each generation  $n$  of an optimization run. An exponential rise  $f(n) = a + b \cdot \exp(-c \cdot n)$  with the fit parameters  $a$ ,  $b$ , and  $c$  is fitted to the average fitness values. The dimensionless parameter  $c$  provides a measure of the convergence speed.

versus the generation  $n$ . The convergence data of every scan were normalized with respect to the SH signal of the original OPA output. An exponential rise  $f(n) = a + b \cdot \exp(-c \cdot n)$  was fitted to the normalized mean SH values (see Fig. 4.5,  $n$  is the generation or loop index,  $a$ ,  $b$ , and  $c$  are the fit parameters). The constant of the exponential rise,  $c$ , may be regarded as a measure of convergence speed. The terminal SH value was calculated by averaging the median SH value over the last 5 generations.

As in the experiments, each simulated optimization was aborted after 50 generations to allow comparisons. The convergence data (final value or convergence speed) were averaged over 50 optimization runs for each single point. Though in the simulations the different parameters were scanned with a much higher resolution, only those data points which were also measured in the experiments are shown, for the sake of clarity.

## Replication

In experiments and simulations, each generation contained 48 individuals. The eight individuals which achieved the highest fitness values were chosen as parents for the next generation. None of the parents were adopted by the next generation. Hence, each parent vector must generate  $48/8 = 6$  descendants, created either by mutation or recombination. Optimization runs have been performed for 2, 3, 4, and 5 descendants by mutation out of these 6 generated. Figs. 4.6 b and 4.7 b show that, in the experiment, the fewer descendants created by mutation, the better and faster the convergence.

The simulations show the same behavior for the convergence speed (Fig. 4.6 a), which again peaks for the smallest number of mutants. The maximum terminal SH value is achieved for three to four (Fig. 4.7 a) descendants by mutation, which indicates that the fast convergence in the case of many descendants by recombination prematurely ended in a sub-optimal solution. Experiments and simulations likewise reveal that a suitable mutation probability is  $\approx 0.1$  where the final SH value finds its maximum. Since a premature convergence is detrimental, four individuals have been generated by mutation during all other optimizations. Furthermore, the investigation of the step length control, which only influences mutation, requires generation of



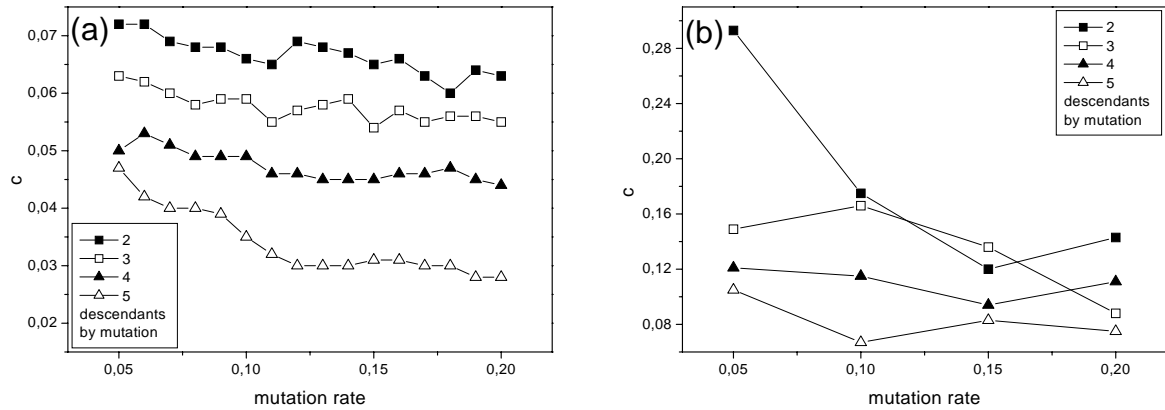


**Figure 4.6:** Influence of the replication process on convergence speed, (a) simulation, (b) experiment. The number of descendants created by mutation is scanned versus the mutation rate. The values for  $q$  and  $\eta_c$  were set to 0.9 and 0.6, respectively. 64 independent variables with 64 possible phase values have been optimized.

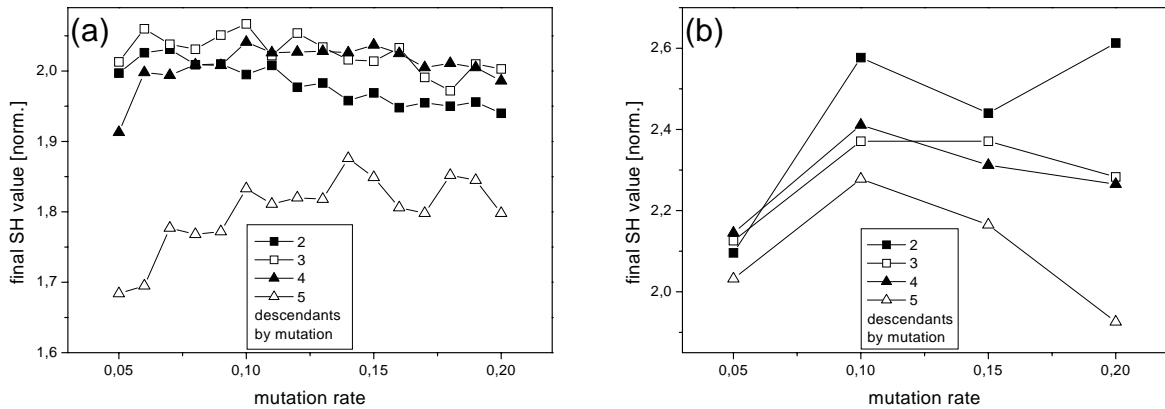


**Figure 4.7:** Influence of the replication process on final SH value. (a) simulations, (b) experiment. The remaining optimization parameters are specified in Fig. 4.6

as many descendants by mutation as acceptable in order to discern any effect.

### Size of parameter space

Our mapping of the phase uses interpolated phase functions and discrete phase values which easily allows for the alteration of the number of points in parameter space. Two questions arise: (a) how does the convergence respond to a change in the number of possible configurations in parameter space, and, (b) how does a decrease of the size in parameter space (and, therefore, shaping capability) affect the quality of the optimization result?

To study the dependence of convergence behavior on the size of parameter space, the number of interpolation points was scanned from 16 to 128 in increments of 16. For each number of interpolation points, the scan range for the number of phases ran from 32 to 128 in steps of 32. Fig. 4.8 reveals that the convergence speed, as should be expected, decreases with increasing number of parameters, both in experiments and simulations. The terminal SH value drops with growing number of parameters. This seems counterintuitive since a finer grid allows better shaping and thus a better SH value should be attainable. The explanation is that the sagging convergence speed eventually precludes the final value being reached within the permitted 50 generations.

The phase discretization is found to be noncritical. A resolution of  $2\pi/32 = \pi/16$  is sufficient. It should be noted, though, that the phases at pixels which do not coincide with an interpolation

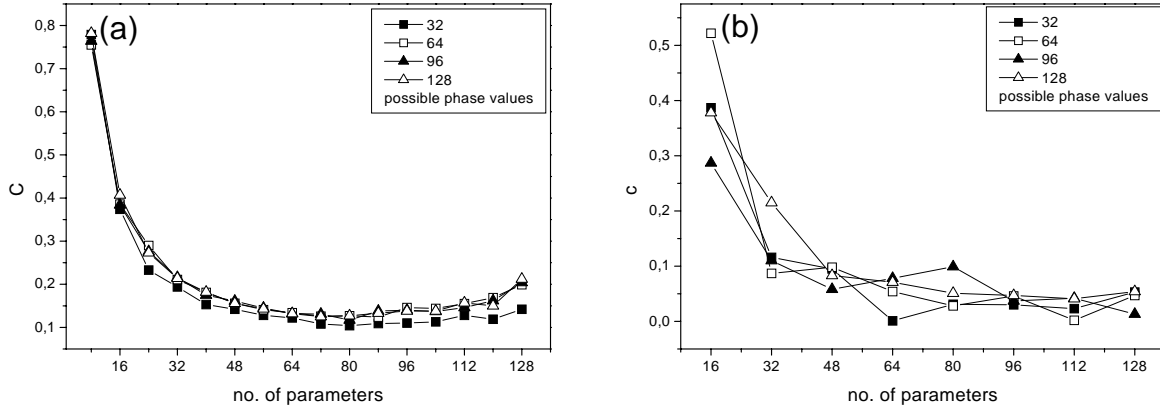


**Figure 4.8:** Influence of discretization of parameters and phases on convergence speed, (a) simulation, (b) experiment. The number of independent variables is scanned versus the number of possible phase values. Four descendants are created by mutation, two by recombination. The values for  $q$  and  $\eta_c$  were set to 0.9 and 0.6, respectively. The mutation rate is set to 0.1.

point are not restricted to the discretized phase values and can have any (interpolated) value. Because the phase functions generated by this parameterization are smooth by construction, they fulfill the physical constraint that efficiently shaped pulses require phase functions which are smooth at least on segments. This is much more important for the quality of the optimization result than a high phase resolution at the interpolation points.

### Step length control

The step length control scheme uses two control parameters (see eq. 4.10). The threshold value  $\eta_c$  and the contraction factor  $q$  were scanned over the range  $\eta_c = 0.3, 0.4, \dots, 0.9$  and  $q = 0.8, 0.85, 0.9, \text{ and } 0.95$ . For each set of  $(\eta_c, q)$ , 16, 32, 64 and 128 independent variables have been optimized.

For all numbers of parameters the scans in Figs. 4.9 and 4.10 show that, except for high threshold values, the contraction factor is not very critical for convergence speed and final SH value. This is clear from the fact that this factor does not really bias any regulation loop. For  $\eta_c$  values near 1, the contraction factor becomes important for both convergence speed and final SH value. With high  $\eta_c$ , the step length will most likely be monotonically decreased. Convergence speed and final SH value then largely depend on a proper choice of the contraction factor. This is a well-known problem in simulated annealing methods, where usually no step length control is implemented but rather a monotonic step length decrease ("annealing schedule").

Comparison of the simulated final convergence values (Fig. 4.9 a to d) indicates that the range of threshold values for which the maximum final value is reached shifts from  $\approx 0.8$  (16 parameters) to  $\approx 0.5$  (128 parameters). Concurrently, at these threshold values the convergence speed is low (compare Fig. 4.10 a to d). Figs. 4.9 and 4.10 both show good agreement with experimental data reproduced in the respective figs. 4.9 e to h and 4.10 e to h.

A low threshold value corresponds to a high step length during the optimization, which means that in each generation the new search points are widely spread in parameter space. For high numbers of parameters the optimal final SH value is achieved with low threshold values. Accordingly, for many independent variables a more widespread search has to be launched. This conclusion is quite obvious and intuitive. The real message of this is that, with  $\eta_c$ , the experimentalist is given a means of adapting to the complexity of the search space to assure secure convergence.

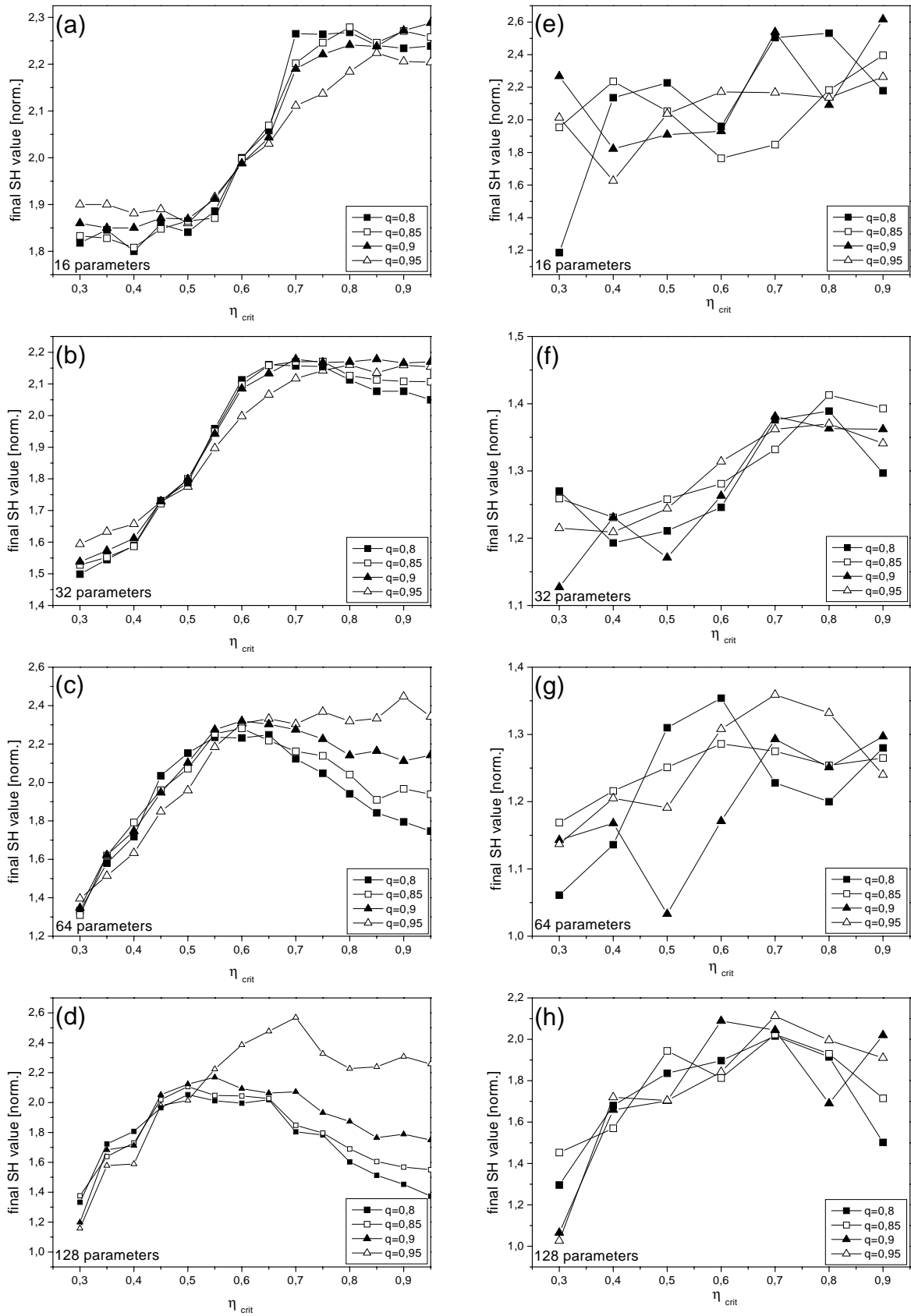


**Figure 4.9:** Influence of the adaptive step length control on final SH value for 16 (a,e), 32 (b,f), 64 (c,g), and 128 (d,h) independent variables. The threshold value  $\eta_c$  is scanned versus the contraction factor  $q$  (see eq. 4.10). Left column: simulation, right column: experiment. Four descendants are created by mutation, two by recombination. The mutation probability is set to 0.1.

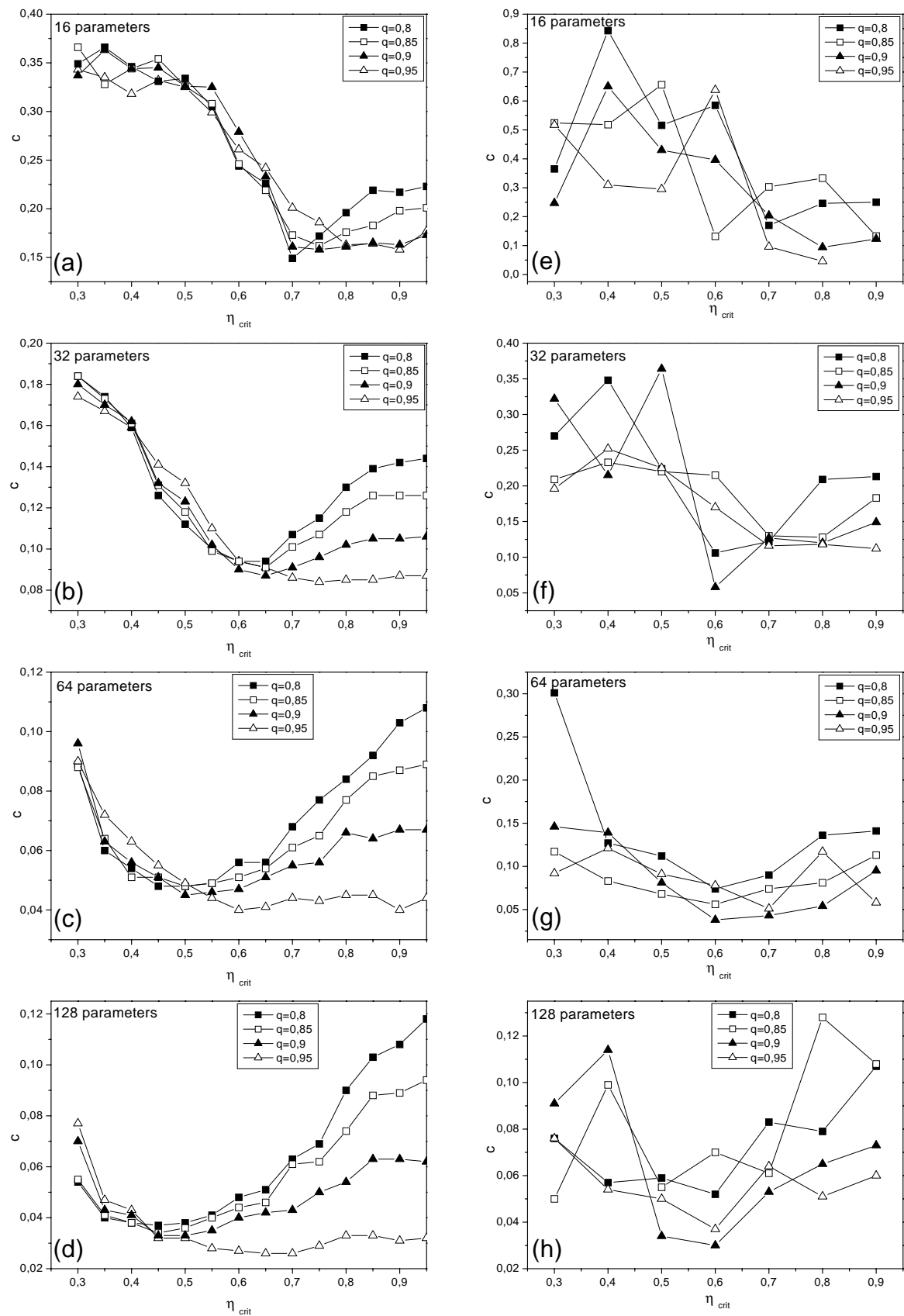


**Figure 4.10:** Influence of the adaptive step length control on convergence speed for 16 (a,e), 32 (b,f), 64 (c,g), and 128 (d,h) independent variables. Left column: simulation, right column: experiment. The remaining optimization parameters are specified in Fig. 4.9

## Noise

The influence of noise was investigated only in simulations. Noise was implemented as a Gaussian-distributed fluctuation in the pulse energy. Its width was one of the scan parameters and is specified relative to the pulse energy. For each scan, the full width at half maximum (FWHM) of the pulse was calculated and normalized with respect to the FWHM of the Fourier limited pulse. These simulations were performed for 16, 32, 64, and 128 parameters. The values for  $\eta_c$  were those which produced the optimal SH values for 16, 32, 64 and 128 parameters ( $\eta_c = 0.8, 0.7, 0.6$  and  $0.5$ ) as determined in section 4.2.3.

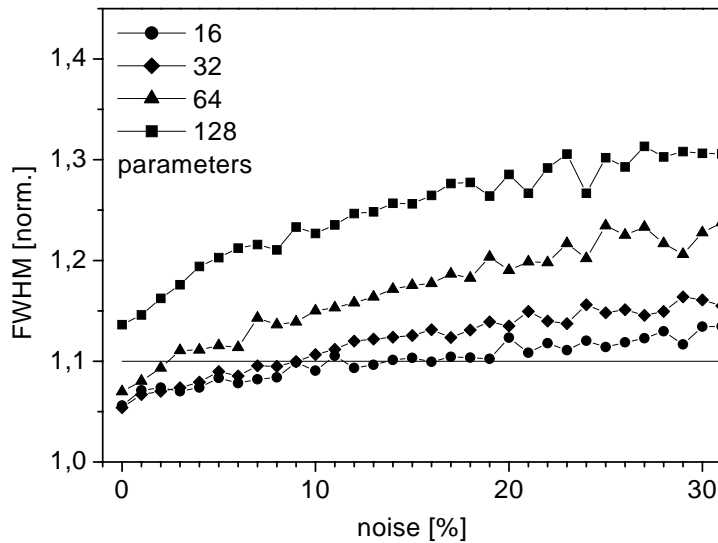


**Figure 4.11:** Noise values acceptable for an optimization run: The FWHM of the optimized pulse is normalized to the FWHM of the Fourier limited pulse. The noise, which is implemented as energy fluctuations of the pulses, is scanned from 0 to 30% for 16, 32, 64, and 128 parameters.

The FWHM values for all numbers of parameters are shown in Fig. 4.11. As long as it is acceptable to approach the optimal relative FWHM value with an accuracy of 10%, the threshold for noise is approximately 14%, 9%, and 3% for 16, 32, and 64 parameters, respectively. For 128 parameters, convergence is clearly missed within 50 loop iterations even for the lowest noise rates. This again indicates that a reduction in the number of parameters to be optimized greatly improves the robustness of the optimization process.

## 4.3 The role of parameterization

A mapping between optimization parameters and experimental parameters which reflects the physical properties of the system [120] is useful in optimization experiments. If, for example, the resulting phase functions to be imposed on the pulses are expected to be chirps of various orders, it is appropriate to express the phase function as a Taylor series and to optimize the pertinent coefficients. Here, a small change in the curvature of the phase function, which is represented by one variable in this parameterization, is equivalent to changes in *all* phase values, possibly by large amounts, in the free parameterization to effect the same result. With an intelligent parameterization, the desired optimization effect can be dissected more efficiently from undesired side effects. By investigating how a particular experiment responds to optimization runs with different parameterizations of the electric field, further insight into the physical process under study may be gained. This can be regarded as the inversion of an optimization. A positive side effect is a reduction in the number of parameters which improves convergence.

In this section, we will discuss several parameterizations with respect to experiments which benefited from their implementation.

### Free parameterization

The above-described linear interpolation of the phase (and amplitude) is a universal approach for a parameterization of the electric field and includes any field which can be physically generated by a pulse shaper. Because this does not presuppose any knowledge about the optimization process except that the phase (and amplitude) functions are smooth by construction, this mapping may be denoted as "free parameterization". It is useful for the uncovering of unintuitive solutions or for the verification of a solution found by another parameterization. In the latter case, a comparison between the retrieved phase and amplitude functions of both optimizations can reveal which peculiarities of the pulse structure are relevant for the optimization process. The free parameterization has been used to this end in virtually all optimizations of the second part of this work.

### Polynomial phase functions

The compensation of the residual phase of ultrashort pulses, which consists of chirps of various orders, calls for restriction of the algorithm to a search for polynomial phase functions. The corresponding representation of the phase function is written as

$$\Phi_n = \sum_{k=2}^K c_k \left( \frac{n - N_0}{N} \right)^k \quad n = 0, \dots, N - 1 = 127 \quad (4.17)$$

with quadratic terms as the lowest polynomial order  $k$  since constant ( $k = 0$ ) or linear ( $k = 1$ ) phase terms only produce a phase or time shift, respectively. The Taylor coefficients  $c_k$  and the offset  $N_0$  are to be optimized by the algorithm.

Adaptive pulse compression uses this parameterization of the phase [65]. The reduction in the number of independent variables results in a rapid convergence. A detailed description of these experiments is given in chapter 5.

Chirps can be used for focusing of a wave packet in molecules. The anharmonicity of the potential causes a dephasing of the wave packet which can be compensated with chirped excitation pulses, as has been demonstrated for the example of  $K_2$  [25, 26].

### Periodic phase functions

For physical systems which are sensitive to symmetry properties in the phase functions, a periodic phase function

$$\Phi_n = a \cdot \cos(b \cdot n + c) \quad n = 0, \dots, 127 \quad (4.18)$$

$n$  being the pixel number, is one appropriate parameterization. The parameters  $a$ ,  $b$ , and  $c$  are optimized by the algorithm.

Non-resonant two-photon transitions are sensitive to symmetry properties of the phase [128, 129]. In the experiment described in chapter 6, the two photon transition in  $\text{Na}(3s \rightarrow 5s)$  has been chosen to demonstrate the feedback-controlled maximization and minimization of population transfer [12, 16]. The parameterization in eq. 4.18 is sufficiently general to include both the generation of dark and bright pulses.

### Multiple pulse structures

Several experiments [8, 19] and theoretical investigations [130] have followed the scheme of Tannor and Rice [6] wherein control has been achieved by the delay between a pump and a dump pulse.

Hence it is intuitive to use a parameterization in the time domain where the interpulse delay is adjusted by the algorithm.

With a mask capable of influencing both phase and amplitude it is possible to produce a train of pulses which can be expressed as (see Eq. 2.16)

$$E_{out}(t) = \sum_{n=-\infty}^{\infty} c_n \cdot E_{in}(t + n \cdot \tau) \quad (4.19)$$

with the input pulse  $E_{in}(t)$ , complex coefficients  $c_n$  for amplitude and relative phase for each pulse and the minimum interpulse delay  $\tau$  which depends on the physical properties of the mask and the input pulse. Only pulses at positions  $n \cdot \tau$ ,  $-N/2 \leq n < N/2$ , can be independently influenced (see section 2.3.2, Eq. 2.20, or [73]) where  $N$  is the number of pixels of the LC mask. This concept has been successfully applied in a study of the wavepacket dynamics in the prototype molecule  $K_2$ . The algorithm adjusted the index and value of a predefined small number of coefficients  $c_n$ . All other coefficients were set to zero. The algorithm thereby generated phase-related multiple pulses to manipulate the excitation of either the ground (X) or excited (A) state in potassium dimers [25, 26].

### Combined phase and amplitude functions

Experiments may require both the temporal shifting of wavelengths into a particular temporal window, which can be described by chirps, and the selection of a wavelength range, which can be performed using a Gaussian amplitude window. This combined phase and amplitude parameterization proved useful in the optimization of ground state dynamics of polydiacetylene in chapter 7.

## 4.4 Summary

Evolutionary strategies have proven to be versatile and are ideally suited to find global optima in coherent control studies. The optimization speed and final result strongly depend on the number of free parameters and/or a suitably chosen parameterization. The steering parameters which control the optimization behavior of the algorithm are non-critical if chosen within reasonable limits. It has been shown that in the presence of noise, the noise level acceptable for a satisfactory final convergence scales inversely with the number of free parameters. The parameterizations can account for physical (or chemical) a-priori knowledge, and help to gain insight into underlying process under study.

With the optimization algorithm, the pulse shaper, and the broadband coherent source, the technical fundamentals for coherent control studies are in hand. The accurate and proper functioning of each component has been demonstrated, and thus a solid foundation has been laid for the control experiments that follow in the second part.

## Part II

# Coherent Control Experiments



## 5

# Adaptive broadband pulse compression

In the first experiment of this section, the adaptive compression of pulses from a noncollinear OPA [38, 51, 108–110] and a hollow fiber in a feedback loop is demonstrated. The advantages and limits of adaptive shaping, in particular with special respect to the optimization algorithm are discussed [65].

The optimization of the second harmonic (SH) of the ultrashort pulses serves as feedback signal [63, 78, 79, 126]. Pulse durations below 16fs are achieved after compression of the non-collinear OPA.

The compression of broadband spectra, produced by optical parametric amplifiers with non-collinear type phase-matching, to pulse durations below 20fs has commonly been achieved by prisms, gratings and chirped mirrors. For compensation of phases of order higher than two, a combination of these elements has to be used [51, 109], which involves tedious and lengthy adjustment efforts. The task which remains, however, is that of maintaining quality while delivering the short pulses to the experiment. This calls for compensation of the group velocity dispersion (GVD) of second and higher orders introduced by dispersive elements installed in the beam path behind the compressor, such as cell windows, wave plates, cuvettes filled with solvents, etc.

An extended version of adaptive compression by phase compensation is presented in the second experiment of this chapter wherein fundamental pulses which are spectrally broadened in an inert-gas filled hollow fiber are compressed close to the Fourier limit by combined phase and amplitude shaping. Since the spectral modulation and phase of the output pulses depend on the length of the hollow fiber and the gas pressure, the tedious task, adjustment of these two parameters such that a quadratic phase and the smoothest possible spectra are obtained, is avoided by the adaptive approach because any spectral amplitude and phase modulation can be compensated.

The main advantages of this setup are the swiftness of the automated compression procedure (typically less than five minutes) and the capability to compensate phase distortions of arbitrary appearance.

## 5.1 Compression of pulses from a non-collinear OPA

A noncollinear OPA as described in chapter 1 is used as the source for ultrashort pulses. The adaptive approach employs a pulse shaper for the compression of the strongly chirped output pulses. Because of the width of the spectra, imaging distortion by chromatic aberration must be avoided in the shaper as has been discussed in section 2.3. The shaper therefore uses all-reflective optics, as shown in Fig. 5.1 [61, 62]. Cylindrical optics are used to reduce the power density impinging on the LC mask and thus prevent damage. The off-axis angles are kept as small as possible ( $< 12^\circ$  in the present case) to alleviate imaging aberrations introduced by the

focusing mirrors. The overall accepted bandwidth of this shaper is  $(d/f) \cdot N \cdot 100\mu\text{m} \approx 140\text{nm}$  which is above that of the pulses generated by the OPA (see Fig. 1.10).

The uncompressed output pulses from the OPA centered around 620nm are fed into the properly aligned shaper. The shaped output is focused by a spherical mirror ( $f=200\text{mm}$ ), frequency doubled (BBO,  $10\mu\text{m}$ ) and recorded by a photomultiplier tube (PMT). A spectral filter (UG-11) in front of the PMT transmits only the wavelength of the doubled pulses. The PMT signal serves as feedback for the evolutionary algorithm (Fig. 5.1) [63, 78, 79, 126]. Other observables such as the spectral blue-shift of the focused pulses [80] have also been used in iterative pulse compression schemes.

Because we applied phase-only filtering, the energy of the pulses leaving the shaper is constant, and therefore high SH intensity is indicative of short pulses. Pulse compression down to 11fs by SH optimization has been demonstrated recently [63].

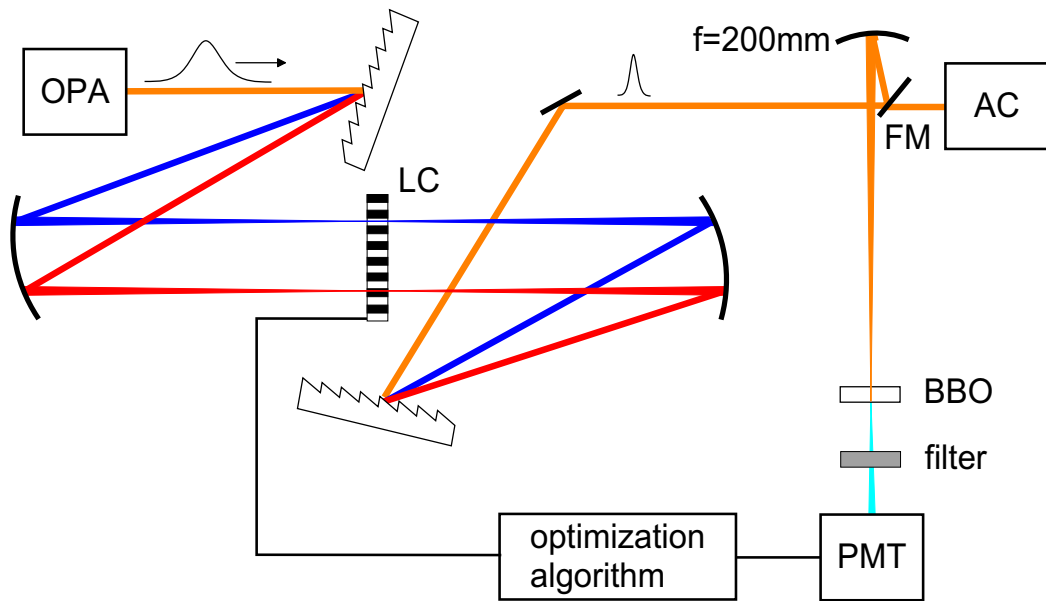


**Figure 5.1:** Setup of the computer-controlled compressing unit. A flipping mirror (FM) steers the pulses either to the BBO crystal or to the autocorrelator (AC). The shaper features  $1/d=600/\text{mm}$  gratings,  $f=150\text{mm}$  cylindrical mirrors, and the CRI phase and amplitude mask.

The uncompressed output pulses of a non-collinear OPA are known to be mostly linearly chirped. Hence it is advisable to restrict the algorithm mainly to a search for polynomial phase functions. We thus chose a polynomial representation of the phase function (see section 4.3, Eq. 4.17),

$$\Phi_n = \sum_{k=2}^K c_k \left( \frac{n - N_0}{N} \right)^k \quad n = 0, \dots, N - 1 = 127 \quad (5.1)$$

with quadratic terms as lowest polynomial order  $k$  since constant ( $k = 0$ ) or linear ( $k = 1$ ) phase terms only produce a phase or time shift, respectively. The parameters  $c_k$  and  $N_0$  are optimized by the algorithm. Because the spectrum of the OPA is widely tunable,  $N_0$  has been included as a parameter to ensure that the offset of the phase function coincides with the center of the spectrum after the optimization has been accomplished.

Alternative concepts of parameterization such as linear approximation or cubic splines were tested as well but resulted in many more loops of the algorithm while eventually achieving comparable pulse durations.

## Results

As illustrated in Fig. 5.2, the shaping apparatus compressed the OPA pulses from about 260 fs to below 16fs. The optimization procedure was confined to the search quadratic and cubic order phases, i.e.  $K=3$  in Eq.( 5.1). Fig. 5.3 shows that the terminal value of the SH signal was approached after about 25 generations. At a pulse repetition rate of 1kHz and with averaging of 50 pulses, the adaptive compressor thus compensates the chirp and produces short output pulses in less than five minutes. This figure should be further reducible with a biased initial population that takes advantage of a-priori physical knowledge such as the supposed sign of the chirp to be compensated.

A major problem in experiments which use ultrashort pulses is the faithful delivery of the pulses to the sample, especially when the ultrafast dynamics of molecules in liquid solvents is to be investigated. Usually, a collection of dispersive elements (cell windows, wave plates, polarizers, solvent-filled cuvettes, etc.) causing phase distortions of second and higher order is installed between the compressor exit and the position where the pulses are required to be short. We have mimicked this situation by installing an ethanol-filled 1mm path length cuvette between shaper exit and SH crystal, thus broadening the output pulses. We then reapplied the algorithm and again obtained a pulse duration below 16fs (see Fig. 5.4). An analogous experiment with a polarizer in the beam path, which introduced a considerable chirp, resulted only in sub-20fs pulses (see Fig. 5.5) as will be discussed below. As before, the optimization in both experiments was confined to the search for second and third order phases.

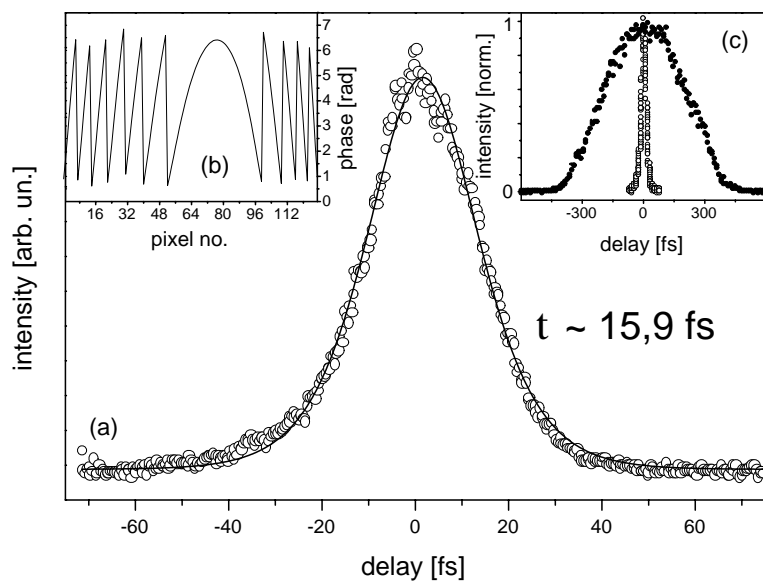


**Figure 5.2:** a) Autocorrelation trace behind shaper after phase optimization. b) Phase values calculated from the coefficients retrieved by the algorithm. The phase was taken modulo  $2\pi$  since this has no effect on the output pulse. c) Comparison between uncompressed ( $\bullet$ ) and compressed ( $\circ$ ) pulses.

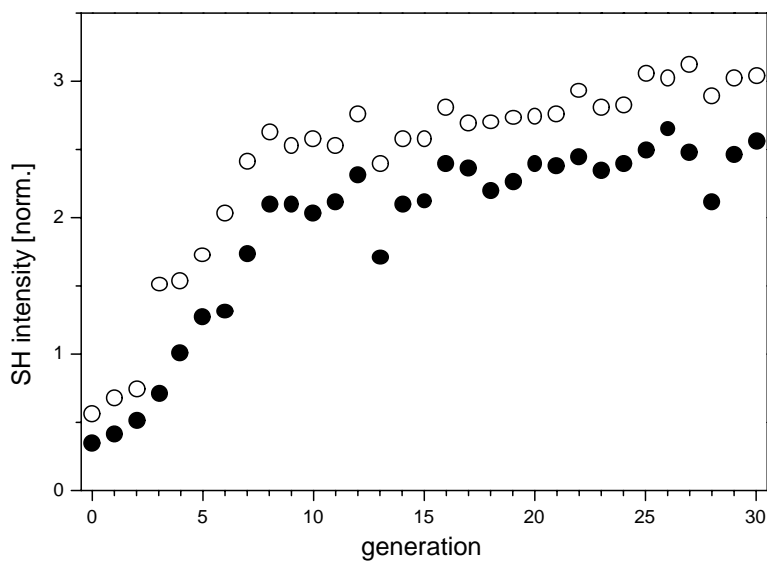


**Figure 5.3:** Evolution of the averaged ( $\bullet$ ) and best ( $\circ$ ) SH signal of each generation (equivalent to 48 trials) during the optimization process. A normalized value of 1 corresponds to the SH intensity when no additional phase is introduced by the mask, i.e. when all LC voltages are turned off.

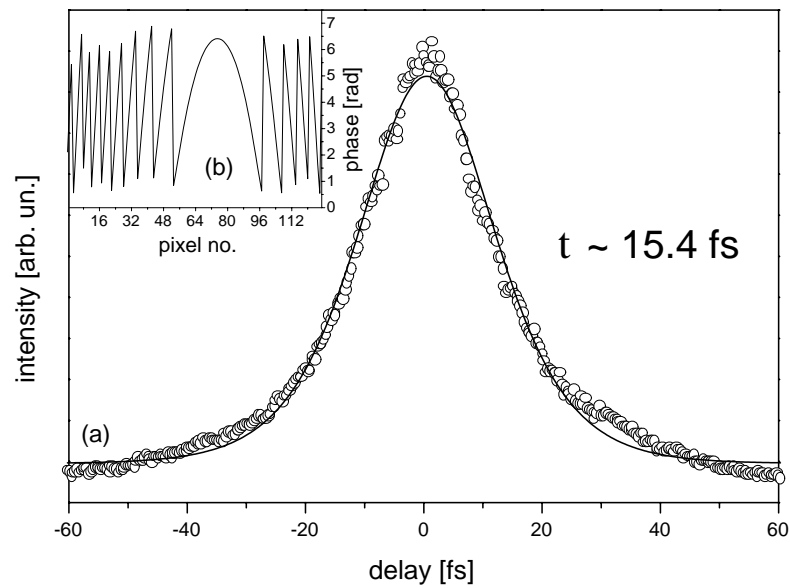


**Figure 5.4:** a) Autocorrelation trace after phase optimization with an ethanol-filled cuvette placed between shaper exit and SH crystal. b) Phase function retrieved by the algorithm.

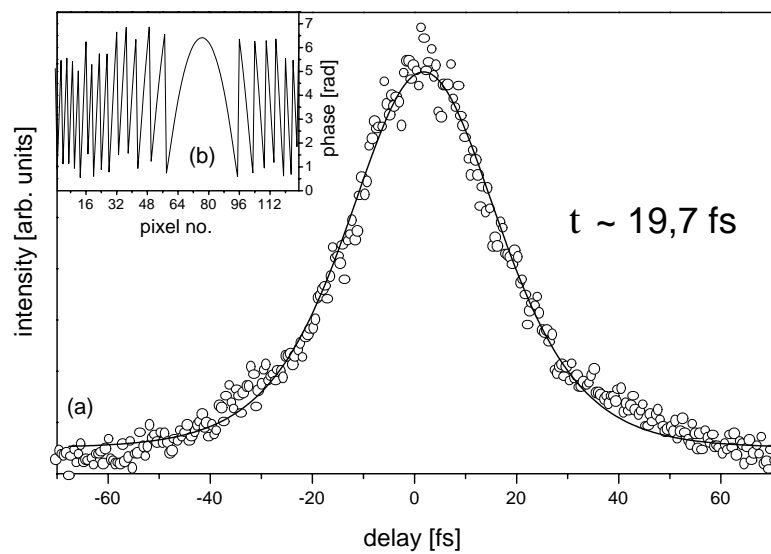


**Figure 5.5:** a) Autocorrelation trace after phase optimization with a Glan-Thompson polarizer placed between shaper exit and SH crystal. b) Phase function retrieved by the algorithm.

### Limits of adaptive phase compensation

The question arises why pulse restoration partly failed when a polarizer was moved into the beam path (Fig. 5.5), i.e. when a large amount of chirp had to be compensated. Two conceivable arguments come to mind: a) shapers with a discrete phase filter cannot synthesize any arbitrary amount of chirp and, b) the algorithm may have missed the globally optimal solution.

The pixelized mask used in our setup causes a discretely modulated spectrum which gives rise to special features that have to be taken into account. This has been discussed in detail elsewhere [71, 73, 131].

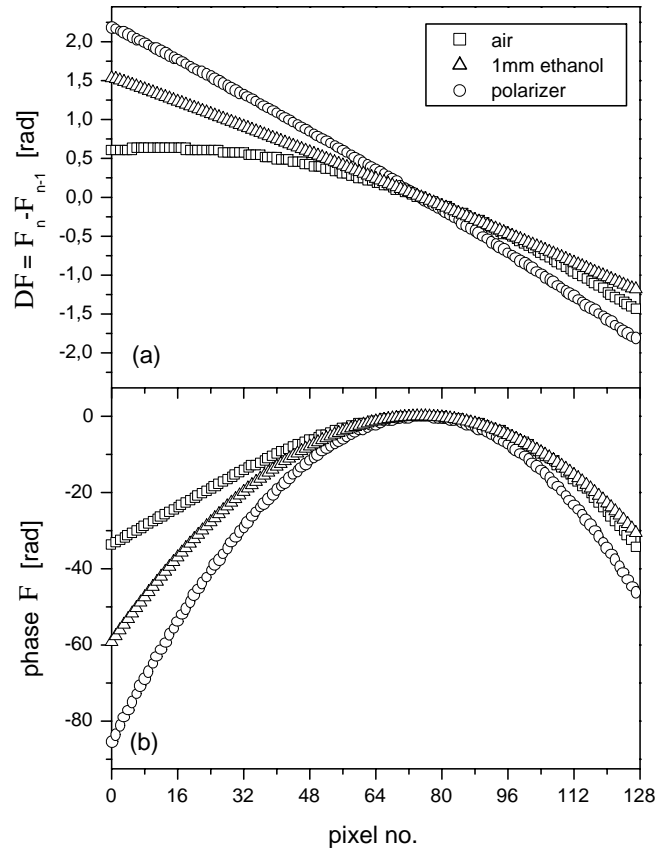


**Figure 5.6:** a) Phase differences  $\Delta\Phi = \Phi_n - \Phi_{n-1}$  between two adjacent pixels and b) phase functions  $\Phi_n$  retrieved by the algorithm (bottom) for three different optical paths ( $\square$ : air,  $\triangle$ : ethanol-filled cuvette,  $\circ$ : Glan-Thompson polarizer).

Nyquist's sampling theorem states that a periodical function must be probed at least twice per period, or twice over a phase interval of  $2\pi$ . Hence concerning the phase function to be imposed onto a spectrum, a phase interval of  $2\pi$  must be sampled by at least two pixels. The absolute value of the phase difference  $\Delta\Phi$  between two adjacent pixels must thus be well below  $\pi$ . Fig. 5.6 shows these differences for all three optimizations. With the polarizer in front of the SH crystal, the phase difference  $\Delta\Phi$  attains  $\approx 2.2$  whereas it remains below 1.6 in all other cases. Since the phase difference  $\Delta\Phi$  should remain well below  $\pi$ , Nyquist's theorem may already be violated for  $\Delta\Phi \approx 2.2$ . Experimental evidence of violation in the case of a linear phase function is the appearance of replica. In the case of nonlinear phase functions, the effect is somewhat less trivial. Experimentally, a temporal smearing out of the pulse shape is observed which is responsible for a decrease of the SH signal.

We believe that the algorithm found an optimal solution for the coefficients even when the

dispersion to be compensated became excessive. Applying a phase function for which  $\Delta\Phi$  was below its critical value proved insufficient to compensate the phase. Thus no short pulses were obtained resulting in a SH signal below the expected value. On the other hand, applying the phase function necessary to obtain the shortest pulse would have violated Nyquist's theorem, resulting in a temporal smearing out of the pulses and therefore, again, in a SH signal lower than expected. The algorithm presumably applied only so much chirp as to compromise between these two scenarios. The net effect was a residual phase remaining after the optimization process, which caused a longer pulse duration.

For those cases where short pulses were obtained, Fig. 5.6 indicates that an estimate for an acceptable phase difference between two adjacent pixels is  $\approx 1.6$ . LC masks with a larger number of pixels should be able to improve the maximum amount of chirp which can be introduced onto a spectrum because more pixels would then cover the same spectral range.

The process of finding an optimum (e.g. a maximum) within a merit function of many parameters largely depends on the structure of this function. The particular function may have many local maxima separated by deep valleys, so that the optimization routine may be fooled by getting stuck in such a local sub-optimal maximum. To gain insight into the structure of the merit function and to offer evidence that the algorithm has indeed found the global optimum, we performed a two-dimensional scan of the SH signal intensity vs. the second and third order phase coefficients  $c_2$  and  $c_3$  without any material in the beam path (see Fig. 5.7).

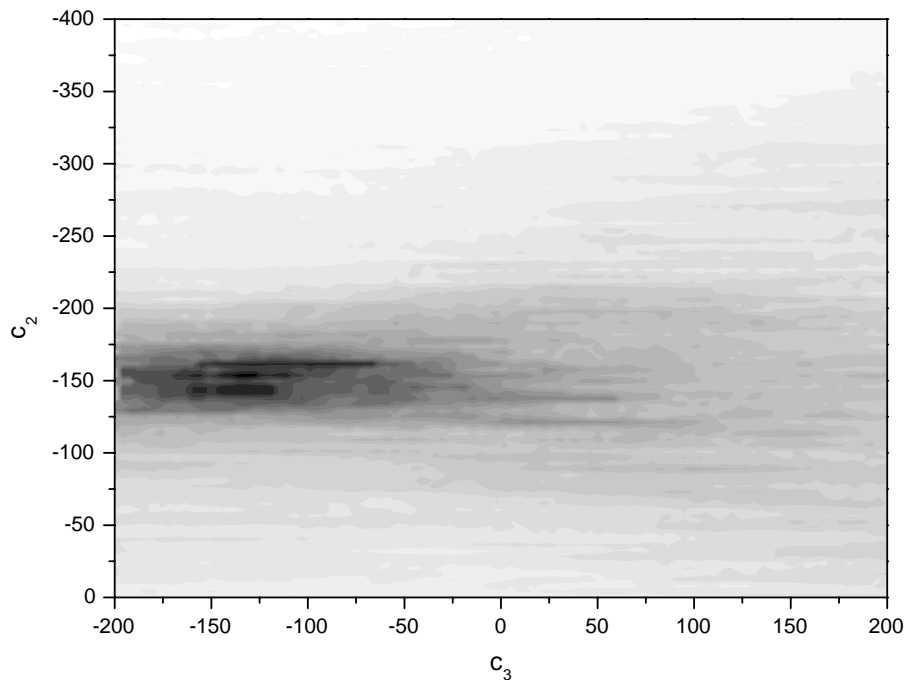


**Figure 5.7:** SH intensity (dark colors indicate high SH signal) vs. second ( $c_2$ ) and third ( $c_3$ ) order chirp parameter.

Obviously, the function  $I_{SH} = f(c_2, c_3)$  is unimodal with its maximum at  $c_2 \approx -160 \pm 10$  and  $c_3 \approx -125 \pm 25$  which comes close to the values  $c_2 = -162$  and  $c_3 = -109$  determined by the algorithm for identical experimental conditions. Thus, the algorithm finds the global optimum of the SH value although, in this case under idealized noiseless conditions, it was a trivial task. In this special optimization case and with this special parametrization a simple algorithm like a Gauss-Seidel strategy [112] should have been sufficient and should have found the optimal solution within a few seconds. We would like to emphasize however that we employed a special parametrization of the phase function which strongly reduced the number of free parameters and, furthermore, decoupled the parameters. Because with other parametrizations the merit function could have had a totally different structure, we would not use deterministic algorithms in

optimizations with unknown – and possibly multimodal – merit functions, since these algorithms may be sensitive to experimental noise [115].

With other parameterizations of the phase function, we found that the convergence speed as well as the final SH value was dependent on the internal strategy parameters of the algorithms. As a rule of thumb, we found that the more complex the optimization, e.g. the more parameters to be optimized, the more carefully the optimum must be approached by proper choice of the internal strategy parameters mentioned above.

## 5.2 Hollow fiber compression

In a second experiment, a hollow fiber filled with an inert gas at high pressure, into which the pulses from the amplified Ti:Sa laser system are focused, serves as the broadband source [132]. The pulses are spectrally broadened by self-phase modulation (SPM) and simultaneously stretched in time by group velocity dispersion [50] depending on gas pressure and propagation length. The output spectra show a complex structure, which requires that the spectrum is additionally smoothed for the generation of side wing free pulses. Up to now, the prime endeavor in almost all hollow fiber applications has been to adjust the propagation length and the gas pressure such that a linear chirp was produced which could be removed by a simple prism compressor. The ability to compensate arbitrary phase functions avoids such restricting limits on interaction length and buffer gas pressure. The unrestrained shaping capability of the mask is used and both phase and amplitude functions are applied to the spectrum.

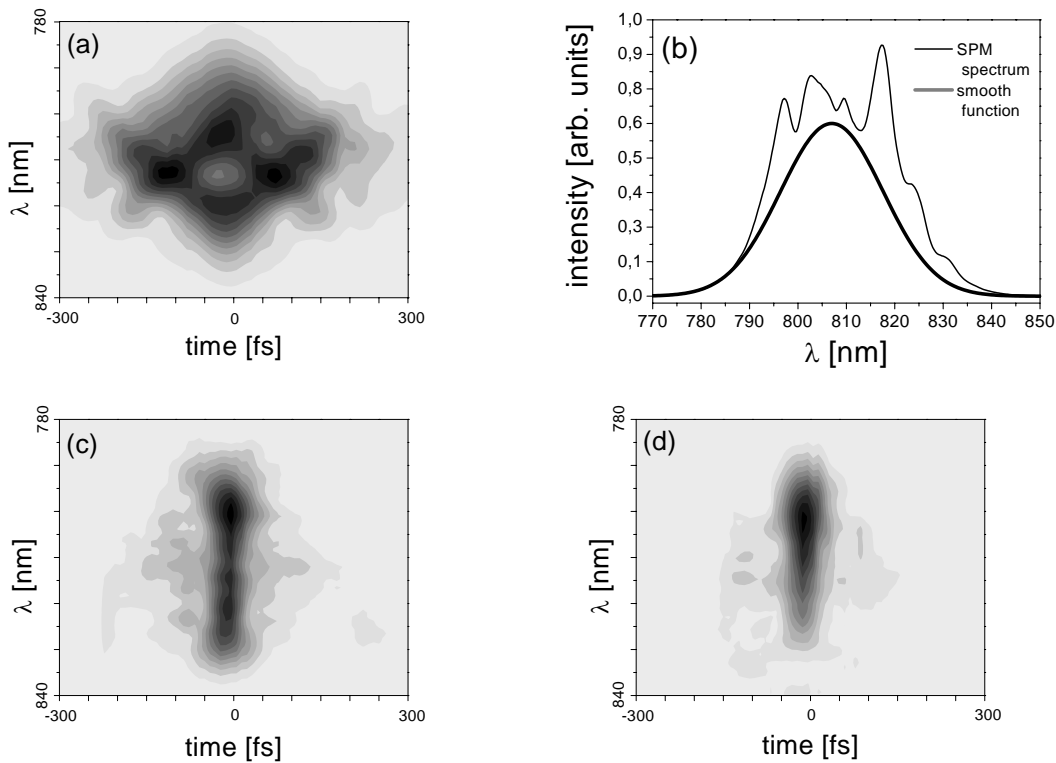
The adaptive compression is accomplished in two independent steps: smoothing the spectrum of the pulse via a pure amplitude modulation by the mask while keeping the phase fixed, and then compensating for the spectral phase under the constraint of the previously determined amplitude function. This dichotomy in the optimization process is made possible by the capability of the LC mask to independently influence the phase and amplitude of the pulse spectrum. It is in fact required because with amplitude filtering, the output energy is no longer constant so the highest SH signal is not necessarily indicative of the shortest pulse.

Fig. 5.8a shows the SHG FROG trace of a pulse after propagation through a 500mm long argon-filled hollow fiber (inner diameter  $225\mu\text{m}$ ) pressurized to 3 bar. The input pulse was a Fourier-limited Gaussian-shaped pulse (120 fs,  $100\mu\text{J}$ ) centered around 810 nm. The pulse duration is broadened to about 400fs; the pulse spectrum is quite inhomogeneous as seen in Fig. 5.8 b. A phase-only optimization returns a pulse with a non-uniform spectrum which still features structured wings, as shown in Fig. 5.8c. The extended approach including spectral smoothing is plotted in Fig. 5.8d and now shows a much more uniform pulse structure. For the spectral smoothing, the deviation of each measured amplitude-modulated spectrum from a well-defined Gaussian smoothing function (see Fig. 5.8b) was minimized. The phase function retrieved by the subsequent SH optimization was in accordance with the one attained in the SH optimization without amplitude shaping.

## 5.3 Summary

The fast adaptive compression of tunable pulses in the visible to below 16 fs has been demonstrated in the presence of additional dispersive material in the beam path before the autocorrelation measurement. The scheme uses a combination of non-collinear OPA design, pulse shaper and learning algorithm. Short pulses at virtually any desired location in an experimental setup can be produced automatically in less than five minutes. It has been shown that our algorithm finds the global optimum solution for the mask settings. An acceptable limit for the phase difference between two adjacent pixels is experimentally found to be 1.6. Given the virtue that the center wavelength of the noncollinear OPA can be adjusted via a single delay without further adjustments, our setup is a powerful tool for spectroscopy experiments with ultrafast pulses.





**Figure 5.8:** FROG-trace (a) and spectrum (b) of a spectrally and temporally broadened pulse after propagation through a hollow fiber, (c) spectral phase compensation resulting in  $\approx 50$ fs (FWHM of temporal marginal) still shows intense side wing structures, (d) optimization with optional smoothing of the spectrum.

The modulation of broadband spectra in the visible is, after all, a prerequisite for the coherent control experiments described in the forthcoming chapters.

The setup is also capable of attenuating the amplitude of each spectral component. Thus, even nasty, deeply modulated spectra with side wings are compressible almost to the Fourier limit by cutting off the unwanted spectral components: much less work is then required to generate smooth spectra, as has been shown in the compression of pulses from a hollow fiber.

The purpose of these two experiments has not been to produce the shortest pulse but rather to show that the principle of feedback controlled pulse shaping is a promising tool for pulse compression [63, 92, 133].

## 6

# Control of two-photon transitions: Dark and bright pulses

This chapter describes an experiment wherein tailored pulses were employed to enhance or cancel the transition probability in the nonresonant two-photon process  $\text{Na}(3s \rightarrow\rightarrow 5s)$  [16]. Using as feedback the fluorescence from the  $4p$  level which is populated from  $5s$  by collisions, these so-called *dark* and *bright* pulses are found with the learning loop approach within few minutes. Different parametrizations of the phase distribution have been examined. Two of these produced solutions which had not previously been predicted by theory, but which still met the objective of the experiment. The study represents the first successful application of a feedback-organized self-learning algorithm to the design of dark pulses.

The nonresonant two-photon process  $\text{Na}(3s \rightarrow\rightarrow 5s)$  represents an example of effectively controlled energy deposition in a two level system by tailoring the spectral phase of the pump pulse, using an additionally implemented feedback scheme.

## 6.1 Experiment

A schematic diagram of the experimental layout as well as the relevant spectroscopic details of the employed pump and detection scheme are displayed in Figs. 6.1 and 6.2. Sodium was evaporated in a heat pipe oven [134] pressurized with 10mbar of Argon as a buffer gas. The temperature was set sufficiently low (250°C) to eliminate pulse propagation effects [135, 136]. The exciting OPA (100fs, 5μJ) was tuned to  $\lambda = 598\text{nm}$  which is close to the  $3s \rightarrow\rightarrow 5s$  resonance, and focused to provide a maximum power density of  $\approx 10^{11} \text{ W/cm}^2$  inside the heat pipe. The population of the  $5s$  target level optically decays to  $3p$  or undergoes collisional relaxation to the  $4p$  state. Both levels are monitored separately via their fluorescence to the  $3s$  ground state at 589nm and 330nm, respectively.

Due to the spectral width of the ultrashort 598nm pulses a competitive (1+1)-photon excitation of  $5s$  via  $3p$  (at 589nm) cannot be immediately excluded. Thus, evidence must be presented that the  $5s$  level is indeed populated as a result of a nonresonant two-photon absorption. In a theoretical treatment of the quantum control of multiphoton transitions by shaped ultrashort pulses which excludes strong field effects, Meshulach et al. [129] have calculated the effect of a  $\pi$  phase step on the probability of  $N$ -photon absorption in a two-level system. The plots of this quantity vs. the normalized step position peak at the frequency of the  $N$ -photon absorption. They are symmetric with respect to this maximum and vanish for  $N$  values of the phase step position. The number of minima is thus indicative of the order of the absorption process.

## 6.2 Results

Fig. 6.3 shows the experimental result for the  $3s \rightarrow\rightarrow 5s$  transition as a function of the  $\pi$  step position induced by the SLM. The position of the maximum and the occurrence of two

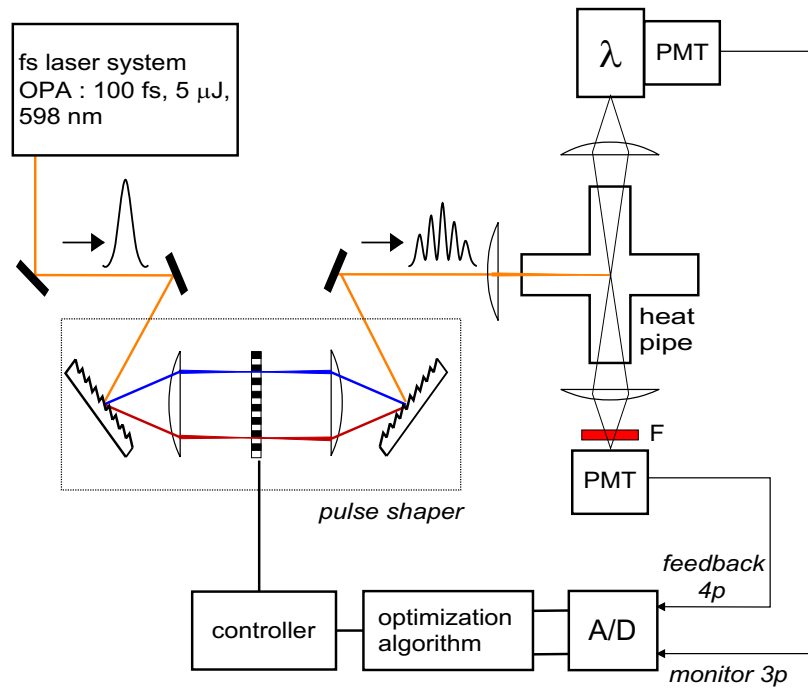


**Figure 6.1:** Experimental layout of the pump- and detection schemes of the two-photon experiment. The pulse shaper used in this experiment is composed of 1800 lines/mm gratings,  $f = 150\text{mm}$  cylindrical lenses, and the CRI phase and amplitude mask. Fluorescence from  $4p$  serves as feedback to the control algorithm.

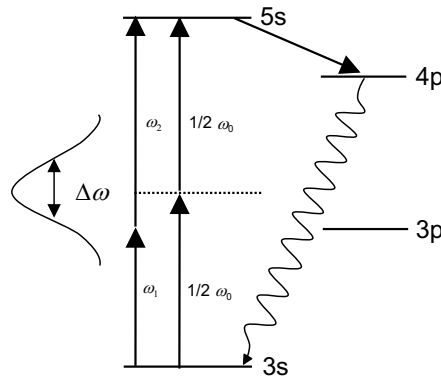


**Figure 6.2:** Grotrian diagram of the sodium transitions important for this experiment (not to scale).

symmetrically arranged minima suggest a two-photon process induced by a wavelength of 602nm. This number is directly read from a spectrum of the laser pulse which was taken while pixel no. 43 (maximum) was blocked (see Fig. 6.3).

The implementation of a feedback controlled optimization routine requires identification of an observable which is uniquely tied to the quantity to be controlled. Population of  $5s$  gives rise to fluorescence from the  $3p$  and  $4p$  levels.  $3p$  may, however, also be pumped in a 589nm one-photon step from  $3s$ . The text to follow describes two experiments which address and settle this ambiguity.

The data from the first test are illustrated in Fig. 6.4 and show the fluorescence from the  $3p$  and  $4p$  levels, following excitation of  $5s$  by 1mW of unchanged pump pulses. The latter were obtained by clipping, in the Fourier plane, the blue wings ( $<591\text{nm}$ ) of the frequency spectrum. The ensuing pulse spectrum is shown in the right panel of Fig. 6.3. Fluorescence

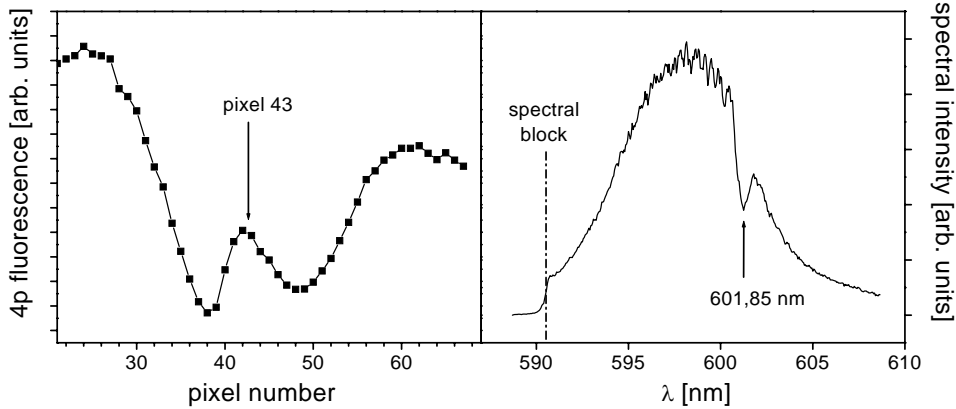


**Figure 6.3:** Left:  $\pi$  phase step shifted across the mask. Fluorescence from collisionally populated  $4p$  shows symmetry around pixel no. 43. Right: OPA spectrum behind SLM observed with pixel no. 43 shut and left wing clipped by blocking part of spectrum.

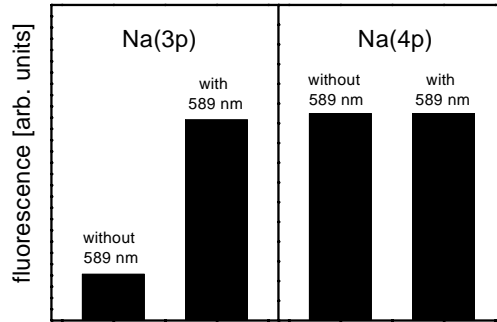


**Figure 6.4:** Response of  $3p$  and  $4p$  fluorescence to the presence or absence of 589nm light (one-photon resonance).

from  $4p$  appears with equal intensity for either excitation condition. The  $3p$  analog, however, is drastically diminished in the absence of the wavelength matching the one-photon resonance.

The previous measurement strongly indicates that  $5s$ , which is the precursor to  $4p$ , is accessed non-resonantly, rather than by a (1+1)-sequence. Supporting evidence comes from an examination of the fluorescence intensities vs. laser power, which is displayed in Fig. 6.5. Again, the  $4p$  signal appears unimpacted by the particularities of the pump laser frequency profile and exhibits a quadratic slope, indicative of a two-photon process. The  $3p$  data are more complex. In the presence of 589nm the signal behaves linearly for low laser intensity and scales as  $I^{3/2}$  above approximately 0.2mW, indicating saturation [137]. Blocking the resonant wavelength produces the same low-intensity behavior, but a quadratic slope beyond 0.2mW.

The bottom line of the above results is as follows: Given the conditions of this experiment (pump  $\approx 1$ mW),  $4p$  is exclusively fed from  $5s$  which owes its population to a non-resonant two-photon excitation. The  $3p$  state draws to some extent from  $5s$ , but is predominantly pumped in a resonant single step when the pulse is left unmodified. We may thus apply Meshulach's model [129] to describe the coherently controlled population of Na( $5s$ ) and we have identified  $4p$  fluorescence as a directly linked criterion suitable to serve as input to the modulator steering algorithm.

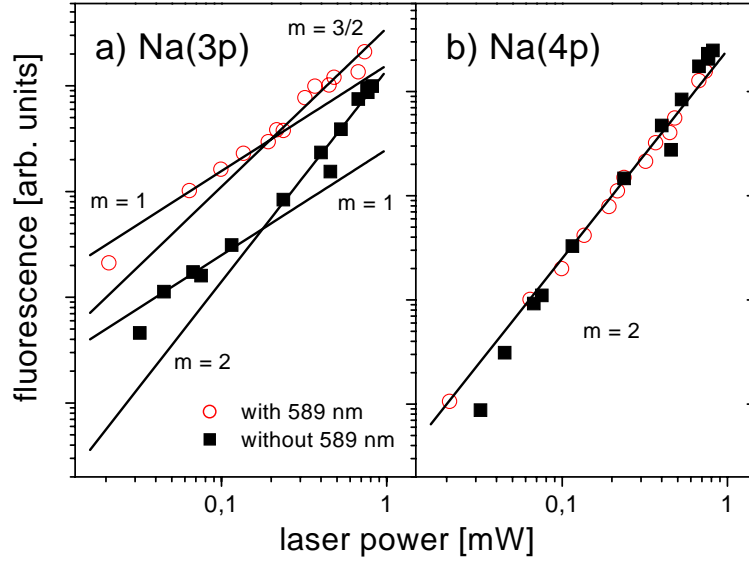


**Figure 6.5:** Power dependence of 3p and 4p fluorescence with or without 589nm light.

The nonresonant two-photon interaction of an ultrashort pulse with a two-level system induces a transition with a probability  $S_2$  [128, 129]:

$$S_2 = \left| \int A \left( \frac{\omega_0}{2} + \Omega \right) \cdot A \left( \frac{\omega_0}{2} - \Omega \right) \cdot \exp \left[ i\Phi \left( \frac{\omega_0}{2} + \Omega \right) + i\Phi \left( \frac{\omega_0}{2} - \Omega \right) \right] d\Omega \right|^2. \quad (6.1)$$

where  $\omega_0$  is the energy of the  $3s \rightarrow 5s$  transition which corresponds to 301nm [138]. Two-photon transitions occur for all pairs of photons  $\omega_1, \omega_2$  which satisfy the condition  $\omega_1 + \omega_2 = \omega_0$ . The detuning of frequencies  $\omega_1, \omega_2$  from  $\omega_0/2$  is denoted by  $\Omega$ . Control of the excitation process is exercised via the interference term and can either maximize or minimize the probability  $S_2$ , as Meshulach et al. [128, 129] have recently demonstrated for the nonresonant two-photon transition of Cesium. Maximization is obviously achieved if the interference term vanishes, which describes the minimum duration transform limited pulse. This solution is not singular, however, since any shaped pulse with the same power spectrum  $A(\omega)$  but with an antisymmetric phase function,  $\Phi(\omega_0/2 - \Omega) = \Phi(\omega_0/2 + \Omega)$ , will yield the same result, irrespective of the particular appearance of the phase distribution. This result is counterintuitive since longer, i.e. less intense, pulses should be less effective in transferring population. In their paper, Meshulach et al. [128, 129] have also formulated phase requirements to produce so-called *dark pulses* which altogether cancel the two-photon pumping probability. No net transitions are induced as long as  $\Phi(\Omega) = \cos(\beta\Omega)$ . The totality of solutions, discriminated by virtue of the parameter  $\beta$ , is symmetric with respect to the center frequency  $\omega_0/2$ .

In the present experiment, the designed pulses were created by phase-only modulation. The task of pinpointing the conditions which either maximize or cancel  $S_2$  was left to the optimization algorithm guided by the 4p fluorescence as feedback. Unbiased by any a-priori modeling the algorithm set out from a phase filter  $\Phi(n) = a \cos(bn + c)$  with  $n$  as the variable which numbers the LC pixels, and  $a, b$ , and  $c$  as free parameters to be optimized. This approach is still tractable but sufficiently general to comprise Meshulach's solution [128, 129]. The experiment was run repeatedly for either objective and achieved convergence within five generations. The phase filters which were retrieved as a result of the optimization procedure are symmetric (cosine) in the case of extinction, and antisymmetric (sine) in the case of enhancement of fluorescence. Symmetry persists with reference to the center frequency  $\omega_0/2$  which impinges on strip no. 43 (see Fig. 6.6). Such good agreement with theory afforded by this three parameter optimization

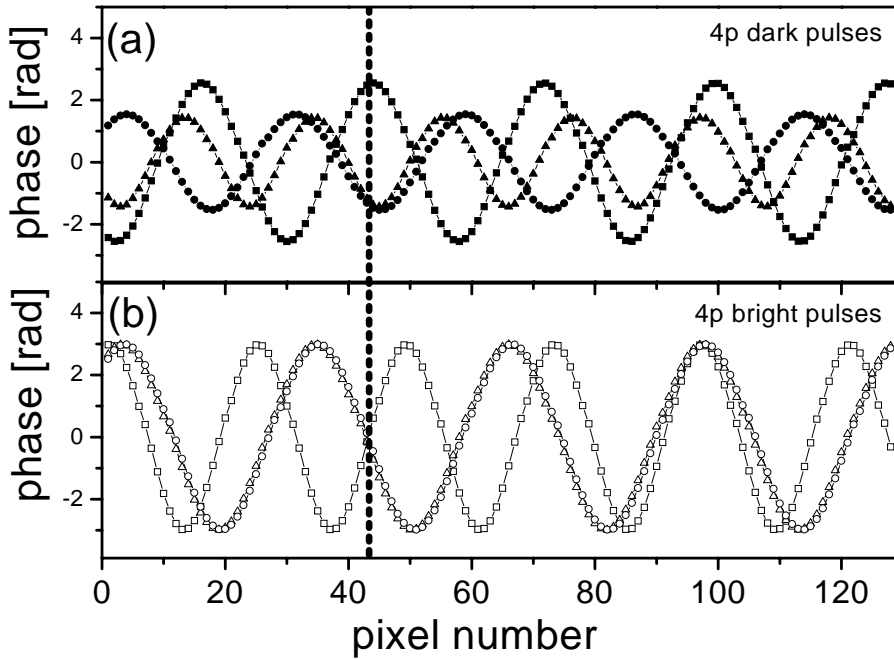


**Figure 6.6:** Generation of dark and bright pulses in the  $\text{Na}(3s \rightarrow 5s)$  transition. The vertical line at pixel 43 marks the symmetry reference position of the phase which has been determined in an auxiliary experiment [16, 128] (a) The phase structures of dark pulses cancelling the transition  $\text{Na}(3s \rightarrow 5s)$  show symmetry (b): Phase structures of bright pulses show antisymmetry.

requires imposition of upper and lower restrictions on the parameter  $b$ . In the bright pulse case,  $b$  must be sufficiently large to allow at least four oscillations of the phase over the width of the mask. In the absence of this lower limit the algorithm would merely compensate the chirp of the incoming pulse to produce the Fourier limited shape, i.e. the pulse having the minimum time duration, which obviously maximizes  $S_2$ . To optimize the dark pulses,  $b$  has been limited to yield a maximum of eight phase oscillations. Lifting this restriction would result in very long pulses which are dark due to insufficient intensity.

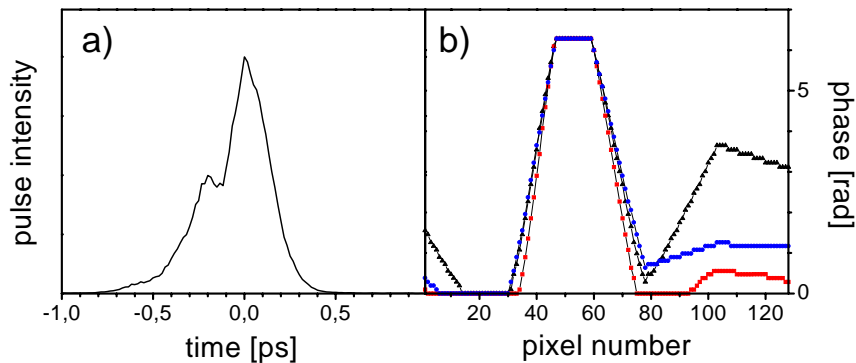


**Figure 6.7:** Free optimization using a six-parameter phase function with linear interpolation. (a) Cross-correlation of a typical dark pulse. (b) Convergence as achieved in three different runs.

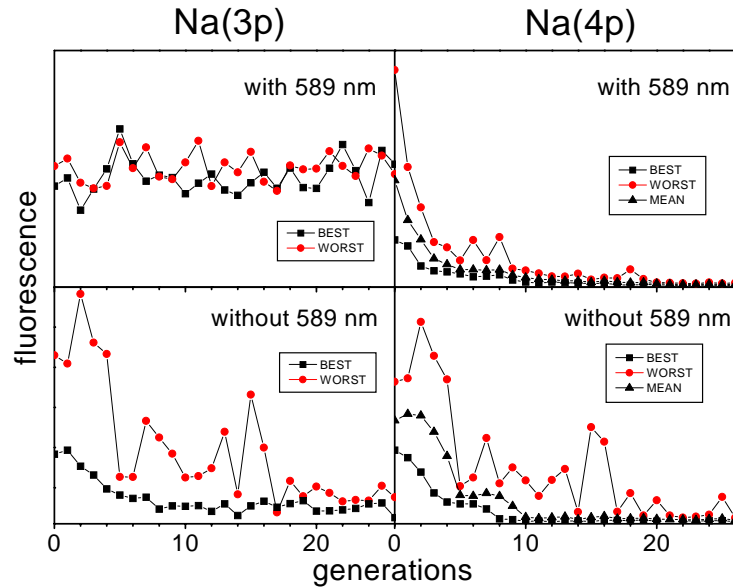


**Figure 6.8:** Convergence data of the six-parameter search for the dark pulse. Figure shows the best and worst mask patterns for each generation. As long as 589nm light is blocked,  $3p$  and  $4p$  fluorescence are equally suited as feedback signal. This is not the case if one-photon transitions are admitted since the direct excitation of  $3p$  is phase insensitive.

In a further experiment we lifted the restriction on the dimensionality of the parameter space and tried a model of the phase filter which permitted an unbiased choice of parameters. Aiming at the generation of dark pulses we introduced a phase function defined by the minimum number of sampling points connected by a linear interpolation. Each of these points may assume 64 discrete values within a range from 0 to  $2\pi$ . Six parameters proved sufficient to achieve this goal. The dark pulse retrieved by the algorithm is shown in Fig. 6.7(a) whereas Fig. 6.7(b) represents the phase setting of the mask. The property of being "dark" is indeed phase-related, which is convincingly shown by comparison with the effect induced by a chirped pulse of equivalent energy and duration. The evolution of a dark pulse as mirrored by the decrease of the  $4p$  fluorescence feedback signal is shown in the top row of Fig. 6.8. Compared to an unmodulated pulse the  $5s$  population is reduced to  $<3\%$ . The left panel proves the insensitivity of the one-photon  $3s \rightarrow 3p$  transition to a phase-only modulation. Once the resonant pumping of  $3p$  is suppressed by blocking the relevant wavelength the fluorescence from this level perfectly matches that of  $4p$  (Fig. 6.8, bottom row).  $3p$  is now populated via radiative decay of  $5s$  and hence is equally suited as feedback input.

Both the three- and the six-parameter approach converge after less than 50 generations, i.e. within less than 5 minutes. A comparative inspection of the phase functions returned by either method raised the question of the existence of further solutions which are of altogether different character. We thus expanded the previous parametrization to 128 sample points, each falling between 0 and  $2\pi$  as before. Fig. 6.9 documents the convergence towards the dark (left) and the bright pulse (right) which was attained after  $\approx 10$  generations. In accordance with theory an antisymmetric phase function causes population enhancement (Fig. 6.9 (b)). No likewise apparent symmetry properties, however, characterize the suppression of two-photon pumping. Re-runs of the optimization procedure produced identical experimental results but differing phase functions. The solutions which the algorithm produced bore no resemblance with the prediction of theory. The shaped pulses show a complex phase- and amplitude-time structure of comparable duration ( $\approx 2ps$ ). It is thus not their peak power but rather their phase distribution which produces qualities such as "bright" or "dark" [139].

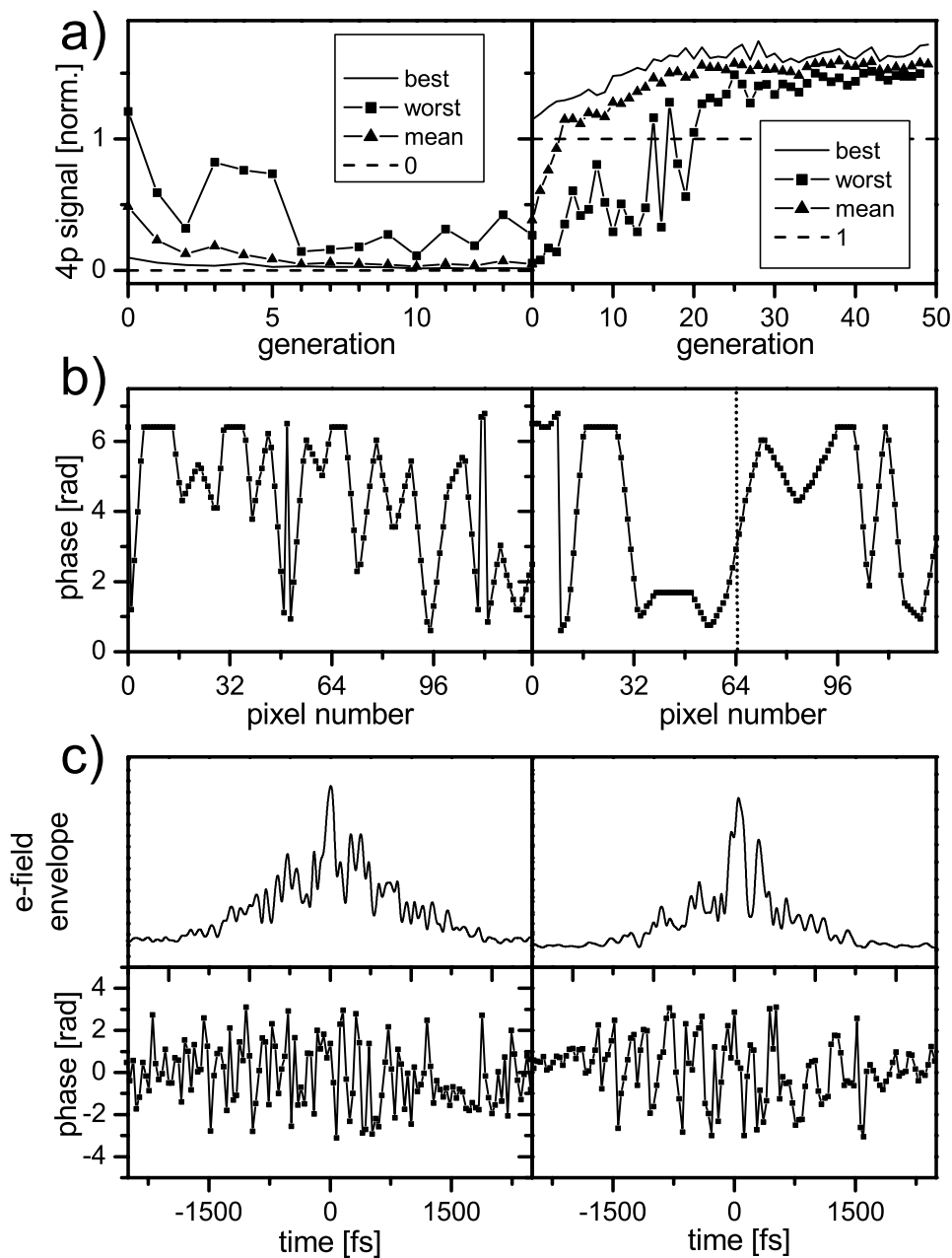


**Figure 6.9:** Convergence data of the 128-parameter search for the dark (left) and bright (right) pulse. (a): Normalized fluorescence intensity to document convergence. Dashed lines mark "no signal" (0) and "unshaped reference pulse" (1). (b): Right: Phase structure of bright pulse showing antisymmetry. Reference position has shifted to 602nm due to re-alignment of optical setup. (c): Pulse shape and phase structure in the time domain. Bright and dark pulses show a complex structure, but are of similar duration.



### 6.3 Summary

In this section, the influence of phase modulated fs laser pulses on two-photon transitions in an atomic prototype system has been studied. The implementation of different parameterizations in the feedback loop has been tested. The phase-modulated excitation of the two-photon-transition shows that the feedback approach can be successfully used to find fs laser pulses for different control objectives, even without an intelligent initial guess supplied by theory. The properties of pulses being either "dark" or "bright" have been demonstrated to be dependent on the phase and not the intensity of the excitation pulse. The results of Meshulach *et al.* [127, 129] regarding the symmetry of the phase functions have been verified autonomously by the adaptive approach, thus confirming the concept of parameterization. The best solutions for both extremes were obtained within five generations. Allowing the feedback algorithm to search in an extended parameter space yielded new phase structures in addition to known analytic solutions. These structures are not intuitively comprehensible and call for further theoretical studies.

## 7

# Control of Ground State Dynamics in Polydiacetylene

## 7.1 Introduction

Many coherent control studies so far have dealt with the control of electronically excited species [140]. Control of ground state dynamics, however, might be even more important since chemical reactions usually take place on the lowest potential energy surface. For mode-selective chemistry it is crucial to focus energy in a local vibrational motion of a certain bond (local mode) or, in a more general sense, to form a superposition of vibrations leading to dynamics along the reaction coordinate. Such dynamics can be described by a superposition of eigenfunctions (normal modes) resulting from the stationary Schrödinger equation. Due to the broad spectra of femtosecond laser pulses, these pulses are capable of coherently exciting more than one normal mode [141, 142]. If the phases of these modes are chosen suitably, the enhancement of normal modes or the preparation of local modes should be possible.

This section reports the selective excitation of ground state vibrational modes in a polymer, polydiacetylene, by a stimulated Raman process. The interaction of the electric field with the molecule cannot be calculated by first-principle methods, which makes any predictions of pulse shapes for selecting a certain mode almost impossible. The process is optimized in a feedback loop using the anti-Stokes Raman signal of a four-wave-mixing (FWM) process as feedback. Polydiacetylene (PDA) has been studied in detail with femtosecond time- and frequency-resolved coherent anti-Stokes Raman Scattering (fs-CARS) [143–145]. In those experiments, several normal modes were excited in a stimulated Raman process and the vibrational dynamics in the electronic ground and self-trapped exciton state were studied by analyzing the anti-Stokes signal. Additionally, two strategies to excite selectively vibrational motion of the  $\tilde{\nu}_2/\tilde{\nu}_{2'}$  modes in the electronic ground state of PDAs were demonstrated. One technique made use of the Tannor–Rice scheme [6], which is related to the vibrational dynamics in the excitonic states of PDA. The other method included the variation of the chirp of the ultrashort Stokes laser pulse [146], already pointing to the important role of the phase in the selective excitation of vibrational motions.

In the experiments presented here, time- and wavelength-resolved CARS serves both as controlling and surveying mechanism for the optimization. Control is achieved by shaping of the Stokes pulse. The different modes of the PDA molecules show different contributions in the frequency-resolved CARS spectrum. Two very similar experiments were performed: the first one with 100fs pulses as supplied by a commercial OPA shows the feasibility of the control [147], whereas the second experiment, involving the non-collinear OPAs with substantially shorter pulses and broader spectra, allowed for the excitation of an additional mode and the observation of shorter oscillation periods.

## 7.2 Experiment

The samples used in the experiments were FBS (bis-*p*-fluorobenzene-sulfonate) diacetylenes. Their structure is shown in Fig. 7.1 [148]. Polydiacetylene is obtained by topochemical solid state polymerization of the monomer single crystal, which can be induced thermally or with UV light. Polymerization occurs with synchronous rotation of the single molecules around their center of mass which does not impact the surrounding lattice. A polymer structure results in which all polydiacetylene (PDA) chains are aligned parallel to the *b*-axis of the diacetylene single crystal. Less than 1% polymer was embedded in the monomer single crystal, thus the interaction between the polymer chains can be neglected.

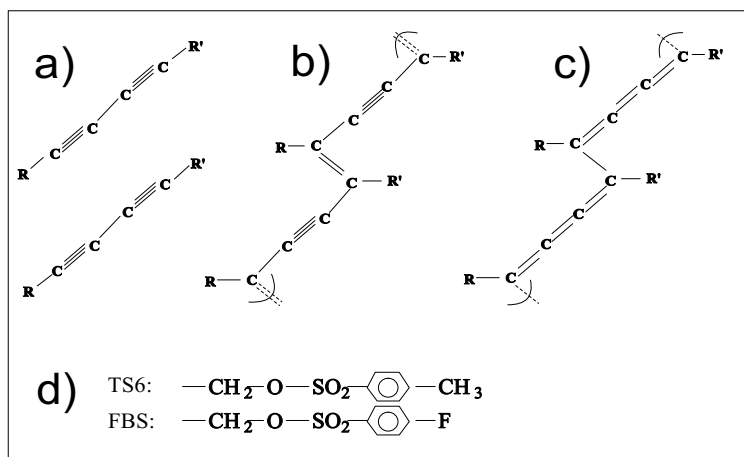


**Figure 7.1:** The molecular structure of (a) the diacetylene monomer and the polymer unit (b) and (c). The polymer chain (backbone) can be described by two mesomeric structures, the acetylenic (b) and the butatrienic (c). The experiments of this section were performed with the FBS side groups (d), although other side groups have been investigated in femtosecond CARS experiments as well [144].

The delocalized  $\pi$ -electrons of the backbone form a quasi one-dimensional system, which results in a strong anisotropy of the physical properties, as for example the dichroism of the PDA crystals. When incident light is polarized perpendicular to the polymer chain direction, the crystals appear nearly transparent, whereas light polarized parallel to the chains is absorbed strongly (see Fig. 7.2). Therefore, the polarization of the CARS beams has to be chosen appropriately to assure efficient excitation.

The sample was cooled to approximately 20 K in a closed-cycle helium cryostat. The electronic ground state of the PDA is best represented by an acetylenic structure, see Fig. 7.1.

Fig. 7.3 shows a part of the resonance Raman spectrum obtained from PDA at 10 K and the motions of the atoms resulting in the four vibrational normal modes  $\tilde{\nu}_1$ ,  $\tilde{\nu}_2/\tilde{\nu}_2'$  (Fermi-coupled modes),  $\tilde{\nu}_3$ , and  $\tilde{\nu}_4$  [151]. The modes are composed mainly of stretching and bending motions of the backbone bonds and were all excited by the pump and Stokes laser pulses of the fs-CARS experiment.

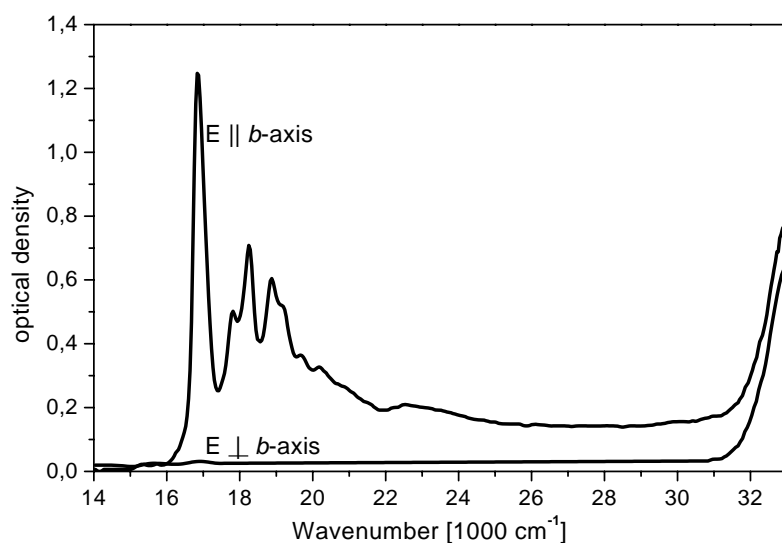


**Figure 7.2:** Absorption spectra of PDA for light polarized perpendicular and parallel to the  $b$ -axis of the single crystal (from [149]). Absorption independent of polarization above  $30000\text{cm}^{-1}$  can be traced back to the absorption of diacetylene monomers. The absorption peak at  $16800\text{cm}^{-1}$  is assigned to the 0-0 transition from the electronic GS  $^1A_g$  to the electronically excited state  $^1B_g$  of the  $\pi$  electron system of the PDA chains. Upon excitation with a pump photon at  $16800\text{cm}^{-1}$ , a free exciton is produced in the  $^1B_g$  state from which a self-trapped exciton is then formed (see [150] for further details).

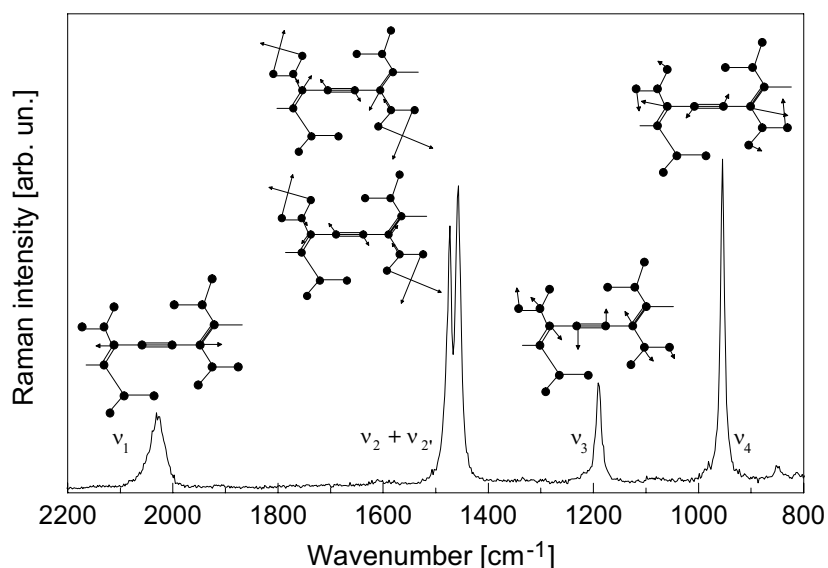


**Figure 7.3:** Resonance Raman spectrum displaying the vibrational modes excited by the fs pump and Stokes pulse. For each principal Raman vibrational mode ( $\tilde{\nu}_1, \tilde{\nu}_3, \tilde{\nu}_4$ ) as well as for the Fermi coupled vibrational modes ( $\tilde{\nu}_2, \tilde{\nu}_{2'}$ ) atomic displacements [151] are given assuming a simplified side group structure. From [149].

The experimental setup (Fig. 7.4) included two collinear, two-stage OPAs [152] for the experiments with 100fs time resolution and two non-collinear OPAs (chapter 1) for experiments with 30fs time resolution.

For the experiments with 100fs pulses, the OPA outputs were tuned to 605 nm and 652 nm. The 605 nm pulses were compressed by a prism pair to yield a FWHM of 100fs and split into pump and probe pulses. The 652 nm pulses served as Stokes beam and were fed through a 4f pulse shaping setup (see caption of Fig. 7.4 for details). With no mask voltages applied, the shaper was adjusted for shortest (Fourier limited) Stokes pulse to remove residual chirp of the OPA output pulses. The shaped pulses were characterized with a multi-shot FROG setup, using SHG in a 100  $\mu\text{m}$  BBO crystal as nonlinear element, and with a commercial SHG autocorrelator.

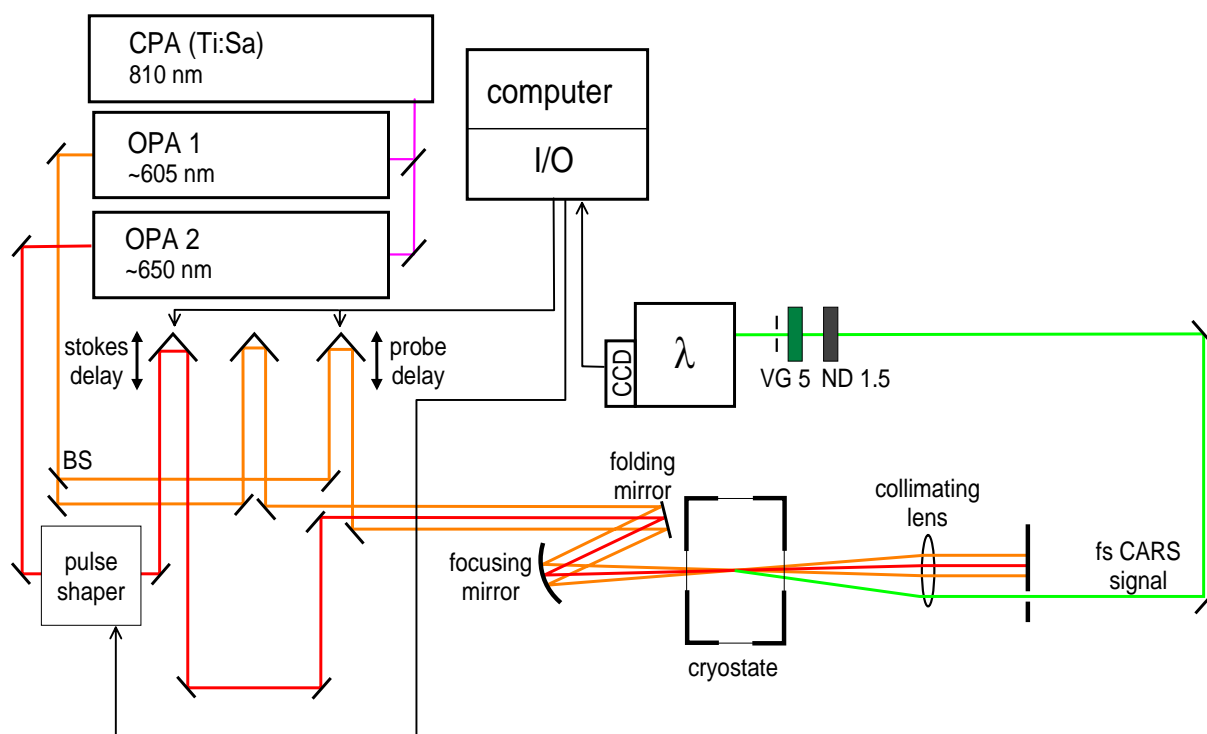


**Figure 7.4:** Layout of the fs CARS experiment. The Stokes pulses are tailored with a pulse shaper which features a pair of  $1/d=1800/\text{mm}$  gratings,  $f=150\text{mm}$  cylindrical mirrors for the 100fs experiments with the collinear OPAs, and  $1/d=600/\text{mm}$  gratings,  $f=150\text{mm}$  cylindrical mirrors for the experiment with non-collinear OPAs. The CRI phase and amplitude mask has been used in both experiments. The accepted bandwidths are above the OPA bandwidths in either case.

Pump, Stokes and probe pulses were focused with a  $f=60\text{ cm}$  spherical focusing mirror into the 20 K cryostat containing the PDA crystal. All beams were polarized horizontally. At the focus, each of the three beams had a pulse energy of  $\approx 100\text{ nJ}$ . The beams were arranged in a folded BoxCARS configuration [153, 154] and placed such that the sum of the wave vectors of pump and Stokes is in the direction of the crystal  $b$  axis which is parallel to the polymer chains (Fig. 7.5c). This assures effective excitation in the exciton band. Behind the cell, the CARS signal was collimated with an  $f=60\text{ cm}$  lens, spectrally dispersed and detected with a cooled CCD line camera.

The spectral bands of the wavelength-resolved CARS signal which correspond to the different modes of PDA served as the feedback signal for the optimization algorithm. The optimization algorithm searched for the optimal settings for the LC mask to enhance the desired mode.

In order to avoid features arising at zero time delay of pump, Stokes, and probe pulses, the delay  $\tau_1$  between pump pulse and the unshaped Stokes pulse was chosen to be  $\tau_1 = +100\text{ fs}$  which is

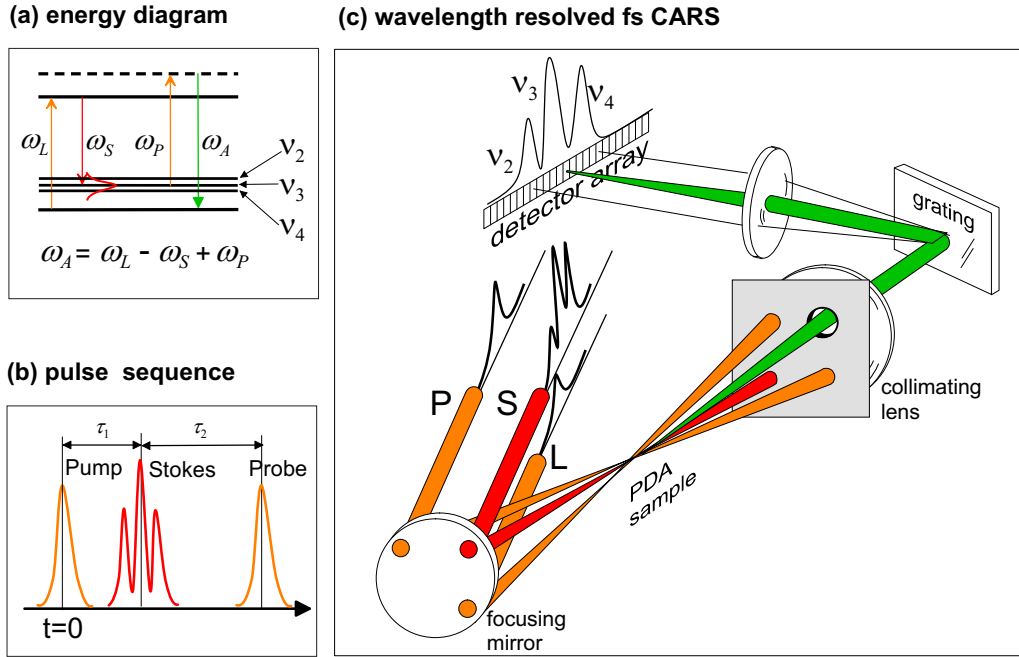


**Figure 7.5:** Setup of the fs-CARS experiment. (a) energy diagram of the CARS pulses, (b) pulse sequence of the three incoming pulses with Stokes pulse shaped, (c) wavelength-resolved folded BoxCARS configuration.

well after the pump pulse (Fig. 7.5b). To overcome possible effects arising from the beating of the modes, the delay of the probe pulses was wobbled over several beatings with a frequency of about 5 Hz between +100 fs and +366 fs. Great care was taken that the density distribution of the delay values versus time was uniform. The averaging was performed by simply recording spectra while the probe delay continuously alternated between the two boundary points as shown in Fig. 7.6.

For the experiments with higher time resolution using non-collinear OPAs, the setup was essentially the same as before, with the only exception that FS prism compressors were used in both beams. The non-collinear OPAs were tuned to  $\approx 605$  nm with a FWHM of 25 nm for the pump and probe and  $\approx 660$  nm with a FWHM of 34 nm for the Stokes pulses. The FS prism compressor for each color was adjusted to compensate for the chirp introduced by the cryostat windows, yielding pulse durations of approximately 30 fs (pump, probe) and 35 fs (Stokes) as measured by autocorrelation. The pulses were attenuated to yield approximately 70 nJ for pump and probe each and 110 nJ for the Stokes in front of the cryostat. The non-resonant CARS signal at the 100  $\mu$ m glass plate mounted inside the cryostat routinely delivered crosscorrelation widths of approximately 30 fs.

## 7.3 Results

The goal was to demonstrate that it is possible to influence the relative population and relative phase of the coherently excited normal modes.

### 7.3.1 Experiments with 100 fs temporal resolution

In the experiments on PDA with the commercial OPAs and 100 fs temporal resolution, the  $\tilde{\nu}_2/\tilde{\nu}_2'$ ,  $\tilde{\nu}_3$ , and  $\tilde{\nu}_4$  vibrations have been excited. If we are able to control the phase and excitation of normal modes, we should also be able to excite normal modes such that certain bonds are

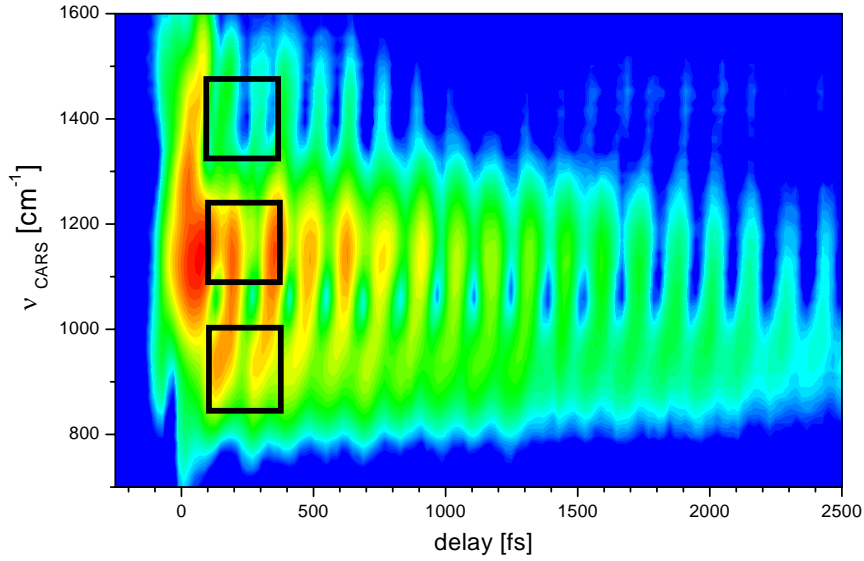


**Figure 7.6:** Derivation of the feedback signal. The probe delay is wobbled continuously between  $\tau_2=100$ fs and  $\tau_2=366$ fs. Spectra are recorded throughout all the time. After a given integration time, the spectral intensity is integrated over a wavelength range corresponding to the  $\tilde{\nu}_{2,2'}$ ,  $\tilde{\nu}_3$ ,  $\tilde{\nu}_4$  modes, respectively. Altogether, this results in an integration over the transients as indicated by the three boxes.

efficiently excited; this scheme would be of great interest for reaction control. Figure 7.7a shows the three dimensional pattern obtained from the CCD detection of the transient anti-Stokes signal with nearly Fourier limited pulses. With a constant time delay of  $\tau_1$  between pump and Stokes pulse, the time delay  $\tau_2$  between Stokes and probe pulses was varied. According to a previous article [145], the relative intensities of the three Gaussian-like peaks, which are centered at about  $1480 \text{ cm}^{-1}$ ,  $1200 \text{ cm}^{-1}$ , and  $960 \text{ cm}^{-1}$ , reflect the relative population of the three coherently excited modes. The time- and frequency-resolved anti-Stokes signal  $I(\omega, \tau_2)$  can be written as [155]:

$$I(\omega, \tau_2) = \sum_{i=2(2'),3,4} Q_i^2(\omega) \exp\left(\frac{-2\tau_2}{T_{2i}}\right) + \sum_{\substack{i,j=2(2'),3,4 \\ i>j}} Q_i(\omega)Q_j(\omega) \exp\left(\frac{-\tau_2}{T_{2i}T_{2j}/(T_{2i}+T_{2j})}\right) \cos(\omega_{ij}\tau_2 + \phi_{ij}), \quad (7.1)$$

where  $Q_i(\omega)$  is the spectral amplitude distribution of mode  $i$ , given by the product of a mode intensity with a frequency-dependent function reflecting the spectral contribution of this mode to the anti-Stokes signal [145],  $T_{2i}$  the coherent dephasing time, and  $\omega_{ij} = |\omega_i - \omega_j|$ , where  $\omega_i$  and  $\omega_j$  are the carrier angular frequencies of modes  $i$  and  $j$ , respectively. Since the probe was wobbled over several beating periods, the CARS signal has to be integrated over several oscillations of the second term in eqn. 7.1, which makes this contribution to the integral small compared to that of the first:

$$A(\omega) = \int_{t_0}^{t_1} I(\omega, \tau_2) d\tau_2 \approx \sum_{i=2(2'),3,4} \frac{1}{2} Q_i^2(\omega) T_{2i} \left( e^{-\frac{2t_0}{T_{2i}}} - e^{-\frac{2t_1}{T_{2i}}} \right) \quad (7.2)$$

The corresponding population in each mode can be obtained by integrating over its spectral profile, which serves as an input for the merit function in the optimization algorithm:

$$P_{\tilde{\nu}_j} = \int_{\omega_j - \Delta\omega_j/2}^{\omega_j + \Delta\omega_j/2} A(\omega) d\omega. \quad (7.3)$$

Correspondingly, the population  $P_{\tilde{\nu}_j}$  of a particular mode  $\nu_j$  was determined in the experiment by summation over the intensities of the corresponding CCD pixel values,

$$P_{\tilde{\nu}_j} = \sum_{n(\tilde{\nu}_j - \Delta\tilde{\nu}_j/2)}^{n(\tilde{\nu}_j + \Delta\tilde{\nu}_j/2)} I(n), \quad (7.4)$$

$n(\tilde{\nu}_j)$  being the CCD pixel corresponding to the Raman shift  $\tilde{\nu}_j$  and  $\Delta\tilde{\nu}_j$  the width of the mode. An efficient optimization function strongly depends on a suitably chosen feedback. The following merit functions  $m_{\tilde{\nu}_{22'}}(P_{\tilde{\nu}_{22'}}, P_{\tilde{\nu}_3}, P_{\tilde{\nu}_4})$  were considered (without loss of generality, maximization of mode  $\tilde{\nu}_{22'}$  is desired):

$$m_{\tilde{\nu}_{22'}}(P_{\tilde{\nu}_{22'}}, P_{\tilde{\nu}_3}, P_{\tilde{\nu}_4}) = P_{\tilde{\nu}_{22'}} \quad (7.5)$$

$$m_{\tilde{\nu}_{22'}}(P_{\tilde{\nu}_{22'}}, P_{\tilde{\nu}_3}, P_{\tilde{\nu}_4}) = P_{\tilde{\nu}_{22'}} - (P_{\tilde{\nu}_3} + P_{\tilde{\nu}_4}) \quad (7.6)$$

$$m_{\tilde{\nu}_{22'}}(P_{\tilde{\nu}_{22'}}, P_{\tilde{\nu}_3}, P_{\tilde{\nu}_4}) = \frac{P_{\tilde{\nu}_{22'}}}{P_{\tilde{\nu}_3} + P_{\tilde{\nu}_4}}. \quad (7.7)$$

Merit function (7.5) usually showed poor results regarding the contrast of the modes. Functions (7.6) and (7.7) achieved comparable optimization results in many cases. The advantage of (7.7) is that, if a similar dependence of  $P_{\tilde{\nu}_{22'}}$ ,  $P_{\tilde{\nu}_3}$ , and  $P_{\tilde{\nu}_4}$  on laser power is assumed, the feedback signal is normalized for laser power. Nevertheless, for low values of the denominator in eq. (7.7) this merit function is sensitive to background noise. One might suspect that (7.7) merely enhances the contrast at the expense of the total signal strength, but this has not been observed. For merit function (7.6), the contrary line of argument may be considered. Nevertheless, we observed that it exhibits good signal intensities as well as a reasonable contrast. For the optimizations shown in Figs. 7.7 and 7.8, merit function (7.7) was used throughout.

In previous experiments [146] it was shown that the distribution of energy in the different modes strongly depends on chirp and delay of the Stokes pulse. Hence it is appropriate to restrict the algorithm mainly to a search for polynomial phase functions, without changing the spectrum of the pulses by an amplitude function. We thus chose a polynomial representation of the phase function, compare Eq. 4.17,

$$\Phi_n = \sum_{k=2}^K c_k \left( \frac{n - N_0}{N} \right)^k \quad n = 0, \dots, N - 1 = 127, \quad (7.8)$$

with quadratic terms as the lowest polynomial order. The parameters  $c_k$  and  $N_0$  are optimized by the algorithm such that the vibrational dynamics are only excited in the desired mode while all other modes are suppressed. In the experiments of section 5 [65],  $N_0$  has been included as parameter to ensure that the offset of the phase function coincides with the center of the spectrum after an optimization has been accomplished. Here,  $N_0$  is a means of adjusting the delay of the pulse shaper, since a linear phase shift can be performed with this parameter as well.

At first,  $m_{\tilde{\nu}_{22'}}$  served as the feedback signal in order to maximize the relative population of the  $\tilde{\nu}_{22'}$  mode. Figure 7.7b is the three dimensional time- and wavenumber-resolved CARS signal obtained after optimization of the  $\tilde{\nu}_{22'}$  mode. The two undesired modes are almost completely suppressed. When the optimization of the  $\tilde{\nu}_{22'}$  mode was repeated with new, randomly-chosen initial parameters, the retrieved phase function was nearly identical, indicating that the phase functions retrieved by an optimization are physically significant. The optimum phase function is characterized by a linear chirp which is in accordance with former results. [146].

The same method has been applied for the selective optimization of the  $\tilde{\nu}_3$  and  $\tilde{\nu}_4$  modes. The results are shown in Figs. 7.7c and 7.7d. In each case it was possible to suppress the two other modes. In addition, the decay times of the optimized mode could be increased by a factor of two. The strong beating between the modes, as observed in Fig. 7.7a, disappeared.



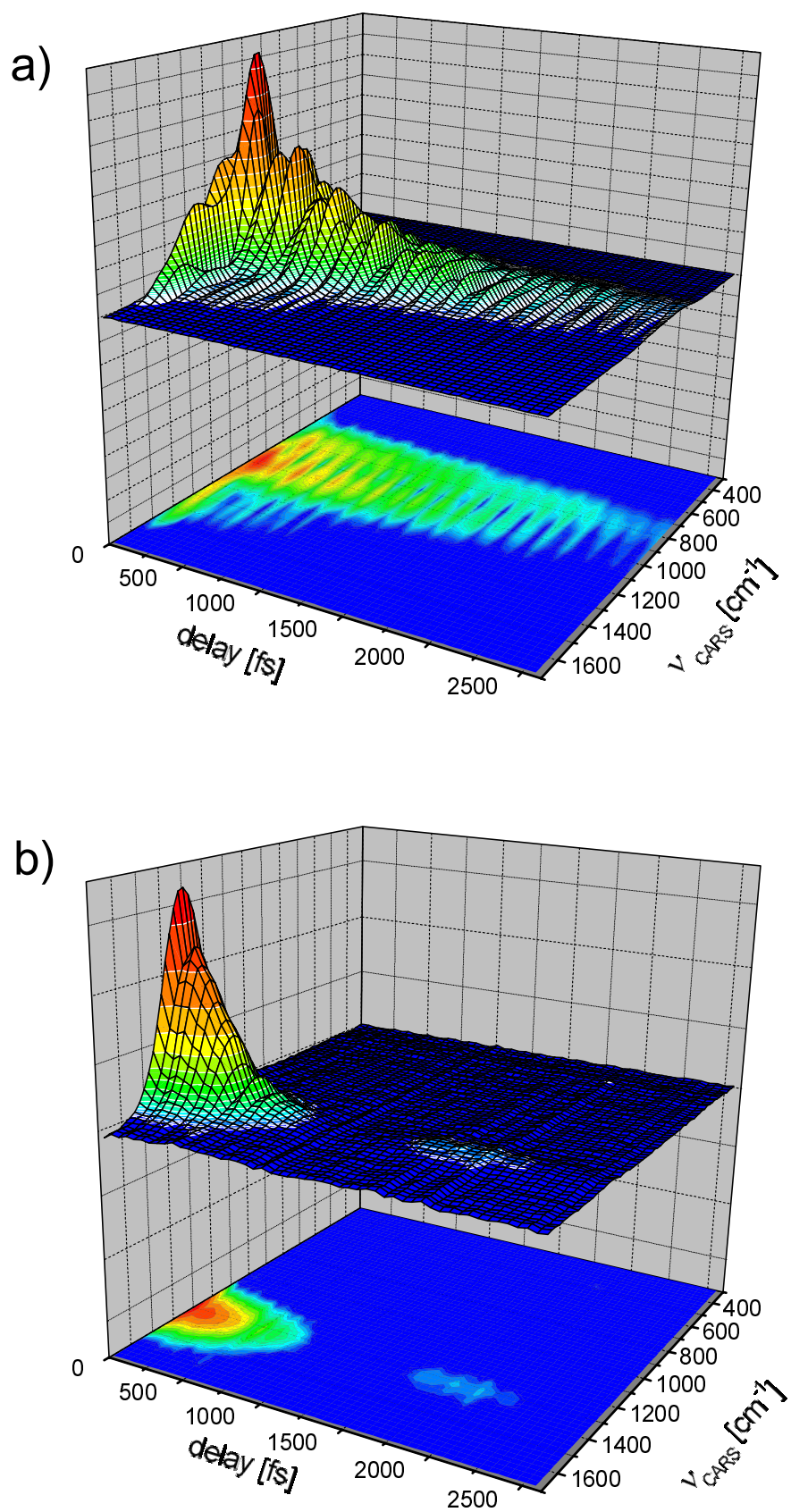


**Figure 7.7:** Spectrally resolved CARS transients on polydiacetylene with shaped Stokes pulse for optimization of different modes: a) unshaped pulses (Fourier limited); b) Optimization of the  $\tilde{\nu}_2/\tilde{\nu}_2'$  mode.

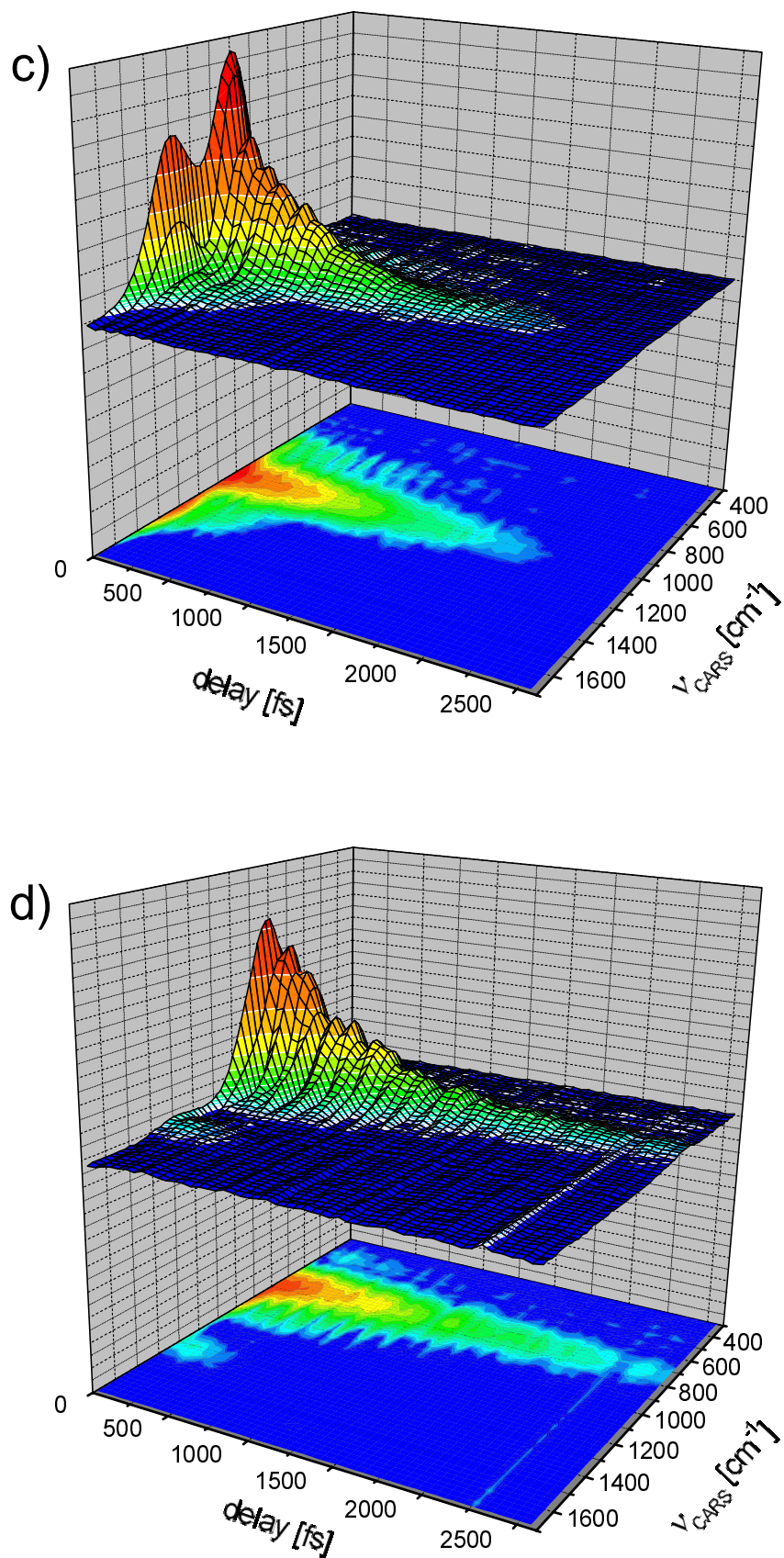


**Figure 7.8:** Spectrally resolved CARS transients on polydiacetylene with shaped Stokes pulse for optimization of different modes: c) Optimization of the  $\tilde{\nu}_3$  mode; d) Optimization of the  $\tilde{\nu}_4$  mode.

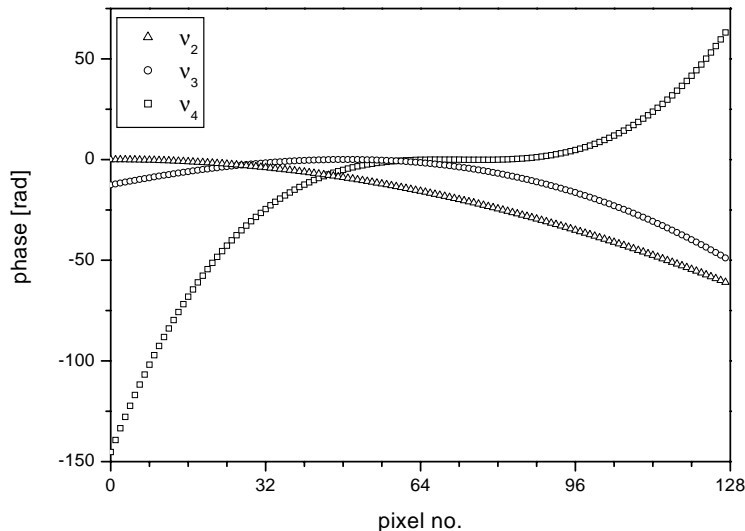


**Figure 7.9:** Phases retrieved by the algorithm for the optimization of the  $\tilde{\nu}_{22'}$ ,  $\tilde{\nu}_3$ , and  $\tilde{\nu}_4$  mode. The parameters in eq. 7.8 retrieved during the optimization are  $N_0 = 0$ ,  $c_2 = -7.88$ ,  $c_3 = 0.79(\tilde{\nu}_{22'})$ ,  $N_0 = 48.86$ ,  $c_2 = -10.10$ ,  $c_3 = -3.45(\tilde{\nu}_3)$ , and  $N_0 = 68.22$ ,  $c_2 = -9.29$ ,  $c_3 = 9.78(\tilde{\nu}_4)$ , respectively.

In Fig. 7.9 the phase functions for the three optimizations are shown. Since the excitation of the modes is caused by a stimulated Raman process, the frequencies for the excitation of a certain mode are given by the convolution of the pump and the Stokes pulse. This means that a certain range of the Stokes spectrum is responsible for the excitation of a specific mode. The center of the Raman resonance for the  $\tilde{\nu}_4$  mode corresponds to mask pixel 80 at the given laser wavelengths for pump and Stokes pulse, to pixel 48 for  $\tilde{\nu}_3$ , and to pixel 14 for  $\tilde{\nu}_{22'}$ . These values agree well with the retrieved values for  $N_0$  of the polynomial. Since the derivative of the phase functions with respect to frequency is zero at  $N_0$ , the phases of the frequency components are not changed at these positions. On the other hand, the phase function temporally shifts the frequency components responsible for the other two modes out of the Franck-Condon window between the self-trapped exciton state and the electronic ground state, thereby minimizing their contributions. In addition, the shape of the phase function might be interpreted in terms of symmetric and antisymmetric phase functions around the corresponding Raman resonances which suppress or enhance this two-photon transition according to control studies on multi-photon transitions [129]. Applying instead predefined phase functions in which only the coefficient  $c_2$  (eq. 7.8) has been varied, the beating structure could be changed in a defined manner giving rise to any superposition of normal modes.

A linear interpolation of the phase function with 64 parameters (see section 4.3) was also tested for the optimization of the  $\tilde{\nu}_{22'}$  mode and also proved to be highly efficient. The results are shown in Fig. 7.10. The non-trivial phase function resulted in a highly complex pulse, though a smooth, linear phase can be observed around pixel 16 which corresponds to the Stokes wavelength of the  $\tilde{\nu}_{22'}$  mode. This means that the optimization shifted the frequency components that dump population from the STE state to the  $\tilde{\nu}_{22'}$  mode of the ground state to a suitable temporal delay, thus ensuring efficient population transfer, whereas it scattered all other frequencies in time.

As can be clearly seen from the results above, the three modes have been controlled and the transients could be modified. If the reaction coordinate for a certain chemical reaction requires the interplay of several normal modes, the corresponding superposition of the eigenstates can already be achieved by this population and phase control.

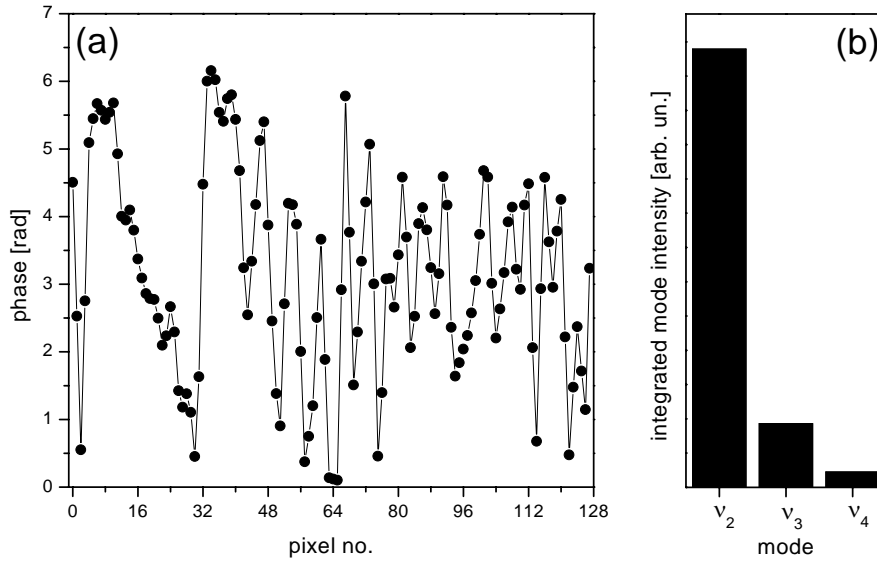


**Figure 7.10:** (a) LCM phase retrieved after optimization of the  $\tilde{\nu}_{22'}$  mode. A linear phase approximation with 64 interpolation points and feedback function 7.6 has been used. (b) The integrated mode intensities exhibit a high selectivity for the retrieved pulse.

### 7.3.2 Experiments with 30 fs time resolution

For a better description of the control mechanism, investigations with a better time resolution are needed. With the ultrabroad spectra of the non-collinear OPAs, excitation of a fourth mode,  $\tilde{\nu}_1$  at  $2030 \text{ cm}^{-1}$ , is achieved in addition to the three modes  $\tilde{\nu}_{22'}$ ,  $\tilde{\nu}_3$ , and  $\tilde{\nu}_4$ . Even with this increase in complexity of the control task, control is still possible.

A wavelength-resolved transient of an unshaped Stokes pulse and a pump delay  $\tau_1 = 0$  is shown in Fig. 7.11. With the enhanced temporal resolution, the beating between the  $\tilde{\nu}_{22'}$  and  $\tilde{\nu}_4$  mode appears, as can be seen in Fig. 7.12 and 7.13. The  $\tilde{\nu}_3$  mode is not clearly distinguishable from the strong neighbouring modes and can only be deduced from the low-frequency beating structure (see Fig. 7.13). Thus, only the optimizations of the modes  $\tilde{\nu}_1$ ,  $\tilde{\nu}_{22'}$ , and  $\tilde{\nu}_4$  are discussed here.

With the shorter pulses, a temporal delay  $\tau_1 = 50$  fs between pump and stokes (instead of 100 fs as chosen with the 100 fs pulses) proved sufficient to minimize time zero features. The probe delay was again wobbled by the same amount, but between  $\tau_2 = 50$  fs and  $\tau_2 = 316$  fs.

Merit function 7.7 was changed accordingly to account for the  $\tilde{\nu}_1$  mode and was used in these optimizations throughout unless otherwise noted.

A preliminary optimization experiment using a chirp parameterization (Eq. 7.8) yielded only poor results regarding mode contrast. The spectrum of the pump and probe pulses had to be reduced from 25 nm down to 20 nm FWHM with a slit behind the second compressor prism in order to get sufficiently high contrast with the chirp parameterization. Optimization of the  $\tilde{\nu}_3$  mode was only achieved with low selectivity which is traced back to the fact that the  $\tilde{\nu}_3$  mode is overlapped by the  $\tilde{\nu}_{22'}$  and  $\tilde{\nu}_4$  modes (see Figs. 7.11 and 7.12).

From the results of the experiments in the previous section, it was deduced that the incidence of the Stokes frequencies at the correct time for dumping the desired part of the population from the self-trapped exciton state to the ground state is one of the mechanisms responsible for the optimization results. In order to test this hypothesis, a parameterization was chosen that used a Taylor series for the phase, as before, and additionally a Gaussian amplitude window with adjustable width and center. This parameterization used only 6 parameters, and the corresponding optimizations achieved high selectivity and fast convergence. After optimization of each single mode, the optimal values for the pixel of the center of the Gaussian window as well

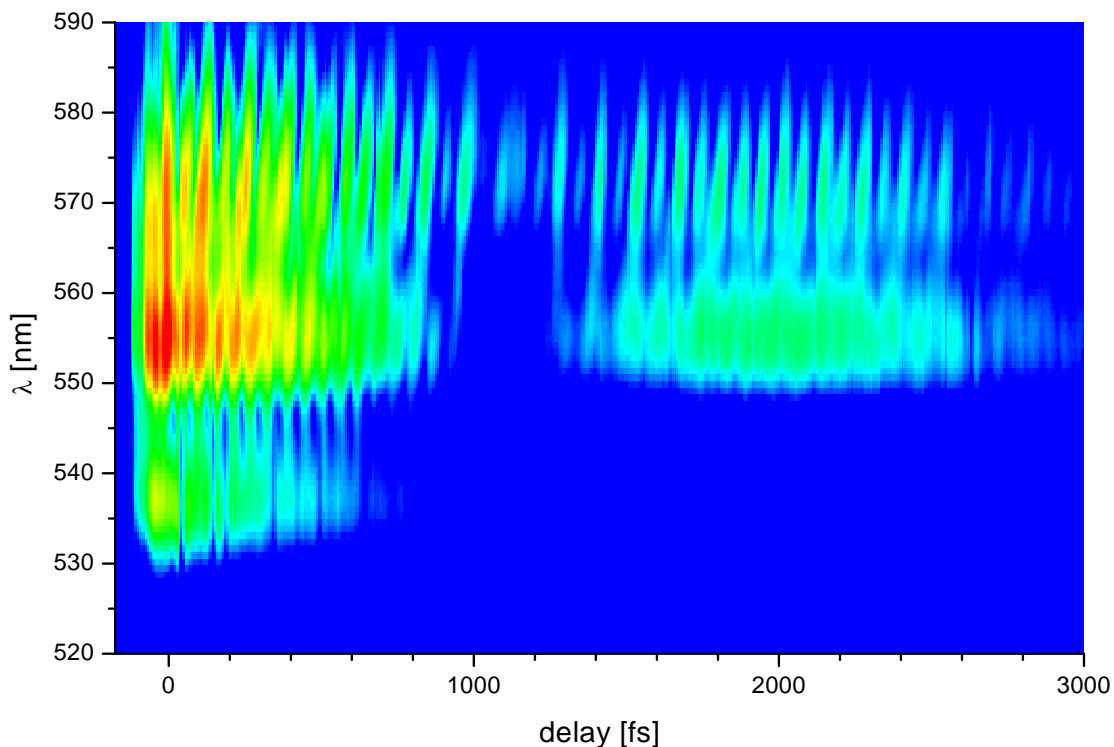


**Figure 7.11:** Wavelength-resolved CARS transient using broadband pulses from non-collinear OPAs.

as the pixel of the zenith of the phase parabola were near the values for the pixel corresponding to the Stokes wavelength of each mode (see Fig. 7.14). Additionally, the curvature of the phase function retrieved for the optimization of the middle,  $\tilde{\nu}_{22'}$ , mode (Fig. 7.14b) is observed to be larger than for the optimization of the two outer modes,  $\tilde{\nu}_1$  and  $\tilde{\nu}_4$ . An explanation for this is that the Stokes frequencies corresponding to the  $\tilde{\nu}_1$  and  $\tilde{\nu}_4$  modes have to be shifted temporally farther in order to suppress the dump process of these two modes. Altogether, the data enforce the explanation of the previous section that one mechanism for achieving selectivity in the excitation of ground state vibrational modes is a Tannor-Rice pump-dump scheme.

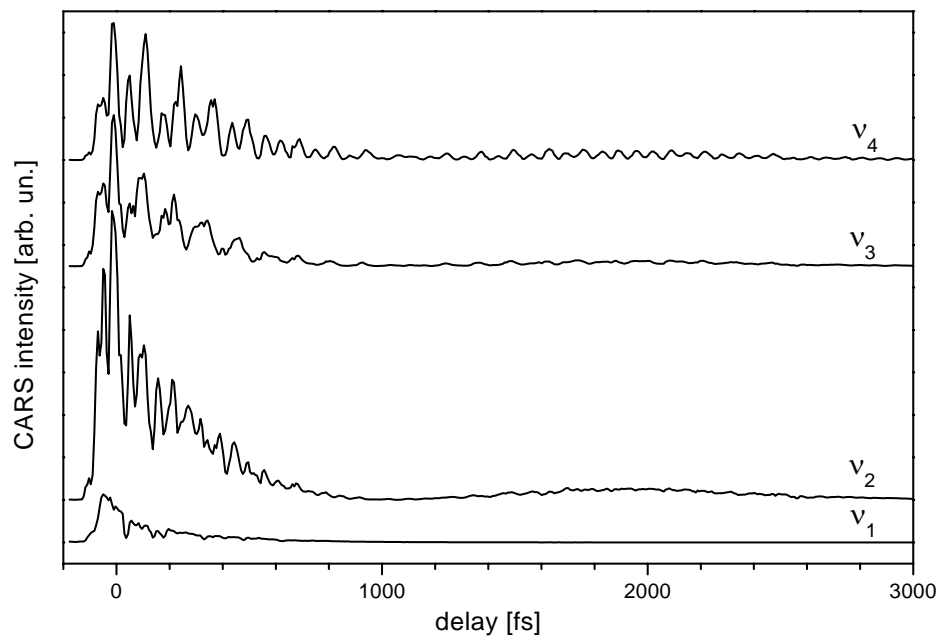
Optimizations using a free parameterization with 32 interpolation points each for phase and amplitude (section 4.3) have been performed as well and produced high selectivity, though the retrieved phase and amplitude functions were complex and unintuitive. No smooth function for a range of pixels corresponding to the Stokes frequencies of the mode for which maximization was sought has been observed, as was the case in Fig. 7.10.

Fig. 7.15(b) and 7.16(a) and (b) compile the transients obtained after optimization of the mode  $\tilde{\nu}_1$  as well as the combination modes  $\tilde{\nu}_1 + \tilde{\nu}_{22'}$  and  $\tilde{\nu}_{22'} + \tilde{\nu}_4$ . Fig. 7.15(a) shows the corresponding reference transient. It was also possible to excite the remaining single modes  $\tilde{\nu}_{22'}$  and  $\tilde{\nu}_4$  with high selectivity as well as the  $\tilde{\nu}_1 + \tilde{\nu}_4$  mode, which is not shown here.

The combination modes  $\tilde{\nu}_1 + \tilde{\nu}_{22'}$ ,  $\tilde{\nu}_1 + \tilde{\nu}_4$ , and  $\tilde{\nu}_{22'} + \tilde{\nu}_4$  were optimized with a merit function similar to Eq. 7.7 (without loss of generality, optimization of the  $\tilde{\nu}_1 + \tilde{\nu}_{22'}$  combinatorial mode is desired):

$$m_{\tilde{\nu}_1\tilde{\nu}_{22'}}(P_{\tilde{\nu}_1}, P_{\tilde{\nu}_{22'}}, P_{\tilde{\nu}_3}, P_{\tilde{\nu}_4}) = \frac{P_{\tilde{\nu}_1}P_{\tilde{\nu}_{22'}}}{P_{\tilde{\nu}_4}} \quad (7.9)$$

Altogether, all combinations of the modes  $\tilde{\nu}_1$ ,  $\tilde{\nu}_{22'}$  and  $\tilde{\nu}_4$  could be prepared.



**Figure 7.12:** Cuts along wavelengths corresponding to the  $\tilde{\nu}_1 - \tilde{\nu}_4$  modes of the wavelength-resolved transient in Fig. 7.11.

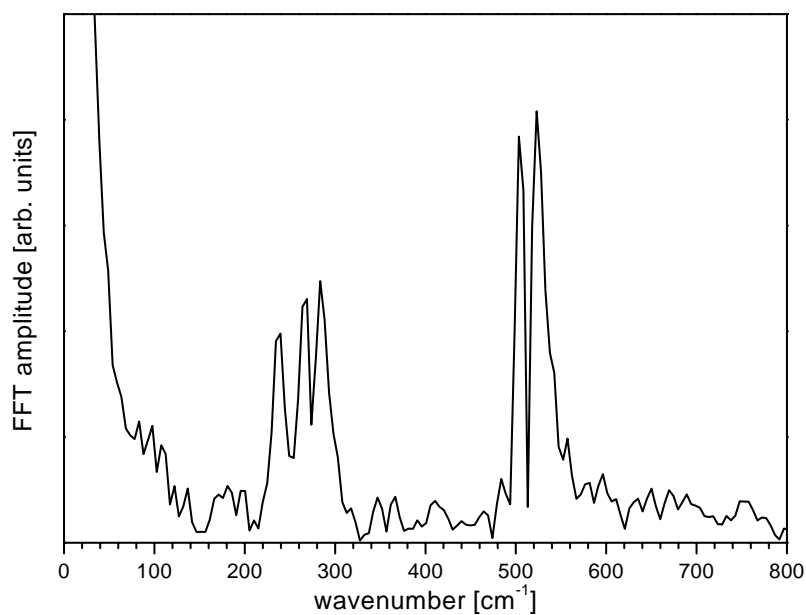


**Figure 7.13:** FFT analysis of the  $\tilde{\nu}_4$  mode in Fig. 7.12. FFT components at  $238 \text{ cm}^{-1}$ ,  $266 \text{ cm}^{-1}$ ,  $284 \text{ cm}^{-1}$ ,  $503 \text{ cm}^{-1}$ , and  $523 \text{ cm}^{-1}$  are visible, corresponding to the beating of the  $\tilde{\nu}_3/\tilde{\nu}_4$ ,  $\tilde{\nu}_2/\tilde{\nu}_3$ ,  $\tilde{\nu}_2'/\tilde{\nu}_3$ ,  $\tilde{\nu}_1/\tilde{\nu}_2$ , and  $\tilde{\nu}_1/\tilde{\nu}_2'$  modes, respectively.

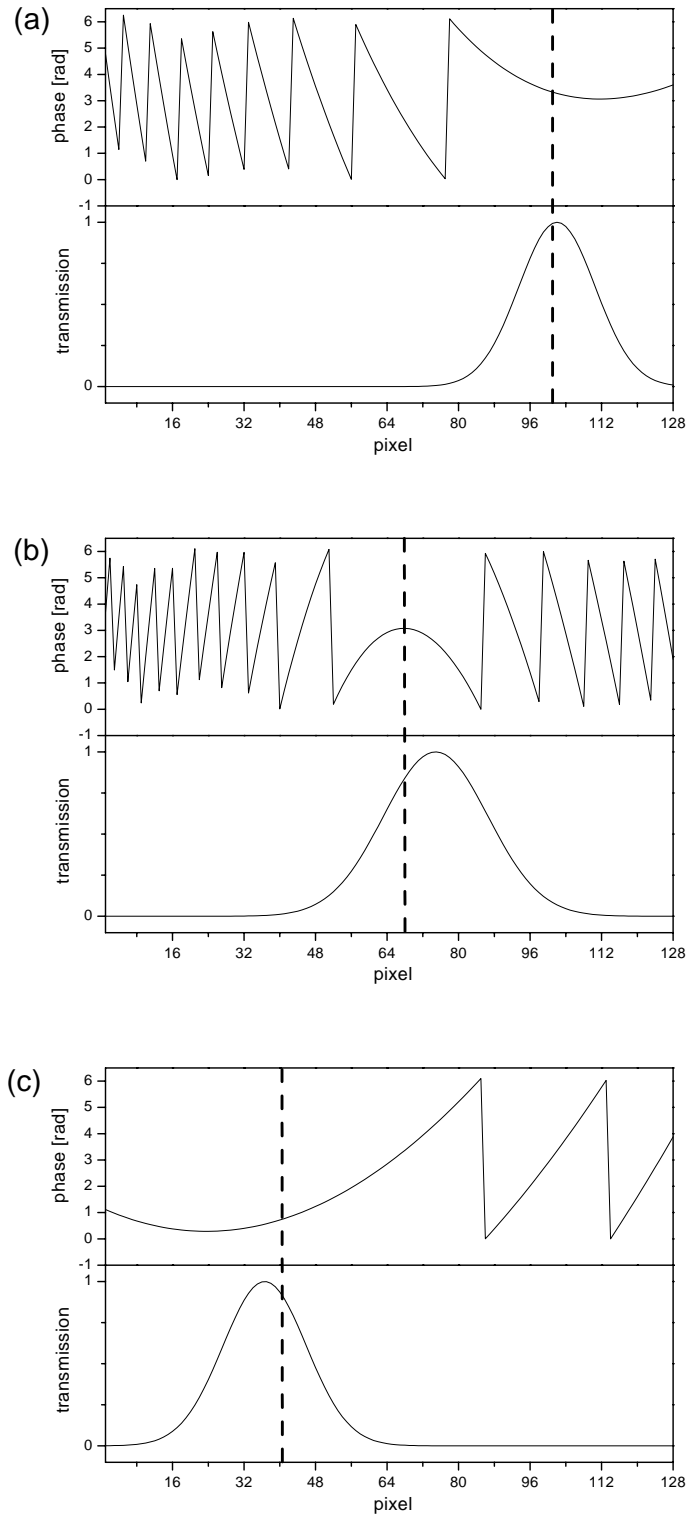
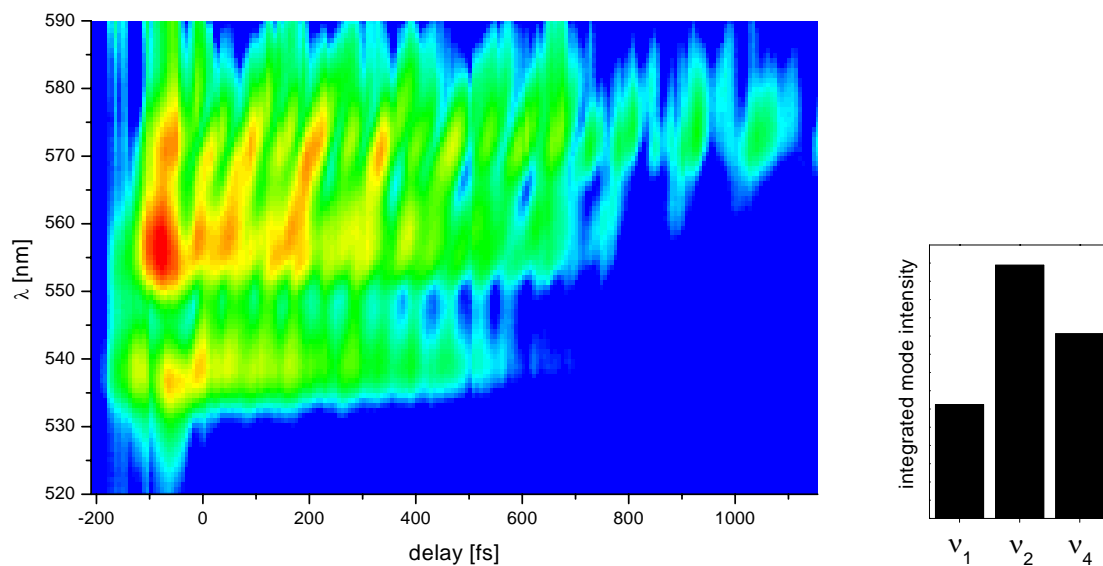


**Figure 7.14:** Phase and amplitude functions retrieved with the combined chirp/ Gaussian amplitude parameterization after optimization of the  $\tilde{\nu}_1$  (a),  $\tilde{\nu}_{22'}$  (b), and  $\tilde{\nu}_4$  (c) modes, respectively. The center of the Gaussian amplitude window as well as the zenith of the quadratic phase function coincides with the pixels corresponding to the Stokes wavelengths of each mode (pixel 100, 66 and 40 for the  $\tilde{\nu}_1$ ,  $\tilde{\nu}_{22'}$ , and  $\tilde{\nu}_4$  modes, respectively, as indicated by dashed lines) assuming a central wavelength of the pump of 602nm.

(a)



(b)

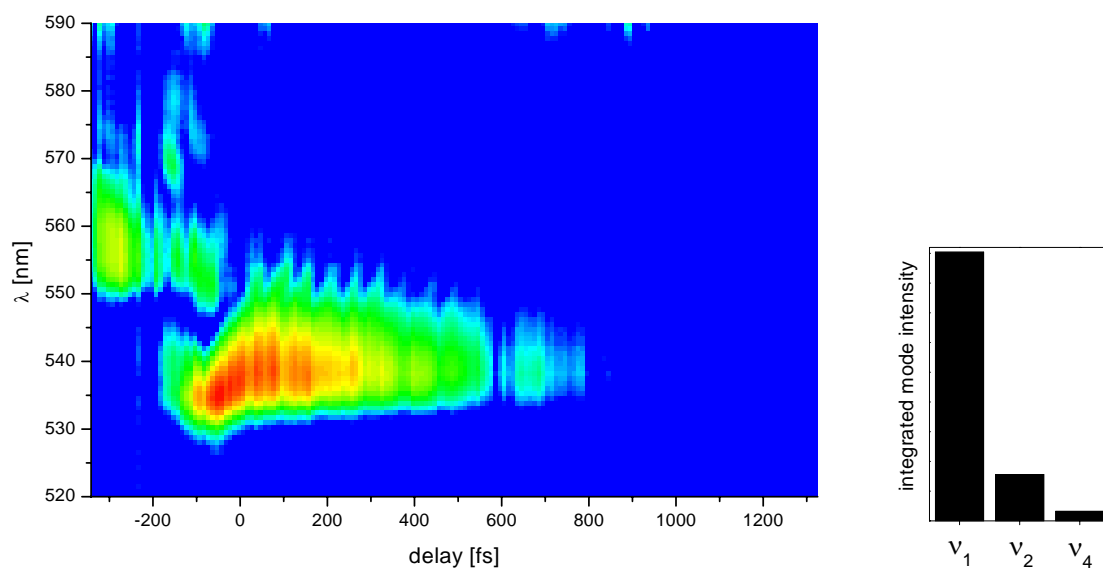
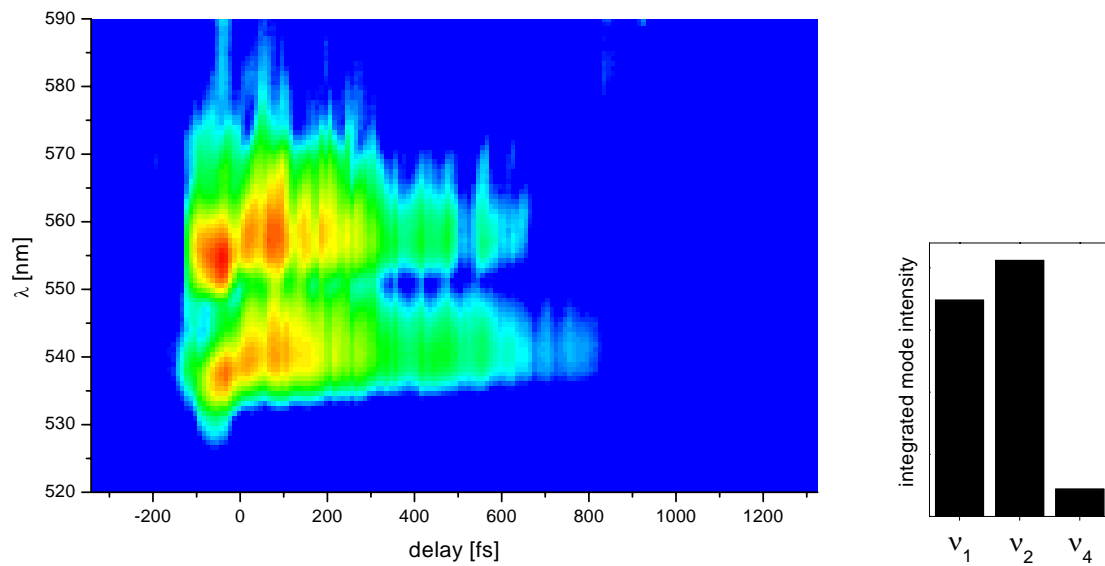


**Figure 7.15:** Wavelength-resolved transients (2D plots, left) and distribution of the mode intensities (bar charts, right) after optimization with free phases and amplitudes, using 32 interpolation points. (a) Reference transient, showing the  $\tilde{v}_1$ , ( $\tilde{v}_3$ ),  $\tilde{v}_{22'}$ , and  $\tilde{v}_4$  mode. (b) After optimization of the  $\tilde{v}_1$  mode.



(a)



(b)

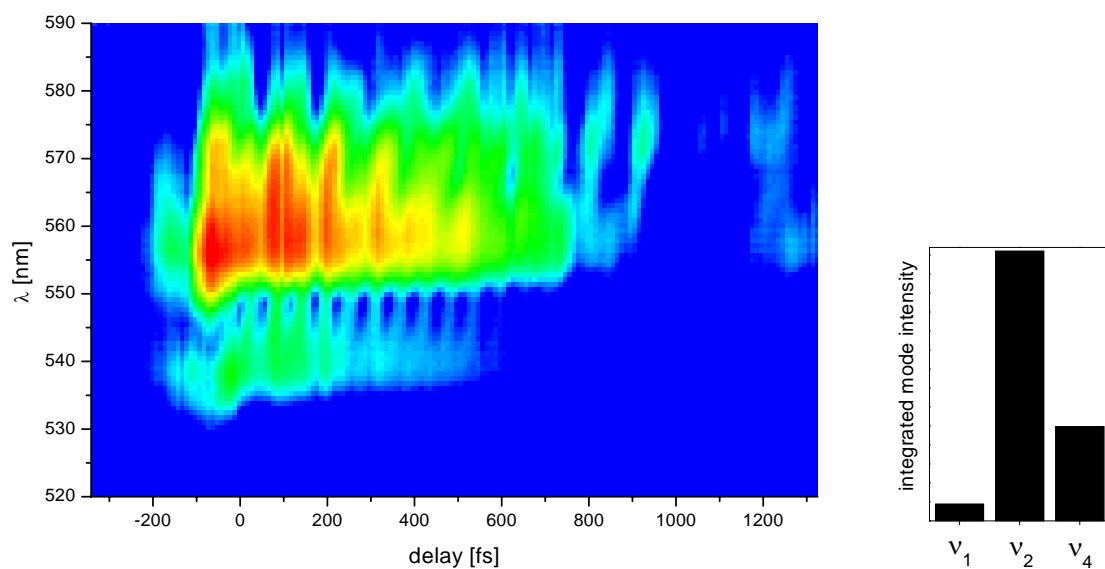


**Figure 7.16:** Wavelength-resolved transients (2D plots, left) and distribution of the mode intensities (bar charts, right) after optimization with free phases and amplitudes, using 32 interpolation points. (a) After optimization of the  $\tilde{v}_1$  and  $\tilde{v}_{22'}$  mode, (b) after optimization of the  $\tilde{v}_{22'}$  and  $\tilde{v}_4$  mode.

The question remains whether mode-selective excitation is still possible with the full pump/probe spectrum.

With a free phase-only parameterization (see section 4.3) using 32 interpolation points, it was still necessary to use spectrally clipped pump and probe pulses in order to get a good contrast ratio of the modes after optimization. A combined phase and amplitude function with 32 interpolation points each had to be used in order to achieve a good contrast ratio with the full pump/probe spectrum, whereas 16 points each for phase and amplitude did not suffice.

This suggests that the 16-parameter phase and amplitude approximation as well as the chirp parameterization does not offer enough free parameters to obtain a faithful optimization result. Therefore, between 33 and 64 free parameters are needed in order to obtain a sufficiently large subspace of the complete space of possible pulse shapes that contains the optimal solution.

For the focusing of a wave packet in order to produce a local mode, it is essential to be able to control the phases of the normal modes. In order to verify that the phase of the oscillations changes with the phase of the controlling Stokes pulse, a phase step was introduced onto the spectrum of the Stokes pulse between the pixels corresponding to the Stokes wavelength of the  $\tilde{\nu}_1$  and  $\tilde{\nu}_{22'}$  mode. Seven transients were averaged for phase steps of  $0$ ,  $\pi/2$ ,  $\pi$ , and  $3\pi/2$ . Cuts through the transients at the anti-Stokes wavelength corresponding to the  $\tilde{\nu}_1$  mode are shown in Fig. 7.17. The phase of the beat structure shifts linearly (dashed lines) with the phase step. This indicates that the phases of the normal modes can be influenced. Hence, the generation of local modes is feasible.

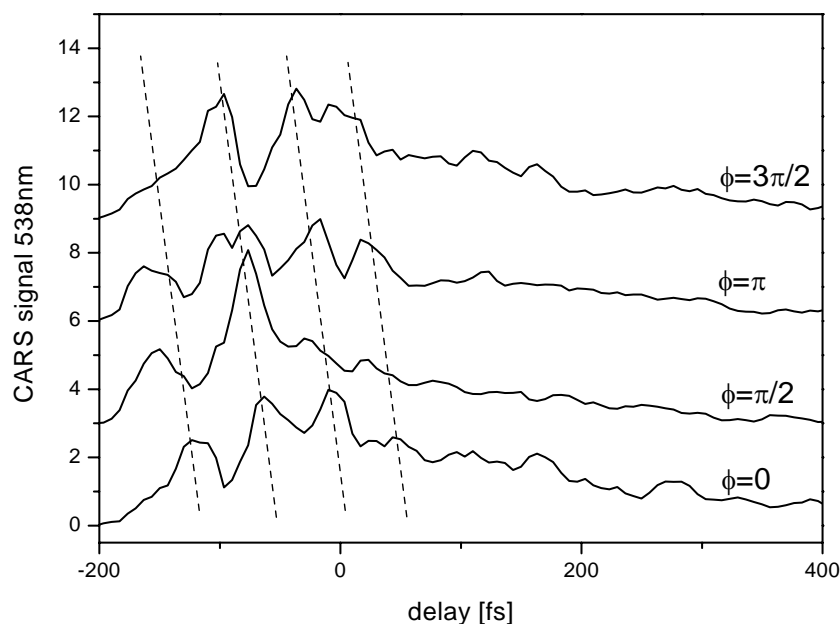


**Figure 7.17:** Cuts through the transients at a Stokes wavelength corresponding to the  $\tilde{\nu}_1$  mode for phase steps  $0$ ,  $\pi/2$ ,  $\pi$ , and  $3\pi/2$  between the wavelengths of the Stokes spectrum corresponding to the  $\tilde{\nu}_1$  and  $\tilde{\nu}_{22'}$  mode.

## 7.4 Summary

Optimal control of the ground state dynamics in PDA by a stimulated Raman process in a computer-controlled feedback loop has been demonstrated. It has been shown that selective excitation of one vibrational ground state mode and suppression of all other modes is possible in a complex molecular system.

In a second experiment with higher temporal resolution, a further mode could be excited. The ultrafast beating of the modes up to  $523\text{ cm}^{-1}$  has been observed. Despite the increased complexity of the optimization problem, selectivity could be achieved for the excitation of single and combination modes.

With a special parameterization consisting of Gaussian amplitudes and polynomial phases, the algorithm could select the timing of the frequencies that dumped the population from the self-trapped exciton state to the ground state and achieved high selectivity in the excitation of ground state modes. Therefore, a Tannor-Rice scheme has been identified as one of the processes responsible for the mode-selective excitation.

The optimizations using a free parameterization for phases and amplitudes revealed further, unintuitive solutions which in combination with the dependence of the transients on the phase structure of the Stokes pulse suggest that a phase-sensitive control mechanism still exists.

Since the relative phase of the three normal modes can also be set, any desired superposition of normal modes can be produced. The excitation of local modes or the excitation along a reaction coordinate to open a specific reaction channel on the ground state potential surface should be therefore possible.

## 8

# Towards control of bimolecular reactions: Dynamics of the $\text{NaH}_2$ exciplex

One of the goals of coherent control studies is to guide a chemical reaction from the educt to the product state. Starting from the control of unimolecular reactions, as successfully performed in the previous chapter, the next step would be to control a simple bimolecular reaction. We chose a simple system with only few atoms that is accessible to theoretical treatment on a quantum mechanical level.

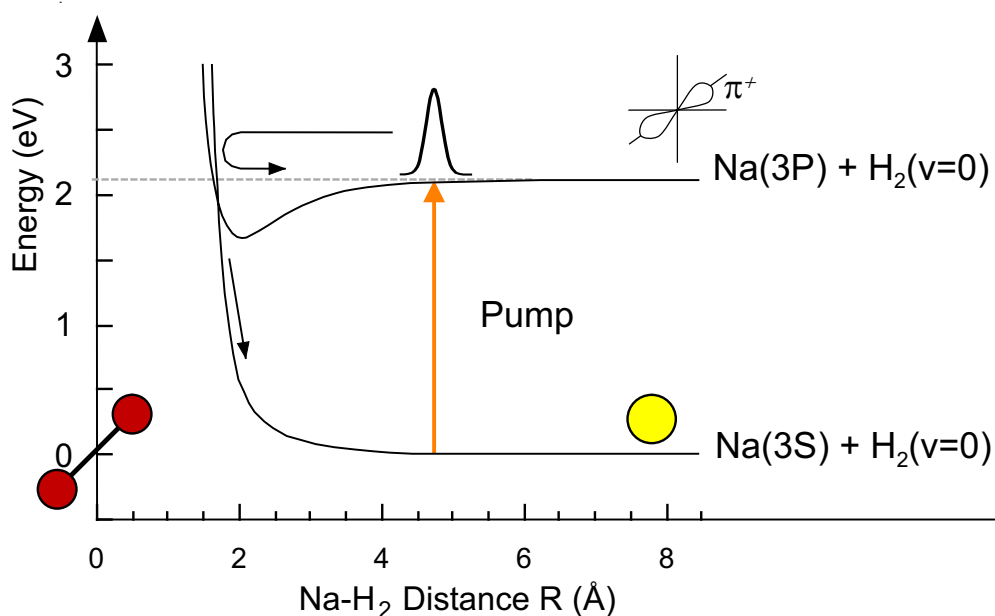


**Figure 8.1:** Scheme of the  $\text{NaH}_2$  ground state and first excited state (exciplex) PES in  $C_{2v}$  symmetry. The abscissa represents the distance  $R$  between the sodium atom and the center of mass of the  $\text{H}_2$  molecule. Upon excitation with a red-detuned fs laser pulse, a wave packet oscillates between the inner and outer turning points. A non-adiabatic crossing near the inner turning point couples the repulsive ground state and the bound excited state.

The  $\text{NaH}_2$  collision complex is advantageous for several reasons: (a) Collisions between Alkali atoms and molecules in the gas phase represent an important class of bimolecular reactions, namely photo induced reactions, and are well-studied ([156–162] and references therein). (b)

The non-adiabatic crossing takes place via a conical intersection, *vide infra*. (c) Since only three atoms are involved in this reaction, with  $H_2$  being the simplest conceivable molecule and sodium a hydrogen-like atom with only one outer shell electron, a theoretical simulation of the atom-molecule system with only three internal degrees of freedom is feasible [160, 163–169].

After excitation of the unbound ( $Na(3s)+H_2$ ) system with a red-detuned laser pulse, a bound collision complex ( $Na(3p)+H_2$ ) is formed (exciplex) with a well depth of 0.4 eV [159], due to the wave function overlap of the orbital of the  $H_2$  molecule and the lobes of the valence electron of the  $Na(3p)$  atom [168]. The population of the excited state is reflected at the inner turning point of the well in the bound PES and oscillates in the well of the excited state. A fraction of the population leaks to the ground state via a non-adiabatic crossing between these two states located near the inner turning point of the PES. The excess energy is transferred very effectively into rovibrational states of the  $H_2$  molecule. This process is called *quenching* and has been observed as early as 1911 [170, 171].

Figure 8.1 shows a cut through the ground ( $X^2A_1$ ) and first electronically excited ( $A^2B_2$ ) PES of the  $NaH_2$  collision system in  $C_{2v}$  symmetry. This symmetry gives the largest contribution for the quenching process as has been shown by Botschwina [168] and de Vivie-Riedle *et al.* [169]. A qualitative description based upon *ab-initio* calculations has been given by Botschwina [168] in the context of the "bond-stretch-attraction" model. To achieve a bound PES via the wave function overlap between the  $Na(3p)$  lobes and the  $H_2$  orbitals, the p-orbital must be aligned parallel to the  $H_2$  axis, whereas the remaining two p-orientations lead to repulsive PES. The energetic minimum of the crossing between excited and ground PES is achieved for a stretched  $H_2$  bond. A transition to the ground state PES causes a dissociation of the complex into  $Na(3p)$  and rovibrationally highly excited  $H_2$ . These results, as first deduced from qualitative considerations on static potential energy surfaces, could be confirmed by dynamical calculations [167, 172–179] and experiments [156].

The non-adiabatic crossing between the two PES in Fig. 8.1 has been shown to be a conical intersection [168]. The crossing point is energetically below the asymptote of the excited state [168, 169], which is consistent with the experimentally observed high efficiency of the quenching process [156]. The transition at the conical intersection is therefore ultrafast, and the lifetime of the exciplex is expected to be on the order of several hundred femtoseconds, which is supported by quantum-mechanical calculations [169, 175]. All studies on this system to date only employed

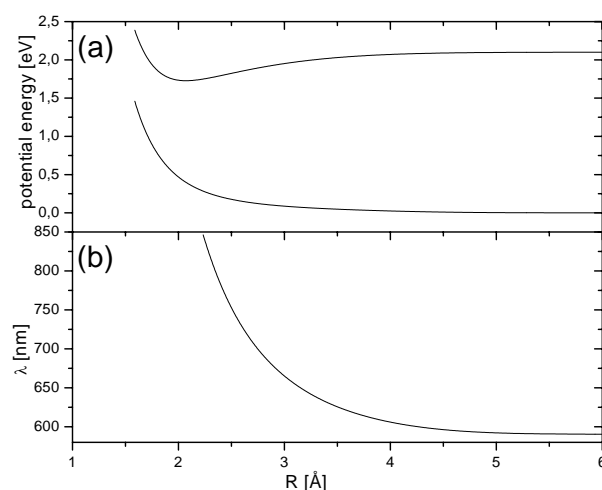


**Figure 8.2:** (a) Potential energy curves for  $Na(3S)H_2$  and  $Na(3P)H_2$  and (b) their difference potential in units of nm for the  $NaH_2$  complex for the H–H distance  $r$  fixed at the  $H_2$  equilibrium distance.

nanosecond time resolution. For example, the distribution of the rovibrational excitation of the  $H_2$  molecules after the collision has been extensively studied with ns CARS spectroscopy [159, 180–183]. Hertel *et al.* have investigated the collision complex in crossed beam experiments

[160, 184] and have demonstrated that the non-adiabatic crossing can be explained by energy transfer from electronic to rovibrational and translational energy.

However, none of these nanosecond experiments could verify the theoretically predicted ultrafast dynamics, hence the present investigation. In any ultrafast time-resolved experiment, the definition of the time zero, which corresponds here to the onset of the reaction, has to be defined properly. This is the main reason why femtosecond experiments on reaction dynamics have dealt only with unimolecular reactions and precursors so far. In this experiment, the onset of the reaction is defined by selection of an impact parameter with a laser pulse red-detuned from the Na-D line<sup>1</sup>. Only those collision partners are excited whose distance  $R$  equals the position on the PES at which the energy of the difference potential equals that of the exciting laser photons (Fig. 8.2b). Thus, the  $\text{NaH}_2$  distance which defines the time zero of the collision is exactly defined. This corresponds to a so-called photoassociation process which has been demonstrated so far only with the  $\text{Hg}_2$  system [185] with fs laser pulses.

As a first step towards control of the photoassociation [179], the goal of this experiment was the temporally resolved direct observation of the  $\text{NaH}_2$  collision complex. Several obstacles called for explicit attention regarding experimental constraints in order to ensure transients which could faithfully be traced back to the collision complex.

- The pulses have to be sufficiently short since recent quantum mechanical calculations by de Vivie-Riedle *et al.* suggested an oscillation period of the bound state of about 50-100fs [179].
- The absolute number of  $\text{NaH}_2$  complexes that are generated upon excitation along the direction of the  $R$  coordinate with a red-detuned laser pulse is given by the density of the Maxwell tail for high temperatures since only collision partners with sufficient thermal energy can approach the excitation window defined by the red-detuning of the laser pulse. Calculations reveal that this number reaches the lower limit of FWM detection schemes, which are the only feasible detection schemes, as will be discussed further.
- The sodium dimers, which show absorption in the same spectral range as the collision complex, have to be removed. This calls for a cell with a differential superheating since the ratio between  $[\text{Na}]$  and  $[\text{Na}_2]$  is dependent on the vapor pressure of the liquid sodium which, in turn, depends on the temperature of the reservoir. The local superheating of the observation zone is supposed to crack the dimers.
- In order to enhance the number of collision complexes, which is dependent on the pressure of both reactants, the buffer gas pressure must be raised, since an upper limit of  $[\text{Na}]$  is given by the maximal tolerable temperature in the cell. This calls for a high pressure cell.
- On the other hand, the sodium concentration has to be sufficiently low to avoid pulse propagation effects due to power broadening of the Na-D line. It should be kept in mind that the excitation occurs close to the transition of the Na-D line which features an oscillator strength close to 1.
- Hot Alkali metal vapors are highly reactive and attack most window materials. Only few transparent materials, such as Sapphire, can withstand these extreme conditions. Nevertheless, these materials cause severe problems with stray light and birefringence when used as windows since no high grade polishing is possible.

Aside from quenching, the laser-induced formation of  $\text{NaH}$  is also possible. This has been observed with  $\text{Na}(4p)+\text{H}_2$  for  $\text{H}_2$  in the ( $v = 0$ ) state [161, 162] as well as for the  $\text{Na}(3p)+\text{H}_2$  system if the  $\text{H}_2$  molecules possess sufficiently high vibrational energy [183]. Since the  $\text{NaH}_2$  system thus features both the reactive and the quenching channel, the question arises whether

<sup>1</sup>The  $D_1/D_2$  splitting is neglected here since a quantum beat between these lines appears on a ps time scale.

the branching ratio between these two channels can be controlled with a suitably modulated pump pulse. This experiment focuses on the observation of the dynamics of the quenching channel.

## 8.1 High pressure Alkali vapor cell

One of the major tasks in this experiment was to develop a cell with differential heating which could produce hot, reactive, dimer-free Alkali vapors at high buffer gas pressures. In collaboration with Hrvoje Skenderović and Goran Pichler from the Institut za Fisiku in Zagreb, Croatia, a twin tube heat pipe was developed.

The principle of a conventional heat pipe [186,187] is that the liquid Alkali metal is evaporated within a heated section and circulates by convection with a cooled part of the cell. A mesh acts as a wick which enhances the backflow of the liquid Alkali metal to the heated zone. Because of convection, the Alkali vapor does not approach the windows which are installed in the cooled region, and the problem of the reactivity of the Alkali vapors is solved, which enables the use of simple glass windows. Furthermore, since the windows are kept at room temperature, no intricate high temperature sealings are necessary. These standard spectroscopic heat pipes as investigated by Vidal [186] cannot be used in this experiment since the temperatures of the sodium reservoir and the observation zone are identical, which induces the  $\text{Na}_2$  problem, as discussed above. Operation of convection in heat pipes has only been reported for relatively low pressures, and it remains to be shown that it works as well for high buffer gas pressures.

There have been preliminary attempts to build a conventional heat pipe with a superheating zone by the group of Pichler. Differentially heated cells which produce dimer-free vapors in the superheated part are available as well. Again, operation of both cell types has been reported only with low pressures.

Superheating can be accomplished in two basic approaches. (a) The two-chamber principle uses a sodium reservoir which is connected to a separate superheated probe chamber. (b) The one-chamber approach features a small superheated region inside a heat pipe.

The cell development as described in [153] resulted in a new cell that follows the two-chamber approach and features a conventional heat pipe in the lower part (the reservoir) and a superheated zone in its upper part. The heat pipe design had been chosen for the reservoir because it prevents the formation of an oxide layer on the sodium surface which has been observed with simpler types of reservoirs. A drawing is provided in Fig. 8.3. As in the conventional heat pipe, cooled flanges are attached on both sides of the heating zone of each tube so that no hot Alkali vapor can reach the FS windows. The heated zones of both tubes are connected via a high-temperature tube which allows sodium transfer. Two additional, unheated connection tubes in the cooled regions support convection between upper and lower part. The cell has been designed and tested to withstand 40bar while cold and up to 25bar at 400 °C. To achieve these operation pressures, considerable attention had to be paid to the windows and their sealing. The required window thickness amounts to 15mm at a window diameter of 25mm and an accessible aperture of 18mm. Gold rings were used as sealing gaskets and proved to withstand both high pressures and high operation temperatures. During operation, a slight tarnish of the windows was observed which could be removed by additionally heating the windows to 150 °C and only slightly decreasing the maximal operation pressure of the cell.

Fig. 8.4 provides an absorption measurement in the upper and lower part of the cell. In the lower part, the dimer absorption bands are observed. The upper part is superheated and exhibits a structureless absorption. This shows that superheating, as desired, causes a reduction of dimer concentration. As will be explained later, buffer gas pressures above 5 bar lead to the formation of a refractive index gradient in the upper part which causes large beam deflections of the laser pulses.

It is important to determine the optimal cell operation parameters, such as buffer gas pressure and temperatures of the three tubes. The number of duty cycles of the cell is still quite low.

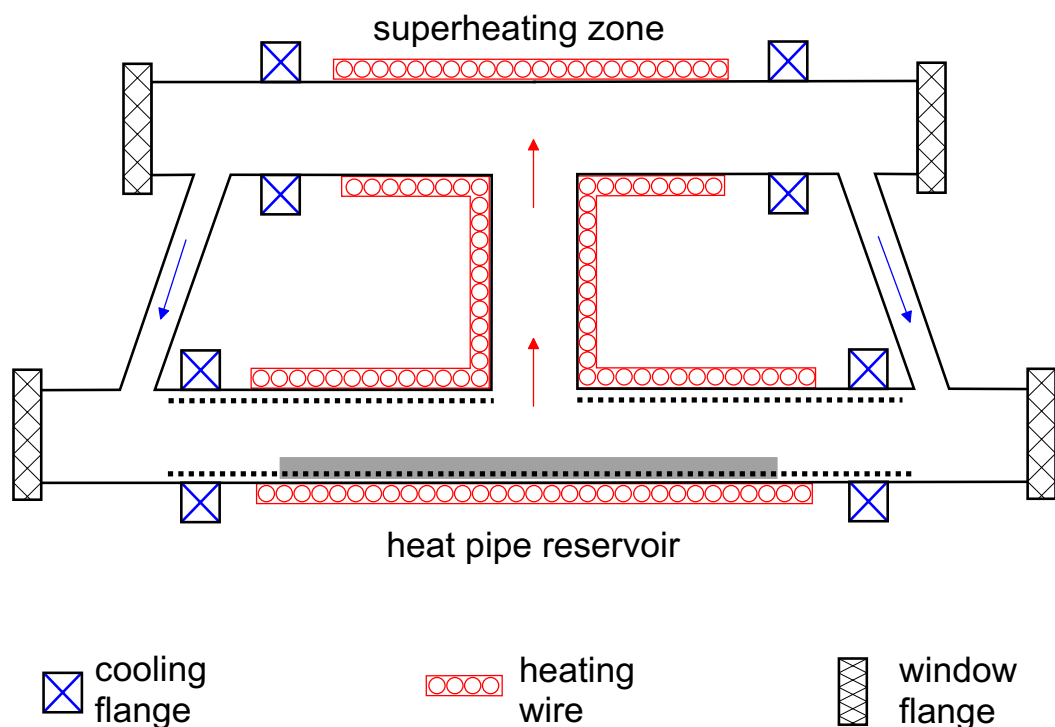


**Figure 8.3:** Sketch of the high pressure cell. The region between the two cooling flanges is heated with a heating wire in the upper and the lower tube, as well as the connecting tube. The window flanges are designed for quick exchange: The window is mounted with two gold rings in the window holder which is connected to the cell via a CF-40 flange. The thickness of the heat-resistant stainless steel (1-41-45) tubing wall is approximately 5mm. The overall length of the upper cell without windows flanges amounts to 260mm, that of the lower cell to 360mm. The distance between the upper and lower tube centers is approximately 120mm.

After a few hours of operation with pump pulses entering the cell, the formation of NaH crystals ("laser snow") was observed. These crystals can be removed several times after cooling down the cell, but after approximately five consecutive days of operation, the cell has to be thoroughly cleaned because the NaH formation completely occludes the upper tube.

## 8.2 Experiment

The fs pump pulses from a two-stage non-collinear OPA were detuned from the Na-D resonance to approximately 607nm with a FWHM of approximately 23nm. The output energy was  $\approx 5 \mu\text{J}$ . The amplified non-collinear OPA was preferred to a single stage version for this experiment since we observed that it produces more stable spectra and output energies. Residual spectral components at the Na-D resonance were intercepted by a beam block behind the second prism of the pulse compressor. This unit was adjusted to compensate for the chirp of the OPA output as well as the dispersion in the 15mm thick windows of the heat pipe. A pulse width of approximately 40 fs FWHM was obtained with an autocorrelator measurement, mainly due to the non-linear chirp in the thick windows. The autocorrelation has not been determined inside the cell, but rather with a spare window. Therefore, propagation effects inside the cell caused by the proximal sodium D-line have not been accounted for. In this first experiment, the adaptive pulse compression approach as described in chapter 5 was not employed, so as to avoid the intensity losses occurring at the shaper. In future experiments, the use of a shaper in the pump beam is mandatory, since not only can ultrashort pulses easily be delivered to the cell, but also feedback-controlled experiments to control the wave packet dynamics at the conical intersection are possible.



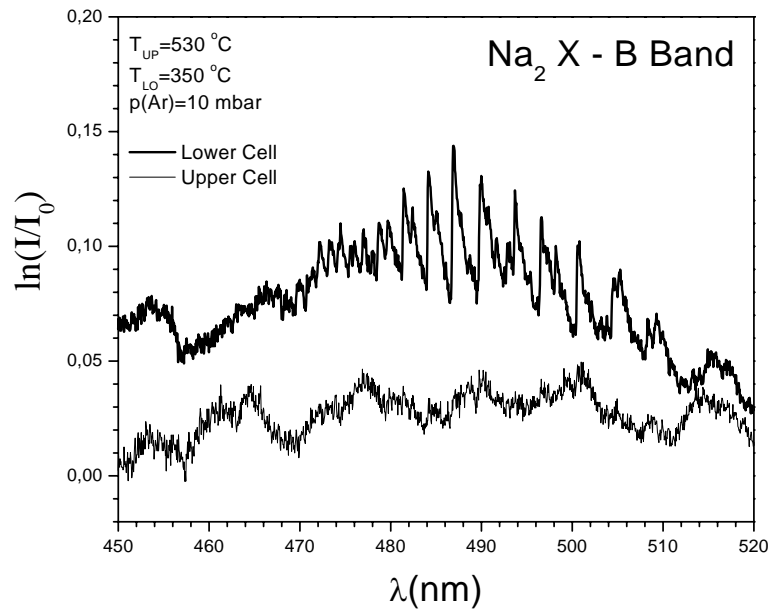


**Figure 8.4:** Absorption spectra of the double heat pipe in the lower part (thick line) and the upper, superheated part (thin line). The superheated upper part does not exhibit the  $\text{Na}_2$  absorption bands.

The detection of the wave packet dynamics in the excited state of the exciplex relies on near resonant DFWM at the  $\text{Na}(3p-6s)$  transition. This scheme has several advantages. We chose DFWM as proposed in [154] because all excited states of the exciplex are expected to cut across the ground state surface, leading to a short lifetime at high buffer gas pressures. Motzkus *et al.* [154] proposed the  $\text{Na}(3p-4d)$  transition wavelength for DFWM detection. The  $\text{Na}(3p-4d)$  has the advantage that the fundamental pulses of the Ti:Sa regenerative amplifier can be used in the DFWM scheme, which makes wavelength conversion unnecessary. Nevertheless, because the oscillation period of the exciplex was calculated to be below the pulse duration of our Ti:Sa fundamental pulses, a pulse shortening had to be performed in any case. We found that pulse shortening by a non-collinear OPA process is superior to spectral broadening in a hollow fiber inasmuch as it produces smooth spectra and pulses with a high contrast ratio. Finally, the  $\text{Na}(3p-6s)$  transition was chosen because the 6s level is energetically above the 5s level and therefore unaffected by the two-photon transitions from 3s to 5s induced by the pump pulses as discussed in chapter 6.

A LIF detection scheme would be much less complicated but nonetheless cannot be used, since it relies on spontaneous emission requiring an excited state lifetime of several ns. For higher buffer gas pressures, the quenching channel is much more probable than the LIF channel because of the high number of collisions; thus the LIF signal vanishes exactly at those cell conditions which support the appearance of an intense signal from the exciplex. Moreover, since LIF detection funnels all population from upper levels which can decay to the detected level, it is sensitive to multi-photon absorption of the pump as well, which is unfavorable.

The probe pulses have been produced with a second single stage non-collinear OPA which provides sufficient pulse energy. Again, great care was taken to obtain a smooth beam profile. Rather than being centered on the  $\text{Na}(3p-6s)$  transition, which corresponds to 515nm, its spectrum with a FWHM of 15nm was blue-detuned to approximately 507nm. The reason to do so is illustrated in Fig. 8.5. After excitation with a red-detuned pump pulse, the wave packet oscillates in the well. In order to observe the collision complex but not the free Na, the probe pulses must be detuned to match the transition between the  $\text{Na}(3P)\text{H}_2$  and the  $\text{Na}(6S)\text{H}_2$  exciplex states at the outer turning point of the wave packet. A small amount of spectral intensity at the  $\text{Na}(3p-6s)$  resonance was left to facilitate the detection of signal in the first run of the experiment. To compensate for the 15mm FS cell windows, the probe pulses have also been

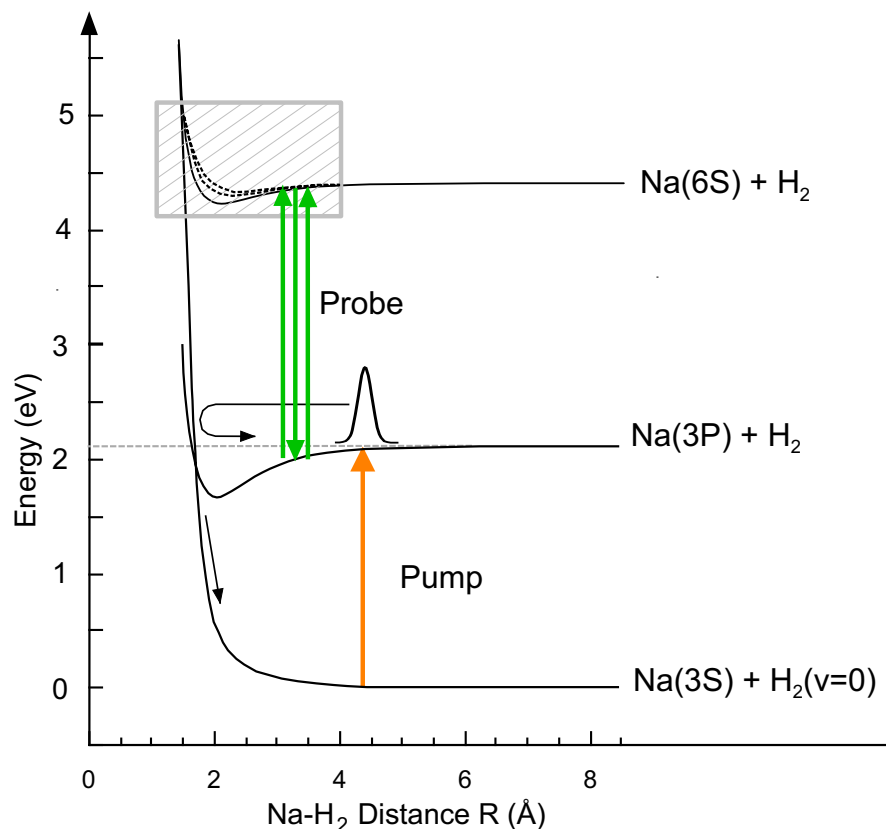


**Figure 8.5:** Near-resonant DFWM detection scheme based upon the  $\text{Na}(3\text{P}-6\text{S})\text{H}_2$  transition. The potential energy surfaces in the region of the dashed box are not precisely known. The potential of the  $\text{Na}(6\text{S})\text{H}_2$  exciplex is expected to be bound with a smaller well depth ( $< 0.1\text{eV}$ ) than the  $\text{Na}(3\text{P})\text{H}_2$  exciplex [188, 189]. Therefore, the DFWM wavelength has to be blue-detuned from the  $\text{Na}(3\text{p}-6\text{s})$  transition.

compressed with a FS prism compressor. Nevertheless, presumably due to the greater dispersion at lower wavelengths, pulse lengths of 40fs to 50fs FWHM as measured by autocorrelation have been obtained. Without the FS windows, the DFWM pulses could be compressed down to approximately 40fs. Pump and probe pulse spectra are sketched in Fig. 8.7.

The experimental setup is basically the same as in the 30fs CARS experiments on PDA (see section 7 and Fig. 8.6 in this chapter). The only difference is that one color (the probe pulse) is split into three sub-pulses of equal energy rather than into two as in the CARS experiments. Compensation plates for the beam splitters are inserted in all three arms of the DFWM setup such that every beam passes the same amount of dispersive material, thus eliminating the need for three separate prism compressors. The pump pulse is guided through the center of the DFWM pulse arrangement, as depicted in Fig. 8.6. All four beams are focused into the high pressure heat pipe described in section 8.1. The DFWM signal emerges separate from all other beams, as depicted in Fig. 8.6. It is spatially filtered, routed along a path of approximately 10m to further reduce stray light, spectrally filtered in a 30cm monochromator and recorded by a cooled photomultiplier tube. The PMT signal is recorded by an A/D converter. Since the registered signal contains contributions not only from the near-resonant DFWM signal of the  $\text{Na}(3\text{P}-6\text{S})\text{H}_2$  transition, but also from the non-resonant background of the sodium atoms and the  $\text{H}_2$  molecules in the cell, a chopper synchronized to the fs laser is installed in the pump beam. The chopping frequency is chosen such that every other pump pulse may pass. Two consecutive laser pulses are binned to form one event, and for every event the signal without pump pulse is subtracted from the signal with pump pulse. The differences of a number of events (usually 100) are then averaged for each delay. This scheme assures proper subtraction of the background signal since the pulse-to-pulse stability of the pump and probe sources is better

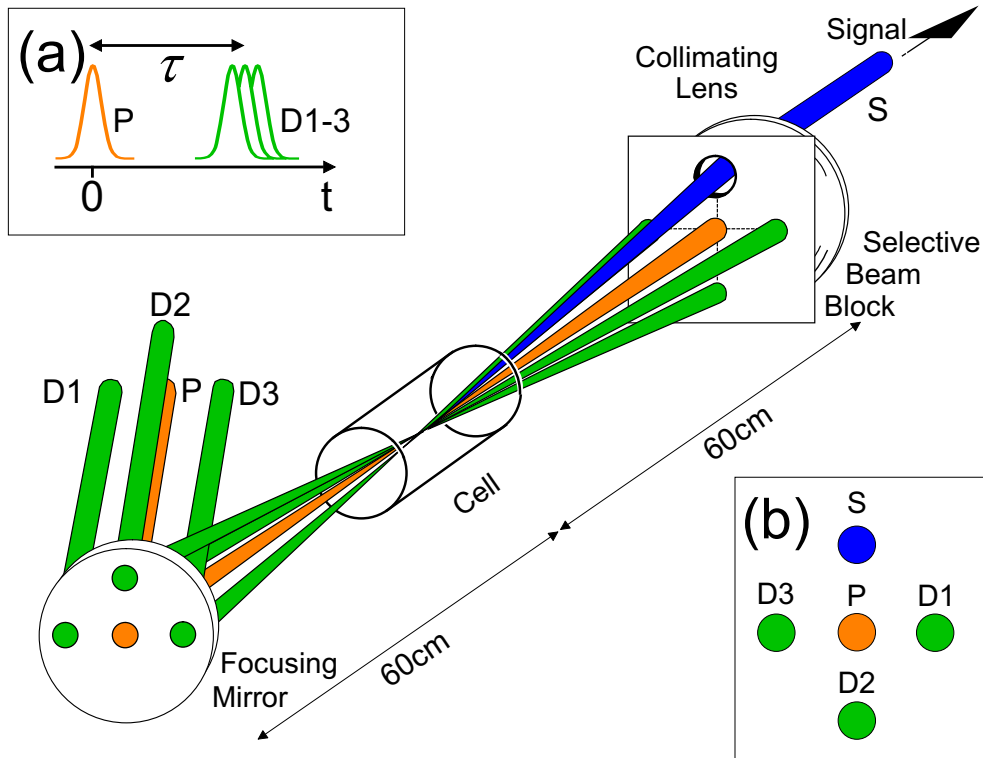


**Figure 8.6:** Schematic setup of the pump-DFWM experiment. (a) Timing of the pump pulse and the three concurrent probe pulses with definition of delay  $\tau$ . (b) Pattern of the pulses at the position of the beam block.

than the long-term stability.

A first transient measured with the new cell and the above-described setup is shown in Fig. 8.8. The buffer gas pressure was slightly below one bar. A coherence spike near  $t = 0$  is visible which is expected to originate from residual spectral intensity on the Na(3s-3p) and the Na(3p-6s) resonances, causing a resonance-enhanced multi-photon transition. The FWHM of the coherence spike is approximately 40fs. No oscillations are visible: only a stepwise decrease of the signal can be ascertained. The noise originates from the high background signal and could only be detected with the above-described chopper technique since the signal-to-background ratio is worse than 1:10.

More experiments have been performed with higher buffer gas pressures (up to 25bar). Under these conditions, the cell still produces dimer-free sodium vapor. Nevertheless, horizontal layers with different refractive indices were observed, forming a "gas lens" at high temperatures and pressures which caused a large beam deflection downwards. Under these conditions, no DFWM signal could be observed, since no spatial overlap of the focused beams could be assured, and even if the beams met at the focus, the DFWM signal would point in an unpredictable direction. This effect is caused by the buffer gas, and it vanishes immediately once the temperature approaches room temperature. The origin of this effect is still not clear and is the subject of current investigations. For higher temperatures at lower pressures ( $\sim 5$  bar), the high sodium vapor pressure and long sodium vapor zone led to further problematic pulse propagation effects.

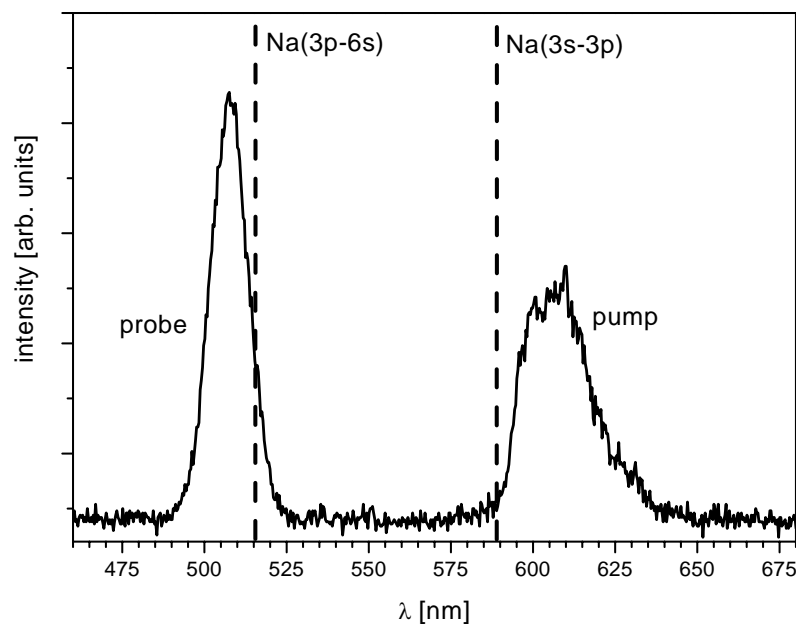


**Figure 8.7:** Spectra of pump and probe pulses, as recorded simultaneously at the location of the focus. The  $\text{Na}(3s-3p)$  and  $\text{Na}(3p-6s)$  resonances are marked by two vertical lines.

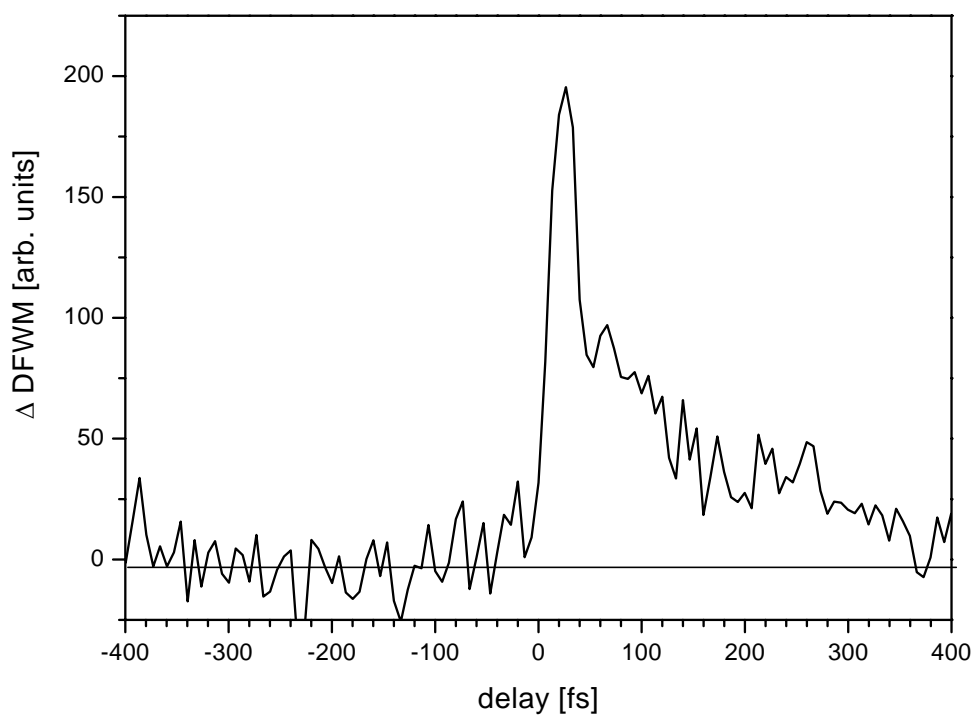


**Figure 8.8:** Transient recorded at  $< 1\text{ bar H}_2$  buffer gas pressure,  $T_{\text{lower}} = 400^\circ\text{C}$ ,  $T_{\text{middle}} = 450^\circ\text{C}$ ,  $T_{\text{upper}} = 450^\circ\text{C}$ . The window flanges were heated to  $150^\circ\text{C}$  in order to prevent sodium desorption on the FS windows. 50 scans have been averaged, and each point of each scan was averaged over 100 single measurements.

### 8.3 Discussion

The transient obtained in the above experiment in all likelihood represents real-time observation of the exciplex, since the observed transient exhibits the expected feature of an ultrafast decay of the  $\text{Na}(3\text{P})\text{H}_2$  population. Moreover, the temporal features of the transient are close to those predicted by theory [179, 190], as shown in Fig. 8.9. Both in experiment and theory, the  $\text{Na}(3\text{P})\text{H}_2$  population decays within roughly 300fs. It should be noted that assignment of the transient in Fig. 8.8 to the exciplex lacks direct proof, though we consider it highly likely because all parameters and experimental considerations known to date (see list at the beginning of this chapter) have been set correctly.

Further experiments are necessary to verify that the  $\text{NaH}_2$  collision complex has been indeed observed. These include experiments with different buffer gases that are not expected to form an exciplex, and measurements with chirped pump pulses which should influence the wave packet dynamics [191]. A further optimization of the cell parameters, more stable OPA outputs, a low-noise PMT detector and lock-in detection should all enhance the signal-to-noise ratio.

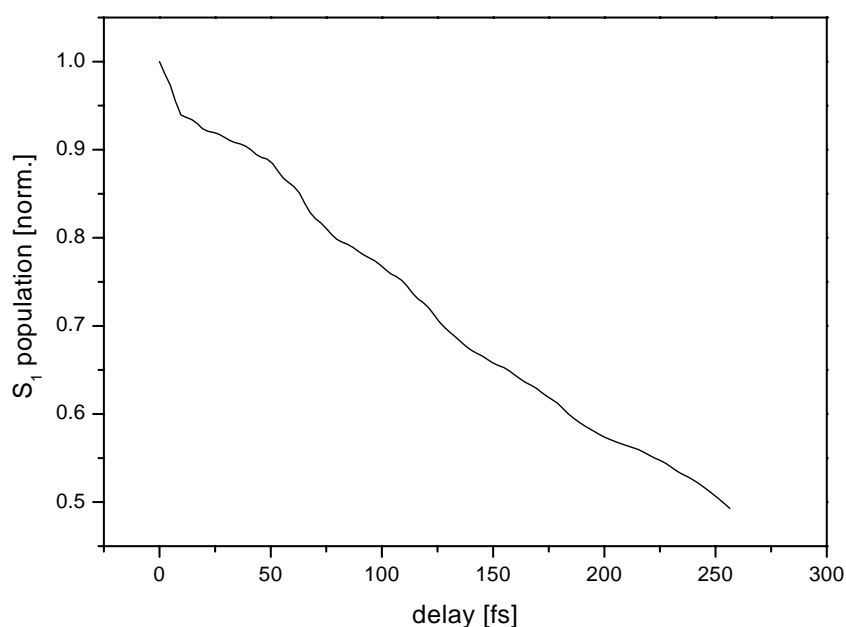


**Figure 8.9:** Three-dimensional propagation of a Gaussian wave packet on the  $S_1$  PES (equivalent to the  $\text{Na}(3\text{p})+\text{H}_2$  PES). The initial wave packet has been placed at  $R=1.88 \text{ \AA}$  (conical intersection),  $r=0.794 \text{ \AA}$  (equilibrium distance),  $r$  being the H-H distance. From [190].

If the observation of the temporal dynamics of the exciplex can be verified, the next step would be to control the wavepacket dynamics at the conical intersection. Further control experiments could entail manipulation of the rovibrational population distribution of the  $\text{H}_2$  molecule after the collision, which could be detected by ns CARS [156, 159, 180], or opening the  $\text{NaH}$  formation channel. It should be noted that this (reactive) channel has already been observed in the above experiments ("laser snow") [181, 182, 192, 193].

The door to control experiments on the  $\text{NaH}_2$  exciplex, as already described theoretically, is very nearly open. The control of a prototypical bimolecular reaction seems now to be within reach.

# Summary and outlook

This work deals with the fundamentals of feedback-controlled shaping of ultrashort laser pulses with respect to both the establishment of its technical prerequisites and the application to suitable model systems. The feedback loop has been tested using a simple optimization experiment with known outcome; then it was applied to experiments of progressively increasing complexity. From the optimized pulses, physical insight into the optimization process has been gained.

In the first part of this work, the implementation of the required technology has been detailed such that control experiments might employ it as a standard tool. One of the technical prerequisites was the frequency conversion of the 800 nm Ti:Sa laser pulses to a wavelength range suited to the particular systems. To this end, non-collinear optical parametric amplifiers have been built in different designs that routinely produce tunable sub-20 fs pulses in the visible. The characterization techniques for ultrashort pulses have been implemented as well.

Pulse shapers with cylindrical instead of spherical mirrors have been implemented for the modulation of broadband pulses, and their functionality has been explained both theoretically and experimentally. A new liquid crystal device, the core of our pulse shapers, has been developed in cooperation with the group of Thomas Feurer at the Universität Jena and the Jenoptik GmbH which allows for the generation of more complex pulse shapes than with other commercially available devices to date.

Using a pulse shaper to modulate the white light continuum that serves as the seed for the non-collinear optical parametric amplifier, generation of phase-locked two-color double pulses has been achieved, with tunable wavelengths, delays, and relative carrier phases between the single pulses. The basic principle, phase conservation during optical parametric amplification, has been demonstrated. With this setup, control experiments which require pulses with the above described attributes in electronically controllable form are possible for the first time.

An evolutionary strategy used as the optimization algorithm in the feedback loop has been programmed and characterized both in simulation and experiment using a simple optimization experiment, namely pulse recompression by phase compensation.

In the second part of this work, pulse recompression of ultra-broadband spectra in the sub-20fs regime serves as an example of utility of feedback-controlled optimization. This experiment simultaneously served as a further test of the feedback loop in the limit of a physically unreachable optimization goal.

It has been demonstrated that a suitable parameterization of the electric field, implemented by a mapping of the optimization parameters adjusted by the algorithm to the physical parameters controlling the liquid crystal mask affords a means of acquiring physical knowledge from the retrieved optimal electric fields. A parameterization helps to dissect the physical processes mediating the control process, thereby assuring fast, secure convergence and robustness against signal noise.

So-called "bright" and "dark" pulses, i.e. pulses that are absorbed by a medium or transmitted, respectively, have been demonstrated for the case of the two-photon transition  $\text{Na}(3s \rightarrow 5s)$ . The physical constraints responsible for pulses being either "bright" or "dark", namely a symmetric or anti-symmetric spectral phase, have been incorporated in the parameterization with the purpose of testing the concept of parameterization for such studies.

An example of mode-selective preparation of vibrational states in a polyatomic molecule is the control of the ground state dynamics in polydiacetylene. In a Raman step with a shaped Stokes pulse, the population of the backbone vibrations of polydiacetylene in its ground state could be controlled. A consecutive probe pulse in a CARS (coherent anti-Stokes Raman scattering) arrangement generates an anti-Stokes signal which, once frequency-resolved, served as feedback. Of the three or four modes, respectively, accessible within the pulse bandwidth, single modes as well as combinations of modes could be excited with high selectivity. Again, suitable parameterizations helped to identify one of the processes responsible for the control as a Tannor-Rice scheme. Since both the amplitude and the phase of each mode could be influenced, the focusing of a wave packet at a predefined time, or, equivalently, the generation of local modes represents the control of a unimolecular reaction.

Starting from the control of a unimolecular reaction, the possibilities of controlling a bimolecular reaction were addressed. The  $\text{NaH}_2$  collision complex was chosen as a suitable system for the control of bimolecular reactions generally and a conical intersection in particular. First time-resolved experiments have been presented.

First time-resolved experiments have been presented in a pump-DFWM experiment with  $\approx 50\text{fs}$  temporal resolution. The obtained transient strongly supports the real-time observation of the exciplex, since the temporal features of the transient are close to that predicted from theory [179].

In the near future, several experimental results of this work call for further investigation:

The development and testing of the optimization routines will, of course, never reach a steady state condition. Several modifications are envisioned in the near future, such as the development of a front end interface that automatically sets the internal parameters, so that users need not be concerned with internal parameters of the algorithm. A meaningful modularization of the optimization algorithm should result in a program package in which the user has only to provide a parameterization of the electric field and a routine for the feedback signal. An algorithm that autonomously tests different parameterizations and chooses the most appropriate one is envisioned.

The successful demonstration of phase-locked pulses with different colors calls for an experiment which exploits the specific properties of such pulse structures. An experiment following the Tannor-Rice scheme seems appropriate in this context. Moreover, the implementation of qubits in iodine within a CARS experiment has been suggested [194] and seems to be a promising experiment for the use of phase-locked multi-colour pulses.

As an extension to the control of two-photon transition in an atomic system, experiments with laser pulses which give rise to light-induced transparency, as well as lasing without inversion should be possible for complex multi-level systems. The feedback approach also offers the possibility of suppressing unwanted competitive multi-photon absorptions while a specific transition is excited.

In the control of ground state vibrations of polydiacetylene, a fit of the transients using the model of T. Chen [155] must be performed in order to obtain information about the relative phases of the normal modes in a more accurate way. The dependence of these relative phases on the Stokes pulse should then offer information on how the phase of the Stokes pulse must be chosen to focus the wave packet dynamics into a specific local mode at a predefined time.

If the observation of the temporal dynamics of the  $\text{NaH}_2$  exciplex can be verified in a forthcoming experiment, the next step would be to use shaped pulses for the excitation. Numerical simulations revealed a strong dependence of the efficiency of the transition at the crossing on the shape of the wave packet at the conical intersection [179, 190]. Since the shape of the wave packet at this location is given by the properties of the pump pulse, control of the wave packet dynamics at the conical intersection appears to be feasible. With suitably modulated excitation pulses, the reactive channel  $(\text{NaH}_2)^* \longrightarrow \text{NaH} + \text{H}$  should be accessible. Detection of NaH formation is possible using a narrowband CARS or DFWM setup [192, 193].

In the longer term, the control of a photochemical reaction represents a promising experiment. The dynamics of cyclic polyenes is well-studied both experimentally [195, 196] and theoretically [191, 197–199]. The ring opening has been shown to proceed on an ultrafast time scale and to take place via conical intersections between the excited and ground potential energy surface. A compelling experiment should therefore employ feedback control in an attempt to influence the branching ratio of ring opening to relaxation back to the ground state closed ring using modulated excitation pulses.



## Appendix A

# The Titanium:Sapphire laser system

The core of all experiments in this thesis is the femtosecond Titanium-Sapphire regenerative laser system (CPA-1000) supplied by Clark MXR (Fig. A.1). Since it has been described in great detail in [153], only the main features of the system are summarized. The coherent

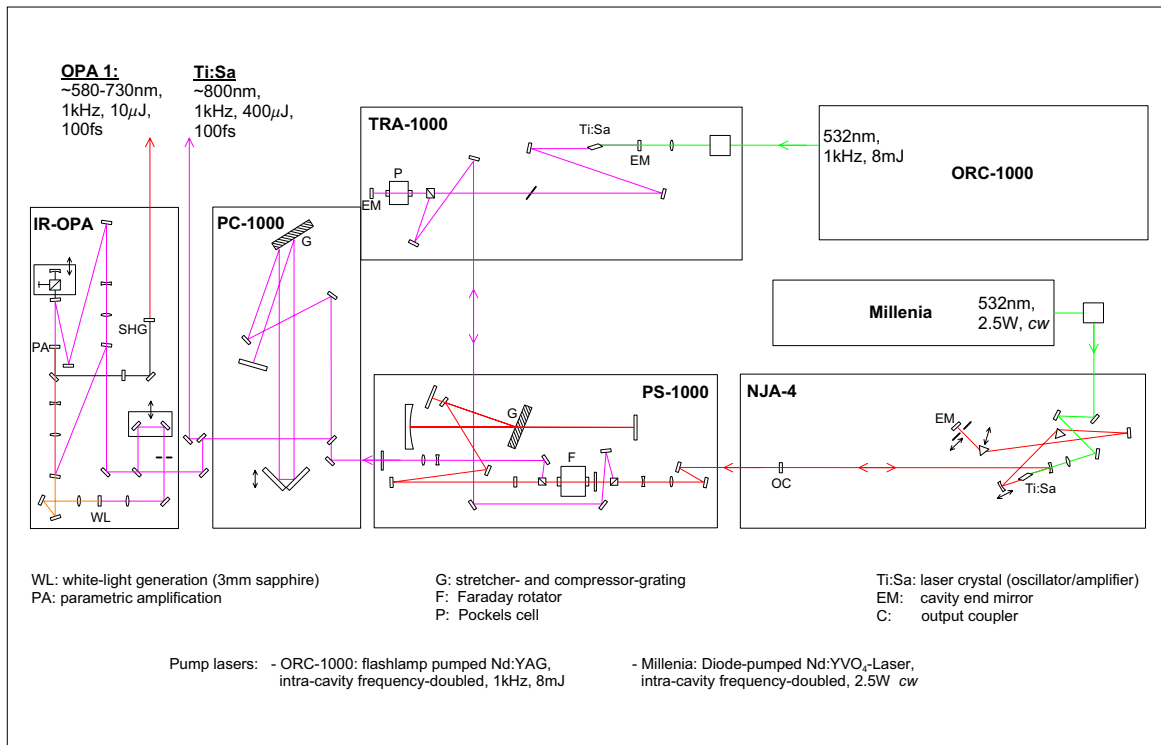


**Figure A.1:** Setup of the Ti:Sapphire laser system. Only one of the two OPAs is shown, the missing one is pumped with the residual 400 $\mu$ J. With friendly permission by Tobias Lang.

broadband spectra are produced in the Kerr-lens mode-locked Ti:Sapphire oscillator (NJA-4) which is pumped by a diode-pumped intra-cavity doubled Nd:YVO<sub>4</sub> laser (Millenia). The oscillator emits pulses at an energy of about 3nJ and a repetition rate of approximately 80MHz. Their central wavelength is typically 810nm. The pulses are stretched in the grating stretcher unit (PS-1000) and then coupled into the regenerative amplifier (TRA-1000). This stage is basically a Ti:Sapphire laser cavity which is pumped by a flashlamp-pumped intra-cavity doubled Nd:YAG laser (ORC-1000) delivering 7mJ pulses at a repetition rate of 1kHz. The stretched oscillator pulses are amplified to approximately 1.6mJ. Recompression (PC-1000) down to approximately 100fs FWHM leaves an output energy of 800 $\mu$ J.

Wavelengths other than the Ti:Sapphire fundamental are obtained from two independent collinear two-stage OPA units, of which only one is shown in Fig. A.1. Alternatively, up to three non-collinear OPAs as described in section 1 can be pumped by the fundamental Ti:Sapphire pulses.

## Appendix B

# Characterization of ultrashort pulses

The characterization of shaped ultrashort pulses is an important prerequisite for the adjustment of a pulse shaper and the generation of faithfully shaped pulses. In this section, the basic principles of pulse characterization are presented. It follows the review article by Trebino *et al.* [200]; for more detailed information, the reader is referred to this publication.

### Mathematical description of ultrashort pulses

Laser pulses are defined by their electric field  $E(t)$ . The field is regarded as linearly polarized, and therefore only its scalar component is considered. If the electric field can be separated into a product of spatial and temporal factors, the time-dependent component of the pulse can be written as:

$$E(t) = \text{Re} \{ A(t) \exp [i (\omega_0 t - \phi(t))] \} \quad (\text{B.1})$$

where  $A(t) = I(t)^{1/2}$  and  $\phi(t)$  are the envelope and time-dependent phase of the pulse,  $\omega_0$  is the carrier frequency, and  $I(t)$  the time-dependent intensity. The time-dependent phase contains the frequency versus time information. The instantaneous frequency of the pulse,  $\omega(t)$ , is given by

$$\omega(t) = \omega_0 - \frac{\partial \phi}{\partial t}. \quad (\text{B.2})$$

Thus, a constant-phase pulse shows no frequency variation in time. Linear variation of  $\phi$  in time simply corresponds to a frequency shift. Quadratic variation of  $\phi$  in time represents a linear ramp of frequency versus time. Pulses with increasing (or decreasing) frequency versus time are said to be positively (or negatively) chirped. If the phase function is quadratic, the chirp is said to be linear. Higher-order phase functions are termed "nonlinear chirp". The field can also be expressed in the frequency domain<sup>1</sup>:

$$\tilde{E}(\omega) = \tilde{A}(\omega - \omega_0) \exp [i \tilde{\phi}(\omega - \omega_0)], \quad (\text{B.3})$$

where  $\tilde{E}(\omega)$  is the Fourier transform of  $E(t)$ .  $\tilde{I}(\omega - \omega_0)$  is the spectrum,  $\tilde{A}(\omega - \omega_0) = \tilde{I}(\omega - \omega_0)^{1/2}$ , and  $\tilde{\phi}(\omega - \omega_0)$  is the spectral phase. The spectral phase contains time versus frequency information. The group delay versus frequency,  $\tilde{t}(\omega) \neq \omega(t)^{-1}$ , is defined by

$$\tilde{t}(\omega) = \frac{\partial \tilde{\phi}}{\partial \omega}. \quad (\text{B.4})$$

As in the time domain, a frequency-domain constant-phase pulse experiences no frequency variation with time. Linear variation of  $\tilde{\phi}(\omega - \omega_0)$  with frequency is simply a shift in time, that

---

<sup>1</sup>In this expression, the negative-frequency terms arising from the Fourier transformation are neglected. See [201].

is, a delay. Quadratic variation of  $\tilde{\phi}(\omega - \omega_0)$  with frequency represents a linear ramp of group delay versus frequency and corresponds to a linearly chirped pulse. As in the time domain, higher-order terms imply nonlinear chirp.

In order to completely characterize  $E(t)$  or  $\tilde{E}(\omega)$ , respectively, it is necessary to measure both the intensity and phase, either in the frequency or the time domain.

## B.1 Autocorrelation

The most commonly used device for time-domain characterization of ultrashort pulses is the autocorrelator [202–204] which, since no shorter event is available, uses the pulse to measure itself. Figure B.1 shows a schematic setup.

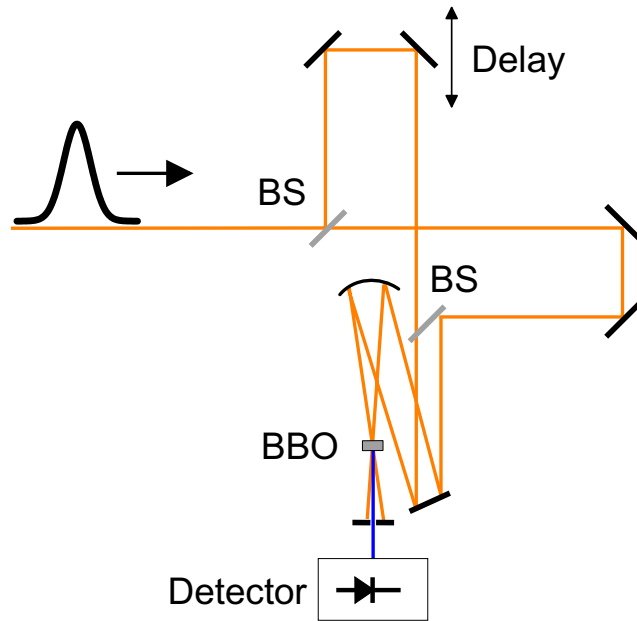


**Figure B.1:** Setup of a non-collinear SHG autocorrelator. The input pulse is split with a metallic beamsplitter into two replica of equal energy. These are focused onto a  $10\mu\text{m}$  BBO crystal. The wave vector of the signal,  $\vec{k}_{sig}^{2\omega}$ , is determined by the conservation of momentum  $\vec{k}_{sig}^{2\omega} = \vec{k}_1^\omega + \vec{k}_2^\omega$ . Signal is produced if and only if the pulses overlap. Thus, the autocorrelator signal is background-free.

Autocorrelation entails the superposition of a pulse with its adjustably delayed replica in some instantaneously responding nonlinear-optical medium, such as a SHG crystal. The instantaneous magnitude of the SHG signal is proportional to the product of the instantaneous intensities of the two input pulses. A detector measures the temporally integrated SHG intensities. The SHG autocorrelator signal in a non-collinear arrangement as depicted in Fig. B.1 can thus be written as

$$A(\tau) = \int_{-\infty}^{\infty} I(t)I(t - \tau)dt, \quad (\text{B.5})$$

where  $\tau$  is the relative delay between the pulses. Other types of nonlinearity can be used, as well, such as THG or optical Kerr effect [205]. Using different types of nonlinearities, autocorrelation measurements can be performed in a wavelength range from the UV (using, e.g. Kerr effect) to the IR.

The main advantages of SHG autocorrelation are sensitivity, since it involves only a second-order nonlinearity, while third-order optical nonlinearities are much weaker, and the simple setup.

The main disadvantage is that, unlike third-order autocorrelation, the SHG autocorrelation trace is symmetrical with respect to delay, and, as a result, it has an ambiguity in the direction of time. The pulse,  $E(t)$ , and its time-reversed replica,  $E(-t)$ , both yield the same autocorrelation trace. Autocorrelation measurements yield a smeared out version of  $I(t)$ , and it often hides structure. In order to merely obtain the pulse duration, an educated guess must be made for a pulse shape, yielding a multiplicative factor that relates the autocorrelation FWHM to that of the pulse itself. This factor varies significantly for different common pulse shapes, such as  $\text{sech}^2(t)$ , which yields a large multiplicative factor and hence a shorter pulse length for a given measured autocorrelation width compared to other assumptions, as for example a Gaussian pulse [201]. Moreover, even when the spectrum or another quantity, such as the interferometric autocorrelation [201], is also measured, there is not sufficient information to completely characterize the pulse. Finally, systematic error can be present in the measured autocorrelation, e.g. misalignment effects that can introduce distortions, and it is difficult to know when the measured autocorrelation is free of such effects. One of the most common sources of error is a insufficient phasematching bandwidth of the SHG crystal. This is discussed in the SHG FROG section.

## B.2 Cross-correlation

Cross-correlation is also based on the spatiotemporal overlap of two pulses in a nonlinear medium, but the second pulse which serves as reference pulse is no longer a replica of the pulse to be characterized. As previously, any physical process which depends on the product of the intensity of the reference ("gate") pulse and the pulse to be characterized ("probe"), can be exploited. In analogy to Eq. B.5, the cross-correlation signal can be expressed as

$$C(\tau) = \int_{-\infty}^{\infty} I_p(t)I_g(t - \tau)dt, \quad (\text{B.6})$$

where  $I_p(t)$  represents the temporal evolution of the probe pulse and  $I_g(t)$  that of the gate pulse. Provided  $I_g(t)$  is known,  $I_p(t)$  can be determined by deconvolution. If both pulses can be written as Gaussian pulses with duration  $\tau_p$  and  $\tau_g$ , respectively, the cross-correlation can also be described as a Gaussian pulse with duration  $\tau_c$ . With  $\tau_c$  and  $\tau_g$  known,  $\tau_p$  can be calculated by solving Eq. B.6 for  $\tau_p$  and is given by  $\tau_p = \sqrt{\tau_c^2 - \tau_g^2}$ .

Cross-correlation measurements feature a number of advantages over autocorrelation measurements. First, cross-correlation can be used to determine very weak signals since the gate pulse can be used for amplification. Second, the wavelength range of the cross-correlation signal can be shifted to a region where detection is convenient. This is used quite commonly in the characterization of IR or UV pulses via the use of SFG or DFG. Third, no time-reversal ambiguity exists since gate and probe pulse can be well distinguished. In pump-probe experiments, cross-correlation measurements are often the only way of determining the pulse properties at the location of the sample (e.g. inside a cell) by observing the signal of a non-resonant material instead of the sample under investigation.

Nevertheless, cross-correlation also features several drawbacks, one of the largest of which is that the temporal delay zero between gate and probe pulse has to be maintained for the measurement. Another drawback is that the gate pulse has to be characterized very faithfully in order to obtain true information on the probe pulse.

## B.3 Frequency-resolved optical gating

Techniques for a full characterization of ultrashort pulses operate in the "time-frequency domain" [206, 207]. Measurements in this domain involve both temporal resolution and frequency resolution simultaneously. Basically, this involves two consecutive steps: the application of a

gate function which slices out a defined part of the pulse temporally and thereby creates the temporal information on the pulse, and a frequency gate which produces the spectral information. Scanning all delays and frequencies, a so-called *spectrogram* is obtained, which is the description of a pulse in the time-frequency domain and can be expressed as

$$S(\omega, \tau) = \left| \int_{-\infty}^{\infty} E(t)g(t - \tau) \exp(-i\omega t) dt \right|^2 \quad (\text{B.7})$$

where  $g(t - \tau)$  is a variable-delay gate function. Knowledge of the spectrogram is essentially sufficient to completely determine  $E(t)$  [49,51] except for an absolute phase factor. The first step of FROG [208,208–212] involves measuring the spectrogram of the pulse; the second is the reconstruction of  $I(t)$  and  $\phi(t)$  from the spectrogram.

Unlike other ultrashort-pulse-measurement methods, FROG needs no *a priori* assumptions about the pulse. Even the assumption of a nearly instantaneous response of the nonlinear medium has been shown to be unnecessary, as this can be included in the algorithm [213]. Similarly, any known systematic error in the measurement may also be modeled in the algorithm [214] although this is not generally necessary, except for extremely short pulses ( $< 10$  fs).

FROG uses the time domain to obtain long-time resolution and the frequency domain for short-time resolution. Consequently, if the full pulse spectrogram is entirely contained within the measured trace, there can be no other long-time pulse structure (since the spectrogram is essentially zero for off-scale delays), nor any additional short-time pulse structure (since the spectrogram is essentially zero for off-scale frequency offsets).

Another useful and important feature of FROG is that it provides feedback regarding the validity of the measurement data. FROG actually contains two different types of feedback. The first results from the fact that the FROG trace is a time-frequency plot, that is, an  $N \times N$  array of points, which are then used to determine  $N$  intensity points and  $N$  phase points. Pulse intensity and phase are thus significantly overdetermined, and it is highly unlikely that a trace composed of randomly generated points corresponds to an actual pulse. Similarly, a measured trace that has been contaminated by systematic error is unlikely to correspond to an actual pulse. Thus, convergence of the FROG algorithm to a pulse whose trace agrees well with the measured trace virtually assures that the measured trace is free of systematic error. Conversely, non-convergence of the FROG algorithm indicates the presence of systematic error.

Another feedback mechanism in FROG is deterministic and has proven extremely effective in revealing systematic error in SHG FROG measurements of 10 fs pulses, where crystal phase-matching bandwidths are insufficient to cope with the bandwidths of the pulses to be measured. It involves computing the "marginals" of the FROG trace, that is, integrals of the trace with respect to delay or frequency. The marginals can be compared to the independently measured spectrum or autocorrelation, and expressions have been derived relating these quantities. The marginals can furthermore be used to correct an erroneous trace [208,214].

In principle, any autocorrelation measurement in which the autocorrelator signal beam is spectrally resolved is a FROG measurement. Depending on the type of nonlinearity which is used to perform the temporal gating, several types of FROG exist. Out of the approximately five different FROG setups which are common today [200], only two, SHG FROG and TG FROG will be described.

### Second-harmonic-generation FROG

If the signal pulse in a SHG-based autocorrelator is spectrally resolved, the result is the SH spectrogram, also referred to as the "SHG FROG trace":

$$I_{\text{FROG}}^{\text{SHG}}(\omega, \tau) = \left| \int_{-\infty}^{\infty} E(t)E(t - \tau) \exp(-i\omega t) dt \right|^2 \quad (\text{B.8})$$

SHG FROG [208, 209, 211, 215–217] is only slightly less sensitive than an autocorrelator. The main disadvantages of SHG FROG are again that the SHG FROG trace is symmetrical with respect to delay. This ambiguity can easily be removed in a number of ways. One may, for example, perform another SHG FROG measurement of the pulse after it has been distorted in some known manner, e.g. by placing a piece of glass in the beam which introduces chirp. Only one of the two possible pulses is consistent with both measurements.

A further class of ambiguities exists in SHG FROG though they rarely appear in practical measurements. If the pulse consists of two (or more) well separated pulses, then their relative phase has an ambiguity. Specifically, the relative phases  $\phi$  and  $\phi + \pi$  yield the same SHG FROG trace and hence cannot be discriminated.

The most important experimental consideration in SHG FROG is that the SHG crystal has to provide sufficient bandwidth: it must be thin enough to frequency double the entire bandwidth of the pulse to be measured. If the crystal is too thick, then the SHG FROG trace will be too narrow along the spectral axis, leading to nonconvergence of the algorithm. It is important to realize that autocorrelators carry the same crystal-bandwidth requirement, but this requirement is often violated in practice because, unlike FROG, no independent check of the autocorrelation trace exists.

### Transient-grating FROG

This setup is mentioned here because it uses an experimental technique which is fundamental to this work. The transient-grating (TG) beam geometry uses a DFWM type setup with three beams, which requires splitting the input pulse into three pulses. Two of these are overlapped in time and space at the optical Kerr medium, producing a refractive-index grating. The third pulse is variably delayed and is diffracted off the induced grating to produce the signal which emerges in a fourth, unique direction. The four beams in TG geometries usually take the form of what is known as the BoxCARS arrangement [156, 218].

In principle, a four-wave mixing experiment is performed. The setup of a DFWM experiment is described in chapter 8, Fig. 8.6.

TG FROG has several advantages over other  $\chi^{(3)}$  FROG setups such as polarization gate, self-diffraction or third harmonic generation FROG [200]. Since it avoids polarizers as used in PG FROG, it does not distort extremely short pulses, and hence can be used in the deep UV. The mutual polarizations of all three beams may be parallel, which yields greater signal strength because  $\chi_{1111}^{(3)}$  is usually the largest element of the susceptibility tensor. TG FROG is inherently phase matched, and long interaction lengths in the nonlinear medium may be used, which enhance the signal. TG FROG traces are more intuitive than their SHG analog and free from ambiguities. The only disadvantage of TG FROG is the need for three beams and the critical adjustment of the temporal overlap of the two constant-delay beams. The large bandwidth of this entirely phase-matched geometry and the avoidance of potentially pulse-distorting polarizers make TG FROG ideal for measuring extremely short pulses.

### Phase retrieval algorithm

The use of the pulse to gate itself in a spectrogram complicates the reconstruction problem. Spectrogram inversion algorithms require knowledge of the gate function and hence cannot be used. The problem must then be recast into another form. The solution is to rewrite the above expression as the "two-dimensional phase-retrieval problem" [211, 212, 215, 219]. The autocorrelator signal field,  $E(t)E(t - \tau)$  for a SHG autocorrelator, is referred to as  $E_{sig}(t, \tau)$ . Now, consider  $E_{sig}(t, \tau)$  to be the Fourier transform with respect to  $\tau$  of a new quantity that will be called  $\hat{E}_{sig}(t, \Omega)$ . Once this quantity has been determined,  $\hat{E}_{sig}(t, \Omega)$  yields the electric field,  $E(t)$  since  $E(t) = E_{sig}(t, \tau = 0)$ . Thus, it is sufficient to find  $\hat{E}_{sig}(t, \Omega)$ . Rewriting the expression for the FROG trace B.7 in terms of  $\hat{E}_{sig}(t, \Omega)$  yields:

$$I_{\text{FROG}}(\omega, \tau) = \left| \int_{-\infty}^{\infty} \hat{E}_{\text{sig}}(t, \Omega) \exp(-i\omega t - i\Omega\tau) dt d\Omega \right|^2. \quad (\text{B.9})$$

This expression can be verified by simply performing the  $\Omega$  integration, which then yields Eq. B.8. The measured quantity,  $I_{\text{FROG}}^{\text{SHG}}(\omega, \tau)$ , is the squared magnitude of the 2D Fourier transform of  $\hat{E}_{\text{sig}}(t, \Omega)$ . The spectrogram measurement thus yields the magnitude, but not the phase, of the two-dimensional Fourier transform of the desired quantity  $\hat{E}_{\text{sig}}(t, \Omega)$ . The problem is then to find the phase of the Fourier transform of  $\hat{E}_{\text{sig}}(t, \Omega)$ , which is the 2D phase-retrieval problem [220, 221].

This problem is solvable when certain additional information on  $\hat{E}_{\text{sig}}(t, \Omega)$  is available. In ultrashort-pulse measurements, the required additional information is the knowledge of the mathematical form of  $\hat{E}_{\text{sig}}(t, \Omega)$ . For example, in SHG FROG [209], it is known that

$$E_{\text{sig}}(t, \tau) = E(t)E(t - \tau). \quad (\text{B.10})$$

In transient grating FROG,

$$E_{\text{sig}}(t, \tau) = E(t)|E(t - \tau)|^2 \quad \text{or} \quad (\text{B.11})$$

$$E_{\text{sig}}(t, \tau) = E^2(t)E^*(t - \tau), \quad (\text{B.12})$$

depending on which of the two delays is scanned. This additional information turns out to be sufficient.

The pulse-retrieval is supposed to find  $E(t)$ , or, equivalently,  $E_{\text{sig}}(t, \tau)$ . There are two equations, or constraints, that  $E_{\text{sig}}(t, \tau)$  must satisfy. One is that the measured FROG trace is the squared magnitude of the 1D Fourier transform of  $E_{\text{sig}}(t, \tau)$  with respect to time (intensity constraint):

$$I_{\text{FROG}}(\omega, \tau) = \left| \int_{-\infty}^{\infty} E_{\text{sig}}(t, \tau) \exp(-i\omega t) dt \right|^2 \quad (\text{B.13})$$

The other constraint (gate constraint) is the mathematical form of the signal field in terms of the pulse field,  $E(t)$ , for the particular nonlinear-optical process used in the measurement. For SHG FROG and TG FROG,  $E_{\text{sig}}(t, \tau)$  is given by Eqs. B.10-B.12.

These two constraints can be regarded as sub-spaces of the entire space of signal fields which meet the Maxwell equations.

In essence, the FROG retrieval algorithm is very simple: Beginning with an initial guess for the signal field which can be generated, for example, at random, the retrieval algorithm mutually projects the solution iteratively onto both of these sub-spaces given by the two constraints until convergence is achieved. Instead of standard projection, a special type of projections is used which is called "generalized projections" (GP) and which assures convergence of the above scheme for a broader variety of constraints.

GP is implemented in FROG by considering the pulse field,  $E^{(k)}(t_i)$ , the signal field in the  $t - \tau$  domain,  $E_{\text{sig}}^{(k)}(t_i, \tau_j)$ , and the signal field's Fourier transform with respect to time,  $\tilde{E}_{\text{sig}}^{(k)}(\omega_i, \tau_j)$ , where  $i = 1, \dots, N$  for all  $t_i, \tau_i, \omega_i$ . These quantities are each  $N$  or  $N^2$  complex numbers. The superscript,  $(k)$ , in all of these definitions indicates that these quantities are  $k$ th iterations of the actual quantities for the pulse.

In order to perform a GP to the FROG-trace data constraint (intensity constraint), one must simply replace the magnitude of  $\tilde{E}_{\text{sig}}^{(k)}(\omega_i, \tau_j)$  with the square root of the measured FROG trace,  $I_{\text{FROG}}(\omega_i, \tau_j)$ .

In order to perform a GP to the gate constraint, the closest signal field to the current iteration for the signal field,  $E_{\text{sig}}^{(k)}(t_i, \tau_j)$ , that has the desired mathematical form for the particular version

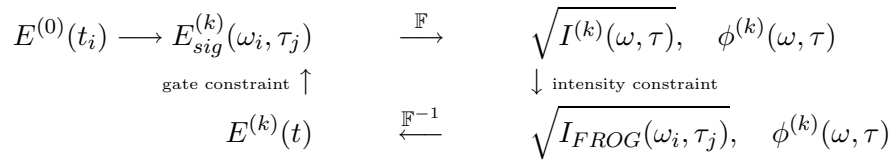


**Figure B.2:** Flow diagram of a FROG inversion algorithm. Within each iteration loop, intensity and gate constraint are applied to the data sets.

of FROG has to be found, depending on the gate function. In other words, a new signal field,  $E_{sig}^{(k+1)}(t_i, \tau_j)$ , that minimizes the merit function:

$$Z = \sum_{i,j=1}^N \left| E_{sig}^{(k)}(t_i, \tau_j) - E_{sig}^{(k+1)}(t_i, \tau_j) \right| \quad (\text{B.14})$$

has to be found. Both of these conditions are met by explicitly substituting Eq. B.10-B.12 into the above distance function and solving directly for the pulse field.

Once  $E^{(k+1)}(t_i)$  is found, the corresponding signal field can be computed for this pulse field using Eq. B.10-B.12 and will be the next iteration for the signal field,  $E_{sig}^{(k+1)}(t_i, \tau_j)$ . By construction,  $E_{sig}^{(k+1)}(t_i, \tau_j)$  satisfies the gate constraint exactly. Since it also minimizes  $Z$ , the process in which  $E_{sig}^{(k)}(t_i, \tau_j)$  is substituted with  $E_{sig}^{(k+1)}(t_i, \tau_j)$  is a GP. The minimization of  $Z$  can, for example, be performed with a conjugate gradient method. Because this minimization is performed in each iteration of the FROG retrieval, it is not necessary to perform the minimization of  $Z$  to its asymptotic limit. The new field then will not be the precise projection, but rather approximate it, which still suffices in FROG pulse retrieval. Later steps make up for this inaccuracy, and, as a result, this approximate procedure results in a significantly faster pulse-retrieval algorithm.

Lately, a new algorithm labeled "principal components generalized projections algorithm" (PCGPA) has been developed which proved to be superior to the above algorithm with respect to stability and computational effort [222]. The phase retrieval problem is mapped to an Eigenvalue problem which finally results in finding the principal component of a diagonal matrix.

The measure of the success of a pulse measurement using FROG is the "FROG error". It is the rms difference between the normalized measured trace  $I_{FROG}(\omega_i, \tau_j)$  and the normalized trace  $I_{FROG}^{(k)}(\omega_i, \tau_j)$  computed from the retrieved pulse field,  $E^{(k)}(t_i)$ , where  $k$  indicates the most recent iteration. It is given by

$$G = \frac{1}{N} \left( \sum_{i,j=1}^N \left| I_{FROG}(\omega_i, \tau_j) - I_{FROG}^{(k)}(\omega_i, \tau_j) \right|^2 \right)^{1/2}. \quad (\text{B.15})$$

The resulting FROG error for experimental traces should reflect the experimental error. Typical values achieved in experiments with  $128 \times 128$  arrays are 1% using PG FROG and 0.5% using SHG FROG. Errors tend to be lower for larger arrays because, due to the fast Fourier transform relations between the delay and frequency axis ranges and increments, the fractional area of the trace that is nonzero is less in the larger array traces.

In this work, FROG traces and the reconstructed fields can be seen in section 3 wherein a commercial FROG retrieval software (FROG 3.03, Femtosoft technologies) has been used. The PCGPA algorithm has also been realized in a Labview<sup>TM</sup> environment, but the reconstruction with the commercial software was preferred since it proved to be more robust.



# Abbreviations

AC	autocorrelation
AOM	acousto-optical modulator
BBO	$\beta$ -Barium Borate
CARS	coherent anti-Stokes Raman scattering
CC	cross-correlation
CCD	charge-coupled device
CPA	chirped pulse amplification
DFM / DFG	difference frequency generation
DFWM	degenerate four-wave mixing
FIR	far infrared
FROG	frequency-resolved optical gating
FRAC	fringe-resolved autocorrelation
FS	fused silica
FWHM	full width at half maximum
FWM	four-wave mixing
GP	generalized projections
GVD / GVM	group velocity dispersion / mismatch
IVR	intramolecular vibrational relaxation
KTP	Potassium Titanyl Phosphate
LBO	Lithium Triborate
LC	liquid crystal
LIF	laser-induced fluorescence
MMDM	micro-machined membrane deformable mirror
MIR	mid infrared (ca. 2-10 $\mu\text{m}$ )
NIR	near infrared (ca. 0.8-2 $\mu\text{m}$ )
OPA	optical parametric amplifier
OCT	optimal control theory
PCGPA	principal components generalized projections algorithm
PDA	Polydiacetylene
PDE	partial differential equation
PES	potential energy surface
PMT	photomultiplier tube
rf	radio frequency
rms	root mean square
SFM / SFG	sum frequency mixing / generation
SH / SHG	second harmonic / second harmonic generation
SiC	silicon carbide
SPM	self-phase modulation
SLM	spatial light modulator
STIRAP	Stimulated Raman scattering involving adiabatic passage
TG FROG	transient gating frequency-resolved optical gating
UV	ultraviolet
VIS	visible (ca. 430-750 nm)
WLC	white light continuum
XFROG	cross correlation frequency-resolved optical gating

# References

- [1] D. J. Nesbitt and R. W. Field, *J. Phys. Chem.* **100**, 12735 (1996).
- [2] P. Brumer and M. Shapiro, *Chem. Phys. Lett.* **126**, 541 (1986).
- [3] C. Chen, Y.-Y. Yin, and D. S. Elliott, *Phys. Rev. Lett.* **64**, 507 (1990).
- [4] S. M. Park, S.-P. Lu, and R. J. Gordon, *J. Chem. Phys.* **94**, 8622 (1991).
- [5] S. Schiemann, A. Kuhn, S. Steuerwald, and K. Bergmann, *Phys. Rev. Lett.* **71**, 3637 (1993).
- [6] D. J. Tannor, R. Kosloff, and S. A. Rice, *J. Chem. Phys.* **85**, 5805 (1986).
- [7] E. D. Potter, J. L. Herek, S. Pederson, Q. Liu, and A. H. Zewail, *Nature* **355**, 66 (1992).
- [8] T. Baumert, M. Grosser, R. Thalweiser, and G. Gerber, *Phys. Rev. Lett.* **67**, 3753 (1991).
- [9] T. Baumert and G. Gerber, *Isr. J. Chem.* **34**, 103 (1994).
- [10] R. S. Judson and H. Rabitz, *Phys. Rev. Lett.* **68**, 1500 (1992).
- [11] W. S. Warren, H. Rabitz, and M. Dahleh, *Science* **259**, 1581 (1993).
- [12] H. Rabitz, R. de Vivie-Riedle, M. Motzkus, and K. Kompa, *Science* **288**, 824 (2000).
- [13] A. Assion, T. Baumert, M. Bergt, T. Brixner, B. Kiefer, V. Seyfried, M. Strehle, and G. Gerber, *Science* **282**, 919 (1998).
- [14] C. J. Bardeen, V. V. Yakovlev, K. R. Wilson, S. D. Carpenter, P. M. Weber, and W. S. Warren, *Chem. Phys. Lett.* **280**, 151 (1997).
- [15] T. C. Weinacht, J. Ahn, and P. H. Bucksbaum, *Nature* **397**, 233 (1999).
- [16] T. Hornung, R. Meier, D. Zeidler, K.-L. Kompa, D. Proch, and M. Motzkus, *Applied Physics B* **71**, 277 (2000).
- [17] R. Bartels, S. Backus, E. Zeek, L. Misoguti, G. Vdovin, I. P. Christov, M. M. Murnane, and H. C. Kapteyn, *Nature* **406**, 164 (2000).
- [18] R. Bartels, S. Backus, I. Christov, H. Kapteyn, and M. Murnane, *Chem. Phys.* **267**, 277 (2001).
- [19] A. Glaß, T. Rozgonyi, T. Feurer, R. Sauerbrey, and G. Szabó, *Appl. Phys. B* **71**, 267 (2000).
- [20] T. Feurer, A. Glaß, T. Rozgonyi, R. Sauerbrey, and G. Szabó, *Chem. Phys.* **267**, 223 (2001).
- [21] M. Bergt, T. Brixner, B. Kiefer, M. Strehle, and G. Gerber, *J. Phys. Chem. A* **103**, 10381 (1999).

- [22] T. Brixner, B. Kiefer, and G. Gerber, *Chem. Phys.* **267**, 241 (2001).
- [23] C. Daniel *et al.*, *Chem. Phys.* **267**, 247 (2001).
- [24] R. J. Levis, G. M. Menhir, and H. Rabitz, *Science* **292**, 709 (2001).
- [25] T. Hornung, R. Meier, and M. Motzkus, *Chem. Phys. Lett.* **326**, 445 (2000).
- [26] T. Hornung, R. Meier, R. de Vivie-Riedle, and M. Motzkus, *Chem. Phys.* **267**, 261 (2001).
- [27] T. C. Weinacht, R. Bartels, S. Backus, P. H. Bucksbaum, B. Pearson, J. M. Geremia, H. Rabitz, H. C. Kapteyn, and M. M. Murnane, *Chem. Phys. Lett.* **344**, 333 (2001).
- [28] Z. Amitay, J. B. Ballard, H. U. Stauffer, and S. R. Leone, *Chem. Phys.* **267**, 141 (2001).
- [29] Š. Vajda, A. Bartelt, E.-C. Kaposta, T. Leisner, C. Lupulescu, S. Minemoto, P. Rosendo-Francisco, and L. Wöste, *Chem. Phys.* **267**, 231 (2001).
- [30] T. C. Weinacht, J. L. White, and P. H. Bucksbaum, *J. Phys. Chem. A* **103**, 10166 (1999).
- [31] W. Lauterborn, T. Kurz, and M. Wiesenfeldt, *Coherent Optics* (Springer, Berlin, Heidelberg, New York, 1995).
- [32] Y. R. Shen, *The Principles of Nonlinear Optics* (John Wiley & Sons, New York, 1984).
- [33] R. W. Boyd, *Nonlinear Optics* (Academic Press, New York, 1992).
- [34] A. Yariv, *Quantum Electronics* (John Wiley & Sons, New York, 1989).
- [35] V. G. Dmitriev, G. G. Gurzadyan, and D. N. Nikogosyan, *Handbook of Nonlinear Optical Crystals*, Vol. 64 of *Springer Series in Optical Sciences* (Springer, Berlin, Heidelberg, New York, 1997).
- [36] D. Eimerl, L. Davis, S. Velsko, E. K. Graham, and A. Zalkin, *J. Appl. Phys.* **62**, 1968 (1987).
- [37] K. Kato, *IEEE J. Quant. Electron.* **22**, 1013 (1986).
- [38] T. Wilhelm, J. Piel, and E. Riedle, *Opt. Lett.* **22**, 1494 (1997).
- [39] V. Krylov, J. Gallus, U. P. Wild, A. Kalintsev, and A. Rebane, *Appl. Phys. B* **70**, 163 (2000).
- [40] V. V. Yakovlev, B. Kohler, and K. R. Wilson, *Opt. Lett.* **19**, 2000 (1994).
- [41] T. S. Sosnowski, P. B. Stephens, and T. B. Norris, *Opt. Lett.* **21**, 140 (1996).
- [42] E. Riedle, M. Beutter, S. Lochbrunner, J. Piel, S. Schenkl, S. Spörlein, and W. Zinth, *Appl. Phys. B* **71**, 457 (2000).
- [43] A. Kummrow, M. Wittmann, F. Tschirschwitz, G. Korn, and E. T. J. Nibbering, *Appl. Phys. B* **71**, 885 (2000).
- [44] J. Piel, M. Beutter, and E. Riedle, *Opt. Lett.* **25**, 180 (2000).
- [45] F. Hache, M. Cavallari, and G. M. Gale, "Ultrafast Visible Optical Parametric Oscillators: A Route to Sub-10-Femtosecond Pulses?," In *Ultrafast Phenomena X*, P. F. Barbara, J. G. Fujimoto, W. H. Knox, and W. Zinth, eds., p. 33 (Springer Verlag, Berlin, 1996).
- [46] L. A. W. Gloster, Z. X. Jiang, and T. A. King, *IEEE J. Quant. Electron.* **30**, 2961 (1994).

- [47] P. Di Trapani, A. Andreoni, G. P. Banfi, C. Solcia, R. Danielius, A. Piskarskas, P. Foggi, M. Monguzzi, and C. Sozzi, *Phys. Rev. A* **51**, 3164 (1995).
- [48] P. Di Trapani, A. Andreoni, C. Solcia, P. Foggi, R. Danielius, D. Dubietis, and A. Piskarskas, *J. Opt. Soc. Am. B* **12**, 2237 (1995).
- [49] P. Di Trapani, A. Andreoni, P. Foggi, C. Solcia, R. Danielius, and A. Piskarskas, *Optics Communications* **119**, 327 (1995).
- [50] M. Nisoli, S. Stagira, S. De Silvestri, O. Svelto, S. Sartania, Z. Cheng, G. Tempea, C. Spielmann, and F. Krausz, *IEEE J. Sel. Top. Quant. Electron.* **4**, 414 (1998).
- [51] A. Shirakawa, I. Sakane, M. Takasaka, and T. Kobayashi, *Appl. Phys. Lett.* **74**, 2268 (1999).
- [52] S. Lochbrunner, pers. comm. (1998).
- [53] T. Feurer, A. Glass, and R. Sauerbrey, *Appl. Phys. B* **65**, 295 (1997).
- [54] J. P. Heritage, R. N. Thurston, W. J. Tomlinson, A. M. Weiner, and R. H. Stolen, *Appl. Phys. Lett.* **47**, 87 (1985).
- [55] M. M. Wefers and K. A. Nelson, *J. Opt. Soc. Am. B* **12**, 1343 (1995).
- [56] A. M. Weiner, *Rev. Sci. Inst.* **71**, 1929 (2000).
- [57] A. M. Weiner, *Prog. Quant. Electr.* **19**, 161 (1995).
- [58] A. M. Weiner, J. P. Heritage, and E. M. Kirschner, *J. Opt. Soc. Am. B* **5**, 1563 (1988).
- [59] A. M. Weiner, J. P. Heritage, and J. A. Salehi, *Opt. Lett.* **13**, 300 (1988).
- [60] T. Hornung, "Amplituden- und Phasenmodulation von ultrakurzen Lichtpulsen mit einer Flüssigkristallmaske und ihre Anwendung zur Kontrolle von Photonenübergängen in Na," MPQ-Report 247, MPI für Quantenoptik (1999) .
- [61] D. H. Reitze, A. M. Weiner, and D. E. Leaird, *Appl. Phys. Lett.* **61**, 1260 (1992).
- [62] A. Efimov, C. Schaffer, and D. H. Reitze, *J. Opt. Soc. Am. B* **12**, 1968 (1995).
- [63] D. Yelin, D. Meshulach, and Y. Silberberg, *Opt. Lett.* **22**, 1793 (1997).
- [64] E. Zeek, K. Maginnis, S. Backus, U. Russek, M. M. Murnane, G. Mourou, H. C. Kapteyn, and G. Vdovin, *Opt. Lett.* **24**, 493 (1999).
- [65] D. Zeidler, T. Hornung, D. Proch, and M. Motzkus, *Appl. Phys. B* **70**, S125 (2000).
- [66] A. M. Weiner, S. Oudin, D. E. Leaird, and D. H. Reitze, *J. Opt. Soc. Am. A* **10**, 1112 (1993).
- [67] M. M. Wefers and K. A. Nelson, *Opt. Lett.* **18**, 2032 (1993).
- [68] K. Takasago, T. Itoh, M. Takekawa, K. Utoh, and F. Kannari, *Jpn. J. Appl. Phys.* **35**, 624 (1996).
- [69] K. Takasago, M. Takekawa, M. Suzuki, K. Komori, and F. Kannari, *IEEE J. Sel. Top. Quant. Electron.* **4**, 346 (1998).
- [70] M. Hacker, G. Stobrawa, and T. Feurer, *Optics Express* **9**, 191 (2001).

- [71] A. M. Weiner, D. E. Leaird, J. S. Patel, and J. R. Wullert, *IEEE J. Quant. Electron.* **28**, 908 (1992).
- [72] M. B. Danailov and I. P. Christov, *J. of Modern Optics* **36**, 725 (1989).
- [73] M. M. Wefers and K. A. Nelson, *IEEE J. Quant. Electron.* **32**, 161 (1996).
- [74] J. Paye and A. Migus, *J. Opt. Soc. Am. B* **12**, 1480 (1995).
- [75] R. N. Thurston, J. P. Heritage, A. M. Weiner, and W. J. Tomlinson, *IEEE J. Quant. Electron.* **22**, 682 (1986).
- [76] C. Dorrer and F. Salin, *IEEE J. Sel. Top. Quant. Electron.* **4**, 342 (1998).
- [77] A. M. Weiner, D. E. Leaird, J. S. Patel, and J. R. Wullert, *Opt. Lett.* **15**, 326 (1990).
- [78] T. Brixner, M. Strehle, and G. Gerber, *Appl. Phys. B* **68**, 281 (1999).
- [79] T. Baumert, T. Brixner, V. Seyfried, M. Strehle, and G. Gerber, *Appl. Phys. B* **65**, 779 (1997).
- [80] A. Efimov and D. H. Reitze, *Opt. Lett.* **23**, 1612 (1998).
- [81] C. Dorrer, F. Salin, F. Verluise, and J. P. Huignard, *Opt. Lett.* **23**, 709 (1998).
- [82] T. Brixner and G. Gerber, *Opt. Lett.* **26**, 557 (2001).
- [83] G. Stobrawa, M. Hacker, T. Feurer, D. Zeidler, M. Motzkus, and F. Reichel, *Appl. Phys. B* **72**, 627 (2001).
- [84] D. J. Kane and R. Trebino, *IEEE J. Quant. Electron.* **29**, 571 (1993).
- [85] W. H. Press, S. A. Teukolsky, W. T. Vetterling, and B. P. Flannery, *Numerical Recipes in C* (Cambridge University Press, Cambridge, 1992).
- [86] G. Stobrawa, M. Hacker, B. Schmidt, and T. Feurer, <http://www.lab2.de> (2000).
- [87] L. Wang and A. M. Weiner, *Opt. Commun.* **167**, 211 (1999).
- [88] M. A. Dugan, J. X. Tull, and W. S. Warren, *J. Opt. Soc. Am. B* **14**, 2348 (1997).
- [89] C. W. Hillegas, J. X. Tull, D. Goswami, D. Strickland, and W. S. Warren, *Opt. Lett.* **19**, 737 (1994).
- [90] J. X. Tull, M. A. Dugan, and W. S. Warren, "High-Resolution, Ultrafast Laser Pulse Shaping and Its Applications," in *Advances in Magnetic and Optical Resonance* (Academic Press, 1997), Vol. 20, p. 1.
- [91] M. R. Fetterman, D. Goswami, D. Keusters, W. Yang, J.-K. Rhee, and W. S. Warren, *Opt. Express* **3**, 366 (1998).
- [92] E. Zeek, R. Bartels, M. M. Murnane, H. C. Kapteyn, and S. Backus, *Opt. Lett.* **25**, 587 (2000).
- [93] G. Chériaux, O. Albert, V. Wänman, J. P. Chambaret, C. Félix, and G. Mourou, *Opt. Lett.* **26**, 169 (2001).
- [94] M. R. Armstrong, P. Plachta, E. A. Ponomarev, and R. J. D. Miller, *Opt. Lett.* **26**, 1152 (2001).
- [95] T. Witte, D. Zeidler, D. Proch, K. L. Kompa, and M. Motzkus, *Opt. Lett.* **27**, 131 (2002).

- [96] M. Hacker, T. Feurer, R. Sauerbrey, T. Lucza, and G. Szabó, *J. Opt. Soc. Am. B* **18**, 866 (2001).
- [97] F. Eickemeyer, R. A. Kaindl, M. Woerner, T. Elsaesser, and A. M. Weiner, *Opt. Lett.* **25**, 1472 (2000).
- [98] R. A. Kaindl, M. Wurm, K. Reimann, P. Hamm, A. M. Weiner, and M. Wörner, *J. Opt. Soc. Am. B* **17**, 2086 (2000).
- [99] G. Trinkunas, J. L. Herek, T. Polivka, V. Sundstrom, and T. Pullerits, *Phys. Rev. Lett.* **86**, 4167 (2001).
- [100] D. Zeidler, T. Witte, D. Proch, and M. Motzkus, *Opt. Lett.* **26**, 1921 (2001).
- [101] H.-S. Tan, W. S. Warren, and E. Schreiber, *Opt. Lett.* **26**, 1812 (2001).
- [102] D. Zeidler, T. Witte, D. Proch, and M. Motzkus, *Appl. Phys. B*, in print (2002).
- [103] W. Zhu, J. Botina, and H. Rabitz, *J. Chem. Phys.* **108**, 1953 (1998).
- [104] K. Sundermann and R. de Vivie-Riedle, *J. Chem. Phys.* **110**, 1896 (1999).
- [105] H. Kawashima, M. M. Wefers, and K. A. Nelson, *Annu. Rev. Phys. Chem.* **46**, 627 (1995).
- [106] N. F. Scherer, A. J. Ruggiero, M. Du, and G. R. Fleming, *J. Chem. Phys.* **93**, 856 (1990).
- [107] R. K. Shelton, L.-S. Ma, H. C. Kapteyn, M. M. Murnane, J. L. Hall, and J. Ye, *Science* **293**, 1286 (2001).
- [108] G. M. Gale, F. Hache, and M. Cavallari, *IEEE J. Sel. Top. Quant. Electron.* **4**, 224 (1998).
- [109] A. Shirakawa, I. Sakane, and T. Kobayashi, *Opt. Lett.* **23**, 1292 (1998).
- [110] G. Cerullo, M. Nisoli, S. Stagira, and S. De Silvestri, *Opt. Lett.* **23**, 1283 (1998).
- [111] D. Zeidler, S. Frey, K.-L. Kompa, and M. Motzkus, *Phys. Rev. A* **64**, 023420 (2001).
- [112] H.-P. Schwefel, *Evolution and Optimum Seeking* (John Wiley & Sons, New York, 1995).
- [113] D. E. Goldberg, *Genetic algorithms in Search, Optimization & Machine Learning* (Addison-Wesley, Reading, 1997).
- [114] J. A. Nelder and R. Mead, *Computer Journal* **7**, 308 (1965).
- [115] T. Feurer, *Appl. Phys. B* **68**, 55 (1999).
- [116] N. Metropolis, A. W. Rosenbluth, M. N. Rosenbluth, A. H. Teller, and E. Teller, *J. Chem. Phys.* **21**, 1087 (1953).
- [117] S. Kirkpatrick, C. D. Gelatt, and M. P. Vecchi, *Science* **220**, 671 (1983).
- [118] G. Dueck and T. Scheuer, *J. Comp. Phys.* **90**, 161 (1990).
- [119] G. J. Tóth, A. Lőrincz, and H. Rabitz, *J. Chem. Phys.* **101**, 3715 (1994).
- [120] B. Amstrup, G. J. Tóth, G. Szabó, H. Rabitz, and A. Lőrincz, *J. Phys. Chem.* **99**, 5206 (1995).
- [121] P. Gross, D. Neuhauser, and H. Rabitz, *J. Chem. Phys.* **98**, 4557 (1993).
- [122] G. Dueck, *J. Comp. Phys.* **104**, 86 (1993).

- [123] G. Schrimpf, J. Schneider, H. Stamm-Wilbrandt, and G. Dueck, *J. Comp. Phys.* **159**, 139 (2000).
- [124] J. D. Watson and F. H. C. Crick, *Nature* **171**, 737 (1953).
- [125] B. J. Pearson, J. L. White, T. C. Weinacht, and P. H. Bucksbaum, *Phys. Rev. A* **63**, 063412 (2001).
- [126] D. Meshulach, D. Yelin, and Y. Silberberg, *Opt. Comm.* **138**, 345 (1997).
- [127] D. Meshulach and Y. Silberberg, *Nature* **396**, 239 (1998).
- [128] D. Meshulach, D. Yelin, and Y. Silberberg, *J. Opt. Soc. Am. B* **15**, 1615 (1998).
- [129] D. Meshulach and Y. Silberberg, *Phys. Rev. A* **60**, 1287 (1999).
- [130] T. Taneichi, T. Kobayashi, Y. Ohtsuki, and Y. Fujimura, *Chem. Phys. Lett.* **231**, 50 (1994).
- [131] M. M. Wefers and K. A. Nelson, *Opt. Lett.* **20**, 1047 (1995).
- [132] R. Meier, Diploma thesis, Technische Universität München, 2000.
- [133] A. Efimov, M. D. Moores, N. M. Beach, J. L. Krause, and D. H. Reitze, *Opt. Lett.* **23**, 1915 (1998).
- [134] C. R. Vidal, in *Atomic, Molecular, and Optical Physics: Atoms and Molecules*, F. Dunning and R. Hulet, eds., (Academic Press, San Diego, 1996), Vol. 29B, p. 67.
- [135] M. D. Crisp, *Phys. Rev. A* **1**, 1604 (1970).
- [136] J. K. Ranka, R. W. Schirmer, and A. L. Gaeta, *Phys. Rev. A* **57**, R36 (1998).
- [137] S. Speiser and J. Jortner, *Chem. Phys. Lett.* **44**, 399 (1976).
- [138] A. Lindgård and S. E. Nielson, *At. Data Nucl. Tab.* **19**, 571 (1977).
- [139] N. Dudovich, B. Dayan, S. M. Gallagher Faeder, and Y. Silberberg, *Phys. Rev. Lett.* **86**, 47 (2001).
- [140] *Chemical Reactions and Their Control on the Femtosecond Timescale*, Vol. 101 of *Advances in Chemical Physics*, P. Gaspard and I. Burghardt, eds., (John Wiley & Sons, Bruxelles, Belgium, 1997).
- [141] *Femtosecond Chemistry*, J. Manz and L. Wöste, eds., (VCH Verlagsgesellschaft, Weinheim, 1995).
- [142] A. H. Zewail, *J. Phys. Chem. A* **104**, 5660 (2000).
- [143] A. Vierheilig, T. Chen, P. Waltner, W. Kiefer, A. Materny, and A. H. Zewail, *Chem. Phys. Lett.* **312**, 349 (1999).
- [144] T. Chen, A. Vierheilig, P. Waltner, W. Kiefer, and A. Materny, *Chem. Phys. Lett.* **325**, 176 (2000).
- [145] T. Chen, A. Vierheilig, W. Kiefer, and A. Materny, *Phys. Chem. Chem. Phys.* **3**, 5408 (2001).
- [146] T. Chen, A. Vierheilig, P. Waltner, M. Heid, W. Kiefer, and A. Materny, *Chem. Phys. Lett.* **326**, 375 (2000).

- [147] D. Zeidler, S. Frey, W. Wohlleben, M. Motzkus, F. Busch, T. Chen, W. Kiefer, and A. Materny, *J. Chem. Phys.* **116**, 5231 (2002).
- [148] M. Materny and W. Kiefer, *Macromolecules* **25**, 5074 (1992).
- [149] A. Materny, PhD thesis, Universität Würzburg, 1992.
- [150] M. Yoshizakawa, Y. Hattori, and T. Kobayashi, *Phys. Rev. B* **49**, 13259 (1994).
- [151] D. N. Batchelder and D. Bloor, *J. Polym. Science: Polym. Phys. Ed.* **17**, 569 (1979).
- [152] T. Lang, K.-L. Kompa, and M. Motzkus, *Chem. Phys. Lett.* **310**, 65 (1999).
- [153] T. Lang, PhD thesis, Technische Universität München, 2001.
- [154] M. Motzkus, S. Pedersen, and A. H. Zewail, *J. Phys. Chem.* **100**, 5260 (1996).
- [155] T. Chen, PhD thesis, Universität Würzburg, 2001.
- [156] M. Motzkus, PhD thesis, Ludwig-Maximilians-Universität München, 1994.
- [157] W. H. Breckenridge and H. Umemoto, "Collisional Quenching of Electronically Excited Metal Atoms," in *Dynamics of the Excited State*, K. P. Lawley, ed., (John Wiley & Sons, 1982), p. 325.
- [158] L. H. Vassie and H. H. Telle, "Radiative lifetimes and collision processes in sodium-rare gas and sodium-hydrogen systems," in *Laser Chemistry* (Harwood Academic Publishers, 1994), Vol. 15, p. 1.
- [159] P. Hering, S. L. Cunha, and K.-L. Kompa, *J. Phys. Chem.* **91**, 5459 (1987).
- [160] I. V. Hertel, "Progress in Electronic-to-Vibrational Energy Transfer," in *Dynamics of the Excited State*, K. Lawley, ed., (John Wiley & Sons, 1982), p. 475.
- [161] S. Bililign and P. D. Kleiber, *Phys. Rev. A* **42**, 6938 (1990).
- [162] S. Bililign and P. D. Kleiber, *J. Chem. Phys.* **96**, 213 (1992).
- [163] D. R. Yarkony, *J. Chem. Phys.* **84**, 3209 (1986).
- [164] M. D. Hack, A. W. Jasper, Y. L. Volobuev, D. W. Schwenke, and D. G. Truhlar, *J. Phys. Chem. A* **103**, 6309 (1999).
- [165] P. Halvick and D. G. Truhlar, *J. Chem. Phys.* **96**, 2895 (1992).
- [166] N. C. Blais and D. G. Truhlar, *J. Chem. Phys.* **79**, 1334 (1983).
- [167] G. W. Tawa, S. L. Mielke, D. G. Truhlar, and D. W. Schwenke, *J. Chem. Phys.* **100**, 5751 (1994).
- [168] P. Botschwina, W. Meyer, I. V. Hertel, and W. Reiland, *J. Chem. Phys.* **75**, 5438 (1981).
- [169] R. de Vivie-Riedle, P. Hering, and K.-L. Kompa, *Z. Phys. D* **17**, 299 (1990).
- [170] J. Franck and R. W. Wood, *Verh. Dt. Phys. Ges.* **13**, 78 (1911).
- [171] R. W. Wood, *Verh. Dt. Phys. Ges.* **13**, 72 (1911).
- [172] D. W. Schwenke, S. L. Mielke, G. J. Tawa, R. S. Friedman, P. Halvick, and D. G. Truhlar, *Chem. Phys. Lett.* **203**, 565 (1993).
- [173] M. S. Topaler and D. G. Truhlar, *J. Chem. Phys.* **107**, 392 (1997).



- [174] M. S. Topaler, M. D. Hack, T. C. Allison, Y.-P. Liu, S. L. Mielke, D. W. Schwenke, and D. G. Truhlar, *J. Chem. Phys.* **106**, 8699 (1997).
- [175] S. L. Mielke, G. J. Tawa, and D. G. Truhlar, *J. Am. Chem. Soc.* **115**, 6436 (1993).
- [176] S. L. Mielke, G. J. Tawa, D. G. Truhlar, and D. W. Schwenke, "Partial widths of Feshbach funnel resonances in the Na(3p)-H<sub>2</sub> exciplex," University of Minnesota Supercomputer Institute Research Report UMSI 93/70, University of Minnesota (1993) .
- [177] M. Ben-Nun, T. J. Martinez, and R. D. Levine, *J. Phys. Chem A* **101**, 7522 (1997).
- [178] T. J. Martinez, M. Ben-Nun, and R. D. Levine, *J. Phys. Chem. A* **101**, 6389 (1997).
- [179] R. de Vivie-Riedle, K. Sundermann, and M. Motzkus, *Faraday Discuss.* 113 (1999).
- [180] M. Motzkus, G. Pichler, K.-L. Kompa, and P. Hering, *J. Chem. Phys.* **106**, 9057 (1997).
- [181] G. Pichler, M. Motzkus, S. L. Cunha, R. R. B. Correia, K.-L. Kompa, and P. Hering, *II Nuovo Cimento* **14**, 1065 (1992).
- [182] M. Motzkus, G. Pichler, K.-L. Kompa, and P. Hering, *Chem. Phys. Lett.* **257**, 181 (1996).
- [183] M. Motzkus, G. Pichler, K. L. Kompa, and P. Hering, *J. Chem. Phys.* **108**, 9291 (1998).
- [184] W. Reiland, U. Tittes, and I. V. Hertel, *Phys. Rev. Lett.* **48**, 1389 (1982).
- [185] U. Marvet and M. Dantos, *Chem. Phys. Lett.* **245**, 393 (1995).
- [186] C. R. Vidal, "Vapor cells and Heat Pipes," in *Experimental Methods in the Physical Science* (Academic Press, London, 1996), Vol. 29B, p. 67.
- [187] P. D. Dunn and D. A. Reay, *Heat Pipes, Pergamon International Library of Science, Technology, Engineering and Social Studies*, 3rd ed. (Pergamon Press, Oxford, 1982).
- [188] R. de Vivie-Riedle, personal communication (2001).
- [189] F. Rossi and J. Pascale, *Phys. Rev. A* **32**, 2657 (1985).
- [190] D. Geppert, Diploma thesis, to be published, Ludwig-Maximilians-Universität München, 2001.
- [191] A. Hofmann, PhD thesis, Ludwig-Maximilians-Universität München, 2001.
- [192] R. R. B. Correia, S. L. S. Cunha, M. Motzkus, G. Pichler, and P. Hering, *Brazilian Journal of Physics* **22**, 11 (1992).
- [193] M. Motzkus, G. Pichler, M. Dillmann, K.-L. Kompa, and P. Hering, *Appl. Phys. B* **57**, 261 (1993).
- [194] R. Zadoyan, D. Kohen, D. A. Lidar, and V. A. Apkarian, *Chem. Phys.* **266**, 323 (2001).
- [195] S. Lochbrunner, W. Fuß, W. E. Schmid, and K.-L. Kompa, *J. Phys. Chem. A* **102**, 9334 (1998).
- [196] W. Fuss, W. E. Schmid, and S. A. Trushin, *J. Chem. Phys.* **112**, 8347 (2000).
- [197] A. Hofmann, L. Kurtz, and R. de Vivie-Riedle, *Appl. Phys. B* **71**, 391 (2000).
- [198] A. Hofmann and R. de Vivie-Riedle, *J. Chem. Phys.* **112**, 5054 (2000).
- [199] L. Kurtz, A. Hofmann, and R. de Vivie-Riedle, *J. Chem. Phys.* **114**, 6151 (2001).

- [200] R. Trebino, K. W. DeLong, D. N. Fittinghoff, J. N. Sweetser, M. A. Krumbügel, B. A. Richman, and D. J. Kane, *Rev. Sci. Instrum.* **68**, 3277 (1997).
- [201] J. C. Diels, J. J. Fontaine, I. C. McMichael, and F. C. Simoni, *Appl. Opt.* **24**, 1270 (1985).
- [202] M. Maier, W. Kaiser, and J. A. Giordmaine, *Phys. Rev. Lett.* **17**, 1275 (1966).
- [203] J. A. Giordmaine, P. M. Rentzepis, S. L. Shapiro, and K. W. Wecht, *Appl. Phys. Lett.* **11**, 216 (1967).
- [204] E. P. Ippen and C. V. Shank, *Ultrashort Light Pulses — Picosecond Techniques and Applications* (Springer, Berlin, 1977).
- [205] D. Zeidler, Diploma thesis, Georg-August-Universität Göttingen, 1998.
- [206] R. A. Altes, *J. Acoust. Soc. Am.* **67**, 1232 (1980).
- [207] L. Cohen, *Proc IEEE* **77**, 941 (1989).
- [208] K. W. DeLong, R. Trebino, and D. J. Kane, *J. Opt. Soc. Am. B* **11**, 1595 (1995).
- [209] K. W. DeLong, R. Trebino, J. Hunter, and W. E. White, *J. Opt. Soc. Am. B* **11**, 2206 (1994).
- [210] D. N. Fittinghoff, J. L. Bowie, J. N. Sweetser, R. T. Jennings, M. A. Krumbügel, K. W. DeLong, R. Trebino, and I. A. Walmsley, *Opt. Lett.* **21**, 884 (1996).
- [211] D. J. Kane and R. Trebino, *Opt. Lett.* **18**, 823 (1993).
- [212] D. J. Kane and R. Trebino, *IEEE J. Quant. Electron.* **29**, 571 (1993).
- [213] K. W. DeLong, C. L. Ladera, R. Trebino, B. Kohler, and K. R. Wilson, *Opt. Lett.* **20**, 486 (1995).
- [214] K. W. DeLong, D. N. Fittinghoff, and R. Trebino, *IEEE J. Quant. Electron.* **32**, 1253 (1996).
- [215] R. Trebino and D. J. Kane, *J. Opt. Soc. Am. A* **10**, 1101 (1993).
- [216] G. Taft, A. Rundquist, M. M. Murnane, H. C. Kapteyn, K. W. DeLong, R. Trebino, and I. P. Christov, *Opt. Lett.* **20**, 743 (1995).
- [217] J. Paye, M. Ramaswamy, J. G. Fujimoto, and E. P. Ippen, *Opt. Lett.* **18**, 1946 (1993).
- [218] A. C. Eckbreth, *Appl. Phys. Lett.* **32**, 421 (1978).
- [219] D. J. Kane and R. Trebino, In *Ultrafast Phenomena VIII*, J. L. Martin, R. Migus, G. A. Mourou, and A. H. Zewail, eds., (Springer, 1993).
- [220] H. Stark, *Image Recovery: Theory and Application* (Academic, Orlando, 1987).
- [221] D. Peri, *Appl. Opt.* **26**, 1782 (1987).
- [222] D. J. Kane, *IEEE J. Quant. Electron.* **35**, 421 (1999).

# Acknowledgments

Finally, the pleasant duty remains to thank all those who contributed to this work.

First of all, I am indebted to Prof. Karl-Ludwig Kompa who generously and continuously supported this work scientifically and financially. He gave me the opportunity to present my results at various conferences and continuously encouraged me to further pursue my goals in science.

I thank Marcus Motzkus for giving me the opportunity to work on all the projects, for giving me the opportunity to pursue experiments my way and thus learn from my mistakes, and for starting all the collaborations that promoted the experiments.

Throughout my time at the institute, Tobias Lang has taught me the might of patience. His jovial composure has always been a great help for me, and his devotion to details an inspiration. I esteem his forthrightness and frankness over the last three years. Thomas Witte has taught me the necessity of discriminating between important and secondary matters in order not to lose sight of the big picture. I thank Tobias and Thomas for the many discussions about physics and the rest of the world during all the lab nights, and for all the belly aches from laughter.

Susanne Frey has taught me the meaning of tenacity in pursuing an objective. I thank her for the enjoyable and constructive time in the lab.

Detlev Proch has taught me the importance of choosing the right words at the right time, though I was, maybe, not the best scholar in this respect. He proofread every single line of everything that has left my desk in these three years. I thank him for teaching me how to express myself in English, and for the many good pieces of advice he gave me whenever I requested them.

Regina de Vivie-Riedle has taught me that every problem has a solution. I thank her, Angelika, and Lukas for patiently explaining theory to someone from the lab bothering them with experimental odds and ends ("reality").

Thomas Feurer, Martin Hacker, Gregor Stobrawa, Arnulf Materny and Felix Busch have taught me that science is fun. I thank them for the pleasant and stimulating lab nights on the high resolution pulse shaper and the polydiacetylene project and Jake Yeston for his endurance in proofreading.

Thomas Hornung, Richard Meier, and Lars Windhorn have taught me how to perform experiments without wasting too much time on inanities. I thank them for a pleasant time in the lab.

Johannes Piel and Stefan Lochbrunner have taught me how to knot my fingers on the adjustment of non-collinear OPAs. I thank them for the many tricks on ultrashort pulse generation.

I thank Hrvoje Skenderović and Wendel Wohlleben for their help with the high pressure heat pipe.

Hans Bauer, Karl Bauer, and Georg Brandl have taught me the vital fundamentals of understanding the Bavarian language. I thank them and the mechanical workshop for their outstanding construction work (and many good laughs). I also thank all the administrative assistants for their help with the bureaucratic zoo.

Finally, I thank Michaela, Oliver, Harald, Catherine, and my parents for returning me to real life once in a while when things went haywire in the lab ("the world will still turn tomorrow"), and Camilla for her patience with a stubborn physicist.



# Curriculum Vitae

Dirk Zeidler

Born on February 26, 1972 in Detmold, Germany as the eldest son of Reinhold Zeidler, and Christiane Zeidler, maiden name Koesling. Two brothers: Frank (born 1974) and Ralf (born 1985)

German citizenship, unmarried.

## Education

- |           |  |
|-----------|--|
| 1978-1982 | Elementary school in Lemgo.  |
| 1982-1991 | Engelbert-Kämpfer-Gymnasium, grammar school in Lemgo. Graduation 1991 with the "Abitur" (general qualification for university entrance). "Leistungskurse" (university preparatory courses) : mathematics and physics.                                |
| 1991-1992 | Military service as radio operator.  |
| 1992-1995 | Study of physics and mathematics at the Technische Universität Clausthal, "Vordiplom" (BSc) in mathematics and physics in 1994.  |
| 1995-1998 | Study of physics and mathematics at the Georg-August-Universität Göttingen. Graduation February 1998 in physics with "Diplom" (MSc) at Drittes Physikalisches Institut. Subject of Diploma thesis "Optischer Kerr-Effekt" (Prof. Dr. W. Lauterborn). |
| 1998-2001 | Graduate student in physics at Max-Planck-Institut für Quantenoptik (Prof. Dr. Dr. h.c. K.-L. Kompa).  |

αυτισ επετα πεδονδε

κυλιυδετο λαασ ανειδησ.